Géry de Saxcé
Abdelbacet Oueslati
Eric Charkaluk
Jean-Bernard Tritsch *Editors*

Limit State of Materials and Structures

Direct Methods 2

Springer

Limit State of Materials and Structures

Géry de Saxcé • Abdelbacet Oueslati •
Eric Charkaluk • Jean-Bernard Tritsch
Editors

Limit State of Materials and Structures

Direct Methods 2

Springer

Editors
Géry de Saxcé
Laboratoire de Mécanique de Lille
Bd Paul Langevin
Villeneuve d'Ascq, France

Eric Charkaluk
Laboratoire de Mécanique de Lille
Bd Paul Langevin
Villeneuve d'Ascq, France

Abdelbacet Oueslati
Laboratoire de Mécanique de Lille
Bd Paul Langevin
Villeneuve d'Ascq, France

Jean-Bernard Tritsch
Laboratoire de Mécanique de Lille
Bd Paul Langevin
Villeneuve d'Ascq, France

ISBN 978-94-007-5424-9 ISBN 978-94-007-5425-6 (eBook)
DOI 10.1007/978-94-007-5425-6
Springer Dordrecht Heidelberg New York London

Library of Congress Control Number: 2012951710

Printed on acid-free paper

Springer is part of Springer Science+Business Media (www.springer.com)

Foreword

To determine limit loads for structures and structural elements operating beyond the elastic limit is since ever one of the most important tasks of engineers. For this purpose, "Direct Methods", embracing Limit Load and Shakedown Analysis, play an increasing role due to the fact that they allow rapid access to the requested information in mathematically constructive manners.

This book reports on recent progress in this exciting field of research and is the outcome of an international workshop dedicated to this subject held at the University of Sciences and Technology of Lille in October 2009. This event gathered about 30 scientists from 6 countries and was a follow-up of a similar meeting at Aachen University of Technology in November 2007.

The contributions in this book stem in particular from the areas of new numerical developments rendering the methods more attractive for industrial design, extensions of the general methodology to new horizons of application, probabilistic approaches and concrete technological applications.

The papers are arranged according to the order of the presentations in the workshop and give an excellent insight into state-of-the-art developments in this broad and growing field of research.

We warmly thank all the scientists, who have contributed by their outstanding contributions to the quality of this edition. Special thanks go to Géry de Saxcé, Abdelbacet Oueslati, Eric Charkaluk and Jean-Bernard Tritsch for their great work in editing this book and putting together the manuscript to its final shape. We hope you may enjoy reading this book!

Leicester, UK — A. Ponter
Aachen, Germany — D. Weichert

Contents

The Ratchet Limit—A Coupled Dual Minimisation Problem

Alan R.S. Ponter

Abstract Ponter and Chen have developed methods for the evaluating of the shakedown limit and ratchet limit for a elastic-perfectly plastic body subjected to cyclic thermal and mechanical loading. The procedure, the Linear Matching Method, was derived from a general minimum theorem and a minimisation process based on the solution of a sequence of linear problems with spatially varying linear moduli. In this paper the fundamentals of these methods are readdressed for elastic/perfect plasticity with two objectives in mind; the first to provide a more general approach for wider classes of problems and potential procedures, and the second to discuss existing methods within this more general context. A von Mises yield condition is assumed. This results in a dual coupled minimisation process. The method is illustrated by the solution of the Bree problem. Issues of convergence are discussed.

1 Introduction

Ponter et al. [1, 2] and Ponter and Chen [3, 4] developed methods for the evaluating the shakedown limit and ratchet limit for a elastic-perfectly plastic body subjected to cyclic thermal and mechanical loading. The procedure was derived upon a general minimum theorem and a minimisation process based on the solution of a sequence of linear problems with spatially varying linear moduli. For each linear problem, conditions of compatibility and equilibrium are satisfied and convergence to the cyclic state corresponding to each limit was achieved by iteratively matching the material properties so that the objective functional was reduced. The derivation for the ratchet limit was restricted to problems with two distinct extremes of the linearly elastic stress history with an additional constant load [4].

These methods, termed Linear Matching Methods, have been extensively applied to problems involving thermo mechanical loading and, through various adaptations, extended to the calculation required for the stages of the UK structure life assessment method R5 [5, 6], including extensions to high temperature creep problems.

A.R.S. Ponter (✉)
University of Leicester, Leicester, UK
e-mail: asp@le.ac.uk

G. Saxcé et al. (eds.), *Limit State of Materials and Structures*,
DOI 10.1007/978-94-007-5425-6_1,

In this paper the fundamentals of these methods are readdressed for elastic/perfect plasticity with two objectives in mind. The first is to provide a more general approach for wider classes of problems and potential procedures. The second objective is to discuss existing method within this more general context. A von Mises yield condition is assumed and the main emphasis of the paper is on methods for the ratchet limit.

An elastic perfectly plastic body is capable of exhibiting a range of modes of behaviour, elastic behaviour, shakedown, reverse plasticity (or plastic accommodation), ratcheting and plastic collapse. Within the ranges of loading corresponding to each of these modes, the plastic strain rate history has certain well defined kinematic properties. At the interface between these ranges, the kinematic properties are a combination of those found in the adjacent regions. Irrespective of the mode of behaviour, the cyclic state has the property of minimising a certain objective functional [3].

The approach adopted in this paper first defines the classes of kinematic histories that correspond to the shakedown, ratchet and collapse limits. The kinematic histories are further subdivided, for the ratchet limit, into components that correspond to either reverse plasticity (no displacement growth) or ratcheting (displacement growth). The objective function may then be minimised for each of the defined kinematics classes and hence the characteristics corresponding to each boundary. The minimisation process is achieved by the Linear Matching Method as described by Ponter and Chen [3, 4]. For the ratcheting limit this defines a coupled dual minimisation problem.

A theory is developed for an arbitrary history of load and temperature scaled by a single load parameter. The special case of a combination of a variable load and a constant load is then considered, recovering earlier results. The method is demonstrated through the classic Bree problem and questions of convergence are considered.

2 The General Cyclic Problem

Consider a body with volume V with surface S. Within V a cyclic history of temperature $\lambda\theta(x_i, t)$ occurs within a typical cycle $0 \le t \le \Delta t$. Over S_T, part of S, a cyclic history of load $\lambda P_i(x_i, t)$ is applied. Here λ denotes a scalar load multiplier. Over the remainder of S, S_u, zero displacements are maintained. Hence we are concerned with a class of loading histories defined by the magnitude of λ. The material is elastic, perfectly plastic. The von Mises yield condition $f(\sigma_{ij}) = \bar{\sigma}(\sigma_{ij}) - \sigma_y = 0$ is assumed, where $\bar{\sigma}$ denotes the von Mises effective stress and σ_y is the uniaxial yield stress. An associated flow rule is also assumed. An arbitrary asymptotic cyclic history is of the form;

$$\sigma_{ij} = \lambda\hat{\sigma}_{ij} + \bar{\rho}_{ij} + \rho^r_{ij} \tag{1}$$

Table 1 Cyclic variables and their relationships

$0 \le t \le \Delta t$ typical cycle
λ—load multiplier
$\lambda\hat{\sigma}_{ij}$—linear elastic solution $0 \le t \le \Delta t$
$\bar{\rho}_{ij}$—*constant* residual stress field $\quad \bar{\varepsilon}'^{T}_{ij} = (1/2\mu)\bar{\rho}'_{kl} + \bar{\varepsilon}'^{p}_{ij}$
$\bar{\varepsilon}^{T}_{kk} = (1/3K)\bar{\rho}_{kk}$
ρ^{r}_{ij}—*varying* residual stress field
$\dot{\varepsilon}'^{rT}_{ij} = (1/2\mu)\dot{\rho}'^{r}_{kl} + \dot{\varepsilon}'^{pr}_{ij}$ and $\dot{\varepsilon}^{rT}_{kk} = (1/3K)\dot{\rho}^{r}_{kk}$
$\varepsilon^{p}_{ij} = \bar{\varepsilon}^{p}_{ij} + \varepsilon^{pr}_{ij}$ total plastic strain
$\rho^{r}_{ij}(0) = \rho^{r}_{ij}(\Delta t)$
$\Delta\varepsilon^{pr}_{ij} = \int_0^{\Delta t} \dot{\varepsilon}^{pr}_{ij}\, dt$ compatible with Δu^{p}_{i}, the ratchet displacement/cycle

where $\lambda\hat{\sigma}_{ij}$ denotes the linear elastic solution, $\bar{\rho}_{ij}$ denote the residual stress field at the beginning and end of the cycle and ρ^{r}_{ij} the deviation from this initial value, where $\rho^{r}_{ij}(0) = \rho^{r}_{ij}(\Delta t)$.

The corresponding plastic strain history is given by;

$$\varepsilon^{p}_{ij} = \bar{\varepsilon}^{p}_{ij} + \varepsilon^{pr}_{ij} \tag{2}$$

where $\bar{\varepsilon}^{p}_{ij}$ denotes the plastic strain at the beginning of the cycle and ε^{pr}_{ij} denotes the variation from this value during the cycle. The relationships between these quantities is given in Table 1 where μ and K denotes the (isotropic) linear elastic shear modulus and bulk modulus respectively, assumed temperature independent. Note that the dash, e.g. ρ'_{ij}, denotes the deviatoric component.

The primary variable in the following discussion is the variation of the plastic strain rate during the cycle $\dot{\varepsilon}^{pr}_{ij}$. Although this strain rate generally does not satisfy compatibility equations, the accumulation over the cycle $\Delta\varepsilon^{pr}_{ij} = \int_0^{\Delta t} \dot{\varepsilon}^{pr}_{ij}\, dt$ is compatible with a displacement increment Δu^{p}_{i}, the ratchet displacement.

3 Kinematic Minimum Theorem

The cyclic solution can be characterised by the following minimum theorem in terms of the plastic strain rate history $\dot{\varepsilon}^{pr}_{ij}$ [3]. A kinematically admissible plastic strain rate history $\dot{\varepsilon}^{c}_{ij}$ is defined as any strain rate history, generally not compatible, that accumulates over the cycle to an increment of strain $\Delta\varepsilon^{c}_{ij} = \int_0^{\Delta t} \dot{\varepsilon}^{c}_{ij} dt$ compatible with a displacement increment Δu^{c}_{i} which is zero over S_u. With this definition, the following functional is minimised by the cyclic solution;

$$I\left(\dot{\varepsilon}^{c}_{ij}, \lambda\right) = \int_V \int_0^{\Delta t} \left\{\sigma^{c}_{ij} - \left(\lambda\hat{\sigma}_{ij} + \rho^{c}_{ij} + \bar{\rho}^{c}_{ij}\right)\right\}\dot{\varepsilon}^{c}_{ij} dt dV \ge I\left(\dot{\varepsilon}^{pr}_{ij}, \lambda\right) = 0 \tag{3}$$

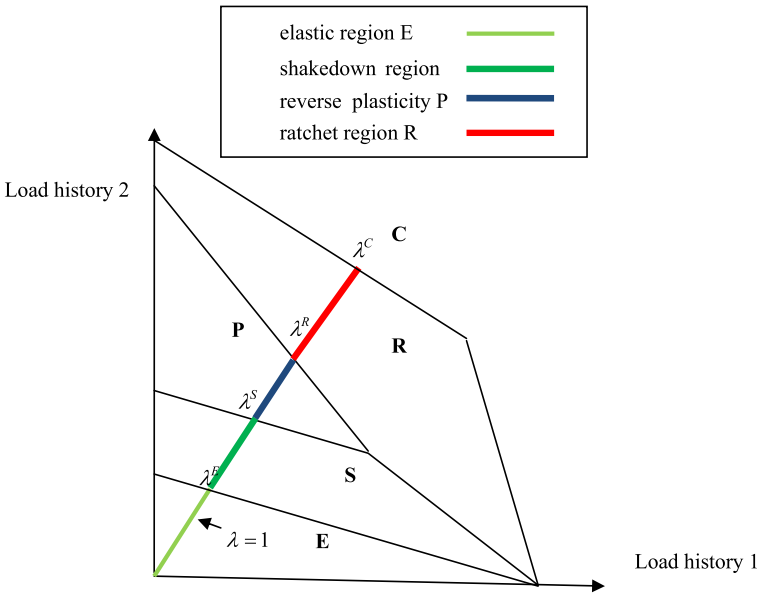

Fig. 1 Schematic of load interaction diagram showing regions characterised by the form of the cyclic strain rate history

The residual stress history ρ^c_{ij} is derived from $\dot{\varepsilon}^c_{ij}$ through the relationships

$$\dot{\varepsilon}'^{cT}_{ij} = (1/2\mu)\dot{\rho}'^{c}_{ij} + \dot{\varepsilon}'^{c}_{ij}, \qquad \dot{\varepsilon}^{cT}_{kk} = (1/3K)\dot{\rho}^{c}_{kk} \quad \text{and} \quad \rho^c_{ij}(0) = 0 \tag{4}$$

where $\dot{\varepsilon}^{cT}_{ij}$ is a compatible strain rate history. Here σ^c_{ij} denotes the stress at yield associated with $\dot{\varepsilon}^c_{ij}$. A further condition requires that the constant residual stress field $\bar{\rho}^c_{ij}$ satisfies the condition,

$$f\left(\lambda\hat{\sigma}_{ij} + \rho^c_{ij} + \bar{\rho}^c_{ij}\right) \le 0 \tag{5}$$

for $0 \le t \le \Delta t$. Note that $\bar{\rho}^c_{ij}$may be eliminated from $I(\dot{\varepsilon}^c_{ij}, \lambda)$, (3), due to the compatibility of the $\Delta\varepsilon^c_{ij}$ [3].

4 The Cyclic Histories

It is useful to consider a problem with two distinct load histories each of which may involve load and temperature changes, referred to as load history 1 and 2. Hence a particular load history can be considered as a point in an interaction diagram defined by the proportion of the two histories and the linear scaling factor λ as shown schematically in Fig. 1. For fixed proportions of the load histories and increasing λ a radial line is described. As λ increases the load point will pass through regions

of the diagram where distinct modes of behaviour occur, bounded by values of λ that define limits of behaviour. The behaviour within each of these regions is characterised by the following properties of the steady state cyclic stress and strain rate fields;

E—Elastic $\quad 0 \le \lambda \le \lambda^E \quad f(\lambda\hat{\sigma}_{ij}) \le 0 \quad \dot{\varepsilon}_{ij}^{pr} = 0$ (6)

S—Shakedown $\quad \lambda^E \le \lambda \le \lambda^S \quad f(\lambda\hat{\sigma}_{ij} + \bar{\rho}_{ij}) \le 0 \quad \dot{\varepsilon}_{ij}^{pr} = 0$ (7)

P—Reverse Plasticity $\quad \lambda^S \le \lambda \le \lambda^R \quad f(\lambda\hat{\sigma}_{ij} + \bar{\rho}_{ij} + \rho_{ij}^r) \le 0 \quad \dot{\varepsilon}_{ij}^{pr} \ne 0$

$$\Delta\varepsilon_{ij}^{pr} = \int_0^{\Delta t} \dot{\varepsilon}_{ij}^{pr}\, dt = 0 \tag{8}$$

R—Ratcheting $\quad \lambda^R \le \lambda \le \lambda^C \quad f(\lambda\hat{\sigma}_{ij} + \bar{\rho}_{ij} + \rho_{ij}^r) \le 0 \quad \dot{\varepsilon}_{ij}^{pr} \ne 0$

$$\Delta\varepsilon_{ij}^{pr} = \int_0^{\Delta t} \dot{\varepsilon}_{ij}^{pr}\, dt \text{ compatible with } \Delta u_{ij}^{pr} \ne 0 \tag{9}$$

C—Collapse $\quad \lambda = \lambda^C,\ \Delta\varepsilon_{ij}^{pr}$ compatible with Δu_{ij}^{pr} at an instant during the cycle (10)

5 Kinematic Conditions at the Plasticity Limits

The limits, therefore, form the interface between these regions where the properties of the cyclic state share those of adjacent regions. Hence the cyclic state has the properties of lower values of λ but gathers *infinitesimally* properties of the region for higher values of λ.

Shakedown Limit At this limit the stress history possesses the properties of the shakedown region, i.e. $\sigma_{ij}^s = \lambda\hat{\sigma}_{ij} + \bar{\rho}_{ij}$, $f(\sigma_{ij}^s) \le 0$ and but there exists an *infinitesimal* kinematically admissible strain rate $\dot{\varepsilon}_{ij}^{pr}$ history that makes no contribution to the residual stress history.

Ratchet Limit Similarly at the ratchet limit the stress history has the form $\sigma_{ij}^R = \lambda\hat{\sigma}_{ij} + \bar{\rho}_{ij} + \rho_{ij}^{1r}$, where ρ_{ij}^{1r} arises from $\dot{\varepsilon}_{ij}^{p1r}$ which satisfies $\int_0^{\Delta t} \dot{\varepsilon}_{ij}^{p1r} dt = \Delta\varepsilon_{ij}^{p1r} = 0$. In addition there is an *infinitesimal* additional strain rate history $\dot{\varepsilon}_{ij}^{p2r}$, (i.e. $\dot{\varepsilon}_{ij}^{pr} = \dot{\varepsilon}_{ij}^{p1r} + \dot{\varepsilon}_{ij}^{p2r}$), that gives rise to a ratchet displacement but makes no contribution to the residual stress field.

Collapse Limit At the collapse limit there exists an increment of plastic train $\Delta\varepsilon_{ij}^{pr}$ compatible with Δu_{ij}^{pr} at an instant during the cycle. This limit will not be discussed further in this paper.

The strategy for identifying each of these limits consists of defining an appropriate class of kinematically admissible strain rate histories $\dot{\varepsilon}_{ij}^{c}$ then defining a corresponding minimising process for $I(\dot{\varepsilon}_{ij}^{c}, \lambda)$. In the next section the processes for minimisation of $I(\dot{\varepsilon}_{ij}^{c}, \lambda)$ is discusses and this is followed by the application to each of the limits.

6 Minimisation Processes

Consider the incremental form of the functional $I(\lambda, \dot{\varepsilon}_{ij}^{c})$, where $\dot{\varepsilon}_{ij}^{c}$ is replaced by a sequence of increments of strain $\Delta\varepsilon_{ij}^{l}$ occurring at a sequence of n times t_l, $l = 1$ to n, during the cycle;

$$
\begin{aligned}
&I\left(\lambda, \Delta\varepsilon_{ij}^{l}\right) = \sum_{l} \Delta I_l, \\
&\Delta I_i = \int_V \left\{\sigma_{ij}^{l} - \left(\lambda\hat{\sigma}_{ij}(t_l) + \rho_{ij}^{l}(t_l) + \bar{\rho}_{ij}\right)\right\}\Delta\varepsilon_{ij}^{l} dV
\end{aligned}
\tag{11}
$$

where

$$
\begin{aligned}
&\rho_{ij}^{l}(t_l) = \sum_{m=1}^{l} \Delta\rho_{ij}^{m}(t_m), \\
&\Delta\varepsilon_{ij}^{\prime Tm} = \frac{1}{2\mu}\Delta\rho_{ij}^{\prime m} + \Delta\varepsilon_{ij}^{\prime m} \quad \text{and} \quad \Delta\varepsilon_{kk}^{Tm} = \frac{1}{3K}\Delta\rho_{kk}^{m}
\end{aligned}
\tag{12}
$$

Strategies for evaluating the limits, discussed in the next section, relies upon strategies for incrementally reducing the functional $I(\lambda, \Delta\varepsilon_{ij}^{l})$. Beginning with a set of plastic strain increments $\Delta\varepsilon_{ij}^{lk}$ the objective is to determine a new set $\Delta\varepsilon_{ij}^{l(k+1)}$ such that $I(\lambda, \Delta\varepsilon_{ij}^{l(k+1)}) \le I(\lambda, \Delta\varepsilon_{ij}^{lk})$. However, practically, this may only be achieved by disconnecting the relationship between $\Delta\varepsilon_{ij}^{l}$ and $\rho_{ij}^{l}(t_l)$ as the later depends on the sum of the increments of residual stress prior to time $t = t_l$; it is not possible to evaluate a sequence of residual stress and strain increments simultaneously. Hence two distinct minimisation processes are considered:

Global Minimisation: The minimisation of $I(\lambda, \Delta\varepsilon_{ij}^{l}) = \sum_l \Delta I_l$ with respect to $\Delta\varepsilon_{ij}^{l}$, assuming that ρ_{ij}^{l} is known.

Incremental Minimisation: The minimisation of ΔI_m with respect to $\Delta\varepsilon_{ij}^{m}$ assuming $\rho_{ij}^{m-1} + \bar{\rho}_{ij}$ is known.

The global minimisation of $I(\lambda, \Delta\varepsilon_{ij}^{l})$ makes use of the compatibility of the sum of the increments of plastic strain over the cycle, whereas the minimisation of increments assumes the prior history of the residual stress is known and compatibility of the total strain (elastic and plastic) in the increment is used. Each processes relies on

a Linear Matching Method, the replacement of the non-linear plasticity behaviour by linear behaviour, resulting in the solution of a linear problem that generates a solution that lowers the value of either $I(\lambda, \Delta\varepsilon_{ij}^{l})$ or ΔI_m.

7 Global Minimisation

A set of increments $\Delta\varepsilon_{ij}^{lk}$ are assumed known. A linear material is defined so that linear shear modulus $\bar{\mu}^{lk}$ ensures that the resulting deviatoric stress is at yield i.e.

$$\frac{2}{3}\bar{\mu}^{lk}\bar{\varepsilon}\left(\Delta\varepsilon_{ij}^{lk}\right) = \sigma_y \tag{13}$$

where $\bar{\varepsilon}$ denotes the von Mises effective strain. A set of linear incremental relationships are then defined by

$$\Delta\varepsilon_{ij}^{l(k+1)} = \frac{1}{2\bar{\mu}^{lk}}\left[\left(\lambda\hat{\sigma}'_{ij}(t_l) + \rho'^{k}_{ij}(t_l)\right) + \bar{\rho}_{ij}^{(k+1)}\right] \qquad \Delta\varepsilon_{kk}^{l(k+1)} = 0 \tag{14}$$

where $\rho'^{k}_{ij}(t)$ is assumed to be known and $\bar{\rho}_{ij}^{(k+1)}$ is a residual stress field that remains constant during the cycle. Summing over the cycle produces a relationship between the compatible strain $\Delta\varepsilon_{ij}^{(k+1)} = \sum_l \Delta\varepsilon_{ij}^{l(k+1)}$ and the constant residual stress $\bar{\rho}_{ij}^{(k+1)}$ with an initial stress state;

$$\Delta\varepsilon_{ij}^{(k+1)} = \frac{1}{2\bar{\mu}^{k}}\left[\sigma_{ij}^{initial} + \bar{\rho}_{ij}^{(k+1)}\right]\Delta\varepsilon_{kk}^{(k+1)} = 0 \tag{15}$$

where

$$\frac{1}{\bar{\mu}^{k}} = \sum_l \frac{1}{\bar{\mu}^{lk}} \quad \text{and} \quad \frac{\sigma_{ij}^{initial}}{\bar{\mu}^{k}} = \sum_l \frac{(\lambda\hat{\sigma}'_{ij}(t_l) + \rho'^{k}_{ij}(t_l))}{\bar{\mu}^{lk}} \tag{16}$$

The solution of the continuum problem corresponding to Eq. (16) has the property that $I(\Delta\varepsilon_{ij}^{l(k+1)}, \lambda) \le I(\Delta\varepsilon_{ij}^{lk}, \lambda)$. The formal proof is given in [3] for the case of $\rho'^{k}_{ij}(t) = 0$, but, as $\rho'^{k}_{ij}(t)$ is assumed to be known, the extension to the present case is trivial.

8 Incremental Minimisation

In this case, we begin, as before, with an initial strain increment $\Delta\varepsilon_{ij}^{lk}$ and a linear modulus defined by $\frac{2}{3}\bar{\mu}^{lk}\bar{\varepsilon}(\Delta\varepsilon_{ij}^{lk}) = \sigma_y$. An incremental linear equation is defined by Eq. (12);

$$\Delta\varepsilon_{ij}^{\prime Tl(k+1)} = \frac{1}{2\mu}\Delta\rho_{ij}^{\prime l(k+1)} + \Delta\varepsilon_{ij}^{\prime l(k+1)} \tag{17}$$

where $\Delta\varepsilon_{ij}^{\prime l(k+1)} = \frac{1}{2\bar{\mu}^{lk}}(\lambda\hat{\sigma}(t_l) + \rho_{ij}^{\prime lk} + \bar{\rho}_{ij}^{k} + \Delta\rho_{ij}^{\prime l(k+1)})$
i.e.

$$\Delta\varepsilon_{ij}^{\prime Tl(k+1)} = \left(\frac{1}{2\mu} + \frac{1}{2\bar{\mu}^{lk}}\right)\Delta\rho_{ij}^{\prime l(k+1)} + \frac{1}{2\bar{\mu}^{lk}}\left(\lambda\hat{\sigma}(t_l) + \rho_{ij}^{\prime lk}(t_l) + \bar{\rho}_{ij}^{k}\right) \quad \text{and}$$
$$\Delta\varepsilon_{kk}^{Tl(k+1)} = \frac{1}{3K}\Delta\rho_{kk}^{l(k+1)} \tag{18}$$

Again this defines a soluble continuum problem as $\Delta\varepsilon_{ij}^{Tl(k+1)}$ is compatible and $\Delta\rho_{ij}^{l(k+1)}$ is an equilibrium residual stress field. The property of this solution is that $\Delta I_l(\lambda, \Delta\varepsilon_{ij}^{l(k+1)}) \leq \Delta I_l(\lambda, \Delta\varepsilon_{ij}^{lk})$, assuming that $(\rho_{ij}^{\prime lk}(t_l) + \bar{\rho}_{ij}^{k})$ is known.

9 Evaluation of the Elastic and Shakedown Limits

The definition of the kinematic properties of the strain history and the minimisation process now allows the development of processes capable of evaluating each of the plasticity limits.

Elastic Limit At the interface $\lambda = \lambda^E$, $f(\lambda\hat{\sigma}_{ij}) \leq 0$ for a maximum value of λ and no further properties are required.

Shakedown Limit Approaching the interface $\lambda = \lambda^S$ from the shakedown region S, $f(\lambda\hat{\sigma}_{ij} + \bar{\rho}_{ij}) \leq 0$ and $\dot{\varepsilon}_{ij}^{pr} = 0$. However, approaching $\lambda = \lambda^S$ from either the ratcheting region R or reverse plasticity region P, there exists a finite $\dot{\varepsilon}_{ij}^{pr}$ which becomes *infinitesimally small* in the limit when $\lambda = \lambda^S$ i.e. $\dot{\rho}_{ij}^{r} = 0$. Hence at the boundary $\lambda = \lambda^S$ we consider a class of kinematically admissible strain rate histories so that $\rho_{ij}^{c} = 0$ and $\dot{\varepsilon}_{ij}^{c}$ is infinitesimally small. Hence with $\bar{\rho}_{ij}^{c}$ eliminated and $\lambda = \lambda^S$ inequality (3) becomes,

$$I\left(\dot{\varepsilon}_{ij}^{c}, \lambda^S\right) = \int_V \int_0^{\Delta t} \left\{\sigma_{ij}^{c} - \lambda^S\hat{\sigma}_{ij}\right\}\dot{\varepsilon}_{ij}^{c}\,dt\,dV \geq I\left(\dot{\varepsilon}_{ij}^{pS}, \lambda^S\right) = 0 \tag{19}$$

i.e.

$$\lambda^S \leq \frac{\int_V \int_0^{\Delta t} \sigma_{ij}^{c}\dot{\varepsilon}_{ij}^{c}\,dt\,dV}{\int_V \int_0^{\Delta t} \hat{\sigma}_{ij}\dot{\varepsilon}_{ij}^{c}\,dt\,dV} = \lambda_{UB}^{S} \tag{20}$$

Equation (20) can be recognised as the upper bound to the shakedown limit. An alternatively expression of this property allows us to connect the upper bound shakedown value to the minimisation process [2]. If there are two kinematically admissible strain rate histories, $\dot{\varepsilon}_{ij}^{c(k+1)}$ and $\dot{\varepsilon}_{ij}^{ck}$ such that,

$$I\left(\dot{\varepsilon}_{ij}^{c(k+1)}, \lambda_{UB}^{Sk}\right) \leq I\left(\dot{\varepsilon}_{ij}^{ck}, \lambda_{UB}^{Sk)}\right) \tag{21}$$

then

$$\lambda_{UB}^{S(k+1)} \leq \lambda_{UB}^{Sk} \tag{22}$$

where $\lambda_{UB}^{S(k+1)}$ and λ_{UB}^{Sk} are the upper bounds (20) associated with $\dot{\varepsilon}_{ij}^{c(k+1)}$ and $\dot{\varepsilon}_{ij}^{ck}$, respectively. Hence in the discrete form, the global minimisation process, may be used to produce a monotonically reducing sequence of upper bound to the shake-down limit by, at each stage identifying λ with the upper bound from current solution. This method was originally discussed in [2] and has been extensive applied in the literature.

10 Evaluation of the Ratchet Limit—A Dual Coupled Minimisation Process

Approaching $\lambda = \lambda^R$ from the reverse plasticity region P $f(\lambda\hat{\sigma}_{ij} + \bar{\rho}_{ij} + \rho_{ij}^r) \leq 0$ and there exists a finite $\dot{\varepsilon}_{ij}^{pr} = \dot{\varepsilon}_{ij}^{p1}$ so that $\int_0^{\Delta t} \dot{\varepsilon}_{ij}^{p1} dt = 0$. However when the boundary $\lambda = \lambda^R$ is approached from the ratchet region there exists in the limit an additional *infinitesimal* $\dot{\varepsilon}_{ij}^{pr} = \dot{\varepsilon}_{ij}^{p2}$ so that $\int_0^{\Delta t} \dot{\varepsilon}_{ij}^{p2} dt = \Delta\varepsilon_{ij}^{p2}$ where $\Delta\varepsilon_{ij}^{p2}$ is compatible with Δu_i^{p2}, a non-zero ratchet mechanism. Hence $\dot{\varepsilon}_{ij}^{pr} = \dot{\varepsilon}_{ij}^{p1} + \dot{\varepsilon}_{ij}^{p2}$, and the associated cyclic stress history is of the form $\sigma_{ij} = \lambda\hat{\sigma}_{ij} + \bar{\rho}_{ij} + \rho_{ij}^{r1}$ where ρ_{ij}^{r1} is the changing residual stress field arising only from $\dot{\varepsilon}_{ij}^{pr} = \dot{\varepsilon}_{ij}^{p1}$.

The kinematically admissible strain rate history is, therefore, subdivided into a finite and additional infinitesimal parts $\dot{\varepsilon}_{ij}^{c} = \dot{\varepsilon}_{ij}^{c1} + \dot{\varepsilon}_{ij}^{c2}$ with the properties;

$$\dot{\varepsilon}_{ij}^{c1} \quad \text{finite and} \quad \int_0^{\Delta t} \dot{\varepsilon}_{ij}^{c1} dt = 0 \tag{23}$$

$$\dot{\varepsilon}_{ij}^{c2} \quad \text{infinitesimal and} \quad \int_0^{\Delta t} \dot{\varepsilon}_{ij}^{c2} dt = \Delta\varepsilon_{ij}^{c2} \quad \text{compatible with } \Delta u_i^{c2}. \tag{24}$$

Similarly

$$I\left(\dot{\varepsilon}_{ij}^{c}, \lambda\right) = I^1\left(\dot{\varepsilon}_{ij}^{c1}, \lambda\right) + I^2\left(\dot{\varepsilon}_{ij}^{c2}, \lambda\right) \tag{25}$$

where

$$I^1\left(\dot{\varepsilon}_{ij}^{c}, \lambda\right) = \int_V \int_0^{\Delta t} \left\{\sigma_{ij}^{c1} - \left(\lambda\hat{\sigma}_{ij} + \rho_{ij}^{c1} + \bar{\rho}_{ij}^{c}\right)\right\} \dot{\varepsilon}_{ij}^{c1} dt dV \tag{26}$$

$$\dot{\varepsilon}_{ij}^{\prime cT1} = (1/2\mu)\dot{\rho}_{kl}^{\prime c1} + \dot{\varepsilon}_{ij}^{\prime c1} \quad \text{and} \quad \dot{\varepsilon}_{kk}^{cT1} = (1/3K)\dot{\rho}_{kk}^{c1} \tag{27}$$

and

$$I^2\left(\dot{\varepsilon}_{ij}^{c2}, \lambda\right) = \int_V \int_0^{\Delta t} \left\{\sigma_{ij}^{c2} - \left(\lambda\hat{\sigma}_{ij} + \rho_{ij}^{c1} + \bar{\rho}_{ij}^{c}\right)\right\} \dot{\varepsilon}_{ij}^{c2} dt dV \tag{28}$$

where $\sigma_{ij}^{c2} = \sigma_{ij}^{c1}$ at those instants when both $\dot{\varepsilon}_{ij}^{c1}$ and $\dot{\varepsilon}_{ij}^{c2}$ occur at the same material point.

This poses a dual coupled minimisation problem for I^1 and I^2 where the coincident minima correspond to the same value of $\lambda = \lambda^R$. The dual problems are coupled through the residual stress field ρ_{ij}^{c1} arising from the finite reverse plasticity mechanism $\dot{\varepsilon}_{ij}^{c1}$, the initial residual stress field $\bar{\rho}_{ij}^{c}$ and also the associated yield stresses σ_{ij}^{c1} and σ_{ij}^{c2}. This process can be subdivided into two phases. The first is the minimising of the increments of I^1 to generate $\dot{\rho}_{ij}^{c1}$ for constant λ, assuming $\bar{\rho}_{ij}^{c}$ is known, and the second a global minimisation of I^2 to generate $\bar{\rho}_{ij}^{c}$, assuming $\dot{\rho}_{ij}^{c1}$ is known. At each stage an upper bound on λ is evaluated. This is described in detail in the following sections for $n = 3$ in the incremental form.

10.1 Phase 1—Minimisation of I^1 for Constant λ

Consider the case of three instants during the cycle. In the following, the superscript 1 is dropped and the remaining superscripts correspond to the instant in the cycle $l = 1, 2, 3$ and the iteration numbers k and $k+1$. The Linear Matching equations (17) and (18) are given for the kth iteration by;

$$
\begin{aligned}
&l = 1\\
&\Delta\varepsilon_{ij}^{\prime(k+1)1} = \frac{1}{2\mu}\Delta\rho_{ij}^{\prime(k+1)1} + \frac{1}{2\bar{\mu}^{1k}}\left(\lambda\hat{\sigma}_{ij}(t_1) + \Delta\rho_{ij}^{(k+1)1} + \bar{\rho}_{ij}^{k}\right)^{\prime}\\
&\Delta\varepsilon_{kk}^{(k+1)1} = \frac{1}{3K}\Delta\rho_{kk}^{(k+1)1}
\end{aligned}
\tag{29}
$$

$$
\begin{aligned}
&l = 2\\
&\Delta\varepsilon_{ij}^{\prime(k+1)2} = \frac{1}{2\mu}\Delta\rho_{ij}^{\prime(k+1)2} + \frac{1}{2\bar{\mu}^{2k}}\left(\lambda\hat{\sigma}_{ij}(t_2) + \Delta\rho_{ij}^{(k+1)1}\right.\\
&\qquad\qquad \left. + \Delta\rho_{ij}^{(k+1)2} + \bar{\rho}_{ij}^{k}\right)^{\prime}\\
&\Delta\varepsilon_{kk}^{(k+1)2} = \frac{1}{3K}\Delta\rho_{kk}^{(k+1)2}
\end{aligned}
\tag{30}
$$

$$
\begin{aligned}
&l = 3\\
&\Delta\varepsilon_{ij}^{\prime(k+1)3} = \frac{1}{2\mu}\Delta\rho_{ij}^{\prime k3} + \frac{1}{2\bar{\mu}^{3k}}\left(\lambda\hat{\sigma}_{ij}(t_2) + \Delta\rho_{ij}^{(k+1)1} + \Delta\rho_{ij}^{(k+1)2}\right.\\
&\qquad\qquad \left. + \Delta\rho_{ij}^{(k+1)3} + \bar{\rho}_{ij}^{k}\right)^{\prime}\\
&\Delta\varepsilon_{kk}^{(k+1)3} = \frac{1}{3K}\Delta\rho_{kk}^{(k+1)3}
\end{aligned}
\tag{31}
$$

with

$$
0 = \Delta\rho_{ij}^{(k+1)1} + \Delta\rho_{ij}^{(k+1)2} + \Delta\rho_{ij}^{(k+1)3} \tag{32}
$$

and

$$0 = \Delta\varepsilon_{ij}^{(k+1)1} + \Delta\varepsilon_{ij}^{(k+1)2} + \Delta\varepsilon_{ij}^{(k+1)3} \tag{33}$$

The linear shear moduli $\mu^{kl} = 3\sigma_y/2\bar{\varepsilon}(\Delta\varepsilon_{ij}^{kl})$ are generated from $\Delta\varepsilon_{ij}^{kl}$, the strain increments from the previous iteration. The sequence of Eqs. (29) to (33) are soluble, sequentially, when $\bar{\rho}_{ij}^{k}$ has been defined. Note that a set of solutions generated by a particular $\bar{\rho}_{ij}^{k}$ does not necessarily satisfy the cyclic conditions (32) and (33). However, in certain conditions Eq. (32) may be used to simplify the procedure.

Consider the case $n = 2$. In this case $\Delta\rho_{ij}^{k1} = -\Delta\rho_{ij}^{k2}$ and the equations for $l = 1$ and $l = 2$ reduces to the single equation;

$$\begin{aligned} \Delta\varepsilon_{ij}^{(k+1)1} &= \frac{1}{2\mu}\Delta\rho_{ij}^{(k+1)1} + \frac{1}{2\mu^{k1}}\left(\lambda\left[\hat{\sigma}_{ij}(t_2) - \hat{\sigma}_{ij}(t_1)\right] + \Delta\rho_{ij}^{(k+1)1}\right) \\ \Delta\varepsilon_{kk}^{(k+1)1} &= \frac{1}{3K}\Delta\rho_{kk}^{(k+1)1} \quad \text{and} \quad \mu^{k1} = 3(2\sigma_y)/2\bar{\varepsilon}\left(\Delta\varepsilon_{ij}^{(k-1)1}\right) \end{aligned} \tag{34}$$

Note that Eqs. (34) are independent of $\bar{\rho}_{ij}^{k}$ and may be solved directly for a prescribed λ. This case was first discussed by Chen and Ponter [4].

10.2 Phase 2—Global Minimisation of I^2

In the following argument we use the form of I^2 with $\bar{\rho}_{ij}^{k}$ removed. The minimisation of I^2 is required for prescribed λ;

$$I^2 = \int_V \sum_l \left\{\sigma_{ij}^{l2} - \left(\lambda\hat{\sigma}_{ij}(t_l) + \rho_{ij}^{l1}(t_l)\right)\right\}\Delta\varepsilon_{ij}^{l2}dV \geq 0 \tag{35}$$

Note that $\Delta\varepsilon_{ij}^{c2} = \sum_l \Delta\varepsilon_{ij}^{l2}$ forms a ratchet mechanism, i.e. $\Delta\varepsilon_{ij}^{c2}$ is compatible with a non-zero displacement increment Δu_i^{c2}. For an arbitrary $\Delta\varepsilon_{ij}^{l2}$ (35) gives the following upper bound on any allowable λ,

$$\lambda \leq \frac{\int_V \sum_l \sigma_{ij}^{l2}\Delta\varepsilon_{ij}^{l2}dV}{\int_V \sum_l (\lambda\hat{\sigma}_{ij}(t_l) + \rho_{ij}^{l1}(t_l))\Delta\varepsilon_{ij}^{l2}dV} = \lambda_{UB}^{R}\left(\Delta\varepsilon_{ij}^{l2}, \rho_{ij}^{l1}(t_l)\right) \tag{36}$$

where $\lambda_{UB}^{R}(\Delta\varepsilon_{ij}^{l2}, \rho_{ij}^{l1}(t_l))$ is an upper bound on the smallest value of λ for which there exists a constant residual stress field $\bar{\rho}_{ij}$ so that $f(\lambda\hat{\sigma}_{ij} + \bar{\rho}_{ij} + \rho_{ij}^{1}) \leq 0$. Note that λ_{UB}^{R} is not necessarily an upper bound on the ratchet limit itself, except when ρ_{ij}^{1} is the correct changing residual stress field.

For a known $\rho_{ij}^{l1}(t_l)$, global minimisation is carried out by the procedure discussed in Sect. 7 with a significant adaptation. It is necessary to eliminate the possibility of a reverse plasticity mechanism occurring. This is achieved by assuming

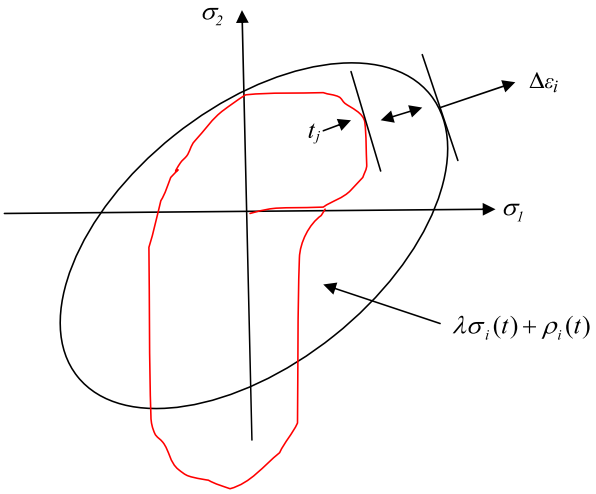

Fig. 2 Schematic representation of the choice of time instant during the cycle associated with the ratchet mechanism

that at each point in the body the increment of compatible strain occurs at single instance. This instance is identified as t_j so that,

$$\left\{\sigma_{ij}^2 - \left(\lambda\hat{\sigma}_{ij}(t_j) + \rho_{ij}^{l1}(t_j)\right)\right\}\Delta\varepsilon_{ij}^2 \le \left\{\sigma_{ij}^2 - \left(\lambda\hat{\sigma}_{ij}(t_l) + \rho_{ij}^{l1}(t_l)\right)\right\}\Delta\varepsilon_{ij}^2$$
$$l = 1, 2, \ldots, n \tag{37}$$

This ensures that the resultant mechanism is a ratchet mechanism and that the upper bound (36) is minimised. This construction is shown schematically in Fig. 2. It is possible to show that this procedure includes the exact cyclic solution.

11 Evaluation of the Ratchet Limit—Two Extremes

For $n = 2$, incremental minimisation reduces to the solution of a single problem for $\Delta\rho_{ij}^{k1} = -\Delta\rho_{ij}^{k2}$, Eqs. (34), which is independent of $\bar{\rho}_{ij}$. For a certain class of problems it is possible to define two independent stages. Consider the case where the loading history consists of a prescribed history defined by a load parameter λ, with an additional constant load $\lambda^P P_i$. In this case the global minimisation becomes a shakedown problem for the unknown load parameter λ^P. This is the method discussed by Ponter and Chen [4] and has been extensive applied to practical problems in structural integrity.

12 Evaluation of the Ratchet Limit—Coupled Minimisation

In the general case the incremental and global minimisation processes are interdependent. Consider the case of $n = 3$, Eqs. (29) to (31) of phase 1. For fixed

λ, $\Delta\rho_{ij}^{(k+1)1}$, $\Delta\rho_{ij}^{(k+1)1}$ and $\Delta\rho_{ij}^{(k+1)1}$ can be evaluated by sequential solution of these equations only if $\bar{\rho}_{ij}^{k}$ is known. Similarly phase (2), global minimisation, may be used to evaluate $\bar{\rho}_{ij}^{k}$ if the $\Delta\rho_{ij}^{kl}$ are known, by the solution of Eqs. (13), (15) and (16). Hence a convergent procedure requires iteration between phase (1) and phase (2). The following methodology is proposed;

(1) Phase (2): An initial value of distribution $\bar{\rho}_{ij}^{0}$ is evaluated from Eq. (13), (15) and (16) assuming $\Delta\rho_{ij}^{l} = 0$, an arbitrary value of λ^0 and for arbitrary constant values of $\bar{\mu}^{0l} = \bar{\mu}^{0}$. This gives an initial distribution of $\bar{\rho}_{ij}^{0}$ expressed in terms of the average of the elastic solutions.
(2) Phase (1): Equations (29) to (31) are solved sequentially for these initial choices λ^0, $\bar{\mu}^{0l} = \bar{\mu}^{0}$ and $\bar{\rho}_{ij}^{0}$, generating solutions $\Delta\rho_{ij}^{1l}$ and $\Delta\varepsilon_{ij}^{1l}$.
(3) Phase (2): Equations (13), (15) and (16) are now solved for $\bar{\rho}_{ij}^{1}$ and $\Delta\varepsilon_{ij}^{2l}$ with $\lambda^1 = \lambda_{UB}^{R}(\bar{\rho}_{ij}^{1}, \Delta\varepsilon_{ij}^{2l})$ evaluated from Eq. (36).
(4) Phase (1) is now repeated with $\lambda = \lambda^{1'}$, $\bar{\rho}_{ij}^{1}$ and μ^{1l} derived from $\Delta\varepsilon_{ij}^{1l}$.
(5) Phase (2) is repeated to evaluate $\bar{\rho}_{ij}^{2}$, $\Delta\varepsilon_{ij}^{2l}$ and $\lambda^{2'}$.

Stages (4) and (5) are repeated to convergence. The process may be varied by repeating phase (1) n_1 times at constant λ', followed by n_2 repeats of phase (2) where λ' is updated for each repeat. An entire cycle of phase (1) and phase (2) then consists of n_1 linear solutions of phase (1) and n_2 linear solutions of phase (2).

13 Numerical Examples

13.1 Cylindrical Tube with Circumferential Crack, Two Extremes

Of the many problems solved by this simplified process discussed in Sect. 11, a class of particular interest involves bodies with cracks subjected to variable temperature and constant load. The elastic stress fields have singularities at the crack tip in the exact solution. Hence no elastic or shakedown region exists and the primary limit of interest is the ratchet limit. For all loads below the ratchet limit, regions of reverse plasticity exist.

Figure 3 shows an example of such a problem [7] where a cylindrical tube is subjected to a constant average axial stress σ_p and a radial temperature field that varies between a uniform temperature and a temperature difference of $\Delta\theta$. A circumferential part-through-thickness crack of depth a penetrates into the tube thickness w from the inner surface. The thermal loading is characterised by σ_t, the maximum von Mises effective value of the thermo-elastic stress away from the crack, i.e. the value associated with a crack free cylinder. The resulting interaction diagram is shown in Fig. 4 where converged values of the ratchet boundary are shown, calculated for a range of values of σ_t/σ_y (phase 1) and associated values of σ_p/σ_y (phase 2). The ratchet boundary is shown for a range of crack length, including the

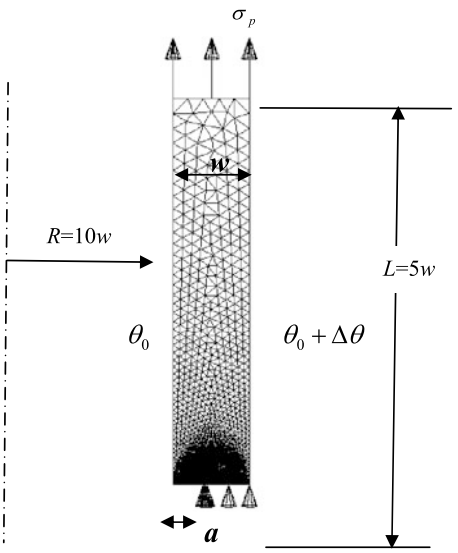

Fig. 3 A cylinder is subjected to an axial constant stress σ_p and a through-thickness varying temperature distribution, varying between a uniform temperature θ_0 and a temperature difference of $\Delta\theta$. A circumferential crack of length a penetrates from the inner surface of the cylinder

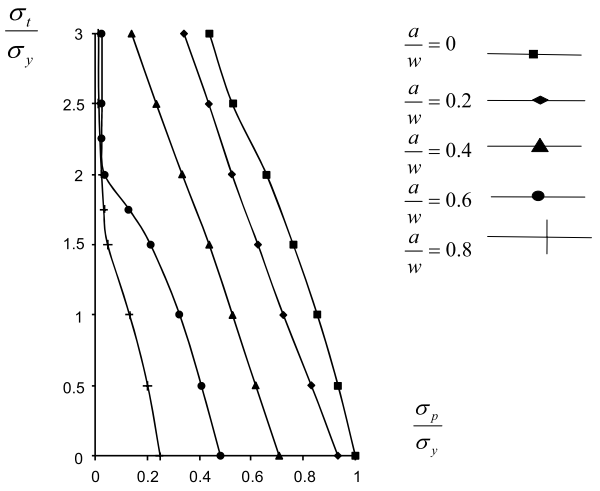

Fig. 4 Ratchet boundaries for the problem of (3) for a range of normalised crack lengths w/a

ratchet boundary for a crack free tube. For a very short crack, the stress σ_p at the ratchet boundary is changed roughly proportionately. When the crack depth reaches a value of $a/w = 0.6$, σ_p decreases to near zero for $\sigma_t/\sigma_y > 2$. The value $\sigma_t/\sigma_y = 2$ is the reverse plasticity shakedown limit for the uncracked cylinder when reverse plastic strains first occur at the surface at positions remote from the crack. Hence for crack lengths $a/w \leq 0.4$ the cylinder retains some capacity to withstand an axial load for a wide range of σ_t/σ_y. For $a/w \geq 0.6$, the cylinder can withstand an axial load without ratcheting only for a very limited range of σ_t/σ_y. This solution demonstrates the broad insight into structural behaviour that may be obtained from ratchet limit solutions.

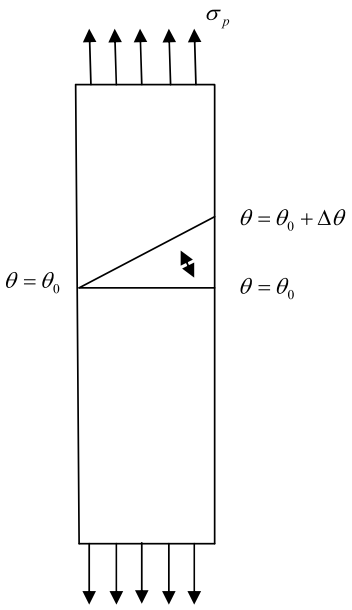

Fig. 5 A Bree problem. A plate is subjected to uniform uniaxial stress σ_p and a varying temperature across the width of the plate, and constrained to prevent in-plane bending

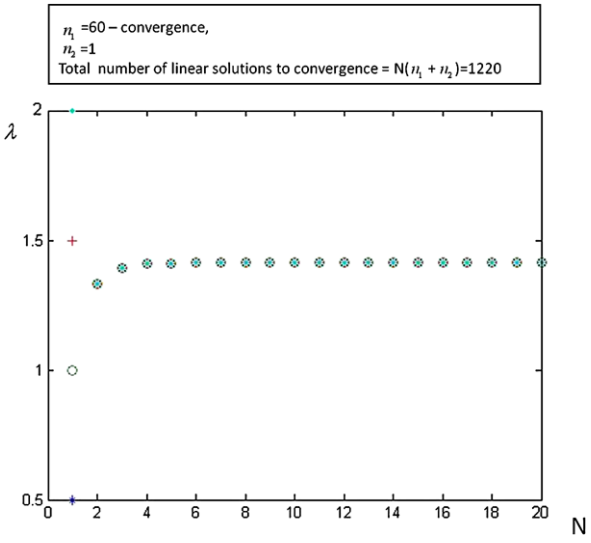

Fig. 6 Convergence of Bree problem of Fig. 5 for differing initial λ^0 when each iteration consists of convergence in phase (1) followed by a single solution in phase (2)

13.2 Ratchet Limit for the Bree Problem—Application of the Coupled Minimisation Process

Consider the Bree problem shown in Fig. 5 where a plate is subjected to an axial stress σ_p and varying temperature difference across its width. The plate is constrained against in plane bending. In the first example σ_p remains constant and a

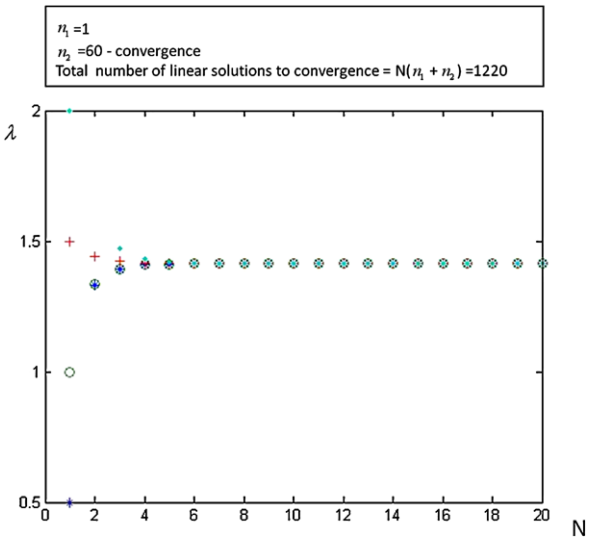

Fig. 7 Convergence of Bree problem of Fig. 5 for differing initial λ^0 when each iteration consists of convergence in phase (2) following a single solution in phase (1)

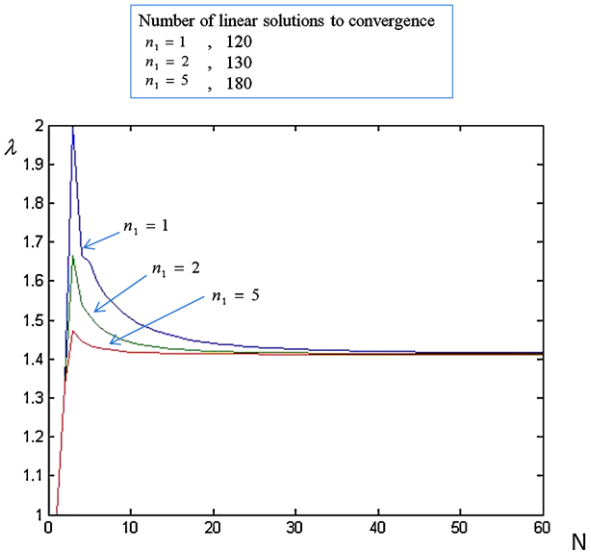

Fig. 8 Convergence of Bree problem of Fig. 5 with differing values of n_1 for $n_2 = 1$

temperature difference across the width of the plate varies cyclically between zero and $\Delta\theta$. The temperature difference of $\Delta\theta$ results in a maximum thermo-elastic stress of σ_t. The general couple minimisation process is used where $\lambda = 1$ corresponds to $\sigma_p/\sigma_y = 0.25$ and $\sigma_t/\sigma_y = 2$. Figures 6 and 7 show the convergence process for λ with iterations N. Each iteration consists of n_1 iterations of Phase (1) and n_2 iterations of Phase (2). Figure 6 shows convergence for a range of values of initial values $\lambda = \lambda^0$ with a sufficient number of iterations in phase (1), $n_1 = 60$, to give convergence, followed by a single iteration $n_2 = 1$ of phase (2). After the first

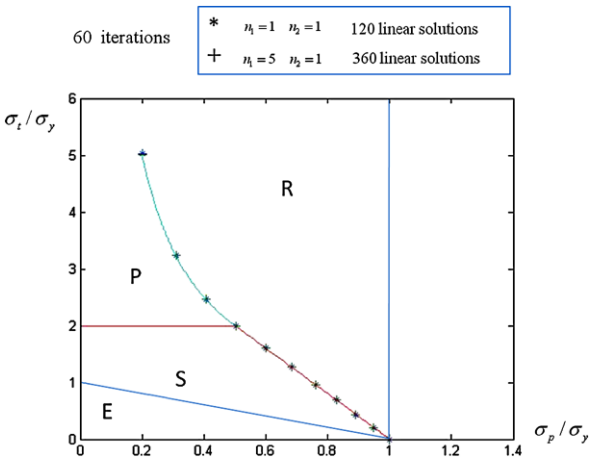

Fig. 9 Converged solutions for the ratchet boundary for the Bree problem of Fig. 5. In all cases, the converged solution is independent of the details of the iterative process

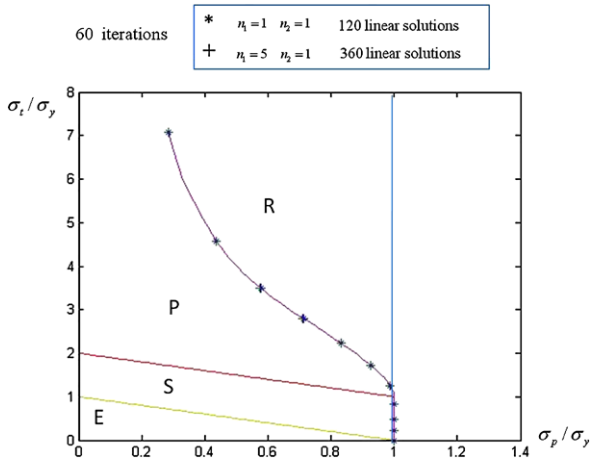

Fig. 10 Converged solutions for case when the applied stress varies between zero and σ_p, while the temperature difference simultaneously varies between zero and $\Delta\theta$

complete cycle, $N = 1$, all solutions give the same value of λ. Subsequently convergence with N takes place with increasing values of λ. Figure 7 shows the convergence process for the opposite extreme, again for a range of values of λ^0 where $n_1 = 1$ and $n_2 = 60$. In all cases convergence is monotonic, converging to the same value in approximately the same number of iterations. Figure 8 shows convergence for a range of values of n_1, retaining $n_2 = 1$. In this case there is some divergence in λ values in the initial iterations, but convergence rapidly becomes monotonic in all cases. Although convergence with respect to N for $n_1 = 5$ is the most rapid, the total number of linear solutions $n_1 + n_2$ is least for $n_1 = 1$ i.e. repeated cycling between phase (1) and phase (2). In all cases convergences is stable and insensitive to initial conditions. Figure 9 shows converged values in both these cases for $N = 60$, which are identical. The same set of solutions are shown in Fig. 10 for the case when the applied stress varies between zero and σ_p at the same time as the temperature variation, showing consistent convergent properties. Although this example is very

simple, it demonstrates that convergence can be achieved and that the process is relatively insensitive to the way the two phases are applied.

14 Conclusions

The evaluation of the ratchet boundary for an elastic perfectly plastic problem can be posed as a coupled minimisation problems consisting of phase 1 (evaluation of the changing residual stress field) and phase 2 (adapted shakedown limit, evaluation of the initial residual stress field). Both processes are achieved by a Linear Matching method where the non-linear material behaviour is replaced by a spatially varying linear material. At each iteration of the method, equilibrium and compatibility are satisfied and the matching process ensures that the matching linear material and the yield properties are matched for the previous strain rate history. The key to the solution method lies in placing very specific restrictions on the classes of kinematically admissible incremental plastic strains involved. Essentially the shakedown and ratchet limits are found by the same process but for differing classes of kinematically admissible strain rate histories. The application of the new ratcheting procedure to a simple Bree problem indicates that the combined process yields is stable numerical method.

Acknowledgements The author gratefully acknowledges the receipt of a Leverhulme Trust Emeritus Fellowship in support of the work in this paper.

References

1. Ponter, A.R.S., Fuschi, P., Engelhardt, M.: Limit analysis for a general class of yield conditions. Eur. J. Mech. A, Solids **19**(3), 401–422 (2000)
2. Ponter, A.R.S., Engelhardt, M.: Shakedown limits for a general yield condition: implementation and examples for a von mises yield condition. Eur. J. Mech. A, Solids **19**(3), 423–446 (2000)
3. Ponter, A.R.S., Chen, H.F.: A minimum theorem for cyclic loading in excess of shakedown, with applications to the evaluation of a ratchet limit. Eur. J. Mech. A, Solids **20**, 539–554 (2001)
4. Chen, H.F., Ponter, A.R.S.: A method for the evaluation of a ratchet limit and the amplitude of plastic strain for bodies subjected to cyclic loading. Eur. J. Mech. A, Solids **20**, 555–572 (2001)
5. Chen, H.F., Ponter, A.R.S., Ainsworth, R.A.: The linear matching method applied to the high temperature life assessment of structures. Part 1. Assessments involving constant residual stress fields. Int. J. Press. Vessels Piping **83**, 123–135 (2006)
6. Chen, H.F., Ponter, A.R.S., Ainsworth, R.A.: The linear matching method applied to the high temperature life assessment of structures. Part 2. Assessments beyond shakedown involving changing residual stress fields. Int. J. Press. Vessels Piping **83**, 136–147 (2006)
7. Habibullah, M.S., Ponter, A.R.S.: Ratcheting limits for cracked bodies subjected to cyclic loads and temperature. Eng. Fract. Mech. **72**, 1702–1716 (2005)

Decomposition Methods and Strain Driven Algorithms for Limit and Shakedown Analysis

Giovanni Garcea and Leonardo Leonetti

Abstract A mathematical programming formulation of strain-driven path-following strategies to perform shakedown and limit analysis for perfectly elastoplastic materials in a FEM context, is presented. From the optimization point of view, standard arc–length strain driven elastoplastic analysis, recently extended to shakedown, are identified as particular decomposition strategies used to solve a proximal point algorithm applied to the static shakedown theorem that is then solved by means of a convergent sequence of safe states. The mathematical programming approach allows: a direct comparison with other nonlinear programming methods, simpler convergence proofs and duality to be exploited. Due to the unified approach in terms of total stresses, the strain driven algorithms become more effective and less nonlinear with respect to a self equilibrated stress formulation and easier to implement in existing codes performing elastoplastic analysis.

1 Introduction

The static and kinematic shakedown theorems, including the limit analysis as a special case, furnish, in a direct and elegant fashion, a reliable safety factor against plastic collapse, loss in functionality due to excessive deformation (ratcheting) or collapse due to low cycle fatigue (plastic shakedown) [1]. Based on these theorems the so called *direct methods* evaluate the safety factor solving a nonlinear convex optimization problem that usually involves hundreds of thousands of unknowns and constraints when real structures are discretized by means of finite elements.

Nowadays this kind of problems could be efficiently solved using interior point methods (IPM) especially when the problem is formulated as a conic programming one and the solution is obtained using primal dual formulations. The work done in this field is impressive and in rapid development: significant references can be

G. Garcea (✉) · L. Leonetti
Dipartimento di Modellistica per l'Ingegneria, Università della Calabria, Rende, Italy
e-mail: giovanni.garcea@unical.it

L. Leonetti
e-mail: leonetti.leonardo@gmail.com

G. Saxcé et al. (eds.), *Limit State of Materials and Structures*,
DOI 10.1007/978-94-007-5425-6_2,

found in the works of Boyd [5], Bertsekas [7], Nemirosky and Todd [8] and Wright [6, 9] among others. As a great number of yield constraints are described as second order cones efficient interior point algorithms for shakedown and limit analysis have been proposed (see [11–17] and references therein). Alternatively the limit load can also be obtained by means of the complete reconstruction of the elasto-plastic equilibrium path, using standard path-following strain driven strategies (see Armero [2] for a review). An extension of these consolidated and widely used algorithms for shakedown analysis was proposed in [3, 4].

In this work it will be show how strain driven elastoplastic analysis based on closest point projection return mapping schemes and Riks arc-length solution, can be obtained from a mathematical programming problem, consisting in the application of the proximal point algorithm to the static shakedown theorem and in the solution of this problem by means of dual decomposition methods [7, 18, 19]. In particular the pseudo elasto-plastic step coincides with a step of the proximal point algorithm (see also [10] for a similar formulation) while the optimization subproblems, deriving from the decomposition techniques, correspond exactly to the standard return mapping by closest point projection scheme used to evaluate the plastically admissible stress.

To obtain a unified formulation for limit and shakedown analysis, the problem is formulated in terms of global stress and equivalent reference load. This choice is particularly advantageous in the strain driven case because it allows a less nonlinear formulation of the problem and makes it easy to fulfill some convergence requirements of the algorithm. The proposed formulation is similar to that presented in [3] and, due to the requirement, in the shakedown case, of a Multi-Surface Return Mapping process, will be called *MS-RM*. The mathematical programming point of view also enables the formulation of a new decomposition strategy based on a Single Surface Return Mapping which will be called *SS-RM*. It requires the solution of the same closest point projection problem as in the standard limit analysis case.

Apart from the mathematical programming reformulation, strain driven incremental analysis due to its classical mechanical interpretation, gives other important information in addition to the shakedown or limit load multiplier evaluation. For the fixed load case, the extremal paths theory of Ponter and Martin [20], gives a coherent justification for the holonomic transformation of the incremental constitutive elasto-plastic relationships obtained by means of a backward Euler integration scheme (closest point return mapping algorithm) and a mechanical sense to the so evaluated equilibrium path allowing the reuse of the static and kinematic parts of the solution at each equilibrium point. A similar interpretation also holds for shakedown where the solution algorithm can be viewed as a step-by-step incremental process aiming to simulate the case of a proportional increase in the domain of the loads such that, for each new point of the equilibrium path, the load recycles within all admissible combinations, up to the achievement of elastic adaptation. This interpretation also allows a possible extension of the strain driven algorithms to the shakedown analysis of more complex materials.

Strain driven algorithms are compared, in terms of performance, accuracy and robustness with the solution obtained with the commercial code MOSEK [24] im-

plementing an Interior Point solution method. The application regards plane stress problems with von Mises yield functions.

The work is organized as follows: in Sect. 2 shakedown theory is presented and rewritten in a discrete FEM form for simpler use in a mathematical programming context; in Sect. 3 shakedown theorems and a mathematical programming version of the elastoplastic step and its relation with proximal point methods is presented; in Sect. 4 we illustrate the numerical methods used to evaluate the shakedown load; in Sect. 5 we give some details on the numerical implementations of the algorithms proposed; in Sect. 6 the finite element discretization is presented; finally in Sect. 7 an extensive series of numerical tests showing the reliability and effectiveness of the proposed formulation is reported.

2 The Discrete Equation for Shakedown and Limit Analysis

In the following, limit and shakedown problems are reformulated in terms of finite element algebraic equations for a better framing in the usual mathematical programming notation.

2.1 The Discrete Representation of Static and Kinematic Fields

Using a mixed finite element format and a vector notation, we assume that the displacement $\mathbf{d}[\mathbf{x}] \in \Re^{n_u}$ and the stress $\boldsymbol{\sigma}[\mathbf{x}] \in \Re^{n_\sigma}$ of a point $\mathbf{x}$ of the body domain $\mathscr{B}$ are interpolated as:

$$\boldsymbol{\sigma}[\mathbf{x}] = \mathbf{N}_\sigma[\mathbf{x}]\mathbf{t}, \qquad \mathbf{d}[\mathbf{x}] = \mathbf{N}_u[\mathbf{x}]\mathbf{u} \tag{1}$$

where $\mathbf{N}_\sigma[\mathbf{x}]$ and $\mathbf{N}_u[\mathbf{x}]$ collect the interpolation functions while global vectors $\mathbf{u}$ and $\mathbf{t}$ collect the N_σ stress node vectors $\boldsymbol{\sigma}_g := \boldsymbol{\sigma}[\mathbf{x}_g]$ and N_u displacement node vectors $\mathbf{d}_i := \mathbf{d}[\mathbf{x}_i]$ in a finite numbers of points as:

$$\mathbf{t} = \begin{bmatrix} \boldsymbol{\sigma}_1 \\ \vdots \\ \boldsymbol{\sigma}_{N_\sigma} \end{bmatrix}, \qquad \mathbf{u} = \begin{bmatrix} \mathbf{d}_1 \\ \vdots \\ \mathbf{d}_{N_u} \end{bmatrix}$$

Making $\mathbf{D}[\mathbf{x}]$ the kinematical operator, the relationship between strain $\boldsymbol{\varepsilon}[\mathbf{x}] \in \Re^{n_\sigma}$ and displacements $\mathbf{d}[\mathbf{x}]$ can be written as:

$$\boldsymbol{\varepsilon}[\mathbf{x}] = \mathbf{N}_\varepsilon[\mathbf{x}]\mathbf{d}, \qquad \mathbf{N}_\varepsilon = \mathbf{D}[\mathbf{x}]\mathbf{N}_u[\mathbf{x}]$$

Using the virtual work expression, the finite element representation of the equilibrium equations becomes:

$$\mathbf{Q}^T\mathbf{t} = \lambda\mathbf{p} \quad \text{with} \quad \mathbf{Q}^T \equiv \int_B \mathbf{N}_\varepsilon[\mathbf{x}]^T\mathbf{N}_\sigma[\mathbf{x}]\,dV \tag{2}$$

and the external force vector, when only mechanical actions are considered, is

$$\mathbf{p} = \int_{\mathscr{B}} \mathbf{N}_u^T \mathbf{b}[\mathbf{x}] dV + \int_{\partial_f \mathscr{B}} \mathbf{N}_u^T \mathbf{f}[\mathbf{x}] dA$$

$\mathbf{b}[\mathbf{x}]$ being the external body forces and $\mathbf{f}[\mathbf{x}]$ the surface force on the boundary $\partial_f \mathscr{B}$. The discrete form of the compatibility condition is

$$\boldsymbol{\rho} = \mathbf{Q}\mathbf{u} \tag{3}$$

where $\boldsymbol{\rho} = [\boldsymbol{\varepsilon}_1, \ldots, \boldsymbol{\varepsilon}_{N_\sigma}]^T$ collects the discrete strain conjugate, in the virtual work sense, to $\mathbf{t}$. Finally linear elastic constitutive law is defined by the elastic operator $\mathbf{E}[\mathbf{x}]$ so that

$$\boldsymbol{\sigma}[\mathbf{x}] = \mathbf{E}[\mathbf{x}]\boldsymbol{\varepsilon}[\mathbf{x}], \quad \boldsymbol{\varepsilon}[\mathbf{x}] = \mathbf{E}[\mathbf{x}]^{-1}\boldsymbol{\sigma}[\mathbf{x}] \tag{4}$$

From now on the dependence of quantities on $\mathbf{x}$ will be omitted for an easier reading.

2.2 The Elastic Envelope of the Stresses

We assume that the external actions $\mathbf{p}$ are expressed as a combination of basic loads $\mathbf{p}_i$ belonging to the admissible closed and convex *load domain*

$$\mathbb{P} := \left\{ \mathbf{p} \equiv \sum_{i=1}^{p} a_i \mathbf{p}_i : \; a_i^{min} \le a_i \le a_i^{max} \right\} \tag{5}$$

Denoting with $\mathbf{t}_{ei}$ the elastic stress solution for $\mathbf{p}_i$, the *elastic envelope* $\mathbb{S}_e$

$$\mathbb{S}_e := \left\{ \mathbf{t}_e \equiv \sum_{i=1}^{p} a_i \mathbf{t}_{ei} : a_i^{min} \le a_i \le a_i^{max} \right\} \tag{6}$$

defines the set of the elastic stresses $\mathbf{t}_e$ produced by each load path contained in $\mathbb{P}$.

By construction $\mathbb{S}_e$ and $\mathbb{P}$ are convex polytopes and each $\mathbf{t}_e \in \mathbb{S}_e$ can be expressed as a convex combination of the N_v elastic envelope vertexes $\mathbf{t}^{E\alpha}$ that can be usefully referred to the reference stress $\mathbf{t}^{E0}$ so obtaining:

$$\mathbf{t}_e = \mathbf{t}^{E0} + \sum_{\alpha=1}^{N_v} t^\alpha \mathbf{t}^{E\alpha}, \quad t^\alpha \ge 0, \quad \sum_{\alpha=1}^{N_v} t^\alpha = 1 \tag{7}$$

If the external loads increase by a real number λ the elastic envelope becomes $\lambda\mathbb{S}_e := \{\lambda \mathbf{t}_e : \; \mathbf{t}_e \in \mathbb{S}_e\}$.

Note that the vertexes of the stress envelope could be a subset of the 2^p vertexes of $\mathbb{P}$, however, to simplify the presentation we assume, from now on, $N_v = 2^p$.

2.3 The Shakedown Elastic Domain

Assuming elastic perfectly plastic material the stress $\boldsymbol{\sigma}$ will be *plastically admissible* if

$$f\big[\boldsymbol{\sigma}[\mathbf{x}]\big] \equiv \phi\big[\boldsymbol{\sigma}[\mathbf{x}]\big] - \sigma_y[\mathbf{x}] \leq 0 \quad \forall \mathbf{x} \in \mathscr{B} \tag{8}$$

where the yield function f is a sum of the homogeneous convex function ϕ and of the yield stress $\sigma_y \in \mathbb{R}$. In a FEM context of analysis the previous condition could be expressed in a weighted sense on the element, as proposed for example in [22], or tested in a finite number of points. For the sake of simplicity we assume control of plastic admissibility in the N_σ stress nodes so that $\mathbf{t}$ will be plastically admissible if

$$\mathbf{f}[\mathbf{t}] \leq \mathbf{0} \quad \Longleftrightarrow \quad f[\boldsymbol{\sigma}_g] \leq 0 \quad \forall g = 1, \ldots, N_\sigma \tag{9}$$

where, from now on, vector inequality will be considered in a componentwise fashion and

$$\mathbf{f}[\mathbf{t}] = \big[f[\boldsymbol{\sigma}_1]\ f[\boldsymbol{\sigma}_2] \ldots\ f[\boldsymbol{\sigma}_{N_\sigma}]\big]^T, \qquad f[\boldsymbol{\sigma}_g] \equiv \phi[\boldsymbol{\sigma}_g] - \sigma_{gy} \tag{10}$$

with $\sigma_{gy} := \sigma_y[\mathbf{x}_g]$.

Finally it is useful to express the plastically admissible condition for all the stresses contained in the amplified elastic envelope $\lambda \mathbb{S}_e$ translated by $\bar{\mathbf{t}}$. Due to the convexity of $\mathbf{f}$ and $\mathbb{S}_e$ this can be easily expressed in terms of the plastic admissibility of all vertex stresses $\mathbf{t}^\alpha = \lambda(\mathbf{t}^{E\alpha} + \mathbf{t}^{E0}) + \bar{\mathbf{t}}$

$$\mathbf{f}[\lambda \mathbf{t}_e + \bar{\mathbf{t}}] \leq \mathbf{0}, \quad \forall \mathbf{t}_e \in \mathbb{S}_e \quad \Longleftrightarrow \quad \mathbf{f}\big[\mathbf{t}^\alpha\big] \leq \mathbf{0}, \quad \forall \alpha \tag{11}$$

From now on we denote with a Greek superscript vertex quantities.

3 Shakedown and Limit Analysis Multipliers

Shakedown theorems used for the evaluation of the larger multiplier λ_a, called *shakedown safety factor*, amplifying the load domain $\mathbb{P}$ are rewritten in a unified format. A particular mathematical programming technique, the proximal point algorithm, to solve the static shakedown theorem will also be introduced. We always refer to shakedown analysis, the limit analysis case being simply obtained when the elastic envelope collapses in a single point.

3.1 Shakedown Theorems

Sufficient and necessary conditions for shakedown are given in the classic shakedown theorems [1] that will be written in a form suitable for FEM numerical implementations. In particular the Bleich–Melan static theorem is formulated in terms of

total stress, instead of self-equilibrated ones, making a unified notation for shakedown and limit analysis possible. The Koiter kinematical theorem is obtained as the dual, from the optimization point of view, of the primal static theorem so as to ensure an easy extension, to these discrete forms, of a series of properties regarding existence, uniqueness, duality gap, etc.

3.1.1 Static Theorem, Safe Multipliers and Multipliers Bounds

The static theorem states that a load domain multiplier λ_s will be safe if there exists a time-independent self-equilibrated stress field $\bar{\mathbf{t}}$ so that each stress in $\lambda_s \mathbb{S}_e + \{\bar{\mathbf{t}}\}$ is plastically admissible. The multiplier λ_a can be evaluated as the maximum of these safe multipliers recasting the static theorems in terms of the reference stress $\mathbf{t}^{E0}$:

$$\begin{aligned} &\text{maximize} && \lambda_s \\ &\text{subject to} && \mathbf{Q}^T \mathbf{t} = \lambda_s \mathbf{p} \\ & && \mathbf{t}^\alpha = \mathbf{t} + \lambda_s \mathbf{t}^{E\alpha}, \quad \alpha = 1, \ldots, N_v \\ & && \mathbf{f}\left[\mathbf{t}^\alpha\right] \le \mathbf{0}, \quad \alpha = 1, \ldots, N_v \end{aligned} \tag{12a}$$

with $\mathbf{p} \equiv \mathbf{Q}^T \mathbf{t}^{E0}$ and $\mathbf{t} \equiv \bar{\mathbf{t}} + \lambda_s \mathbf{t}^{E0}$. When $\mathbf{t}^{E0} = \mathbf{0}$ we have the classic form in terms of the self-equilibrated stress. Furthermore, without any loss in generality, we can set $\mathbf{t}^{E0}$ as a generic vertex of $\mathbb{S}_e$ so $\mathbf{t}$ becomes the total stress of this vertex. We assume $\mathbf{t}^{E1} \equiv \mathbf{0}$ so deleting in (12a) the constraint $\mathbf{t} \equiv \mathbf{t}^1$. An equivalent formulation for (12a) is obtained eliminating all the variables $\mathbf{t}^\alpha$ using the linear equality constraints and so the admissible conditions become:

$$\mathbf{f}^\alpha[\mathbf{t}, \lambda] \equiv \mathbf{f}\left[\mathbf{t} + \lambda \mathbf{t}^{E\alpha}\right] \le \mathbf{0}. \tag{12b}$$

When the external load domain collapses in a single point ($a_i^{min} = a_i^{max}$) Eqs. (12a) directly transform into the standard form of the static theorem of limit analysis. From (12a) we have that λ_a will be no greater than the values of the limit load multiplier obtained for a generic $\mathbf{p} \in \mathbb{P}$, and then also of the limit load of each vertex of $\mathbb{P}$. It is worth noting that the *plastic shakedown multiplier* $\bar{\lambda}$, simply obtained by deleting the equilibrium constraints in Eq. (12a), is not less than λ_a. Its evaluation, as will be better shown in the sequel, is obtained by solving a series of small optimization subproblems.

Finally Eq. (12a) can be rewritten, using a compact notation, in a format similar to that of the static theorem of the limit analysis:

$$\begin{aligned} &\text{maximize} && \lambda_s \\ &\text{subject to} && \tilde{\mathbf{Q}}^T \tilde{\mathbf{t}} = \lambda_s \tilde{\mathbf{p}} \\ & && \tilde{\mathbf{f}}[\tilde{\mathbf{t}}] \le \mathbf{0} \end{aligned} \tag{12c}$$

where the following quantities have been defined

$$\tilde{\mathbf{t}} := \begin{bmatrix} \mathbf{t}^1 \\ \vdots \\ \mathbf{t}^{N_v} \end{bmatrix}, \quad \tilde{\mathbf{f}}[\tilde{\mathbf{t}}] := \begin{bmatrix} \mathbf{f}[\mathbf{t}^1] \\ \vdots \\ \mathbf{f}[\mathbf{t}^{N_v}] \end{bmatrix}, \quad \tilde{\mathbf{p}} := \begin{bmatrix} \mathbf{p} \\ \mathbf{t}^E \end{bmatrix}, \quad \mathbf{t}^E := \begin{bmatrix} \mathbf{t}^{E2} \\ \vdots \\ \mathbf{t}^{EN_v} \end{bmatrix} \tag{13}$$

and

$$\tilde{\mathbf{Q}}^T := \begin{bmatrix} \mathbf{Q}^T & \cdot \\ -\boldsymbol{\Sigma}^T & \mathbf{I}_\alpha \end{bmatrix}, \quad \boldsymbol{\Sigma} := -\begin{bmatrix} \mathbf{I} & \cdots & \mathbf{I} \end{bmatrix} \tag{14}$$

where $\cdot$, $\mathbf{I}$ and $\mathbf{I}_\alpha$ are respectively zero and identity matrices of the appropriate dimension. From now on we denote with a Greek superscript the vertex components of a $(\tilde{\cdot})$ vector or matrix. The superscript 1, that denotes quantities of the reference vertex, will be omitted when inessential.

3.1.2 The Dual Problem: The Kinematical Theorem

Static theorem is a primal nonlinear convex optimization problem. The Lagrangian associated to it is

$$\mathscr{L}[\lambda, \tilde{\mathbf{t}}, \tilde{\boldsymbol{\mu}}, \Delta\tilde{\mathbf{u}}] = \lambda + \Delta\tilde{\mathbf{u}}^T \left(\tilde{\mathbf{Q}}^T \tilde{\mathbf{t}} - \lambda \tilde{\mathbf{p}}\right) - \tilde{\boldsymbol{\mu}}^T \tilde{\mathbf{f}}[\tilde{\mathbf{t}}]$$

where the Lagrange multipliers assume the following expression

$$\tilde{\boldsymbol{\mu}} := \begin{bmatrix} \boldsymbol{\mu}^1 \\ \vdots \\ \boldsymbol{\mu}^{N_v} \end{bmatrix}, \quad \boldsymbol{\mu}^\alpha := \begin{bmatrix} \mu_1^\alpha \\ \vdots \\ \mu_{N_\sigma}^\alpha \end{bmatrix}, \quad \tilde{\mathbf{u}} := \begin{bmatrix} \Delta\mathbf{u} \\ \Delta\boldsymbol{\rho} \end{bmatrix}, \quad \Delta\boldsymbol{\rho} := \begin{bmatrix} \Delta\boldsymbol{\rho}^2 \\ \vdots \\ \Delta\boldsymbol{\rho}^{N_v} \end{bmatrix}$$

with each $\boldsymbol{\mu}^\alpha \geq \mathbf{0}$. In the optimal values the Lagrangian has a saddle point [5, 7] making it possible to obtain the following dual problem that, with simple algebra, becomes the discrete form of the Koiter kinematical theorem:

$$\begin{aligned} \text{minimize} \quad & \lambda_c \equiv \tilde{\boldsymbol{\sigma}}_y^T \tilde{\boldsymbol{\mu}} \\ \text{subject to} \quad & \tilde{\boldsymbol{\mu}} \geq 0 \\ & \tilde{\mathbf{u}}^T \tilde{\mathbf{p}} = 1 \\ & \tilde{\mathbf{Q}}\tilde{\mathbf{u}} - \tilde{\mathbf{A}}[\tilde{\mathbf{t}}]\tilde{\boldsymbol{\mu}} = \mathbf{0} \end{aligned} \tag{15a}$$

where $\tilde{\boldsymbol{\sigma}}_y$ collect the yield stress values

$$\tilde{\boldsymbol{\sigma}}_y = \begin{bmatrix} \boldsymbol{\sigma}_y \\ \vdots \\ \boldsymbol{\sigma}_y \end{bmatrix}, \quad \boldsymbol{\sigma}_y = \begin{bmatrix} \sigma_{y1} \\ \vdots \\ \sigma_{yN_\sigma} \end{bmatrix}$$

and

$$\tilde{\mathbf{A}}[\tilde{\mathbf{t}}] := \left(\frac{\partial \mathbf{f}[\tilde{\mathbf{t}}]}{\partial \tilde{\mathbf{t}}}\right)^T = \text{blockdiag}\left[\mathbf{A}^1 \cdots \mathbf{A}^{N_v}\right] \tag{15b}$$

$\mathbf{A}^\alpha = (\frac{\partial \mathbf{f}[\mathbf{t}^\alpha]}{\partial \mathbf{t}^\alpha})^T$ being a diagonal matrix.

In the previous equations the Euler theorem for the homogeneous functions of order one has been used while the extension to homogeneous functions of order n is simple. Also for kinematical theorem (15a) we have the same format as the limit analysis case.

The saddle point property of the Lagrangian shows that the primal problem is convex and the dual is concave. When the first one has an admissible solution, that is when the elastic limit multiplier is other than zero, both problems have the same optimal value $\lambda_a = \max \lambda_s = \min \lambda_c$. Due to the convexity of the problem the obtained optimum is global such that the shakedown (limit) load factor is unique.

3.2 The Mathematical Programming Formulation of the Finite Step Elasto-plastic Analysis

The shakedown multipliers can also be obtained by evaluating a sequence of states, $\mathbf{z}^{(k)} := \{\lambda^{(k)}, \mathbf{t}^{(k)}, \mathbf{u}^{(k)}, \ldots\}$ solving a series of problems so defined:

$$\begin{aligned} &\text{maximize} && \Delta\xi^{(k)}\lambda^{(k)} - \frac{1}{2}\Delta\tilde{\mathbf{t}}^T\tilde{\mathbf{F}}\Delta\tilde{\mathbf{t}} \\ &\text{subject to} && \tilde{\mathbf{Q}}^T\tilde{\mathbf{t}}^{(k)} = \lambda^{(k)}\tilde{\mathbf{p}} \\ & && \tilde{\mathbf{f}}\left[\tilde{\mathbf{t}}^{(k)}\right] \le \mathbf{0} \end{aligned} \tag{16a}$$

where the superscript $(\cdot)^{(k)}$ will denote quantities evaluated in the kth of problems (16a) called the kth step, the symbol $\Delta(\cdot) = (\cdot)^{(k)} - (\cdot)^{(k-1)}$ is the increment of a quantity from the previous step and $\Delta\xi^{(k)} > 0$ is a real positive number. In the block-diagonal semi-definite positive matrix $\tilde{\mathbf{F}} := \text{blockdiag}[\mathbf{F}^1 \cdots \mathbf{F}^{N_v}]$ only $\mathbf{F}^1$ must be definite positive and can be evaluated through the following energy equivalence

$$\mathbf{F}^1 \equiv \mathbf{F} = \int_B \mathbf{N}_\sigma[\mathbf{x}]^T \mathbf{E}^{-1}[\mathbf{x}]\mathbf{N}_\sigma[\mathbf{x}]\, dV \tag{16b}$$

Note that, due to the local nature of the stress interpolation in Eq. (1), $\mathbf{F}$ also has a block diagonal structure that, usually, couples only the local finite element stress variables. In the following we assume, to simplify the notation and according to the finite element used, each block $\mathbf{F}_g^\alpha$ of $\mathbf{F}^\alpha$ to be defined at the stress node level.

Table 1 First order conditions for the proximal point algorithm

Local level:

Kinem. compatib.:	$\begin{cases} \mathbf{Q}\Delta\mathbf{u} - \sum_{\beta=2}^{N_v} \Delta\boldsymbol{\rho}^{\beta} - \mathbf{F}\Delta\mathbf{t}^{1} - \mathbf{A}^{1}\boldsymbol{\mu}^{1} = 0 \\ \Delta\boldsymbol{\rho}^{\beta} = \mathbf{F}^{\beta}\Delta\mathbf{t}^{\beta} + \mathbf{A}^{\beta(k)}\boldsymbol{\mu}^{\beta(k)} \end{cases}$	$\beta := 2 \cdots N_v$
Yielding:	$\mathbf{f}\left[\mathbf{t}^{\alpha(k)}\right] \leq \mathbf{0}$	$\alpha := 1 \cdots N_v$
Consistency:	$\left(\boldsymbol{\mu}^{\alpha(k)}\right)^{T} \mathbf{f}\left[\mathbf{t}^{\alpha(k)}\right] = 0$	$\alpha := 1 \cdots N_v$
Dual feasibility	$\boldsymbol{\mu}^{\alpha(k)} \geq \mathbf{0}$	$\alpha := 1 \cdots N_v$
Elastic domain:	$\mathbf{t}^{\alpha(k)} = \mathbf{t}^{(k)} + \lambda^{(k)}\mathbf{t}^{E\alpha}$	$\alpha := 1 \cdots N_v$

Global level:

Equilibrium:	$\mathbf{Q}^{T}\mathbf{t}^{(k)} = \lambda^{(k)}\mathbf{p}_0$
Normalization:	$\Delta\mathbf{u}^{T}\mathbf{p} + \sum_{\beta=2}^{N_v} \left(\Delta\boldsymbol{\rho}^{\beta}\right)^{T} \mathbf{t}^{E\beta} = \Delta\xi^{(k)}$

The first order Kunh–Tucker conditions of (16a) are:

$$\begin{array}{ll} \text{Kinematical compat.:} & \tilde{\mathbf{Q}}\Delta\tilde{\mathbf{u}} = \tilde{\mathbf{F}}\Delta\tilde{\mathbf{t}} + \tilde{\mathbf{A}}^{(k)}\tilde{\boldsymbol{\mu}}^{(k)} \\ \text{Yielding:} & \tilde{\mathbf{f}}\left[\tilde{\mathbf{t}}^{(k)}\right] \leq \mathbf{0} \\ \text{Consistency:} & \tilde{\mathbf{f}}\left[\tilde{\mathbf{t}}^{(k)}\right]^{T}\tilde{\boldsymbol{\mu}}^{(k)} = 0 \\ \text{Dual feasibility} & \tilde{\boldsymbol{\mu}}^{(k)} \geq \mathbf{0} \\ \text{Extended equilibrium:} & \tilde{\mathbf{Q}}^{T}\tilde{\mathbf{t}}^{(k)} - \lambda^{(k)}\tilde{\mathbf{p}} = \mathbf{0} \\ \text{Arc-length constraint:} & \tilde{\mathbf{p}}^{T}\Delta\tilde{\mathbf{u}} = \Delta\xi^{(k)} \end{array} \tag{16c}$$

which are also explicitly reported in Table 1. Equations (16c), for $\tilde{\mathbf{F}}\Delta\tilde{\mathbf{t}} = \mathbf{0}$, apart from the inessential scaling for $\Delta\xi^{(k)}$, are the primal–dual conditions of the shakedown theorems. Problem (16a) is similar to that presented in [10].

Note as, for assigned values of $\mathbf{u}$ and λ, the first group of equations in Table 1, due to the block structures of $\mathbf{f}$ and $\mathbf{F}$, can be solved at the *local level* (stress node) of the analysis. Conversely, equilibrium equations and normalization condition, coupling all the variables of the problem, define the *global level* of the analysis.

3.2.1 Convergence Properties of the Sequence of Elasto-plastic Steps

Starting from the known elastic limit $\mathbf{z}^{(0)}$, the sequence $\mathbf{z}^{(k)}$ generated from successive solutions of Eq. (16a) is safe in the sense of the static theorem and monotonously increasing in $\lambda^{(k)}$. In fact, due to Eq. (16c), subtracting the equilibrium equation of the two steps (k) and $(k-1)$ and multiplying the results by $\Delta\tilde{\mathbf{u}}$ we have

$$\Delta\lambda\Delta\xi^{(k)} = \Delta\tilde{\mathbf{t}}^T\tilde{\mathbf{Q}}\Delta\tilde{\mathbf{u}}$$

where the condition $\Delta\tilde{\mathbf{u}}^T\tilde{\mathbf{p}} = \Delta\xi^{(k)}$ was used. Due to the kinematical compatibility equations, we obtain

$$\begin{aligned}\Delta\xi^{(k)}\Delta\lambda &= \Delta\tilde{\mathbf{t}}^T\tilde{\mathbf{F}}\Delta\tilde{\mathbf{t}} + \Delta\tilde{\mathbf{t}}^T\tilde{\mathbf{A}}^{(k)}\tilde{\boldsymbol{\mu}}^{(k)} \\ &= \underbrace{\Delta\tilde{\mathbf{t}}^T\tilde{\mathbf{F}}\Delta\tilde{\mathbf{t}}}_{\geq 0} + \sum_{\alpha=1}^{N_v}\underbrace{\left(\Delta\mathbf{t}^{\alpha}\right)^T\mathbf{A}^{\alpha(k)}\boldsymbol{\mu}^{\alpha(k)})}_{\geq 0} \geq 0 \end{aligned} \tag{17}$$

The last two terms on the right hand side of Eq. (17) are not negative, the former due to the semi-definite positiveness of $\tilde{\mathbf{F}}$ and the latter due to the convexity of the elastic domain. As also $\Delta\xi^{(k)} > 0$ the sequence so generated does not decrease in λ. In the case $\lambda^{(k)} = \lambda^{(k-1)}$ with $\Delta\tilde{\mathbf{u}} \neq \mathbf{0}$ Eq. (17) implies $\Delta\tilde{\mathbf{t}} = \mathbf{0}$ and then also the requirements of the dual theorems (15a) are satisfied from Eq. (16c), that is the convergence to the desired shakedown multiplier. We call this kind of analysis *pseudo elastoplastic*, due to its meaning in the case of fixed loads.

3.2.2 The Mathematical Programming and Mechanical Interpretation of the Pseudo-elastoplastic Analysis

Each step in Eq. (16a) is obtained, apart from the inessential scaling of $\lambda^{(k)}$, by subtracting from the objective function of the static theorem a quadratic positive function in $\Delta\tilde{\mathbf{t}}$. In this respect it can be seen as a particular application of the proximal point algorithm (see Bertesekas [7] pp. 248 and [18, 19]) for solving Eq. (12c), i.e. the optimum solution of the static theorem is obtained by generating a convergent sequence of primal admissible solutions. The algorithm becomes competitive with direct methods if the sequence of steps is efficiently and robustly solved. This is possible by reusing the consolidated strain driven path-following algorithms adopted in elasto-plasticity [3].

Independently of this mathematical programming point of view, first order conditions in Eq. (16c) also have an important mechanical sense: in the fixed load case they define the standard finite step holonomic problem obtained by using a backward Euler scheme for integrating the constitutive elasto-plastic relationships. In this case $\Delta\mathbf{u}^{(k)}$ can be identified with the displacement step increment and the succession of point $\mathbf{z}^{(k)}$ with the equilibrium path. This holonomic transformation, with the irreversible phenomena that can now occur only at the beginning of each new

step, is widely adopted in elasto-plastic analysis. Its use is theoretically justified by the Ponter and Martin [20] extremal path theory that gives a clear mechanical sense to the so evaluated equilibrium path, allowing also the use of the kinematical part of the solution. A similar meaning can also be given for the shakedown case when the following expression of $\tilde{\mathbf{F}}$ is used

$$\tilde{\mathbf{F}} := \text{blockdiag}\left[\mathbf{F}, \mathbf{0}, \ldots, \mathbf{0}\right] \tag{18}$$

In this case Eq. (16c) corresponds to a backward Euler integration scheme of the elasto-plastic equations for a load moving for all vertexes of the monotonously amplified load domain at each step of the analysis so allowing elastic adaptation. In this sense pseudo elasto-plastic analysis, apart from its mathematical programming interpretation, assumes a more general meaning overreaching the shakedown theorems and making the extension to more complex materials simple.

Finally note that, when interest is only in the shakedown multiplier, matrices $\mathbf{F}^{\alpha}$, according to the global semi-definite property of $\tilde{\mathbf{F}}$, can be selected in order to simplify the computations.

4 Numerical Methods for the Evaluation of the Shakedown Multiplier

The proximal point algorithm in Eq. (16a)–(16c) can be efficiently solved by means of decomposition techniques, similar to that employed by Kaneko and Ha [19]. In this way a standard strain driven arc length formulation based on a return mapping by closest point projection scheme, such as that currently used to evaluate the equilibrium path of elasto-plastic structures, is obtained. This mathematical programming approach allows a direct comparison between the strain driven algorithm and direct global solvers in terms of performance and robustness. For a review of decomposition methods in optimization refer to Chap. 6 of Bertsekas [7] and Boyd's course lectures `EE364b` [5].

4.1 The Multisurface Decomposition

By selecting $\tilde{\mathbf{F}}$ as in Eq. (18) and omitting the index k and dependence on $\mathbf{z}^{(k-1)}$ to simplify the notation, the proximal point algorithm in Eq. (16a) becomes:

$$\begin{aligned} \max \quad & \Delta\xi\lambda - \frac{1}{2}\sum_{g=1}^{N_\sigma} \Delta\boldsymbol{\sigma}_g^T \mathbf{F}_g \Delta\boldsymbol{\sigma}_g \\ \text{subj.} \quad & \mathbf{Q}^T\mathbf{t} = \lambda\mathbf{p} \\ & f^{\alpha}[\boldsymbol{\sigma}_g, \lambda] \le 0 \quad \forall\alpha, g \end{aligned} \tag{19a}$$

where the linear equality constraints have been directly substituted.

The complicating equilibrium equation constraints can be eliminated using a dual decomposition strategy, that is by adding them to the objective function forming the following partial Lagrangian:

$$\begin{aligned} \max \quad & \mathscr{L} \equiv \mathscr{L}_\lambda[\lambda, \mathbf{u}] + \sum_{g=1}^{N_\sigma} \mathscr{L}_g[\boldsymbol{\sigma}_g, \mathbf{u}] \\ \text{subj.} \quad & f^\alpha[\boldsymbol{\sigma}_g, \lambda] \leq \mathbf{0} \quad \forall \alpha, g \end{aligned} \tag{19b}$$

where

$$\mathscr{L}_\lambda \equiv \lambda\big(\Delta\xi - \mathbf{p}^T \Delta\mathbf{u}\big), \qquad \mathscr{L}_g \equiv \boldsymbol{\sigma}_g^T \boldsymbol{\varepsilon}_g[\Delta\mathbf{u}] - \frac{1}{2}\Delta\boldsymbol{\sigma}_g^T \mathbf{F}_g \Delta\boldsymbol{\sigma}_g$$

with $\Delta\mathbf{u}$ the vector of the Lagrange multiplier and $\boldsymbol{\varepsilon}_g[\Delta\mathbf{u}]$ the gth component of $\mathbf{Q}\Delta\mathbf{u}$.

The dual of problem (19b) is obtained maximizing $\mathscr{L}$ with respect to the primal variables:

$$\mathscr{D}[\mathbf{u}] := \max_\lambda \left(\mathscr{L}_\lambda[\lambda, \mathbf{u}] + \sum_{g=1}^{N_\sigma} \max_{\substack{\boldsymbol{\sigma}_g, \\ f^\alpha[\boldsymbol{\sigma}_g, \lambda] \leq 0}} \mathscr{L}_g[\boldsymbol{\sigma}_g, \mathbf{u}] \right) \tag{19c}$$

that is now separated for limit analysis while it still has the complicating variables λ that prevent its decomposition for shakedown. The dual function is evaluated by fixing λ and performing the maximization with respect to $\boldsymbol{\sigma}_g$ so obtaining the following, strictly convex, minimization problems for each stress point g

$$\mathscr{D}_g[\lambda, \mathbf{u}] := \begin{cases} \min\limits_{(\boldsymbol{\sigma}_g)} & \frac{1}{2}\big(\boldsymbol{\sigma}_g - \boldsymbol{\sigma}_g^*\big)^T \mathbf{F}_g \big(\boldsymbol{\sigma}_g - \boldsymbol{\sigma}_g^*\big) \\ \text{subj.} & \mathbf{f}_s[\boldsymbol{\sigma}_g, \lambda] := \big[f^1[\boldsymbol{\sigma}_g, \lambda], \ldots, f^{N_v}[\boldsymbol{\sigma}_g, \lambda]\big]^T \leq \mathbf{0} \end{cases} \tag{19d}$$

where the trial stress defined as $\boldsymbol{\sigma}_g^* = \boldsymbol{\sigma}_g^{(k-1)} + \mathbf{F}_g^{-1}\boldsymbol{\varepsilon}_g$. Equation (19d) is a small convex problem in $n_\sigma := \dim\{\boldsymbol{\sigma}_g\}$ variables subject to N_v nonlinear constraints and its solution can be easily performed by means of a *Sequential Quadratic Programming* method (SQP). Each QP problem is, in this work, efficiently solved with the Goldfarb-Idnani dual active set method [25] already used in [4].

Finally the solution of (19a) is obtained by solving the following unconstrained problem:

$$\mathscr{D} := \min_{\Delta\mathbf{u}} \mathscr{D}[\mathbf{u}] = \min_{\Delta\mathbf{u}} \max_\lambda \left(\mathscr{L}_\lambda[\lambda, \mathbf{u}] - \sum_{g=1}^{N_\sigma} \mathscr{D}_g[\lambda, \mathbf{u}] \right) \tag{19e}$$

In the limit analysis case the objective function is independent of λ and the minimization is performed only with respect to $\mathbf{u}$.

The initial problem in (16a) is solved through its dual (19e) that is a free optimization problem nested within a series of simple convex projections (19d) of the

trial stresses in the admissible domain. Denoting with a comma the derivation with respect to the quantity that follows as subscript, and referring to Sect. 6.1 of [7] for the evaluation of the gradient of the dual function, the first order conditions of Eq. (19e) are

$$\mathbf{r}_{eq} \equiv \mathbf{Q}^T \mathbf{t}[\lambda, \mathbf{u}] - \lambda \mathbf{p} = \mathbf{0}, \qquad r_\lambda \equiv \mathbf{p}^T \Delta\mathbf{u} + \sum_g \boldsymbol{\mu}_{sg}^T \mathbf{f}_s[\boldsymbol{\sigma}_g, \lambda]_{,\lambda} - \Delta\xi = 0 \quad (19f)$$

where $\mathbf{t}[\lambda, \mathbf{u}]$ collects all $\boldsymbol{\sigma}_g[\lambda, \mathbf{u}]$ solutions of problems (19d) while $\boldsymbol{\mu}_{sg} = [\mu_{sg}^1, \ldots, \mu_{sg}^{N_v}]$ are the Lagrange multipliers associated with the inequality constraints. The stress is univocally defined in terms of $\Delta\mathbf{u}$ and λ, using Eq. (19d) that so represents an implicit nonlinear elastic constitutive law, the past history being contained in $\mathbf{z}^{(k-1)}$. The strict convexity of the problems (19d) makes the dual function differentiable and then solvable using a Newton method expressed only in terms of the configuration variables λ and $\mathbf{u}$. Equations (19f) are the standard equilibrium equations and the arc-length constraints in Table 1, making it easy to show that

$$\sum_g \boldsymbol{\mu}_{sg}^T \mathbf{f}_{s,\lambda} = \sum_{\beta=2}^{N_v} (\Delta\boldsymbol{\rho})^\beta \mathbf{t}^{E\beta}$$

Finally note that an alternative equivalent formulation for Eq. (19e) is

$$\begin{cases} \min\limits_{\Delta\mathbf{u}} & \mathscr{D}[\mathbf{u}] \\ \text{subj.} & \mathbf{p}^T \Delta\mathbf{u} + \sum\limits_g \boldsymbol{\mu}_g^T \mathbf{f}_{s,\lambda} - \Delta\xi = 0 \end{cases} \quad (19g)$$

4.2 A Further Decomposition Technique

Another possible decomposition technique is obtained relaxing all the complicating constraints defined, in Eq. (16c), by the extended equilibrium equations. Letting $\Delta\tilde{\mathbf{u}}$ be the Lagrange multiplier associated with the relaxed constraint and now making $\mathbf{F}^\alpha = \mathbf{F}$ for all vertexes, with $c \in \mathbb{R}^+$ a suitable scale factor, we obtain

$$\begin{aligned} &\text{maximize} \quad \mathscr{L}_\lambda[\lambda, \Delta\tilde{\mathbf{u}}] + \sum_{\alpha=1}^{N_v} \sum_{g=1}^{N\sigma} \mathscr{L}_g^\alpha[\tilde{\mathbf{t}}, \Delta\tilde{\mathbf{u}}] \\ &\text{subject to} \quad f^\alpha\left[\boldsymbol{\sigma}_g^\alpha\right] \le 0 \quad \forall\alpha, g \end{aligned} \quad (20a)$$

where now

$$\mathscr{L}_\lambda := \lambda\left(\Delta\xi - \Delta\tilde{\mathbf{u}}^T \tilde{\mathbf{p}}\right), \qquad \mathscr{L}_g^\alpha[\tilde{\mathbf{t}}, \Delta\tilde{\mathbf{u}}] := \frac{1}{2}\left(\boldsymbol{\sigma}_g^\alpha\right)^T \mathbf{F}_g \boldsymbol{\sigma}_g^\alpha - \left(\boldsymbol{\sigma}_g^\alpha\right)^T \boldsymbol{\varepsilon}_g^\alpha$$

$\boldsymbol{\sigma}_g^\alpha$ and $\boldsymbol{\varepsilon}_g^\alpha$ are the gth component of $\mathbf{t}^\alpha$ and $\Delta\boldsymbol{\rho}^\alpha$ respectively and $\Delta\boldsymbol{\rho}^1 = \mathbf{Q}\Delta\mathbf{u}$.

In this case too the problem is separable and it is possible to maximize function $\mathscr{L}_{g\alpha}$, at each stress point sub-level and for each α, as follows

$$\mathscr{D}_g^\alpha[\Delta\tilde{\mathbf{u}}] := \begin{cases} \min\limits_{(\boldsymbol{\sigma}_g^\alpha)} & \frac{1}{2}\left(\boldsymbol{\sigma}_g^\alpha - \boldsymbol{\sigma}_g^{\alpha\,*}\right)^T \mathbf{F}_g \left(\boldsymbol{\sigma}_g^\alpha - \boldsymbol{\sigma}_g^{\alpha\,*}\right) \\ \text{subj.} & f\left[\boldsymbol{\sigma}_g^\alpha\right] \le 0 \end{cases} \tag{20b}$$

where the trial stress is now defined as $\boldsymbol{\sigma}_g^{\alpha\,*} = (\boldsymbol{\sigma}_g^\alpha)^{(k-1)} + \mathbf{F}_g^{-1}\Delta\boldsymbol{\varepsilon}_g^\alpha$.

The initial problem in (16a) is then transformed into the following free minimization problem

$$\mathscr{D}[\tilde{\mathbf{u}}] : \begin{cases} \min\limits_{\Delta\tilde{\mathbf{u}}} & \left\{\sum\limits_{g,\alpha} \mathscr{D}_g^\alpha[\Delta\tilde{\mathbf{u}}]\right\} \\ \text{subj.} & \Delta\tilde{\mathbf{u}}^T\tilde{\mathbf{p}} = \Delta\xi \end{cases} \tag{20c}$$

nested within a series of simple convex projections (20b) of the trial stresses in the admissible domain. The first order conditions for (20c) represent the extended equilibrium equation plus the arc–length constraint and are

$$\tilde{\mathbf{r}}_{eq}[\lambda, \tilde{\mathbf{u}}] := \tilde{\mathbf{Q}}^T\tilde{\mathbf{t}}[\Delta\tilde{\mathbf{u}}] - \lambda\tilde{\mathbf{p}} = \mathbf{0}, \qquad r_\lambda[\lambda, \tilde{\mathbf{u}}] := \Delta\xi - \Delta\tilde{\mathbf{u}}^T\tilde{\mathbf{p}} = 0 \tag{20d}$$

with the stress $\mathbf{t}[\tilde{\mathbf{u}}]$ univocally defined in terms of $\Delta\tilde{\mathbf{u}}$ by using (20b). They can be solved iteratively using a Newton scheme. The other equations in Table 1 are solved exactly using Eq. (20b) for each assigned value of $\Delta\tilde{\mathbf{u}}$. Note also that this formulation is more decoupled with respect to the previous one and will be called SS-SD.

4.3 Final Considerations

Strain driven methods, apart from their classic interpretation, can be seen as decomposition strategies well suited for use within the proximal point algorithm. They solve, through a Newton method, the free dual problem obtained by means of a series of very small optimization subproblems (the closest point projection schemes) for each new estimate of the configuration variables. Stresses and other locally defined quantities then become functions of the configuration variables and the problem description is always compatible and usually highly nonlinear, even when the finite element is mixed. For a deeper discussion of how the problem description affects the convergence in Newton methods the reader is referred to [23]. The method fully exploits the information gained from the previously evaluated step handling the problem nonlinearity by means of adaptive arc-length selections. In the fixed load case both the above decomposition strategies are exactly the same.

5 Numerical Implementation of Strain Driven Methods

The implementational aspects of the numerical strategies previously proposed are now discussed. Readers are referred to [3, 4, 23] for details of the arc-length path-following strategies.

5.1 The Global Solution Scheme

Equations (19f) and (20d) are solved using a Newton method that, by means of block elimination of the local defined variables, can be expressed in a common *pseudo-compatible* format in terms of $(\mathbf{u}, \lambda)$ alone:

$$\begin{bmatrix} \mathbf{K}_j & -\mathbf{y}_j \\ -\mathbf{y}_j^T & h_j \end{bmatrix} \begin{bmatrix} \dot{\mathbf{u}} \\ \dot{\lambda} \end{bmatrix} = - \begin{bmatrix} \hat{\mathbf{r}}_{eq} \\ \hat{r}_\lambda \end{bmatrix} \tag{21a}$$

where subscript j denotes quantities evaluated in the current iteration and

$$\mathbf{K}_j = \mathbf{Q}^T \mathbf{E}_t \mathbf{Q}, \quad \mathbf{y}_j = \mathbf{p} + \mathbf{Q}^T \mathbf{t}_\lambda, \quad \hat{\mathbf{r}}_{eq} = \mathbf{r}_{eqj} + \mathbf{r}_{eq}^c, \quad \hat{r}_\lambda = r_{\lambda j} + r_\lambda^c \tag{21b}$$

with $\mathbf{E}_t, \mathbf{t}_\lambda, h_j, \mathbf{r}_{eq}^c$ and r_λ^c having a different expression depending on the algorithm in use. $\mathbf{E}_t$ always maintains the following local level block diagonal structure

$$\mathbf{E}_t = \text{blockdiag}[\mathbf{E}_{t1}, \ldots, \mathbf{E}_{tN_\sigma}] \tag{21c}$$

and is obtained by means of a standard FEM assemblage of local contributions.

The solution of Eq. (21a) is

$$\dot{\mathbf{u}} = \dot{\lambda}\hat{\mathbf{u}} + \bar{\mathbf{u}}, \quad \dot{\lambda} = \frac{\hat{r}_\lambda - \mathbf{y}_j^T \bar{\mathbf{u}}}{(\mathbf{y}_j^T \hat{\mathbf{u}} - h_j)} \quad \text{where} \quad \begin{cases} \hat{\mathbf{u}} = \mathbf{K}_j^{-1} \mathbf{y}_j \\ \bar{\mathbf{u}} = -\mathbf{K}_j^{-1} \hat{\mathbf{r}}_{eq} \end{cases} \tag{21d}$$

Equations in (21a)–(21d) have the same format as a standard arc length nonlinear analysis [3, 23], its solution having the same computational cost for both methods and in both cases of shakedown or limit analysis. The differences lie only in the local level operations which, involving only few variables, are cheaper to perform.

5.2 Numerical Implementation of the MS-RM Formulation

Letting $\mathbf{z}_0 := \mathbf{z}^{(k-1)}$, the scheme produces a sequence of plastically admissible estimates $\mathbf{z}_j$, convergent to the new state $\mathbf{z}^{(k)}$, by recursively updating the configuration variables as:

$$\mathbf{u}_{j+1} := \mathbf{u}_j + \dot{\mathbf{u}}_j, \qquad \lambda_{j+1} := \lambda_j + \dot{\lambda}_j \tag{22}$$

with $\dot{\mathbf{u}}_j$ and $\dot{\lambda}_j$ evaluated according to (21a)–(21d) and the other local variables using the return mapping process Eq. (19d). From the linearization of the first order conditions Eq. (19f) with respect to λ and $\mathbf{u}$ we obtain:

$$\begin{aligned}
&\mathbf{E}_t = \frac{\partial \mathbf{t}}{\partial \boldsymbol{\rho}} = \text{blockdiag}[\mathbf{E}_{t1}, \ldots, \mathbf{E}_{tN_\sigma}], \qquad \mathbf{E}_{tg} := \frac{\partial \boldsymbol{\sigma}_g}{\partial \boldsymbol{\varepsilon}_g} \\
&\mathbf{t}_\lambda := -\frac{\partial \mathbf{t}}{\partial \lambda} = -\begin{bmatrix} \boldsymbol{\sigma}_{1,\lambda} \\ \vdots \\ \boldsymbol{\sigma}_{N_\sigma,\lambda} \end{bmatrix} \\
&\boldsymbol{\sigma}_{g,\lambda} := \frac{\partial \boldsymbol{\sigma}_g}{\partial \lambda}, \qquad h_j = -\sum_{g=1}^{N_\sigma} \left(\boldsymbol{\mu}_g^T \mathbf{f}_{sg,\lambda\lambda} + \mathbf{f}_{sg,\lambda}^T \boldsymbol{\mu}_{g,\lambda} \right)
\end{aligned} \tag{23}$$

where $\boldsymbol{\rho} = \mathbf{Q}\Delta\mathbf{u}_j$ and $\boldsymbol{\varepsilon}_g$ is its gth component and both $\mathbf{r}_{eq}^c \equiv \mathbf{0}$, $r_\lambda^c = 0$.

The sequence so generated is locally convergent due to the presence of the arc-length condition that allows (21a) to be solved even when $\mathbf{K}_j$ becomes singular as happens near the shakedown or the limit load multiplier [3, 23]. For global convergence we can set $\mathbf{K}_j$ as equal to the initial elastic matrix $\mathbf{K}_E$. In this way while the quadratic convergence rate of the Newton method is lost we avoid the matrix decomposition for each $\mathbf{z}_j$. Alternatively a line search algorithm can be useful.

5.2.1 Evaluation of the Incremental Quantities for *MS-RM*

The algorithmic tangent moduli can be obtained from the second derivatives of the dual function once the internal variables are eliminated or, following an approach more common in the computational mechanics community, by the consistent linearization of the return mapping process. Making $n_a > 0$ the number of active constraints, and keeping the notation used to indicate quantities in this active subset unchanged, the first order condition defined by (19d) can be rewritten as

$$\begin{cases} \dot{\boldsymbol{\sigma}}_g = \mathbf{H}_g^{-1}(\dot{\boldsymbol{\varepsilon}}_g - \mathbf{A}_{sg}\dot{\boldsymbol{\mu}}_{sg} - \dot{\lambda}\mathbf{A}_{sg,\lambda}\,\boldsymbol{\mu}_{sg}) \\ \mathbf{A}_{sg}^T\dot{\boldsymbol{\sigma}}_g + \dot{\lambda}\mathbf{f}_{sg,\lambda} = \mathbf{0} \end{cases}$$

where $\boldsymbol{\mu}_{sg}^T = [\mu_{sg}^1, \ldots, \mu_{sg}^{n_a}]$ and

$$\mathbf{A}_{sg} = \left[\frac{\partial f^1}{\partial \boldsymbol{\sigma}_g} \cdots \frac{\partial f^{n_a}}{\partial \boldsymbol{\sigma}_g} \right], \qquad \mathbf{H}_g[\boldsymbol{\sigma}_g] = \mathbf{F}_g + \sum_{\alpha=1}^{n_a} \mu_{sg}^\alpha \frac{\partial^2 f^\alpha}{\partial \boldsymbol{\sigma}_g^2} \tag{24}$$

Making $\mathbf{W}_g = (\mathbf{A}_{sg}^T\mathbf{H}_g^{-1}\mathbf{A}_{sg})^{-1}$ we obtain the required quantities

$$\begin{aligned}
&\mathbf{E}_{tg} = \mathbf{H}_g^{-1} - \mathbf{H}_g^{-1}\mathbf{A}_{sg}\mathbf{W}_g\mathbf{A}_{sg}^T\mathbf{H}_g^{-1} \\
&\boldsymbol{\sigma}_{g,\lambda} = -\mathbf{H}_g^{-1}\mathbf{A}_{sg}\mathbf{W}_g\mathbf{f}_{sg,\lambda} - \mathbf{E}_{tg}\mathbf{A}_{sg,\lambda}\,\boldsymbol{\mu}_{sg}
\end{aligned} \tag{25}$$

Note that $\mathbf{E}_{tg}$ and $\mathbf{H}_j^{-1}\mathbf{A}_{sg}\mathbf{W}_g$ are directly furnished by the QP solution scheme used to solve Eq. (19d) so only $\mathbf{f}_{gs,\lambda}$, $\mathbf{f}_{gs,\lambda\lambda}$ and $\mathbf{A}_{sg,\lambda}$ need to be evaluated. Also note that for $n_a = 0$, we have the elastic step.

5.3 Numerical Implementation of the SS-RM Algorithm

Starting from $\mathbf{z}_0 := \mathbf{z}^{(k-1)}$, the scheme produces once more a sequence of estimates $\mathbf{z}_j$ updating the configuration variables as:

$$\tilde{\mathbf{u}}_{j+1} := \tilde{\mathbf{u}}_j + \dot{\tilde{\mathbf{u}}}_j, \qquad \lambda_{j+1} := \lambda_j + \dot{\lambda}_j \tag{26a}$$

where $\dot{\tilde{\mathbf{u}}}_j$ and $\dot{\lambda}_j$ now satisfy, the first order approximation of (20d):

$$\begin{bmatrix} \tilde{\mathbf{K}}_j & -\tilde{\mathbf{p}} \\ -\tilde{\mathbf{p}}^T & 0 \end{bmatrix} \begin{bmatrix} \dot{\tilde{\mathbf{u}}} \\ \dot{\lambda} \end{bmatrix} = - \begin{bmatrix} \tilde{\mathbf{r}}_{eq}^c \\ r_{\lambda j} \end{bmatrix} \tag{26b}$$

In the previous equation $\tilde{\mathbf{r}}_{eq}^c = \tilde{\mathbf{r}}_{eqj}$ and

$$\tilde{\mathbf{K}}_j = \tilde{\mathbf{Q}}^T \tilde{\mathbf{E}}_t \tilde{\mathbf{Q}}, \qquad \tilde{\mathbf{E}}_t := \text{blockdiag}\left\{\mathbf{E}_t^1, \ldots, \mathbf{E}_t^{N_v}\right\}$$

where, letting $\boldsymbol{\rho}_1 = \mathbf{Q}\Delta\mathbf{u}_j$, we have:

$$\mathbf{E}_t^\alpha := \frac{\partial \mathbf{t}^\alpha}{\partial \boldsymbol{\rho}^\alpha} = \text{blockdiag}\left\{\mathbf{E}_{t1}^1, \ldots, \mathbf{E}_{tN_\sigma}^{N_v}\right\}, \qquad \mathbf{E}_{tg}^\alpha = \frac{\partial \boldsymbol{\sigma}_g^\alpha}{\partial \boldsymbol{\varepsilon}_g^\alpha}$$

$\tilde{\mathbf{E}}_t$ is a block diagonal matrix with each block $\mathbf{E}_t^\alpha$ in turn blockdiagonal and defined by the consistent linearization of the return mapping algorithm (20b) (or of the dual function) as:

$$\mathbf{E}_{tg}^\alpha := \begin{cases} (\mathbf{H}_g^\alpha)^{-1}\left(\mathbf{I} - \frac{\mathbf{a}^\alpha \mathbf{a}^{\alpha T}(\mathbf{H}_g^\alpha)^{-1}}{h + (\mathbf{a}^\alpha)^T (\mathbf{H}_g^\alpha)^{-1}\mathbf{a}^\alpha}\right) & \text{if } \mu_g^\alpha > 0 \\ \mathbf{F}_g^{-1} & \text{otherwise} \end{cases} \tag{26c}$$

where now

$$\mathbf{a}^\alpha = \frac{\partial f[\boldsymbol{\sigma}_g^\alpha]}{\partial \boldsymbol{\sigma}_g^\alpha}, \qquad \mathbf{H}_g^\alpha = \mathbf{F}_g + \mu^\alpha \frac{\partial^2 f[\boldsymbol{\sigma}_g^\alpha]}{\partial (\boldsymbol{\sigma}_g^\alpha)^2}$$

and $h \simeq 1.0^{-4}$–1.0^{-6} is used to avoid singularity.

5.3.1 The Partitioned Solution Scheme

Recalling the definition of $\tilde{\mathbf{Q}}$ and of $\tilde{\mathbf{p}}$ in Eqs. (13), (14), the system in (26b) becomes

$$\begin{bmatrix} \mathbf{K}_{\rho\rho} & \mathbf{K}_{u\rho}^T & -\mathbf{t}_\rho \\ \mathbf{K}_{u\rho} & \mathbf{K}_{uu} & -\mathbf{p} \\ -\mathbf{t}_\rho^T & -\mathbf{p}^T & 0 \end{bmatrix} \begin{bmatrix} \dot{\boldsymbol{\rho}} \\ \dot{\mathbf{u}} \\ \dot{\lambda} \end{bmatrix} = - \begin{bmatrix} \mathbf{r}_{eq\rho} \\ \mathbf{r}_{eq} \\ r_\lambda \end{bmatrix} \tag{27a}$$

where

$$\mathbf{r}_{eq} = \mathbf{Q}^T \mathbf{t}_j - \lambda_j \mathbf{p}, \qquad r_\lambda = \Delta\xi - \mathbf{p}^T \Delta\mathbf{u}_j - \Delta\boldsymbol{\rho}_j^T \mathbf{t}^E \tag{27b}$$

$$\mathbf{r}_{eq\rho} = \begin{bmatrix} \mathbf{t}^2 - \mathbf{t} - \lambda \mathbf{t}^{E2} \\ \vdots \\ \mathbf{t}^{N_v} - \mathbf{t} - \lambda \mathbf{t}^{EN_v} \end{bmatrix} = \begin{bmatrix} \mathbf{r}_{eq}^2 \\ \vdots \\ \mathbf{r}_{eq}^{N_v} \end{bmatrix} \tag{27c}$$

and

$$\mathbf{K}_{uu} = \mathbf{Q}^T \mathbf{E}_t^1 \mathbf{Q}, \qquad \mathbf{K}_{u\rho} = -\mathbf{Q}^T \mathbf{E}_t^1 \boldsymbol{\Sigma}, \qquad \mathbf{K}_{\rho\rho} = \boldsymbol{\Sigma}^T \mathbf{E}_t^1 \boldsymbol{\Sigma} + \mathbf{E}_\rho \tag{27d}$$

with

$$\mathbf{E}_\rho := \text{blockdiag} \begin{bmatrix} \mathbf{E}_t^2 & \cdots & \mathbf{E}_t^{N_v} \end{bmatrix}. \tag{27e}$$

By a block elimination of $\dot{\boldsymbol{\rho}}$, performed at the local level due to the block diagonal structure of $\mathbf{K}_{\rho\rho}$ we obtain the global scheme in the form of Eqs. (21a)–(21d). To avoid the inversion of $\mathbf{K}_{\rho\rho}$, that could be computationally expensive for high values of N_v, it is convenient to use the Woodbury matrix identity so obtaining:

$$\mathbf{K}_{\rho\rho}^{-1} = \mathbf{E}_\rho^{-1} - \mathbf{E}_\rho^{-1} \boldsymbol{\Sigma}^T \mathbf{F}_t^{-1} \boldsymbol{\Sigma} \mathbf{E}_\rho^{-1} \quad \text{with } \mathbf{F}_t = \sum_{\alpha=1}^{N_v} \mathbf{F}_t^\alpha$$

where

$$\mathbf{F}_t^\alpha \equiv \left(\mathbf{E}_t^\alpha\right)^{-1} = \text{blockdiag}\left\{ \left(\mathbf{E}_{t1}^\alpha\right)^{-1}, \ldots, \left(\mathbf{E}_{tN_\sigma}^\alpha\right)^{-1} \right\}$$

Letting

$$\mathbf{q} = \sum_{\beta=2}^{N_v} \mathbf{F}_t^\beta \mathbf{t}^{E\beta}, \qquad \mathbf{r}_q = \sum_{\beta=2}^{N_v} \mathbf{F}_t^\beta \mathbf{r}_{eq}^\beta \tag{28}$$

with some substitutions we obtain the following expression for the quantities in Eqs. (21a)–(21d)

$$\begin{aligned} &\mathbf{E}_t = \mathbf{F}_t^{-1}, \qquad \mathbf{t}_\lambda = \mathbf{E}_t \mathbf{q}, \qquad h_j = \mathbf{q}^T \mathbf{E}_t \mathbf{q} - \sum_{\beta=2}^{N_v} \left(\mathbf{t}^{E\beta}\right)^T \mathbf{F}_t^\beta \mathbf{t}^{E\beta} \\ &\mathbf{r}_{eq}^c = \mathbf{Q}^T \mathbf{E}_t \mathbf{r}_q, \qquad r_\lambda^c = \sum_\beta \left(\mathbf{r}_{eq\rho}^\beta\right)^T \mathbf{F}_t^\beta \mathbf{t}^{E\beta} - \mathbf{q}^T \mathbf{E}_t \mathbf{r}_q \end{aligned} \tag{29}$$

and from back-substitution

$$\dot{\boldsymbol{\rho}}_\beta = \mathbf{F}_t^\beta \left(\dot{\lambda} \mathbf{t}^{E\beta} - \mathbf{r}_{eq}^\beta - \mathbf{E}_t \left(\dot{\lambda} \mathbf{q} - \boldsymbol{\rho}^1 - \mathbf{r}_q\right)\right)$$

Finally note that for a purely elastic behavior we obtain

$$\mathbf{E}_t = \frac{1}{c} \mathbf{F}^{-1}, \quad c = N_v$$

that is, with an appropriate selection of $\mathbf{F}$ we can use, at the global level, $\mathbf{K}_E$ as iteration matrix obtaining, also in this case, a global convergent scheme.

6 The Finite Element Discretization

A finite element suitable for shakedown analysis needs to be accurate with respect to both the evaluation of the elastic envelope stress $\mathbf{t}^{E\alpha}$ necessary for the correct evaluation of $\bar{\lambda}$ and with respect to the description of the ratcheting mechanism that usually require fine meshes. In this work these rules have been satisfied by using two finite elements on different discretization grids. In particular, stresses $\mathbf{t}^{E\alpha}$ are evaluated using the standard eight node compatible quadrilateral isoparametric element Q_8 [26] while the complete shakedown analysis exploits the mixed SIMPLEX (S) finite element [4], free of volumetric locking and sufficiently simple to be used with fine mesh. Note that, apart from the mixed interpolation, the element is similar to that recently proposed in [21].

6.1 The Simplex Finite Element

We briefly recall the SIMPLEX element while referring readers to [4] for details. Body domain B is subdivided into triangular elements of area A_e and thickness h_e with three nodes, located at the vertices of a triangle. A simple bilinear interpolation for the displacements was adopted while the stresses are kept constant on the nodal influence area $A_g = \sum_e A_{ge}/3$, sum of the contributions $A_{ge}/3$ of each element linked to the node g (see Fig. 1).

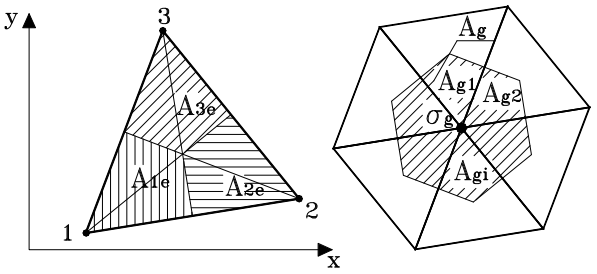

Fig. 1 The Simplex finite element

The compatible strain $\boldsymbol{\varepsilon}_{ge}$ for each of the n_{ge} elements linked to the stress node g is constant and coincident with that of the compatible linear triangle T_3. It can be expressed as

$$\boldsymbol{\varepsilon}_{ge} = \mathbf{D}_e \mathbf{d}_e \tag{30}$$

$\mathbf{d}_e = [\mathbf{u}_1, \mathbf{u}_2, \mathbf{u}_3]^T$ being the displacement element vector collecting the element node displacement vector $\mathbf{u}_k$. Denoting with $\mathbf{u}_g^T = [\mathbf{u}_{g1},\ \mathbf{u}_{g2}, \ldots, \mathbf{u}_{gn_e}]$ the stress node displacement vector, collecting the displacement vectors $\mathbf{u}_{gi}$ of all the elements linked to the stress node g and letting $\mathbf{A}_e$ be the matrix extracting the element displacements from $\mathbf{d}_g$

$$\mathbf{d}_e = \mathbf{A}_{ge} \mathbf{d}_g$$

we obtain the following algebraic form for the quantities required in the analysis:

$$\frac{1}{2}\int_V \boldsymbol{\sigma}^T \mathbf{E}^{-1} \boldsymbol{\sigma}\, dV = \frac{1}{2}\sum_{g=1}^{N_g} \boldsymbol{\sigma}_g^T \mathbf{F}_g \boldsymbol{\sigma}_g, \qquad \int_V \boldsymbol{\sigma}^T \boldsymbol{\varepsilon}\, dV = \sum_{g=1}^{N_g} \boldsymbol{\sigma}_g^T \mathbf{D}_g \mathbf{u}_g \tag{31}$$

and the strain work conjugate with $\boldsymbol{\sigma}_g$ is now defined by the compatibility matrix

$$\mathbf{Q}_g = \sum_{e=1}^{n_{ge}} \mathbf{D}_e \mathbf{A}_{ge} V_{ge}/3$$

where $V_{ge} = A_{ge} h_{ge}$ is the volume of the eth element linked with the stress node g and $V_g = \sum_{e=1}^{n_{ge}} V_{ge}/3$ the total volume related to the stress node and $\mathbf{F}_g = \mathbf{E}^{-1} V_g$.

Letting $\mathbf{t} = [\boldsymbol{\sigma}_1,\ \ldots, \boldsymbol{\sigma}_{N_\sigma}]^T$ and $\mathbf{u} = [\mathbf{u}_1,\ \ldots, \mathbf{u}_{N_u}]^T$ be the global vectors collecting the N_σ nodal stresses and the N_u displacements and denoting with

$$\mathbf{d}_g = \mathbf{T}_{ug} \mathbf{u}, \qquad \boldsymbol{\sigma}_g = \mathbf{T}_{\sigma g} \mathbf{t}$$

the operators linking local and global quantities we obtain

$$\mathbf{Q}^T \mathbf{t} \equiv \sum_g \mathbf{Q}_g^T \boldsymbol{\sigma}_g, \qquad \mathbf{F} = \sum_g \mathbf{T}_{\sigma g}^T \mathbf{F}_g \mathbf{T}_{\sigma g} \quad \text{with } \mathbf{Q}_g = \mathbf{T}_{ug}^T \mathbf{D}_g.$$

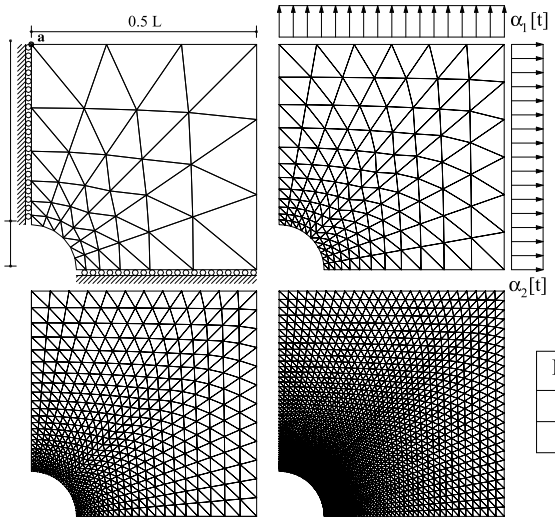

E=200000	ν=0.3
σ_y=10	th=1
p_1=1	p_2=1

Fig. 2 Geometry and finite element mesh for the square plate

7 Numerical Results

The algorithms presented are compared in terms of accuracy, robustness and effectiveness with the interior point method implemented in the commercial software *MOSEK*, using both a SOCP and a quadratic description (QP) of the constraints. We denote with *MS-RM* and *SS-RM* the strain driven return mapping analysis results, the name of the method is followed by K_e to indicate that the initial elastic stiffness matrix for each iteration was used (modified Newton method). Due to the linear convergence rate of the modified Newton method, the tolerance on the equilibrium equation is set equal to $1.0^{-3} \times (\lambda_e \sqrt{\sum_i \mathbf{p}_i^T \mathbf{K}_e^{-1} \mathbf{p}_i / N_v})$, that is not too strict but adequate to produce results affected by an error in λ_a no greater than 0.05 %.

For all tests we will denote with λ_c^i the limit load multiplier for the load combination obtained, for fixed values of α_k^i and corresponding to a given load domain vertex v^i. In this case, due to the coincidence of the formulations, we obtain the same behavior for the *MS-RM* and *SS-RM* algorithms.

7.1 Square Plate with a Central Circular Hole

The first test is the classic plate subject to the biaxial uniform loads p_1 and p_2 (see Fig. 2) considered in numerical shakedown analysis [27–29]. Letting $0 \leq \alpha_1 \leq 1$ and $0 \leq \alpha_2 \leq 1$, some limit analysis and shakedown cases were investigated.

The (6×3), (12×6), (24×12) and (48×24) grids denoted as *meshes 1*, *2*, *3* and *4* respectively were used. The first term indicates the number of elements along the hole, the second that on the opposite boundary.

Table 2 Square plate: discretization error on different meshes. The λ_c values are relative to vertex $v_3 = (1, 0)$ while ($\lambda_a = \bar{\lambda}$). Results are multiplied by 10

	mesh 1		*mesh 2*		*mesh 3*		*mesh 4*	
	λ_c^3	$\bar{\lambda}$	λ_c^3	λ_a	λ_c^3	λ_a	λ_c^3	λ_a
Q_8	8.060	4.333	8.020	4.315	8.008	4.305	8.003	4.302

Table 3 Comparison of λ_c and λ_a values for the square plate

(p_1, p_2)	λ_c			λ_a		
	(1, 1)	(1, 0.5)	(1, 0)	(1, 1)	(1, 0.5)	(1, 0)
Stein et al. [29]	–	–	0.802	0.453	0.539	0.624
Zhang et al. [30]	0.893	0.907	0.789	0.477	0.549	0.647
Gross-Weege [27]	0.882	0.891	0.782	0.446	0.524	0.614
Silveira [28]	0.894	0.911	0.803	0.429	0.500	0.594
Krabbenhøft et al. [11]				0.430	0.499	0.595
Garcea et al. [4]	0.902	0.912	0.806	0.438	0.508	0.604
Present (*mesh* 4)	0.895	0.911	0.800	0.430	0.499	0.595

Table 4 Square Plate: comparison of performance between the algorithms. Limit analysis is performed for vertex load $v_4 = (1.0, 1.0)$. In parentheses the number of steps

	MESH 3				MESH 4			
	λ_c^4		λ_a		λ_c^4		λ_a	
	CPU	loop	CPU	loop	CPU	loop	CPU	loop
MS-RM	5.25	118(31)	0.27	9(2)	31.55	146(39)	1.72	5(2)
MS-RM-$\mathbf{K}_e$	11.26	786(64)	0.10	16(2)	23.19	755(68)	0.38	14(2)
SS-RM	5.25	118(31)	0.40	10(3)	31.55	146(39)	1.96	7(3)
SS-RM-$\mathbf{K}_e$	11.26	786(64)	0.73	32(3)	23.19	755(68)	1.87	31(3)
MOSEK	0.44	15	1.73	14	2.20	13	8.14	10
MOSEK QP	0.62	19	2.02	10	4.64	22	33.70	12

In Table 4 the CPU time, the number of iterations and the number of values of safe state $\mathbf{z}^{(k)}$ (step), evaluated by the proximal point algorithm, are reported. In all cases the values of both the static and kinematic multiplier are coincident and some of them are reported in Table 2. A comparison with some of the results existing in literature is reported in Table 3.

In this example, due to the occurrence $\lambda = \bar{\lambda}$, we have practically the same performance between the *MS-RM* and *SS-RM* analysis also in the shakedown case, with the strain driven procedures more effective than IPM. Obviously this is only due to the practically elastic behavior of the structures for such values of the multiplier. With respect to CPU, at least in the evaluation of the limit analysis multiplier, our implementation pays the greater cost of the single iteration, in MOSEK performed using carefully tuned and very efficient routines for sparse linear algebra.

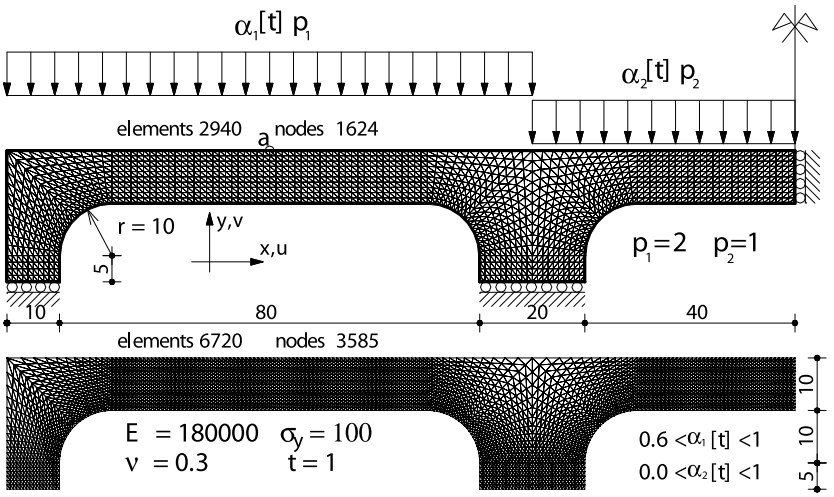

Fig. 3 Geometry and finite element grid for continuous beam

Table 5 Values of the collapse and shakedown multipliers for continuous beam. $v_2 = (0.6, 1)$, $v_3 = (1, 0)$

mesh 1					*mesh 2*				
λ_e	λ_a	$\bar{\lambda}$	λ_c^2	λ_c^3	λ_e	λ_a	$\bar{\lambda}$	λ_c^2	λ_c^3
1.281	3.143	5.995	5.330	3.198	1.276	3.166	5.971	5.368	3.221

7.2 A Symmetric Continuous Beam

The analysis regards the structure, whose geometry, load domain, material properties and the two discretization meshes used (*mesh 1* and *mesh 2*) are reported in Fig. 3. In this case we have ratcheting collapse, that is $\lambda_a < \lambda_c^i < \bar{\lambda}$. Shakedown and the lower limit load multipliers for the two different meshes are reported in Table 5.

In Table 6 performances of the various implementations are reported. Shakedown or limit load multipliers are more effectively evaluated using MOSEK and the *MS-RM* has an overall better behavior with respect to the *SS-RM* that exhibits its worst performances when the tangent matrix is used. Finally the cost of each iteration is highly affected by the number of constraints when using MOSEK.

8 Conclusions

In this work, it has been shown how standard incremental elastoplastic analysis based on closest point projection return mapping schemes, can be obtained from a mathematical programming problem, consisting in the application of the proximal

Table 6 Continuous beam: comparison of performance between the algorithms. Limit analysis is performed for vertex load $v_2 = (0.6, 1.0)$. In parentheses the number of steps

	MESH 1				MESH 2			
	λ_c^2		λ_a		λ_c^2		λ_a	
	CPU	loop	CPU	loop	CPU	loop	CPU	loop
MS-RM	7.68	81(23)	9.75	99(26)	23.22	97(25)	27.55	108(27)
MS-RM-$\mathbf{K}_e$	14.70	892(92)	25.0	1441(144)	32.00	800(84)	60.21	1409(145)
SS-RM	7.68	81(23)	20.14	184(47)	23.22	97(25)	63.40	230(52)
SS-RM-$\mathbf{K}_e$	14.70	892(92)	55.60	1841(185)	32.00	800(84)	136.07	1915(194)
MOSEK	0.96	15	2.52	17	2.75	15	5.37	16
MOSEK QP	2.36	25	11.42	28	7.61	26	30.70	40

point algorithm to the static shakedown theorem and in its solution by means of dual decomposition methods.

Two decomposition procedures, called respectively *MS-RM* and *SS-RM* have been presented. The first scheme, that proves to be the more effective, corresponds to the mathematical programming formulation of that used in [3, 4]. With respect to the previous proposal it proves to be more efficient also due to the use of a reference load formulation that makes the problem less nonlinear. The multisurface return mapping process is performed avoiding any linearization of the elastic domain exploiting an efficient sequential quadratic programming method and an active set strategy, so improving both accuracy and performance. The *SS-RM* is based on a standard return mapping process but requires a greater number of iterations each of which is almost as expensive as in the *MS-RM* case. For both the decomposition methods the elastic stiffness matrix can be exploited to obtain global convergent algorithms and to reduce the computational cost for very large dimension problems.

The shakedown strain driven analysis is easy to implement in existing commercial software performing nonlinear incremental elasto-plastic analysis. The lower efficiency with respect to IPM methods is compensated by its more significant mechanical interpretation that allows the reuse of the kinematical part of the solution and by, nowadays, a greater generality and robustness due to its consolidated and extensive use in this context of analysis.

References

1. Zouain, N.: Shakedown and safety assessment. In: Encyclopedia of Computational Mechanics, vol. 2, pp. 291–334. Wiley, New York (2004)
2. Armero: Elastoplastic and viscoplastic deformations of solids and structures. In: Encyclopedia of Computational Mechanics, vol. 2. Wiley, New York (2004)
3. Casciaro, R., Garcea, G.: An iterative method for shakedown analysis. Comput. Methods Appl. Mech. Eng. **191**, 5761–5792 (2002)
4. Garcea, G., Armentano, G., Petrolo, S., Casciaro, R.: Finite element shakedown analysis of two-dimensional structures. Int. J. Numer. Methods Eng. **63**(8), 1174–1202 (2005)

5. Boyd, S.: Lecture Slides and Notes. Courses EE364a and EE364b, http://www.stanford.edu/class/ee364b/lectures.html
6. Nocedal, Wright, S.J.: Numerical Optimization. Springer, Philadelphia (1997)
7. Bertsekas: Nonlinear Programming. Athena Scientific, Nashua (2003)
8. Nemirovski, A., Todd, M.: Interior-point methods for optimization. Acta Numer. **17**, 191–234 (2008)
9. Wright, M.H.: The interior-point revolution in optimization: history, recent developments, and lasting consequences. Bull. Am. Math. Soc. **42**(1), 39–56 (2005)
10. Krabbenhoft, K., Lyamin, A.V., Sloan, S.W., Wriggers, P.: An interior-point algorithm for elastoplasticity. Int. J. Numer. Methods Eng. **69**(3), 592–626 (2007)
11. Krabbenhoft, K., Damkilde, L.: A general non-linear optimization algorithm for lower bound limit analysis. Int. J. Numer. Methods Eng. **56**(2), 165–184 (2003)
12. Pastor, F., Loute, E.: Solving limit analysis problems: an interior-point method. Commun. Numer. Methods Eng. **21**(11), 631–642 (2005)
13. Vu, D.K., Yan, A.M., Nguyen-Dang, H.: A primal–dual algorithm for shakedown analysis of structures. Comput. Methods Appl. Mech. Eng. **193**, 4663–4674 (2004)
14. Nguyen, A.D., Hachemi, A., Weichert, D.: Application of the interior-point method to shakedown analysis of pavements. Int. J. Numer. Methods Eng. **4**(75), 414–439 (2008)
15. Makrodimopoulos, A.: Computational formulation of shakedown analysis as a conic quadratic optimization problem. Mech. Res. Commun. **33**, 72–83 (2006)
16. Makrodimopoulos, A., Martin, C.M.: Lower: bound limit analysis of cohesive frictional materials using second-order cone programming. Int. J. Numer. Methods Eng. **66**(4), 604–634 (2006)
17. Makrodimopoulos, A., Martin, C.M.: Upper bound limit analysis using simplex strain elements and second-order cone programming. Int. J. Numer. Anal. Methods Geomech. **31**(6), 835–865 (2007)
18. Ha, C.D.: A generalization of the proximal point method. SIAM J. Control Optim. **28**(3), 503–512 (1990)
19. Kaneko, Y., Ha, C.D.: A decomposition procedure for large-scale optimum plastic design problems. Int. J. Numer. Methods Eng. **19**, 873–889 (1983)
20. Ponter, A.R.S., Martin, J.B.: Some extremal properties and energy theorems for inelastic materials and their relationship to the deformation theory of plasticity. Int. J. Mech. Phys. Solids **20**(5), 281–300 (1972)
21. Liu, G.R., Nguyen-Thoi, T., Nguyen-Xuan, H.b., Lam, K.Y.: A node-based smoothed finite element method (NS-FEM) for upper bound solutions to solid mechanics problems. Comput. Struct. **87**, 14–26 (2009)
22. Bilotta, A., Casciaro, R.: An hight–performance element for the analysis of 2D elastoplactic continua. Comput. Methods Appl. Mech. Eng. **196**, 818–828 (2007)
23. Garcea, G., Trunfio, G.A., Casciaro, R.: Mixed formulation and locking in path following nonlinear analysis. Comput. Methods Appl. Mech. Eng. **165**(1–4), 247–272 (1998)
24. A.S.: The MOSEK Optimization Tools Version 3.2 (Revision 8). User's Manual and Reference Available from January (2005). http://www.mosek.com
25. Goldfarb, D., Idnani, A.: A numerically stable dual method for solving strictly convex quadratic programs. Math. Program. **27**, 1–33 (1983)
26. Bathe, K.J.: Finite Element Procedures. Prentice-Hall, New York (1996)
27. Groß-Wedge, J.: On the numerical assessment of the safety factor of elastic-plastic structures under variable loading. Int. J. Mech. Sci. **39**(4), 417–433 (1997)
28. Zouanin, N., Borges, L., Silveira, J.L.: An algorithm for shakedown analysis with nonlinear yield function. Comput. Methods Appl. Mech. Eng. **191**, 2463–2481 (2002)
29. Stein, E., Zhang, G.: Shakedown with nonlinear strain–hardening including structural computation using finite element method. Int. J. Plast. **8**, 1–31 (1992)
30. Zhang, X., Liu, Y., Cen, Z.: Boundary element methods for lower bound limit and shakedown analysis. Eng. Anal. Bound. Methods **28**, 905–917 (2004)

Shakedown and Optimization Analysis of Periodic Composites

M. Chen, A. Hachemi, and D. Weichert

Abstract In this work, non-conforming three-dimensional finite elements are used for the limit and shakedown analysis of periodic metal-matrix composites. The optimal design variables, such as fiber distribution and various volume fractions are investigated. Combined with homogenization theory, the global safe loading domains for the composites, as well as the global homogenized material parameters are determined, which opens the way for global structural design.

1 Introduction

The prediction of structure failure behavior under variable loads with unknown time history is very difficult. Direct methods, namely limit and shakedown analysis, can help to overcome this difficulty. Application of shakedown analysis to composites, especially long fiber-reinforced metal matrix composites, upsurge these years. For heterogeneous materials, there are generally two scales concerned. On the microscopic level, local stress and strain analysis are performed and the influence of each phase (fiber or matrix) is investigated. On the macroscopic scale, the global response of the composite is analyzed with the help of homogenization theory. This methodology was first proposed for the case of limit analysis of heterogeneous media in [37, 39]. In a similar way, some authors carried out shakedown analysis of periodic composites with static approach [46, 47], as well as the kinematic approach [9, 31, 32]. Furthermore, some scholars also considered geometrical effects and damage in micro-level [14, 19, 20, 45].

M. Chen (✉)
School of Mechanical Engineering, Southeast University, Nanjing, China
e-mail: min@iam.rwth-aachen.de

M. Chen · A. Hachemi · D. Weichert
Institut für Allgemeine Mechanik, RWTH-Aachen, Templergraben 64, 52062 Aachen, Germany

A. Hachemi
e-mail: hachemi@iam.rwth-aachen.de

D. Weichert
e-mail: weichert@iam.rwth-aachen.de

G. Saxcé et al. (eds.), *Limit State of Materials and Structures*,
DOI 10.1007/978-94-007-5425-6_3,

Besides the issue of optimization, the implementation of lower bound direct methods includes also the finite element method. Finite elements are used to obtain local stress or local strain, as well as the equilibrium matrix. Previously, two-dimensional finite elements have usually been used to deal with plane strain or plane stress cases [5, 8, 33]. The disadvantage of the plane element is in the restriction of the applied load. Recently, work concerned with metal matrix composites has been extended to solid elements, which makes loads perpendicular to the transverse direction of composites possible [49]. However, the 20-node solid elements usually lead to large numbers of variables, because the scale of the optimization problem depends mainly on the type of finite element.

Moreover, combined with homogenization theory, the material performances as a whole are discussed, such as the influence of fiber distribution and volume fraction [15, 33, 50]. From the knowledge of the local (or microscopic) material properties, the global (or macroscopic) mechanical response of fiber-reinforced composites is predicted. The evaluation of elastic properties involves classical constitutive laws and homogenization theory [10, 35]. The prediction of nonlinear macroscopic behavior has been mostly performed by using 3-D models based on limit analysis for periodic heterogeneous material [40, 41].

In this work, a non-conforming three-dimensional finite element coupled with direct methods and homogenization technique is presented for the limit and shakedown analysis of periodic metal-matrix composites.

2 Analytical Model on Micro-level

2.1 Multi-scale Approach

Periodic composites, especially fiber-reinforced metal matrix composites (MMCs), are investigated in our work. There is at least one ductile phase. For the interface, perfect bonding is assumed. For the ductile phase, we use the theory of elasto-plasticity.

Figure 1 shows the procedure of homogenization theory, which is composed mainly into two steps:

- ***Localization***: Any macroscopic point in a heterogeneous structure is investigated in a representative volume element (RVE). This process is termed localization or representation.
- ***Globalization***: The inverse procedure, by which microscopic properties originating in the RVE are idealized at the marco level is called globalization or homogenization.

Each periodic micro structural block is usually called a Representative Volume Element (RVE) or Unit Cell, denoted by V. We introduce a small parameter δ [2], e.g. the "slow" variables x, y (or global coordinates), and the "fast" variables ξ, η

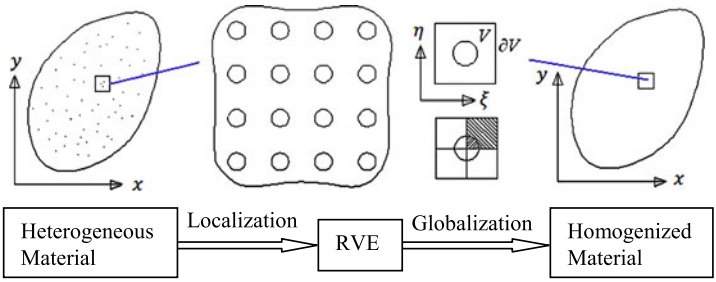

Fig. 1 Homogenization theory

(or local coordinates). The relationship between the two coordinates are as follows:

$$\xi = \frac{x}{\delta}, \qquad \eta = \frac{y}{\delta} \tag{1}$$

δ determines the size of the RVE, which plays an important role in studying the heterogeneous material, especially for non-uniform structure. There has been much research about how to determine a representative volume element. The various classes and definitions of RVE and the main practical approaches can be referred to in [29]. Briefly, the RVE of a heterogeneous material with random spatial distribution is investigated through the "Window" technique [34]. For a heterogeneous material with periodic distribution, the smallest unit is normally defined as the RVE.

The macroscopic strain $\boldsymbol{E}$ and stress $\boldsymbol{\Sigma}$ are linked to the microscopic strain $\boldsymbol{\varepsilon}$ and stress $\boldsymbol{\sigma}$ by the following relationships [37]:

$$\boldsymbol{E}(x, y, z) = \frac{1}{V} \iiint \boldsymbol{\varepsilon}(\xi, \eta, \zeta) dV = \left\langle \boldsymbol{\varepsilon}(\xi, \eta, \zeta) \right\rangle \tag{2}$$

$$\boldsymbol{\Sigma}(x, y, z) = \frac{1}{V} \iiint \boldsymbol{\Sigma}(\xi, \eta, \zeta) dV = \left\langle \boldsymbol{\Sigma}(\xi, \eta, \zeta) \right\rangle \tag{3}$$

Here, $\langle \cdot \rangle$ stands for the averaging operator.

In the static shakedown theory for composite materials with periodic microstructure, the macroscopic stress is decomposed into a purely elastic part $\boldsymbol{\sigma}^E$ and a time-independent residual one $\bar{\boldsymbol{\rho}}$:

$$\boldsymbol{\Sigma}(x, y, z) = \frac{1}{V} \int_V \left(\alpha \boldsymbol{\sigma}^E + \bar{\boldsymbol{\rho}} \right) dV = \frac{1}{V} \int_V \alpha \boldsymbol{\sigma}^E dV + \frac{1}{V} \int_V \bar{\boldsymbol{\rho}} dV \tag{4}$$

On the basis of homogenization theory, the first step is to obtain the local stress and strain in the RVE. According to the type of the prescribed loading condition, either a strain approach or a stress approach can be used.

2.2 Stress and Strain Approaches

For heterogeneous materials, especially random ones, it is impossible to determine the material characteristics precisely. This results from an incomplete knowledge of the material structure, such as the spatial distribution of different phases or the strength of interface coherence. Therefore, effective (or homogenized) material properties are studied to replace the actual ones. Combined with homogenization theory, the stress approach and the strain approach are mainly used [25, 26, 37].

2.2.1 Strain Approach

As the name implies, the macroscopic strain $\boldsymbol{E}$ is imposed at the boundary of a representative volume element. In practice, the macroscopic strain is amounted to displacement loading. Let the displacement $\boldsymbol{u}$ be decomposed as [6, 24]:

$$\boldsymbol{u} = \boldsymbol{E} \cdot x + \boldsymbol{u}^{per} \tag{5}$$

where $\boldsymbol{u}^{per}$ is the periodic displacement field. Then, the local strain $\boldsymbol{\varepsilon}$ can be derived as:

$$\boldsymbol{\varepsilon} = \boldsymbol{E} + \boldsymbol{\varepsilon}^{per} \tag{6}$$

where $\boldsymbol{\varepsilon}^{per}$ is the fluctuating part in every representative volume element. Note that the periodicity of $\boldsymbol{u}^{per}$ implies that the average of $\boldsymbol{\varepsilon}^{per}$ on the RVE vanishes and therefore the average of ε is $\boldsymbol{E}$.

To find $\boldsymbol{\sigma}^{\boldsymbol{E}}$ and $\boldsymbol{\varepsilon}^{\boldsymbol{per}}$, the elastic localization problem can be written as:

$$P_{strain} = \begin{cases} \operatorname{div} \boldsymbol{\sigma}^{\boldsymbol{E}} = 0 & \text{in } V \\ \boldsymbol{\sigma}^{\boldsymbol{E}} = \boldsymbol{d} : (\boldsymbol{E} + \boldsymbol{\varepsilon}^{\boldsymbol{per}}) & \text{in } V \\ \boldsymbol{\sigma}^{\boldsymbol{E}} \cdot \boldsymbol{n} & \text{anti-periodic on } \partial V \\ \boldsymbol{u}^{per} & \text{periodic on } \partial V \end{cases} \tag{7}$$

Here, V is the domain of the representative volume element in R^3. Furthermore, $\boldsymbol{\sigma}^{E}$ is the purely elastic stress and $\boldsymbol{n}$ is the out-normal vector on the surface of the RVE under consideration. The anti-periodicity of $\boldsymbol{\sigma}^{\boldsymbol{E}} \cdot \boldsymbol{n}$ on ∂V implies that $\boldsymbol{\sigma}^{\boldsymbol{E}} \cdot \boldsymbol{n}$ has opposite values on opposite sides of ∂V. The periodicity of $\boldsymbol{u}^{per}$ means that $\boldsymbol{u}^{per}$ is the same at two opposite points of the boundary.

In our work, we consider the particular case that a uniform displacement is imposed on the boundary. After deformation, the edges of each element are still straight (Fig. 2). Considering symmetry, the investigated model can be simplified to one quarter of the representative volume element.

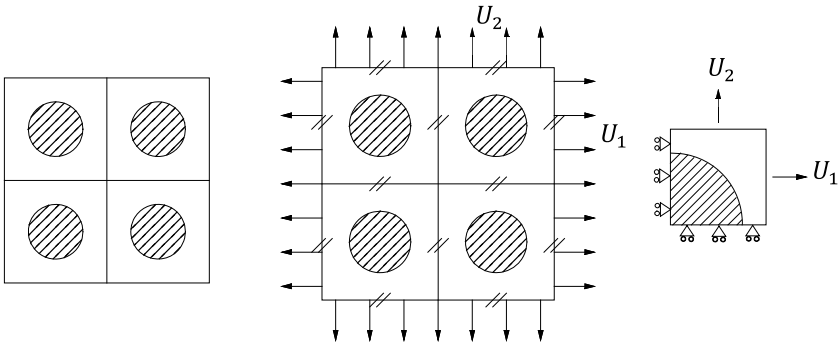

Fig. 2 Strain method

Fig. 3 Stress method

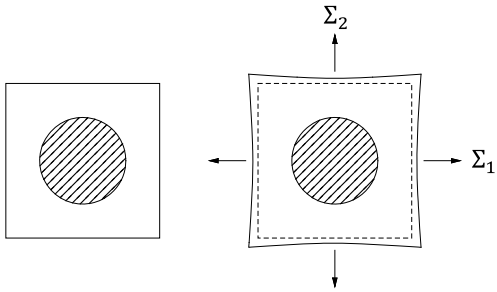

Thus, the problem can be formulated as [37]:

$$P^*_{strain} = \begin{cases} \operatorname{div} \boldsymbol{\sigma}^{\boldsymbol{E}} = 0 & \text{in } V \\ \boldsymbol{\sigma}^{\boldsymbol{E}} = \boldsymbol{d} : \boldsymbol{E} & \text{in } V \\ \boldsymbol{u}^{s} & \text{symetric condition on } \partial V \\ \boldsymbol{u}^{per} = 0 & \text{on } \partial V \end{cases} \tag{8}$$

For the shakedown analysis of composites, we still need to consider the residual stress field $\bar{\boldsymbol{\rho}}$, which should satisfy the self-equilibrated condition and periodicity conditions.

$$P^{res}_{strain} = \begin{cases} \operatorname{div} \bar{\boldsymbol{\rho}} = 0 & \text{in } V \\ \bar{\boldsymbol{\rho}} \cdot \boldsymbol{n} & \text{anti-periodic on } \partial V \end{cases} \tag{9}$$

2.2.2 Stress Approach

In this approach, the macroscopic stress $\boldsymbol{\Sigma}$ is imposed at the boundary. After deformation, the boundary displacement is not uniform anymore (Fig. 3).

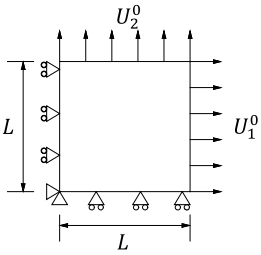

Fig. 4 2D homogeneous material under plane stress

The elastic localization problem can then be written as [37]:

$$P_{stress} = \begin{cases} \operatorname{div} \boldsymbol{\sigma}^{\boldsymbol{E}} = 0 & \text{in } V \\ \boldsymbol{\sigma}^{\boldsymbol{E}} = \boldsymbol{d} : \boldsymbol{\varepsilon} & \text{in } V \\ \boldsymbol{\sigma}^{\boldsymbol{E}} \cdot \boldsymbol{n} = \boldsymbol{\Sigma} \cdot \boldsymbol{n} & \text{on } \partial V \end{cases} \tag{10}$$

The residual stress field $\bar{\boldsymbol{\rho}}$ is also self-equilibrated and satisfies the periodicity condition. However, in the stress method, we need an additional condition, that the average value of $\bar{\boldsymbol{\rho}}$ should equal zero.

$$P_{stress}^{res} = \begin{cases} \operatorname{div} \bar{\boldsymbol{\rho}} = 0 & \text{in } V \\ \bar{\boldsymbol{\rho}} \cdot \boldsymbol{n} = 0 & \text{on } \partial V \end{cases} \tag{11}$$

For the finite element solution, this requirement could be satisfied by adding a fictive node in each element of the meshed RVE [12, 25, 40].

2.3 Transformation Between Two Scales

After analysis on the level of a representative volume element, we may transfer the local displacement domain to a global stress domain in the principal direction with the help of the particular case of the homogenization theory presented in Sect. 2.2.1 [33]. Take the case of two-dimensional plane stress as an example (Fig. 4). The material is homogeneous, with Young's modulus E and Poisson's ratio ν. In terms of Hooke's law:

$$\begin{cases} \varepsilon_x = \frac{1}{E}(\sigma_x - \nu\sigma_y) \\ \varepsilon_y = \frac{1}{E}(\sigma_y - \nu\sigma_x) \\ \gamma_{xy} = \frac{2(1+\nu)}{E}\tau_{xy} \end{cases} \quad \Longrightarrow \quad \begin{cases} \sigma_x = \frac{E}{1-\nu^2}(\varepsilon_x + \nu\varepsilon_y) \\ \sigma_y = \frac{E}{1-\nu^2}(\varepsilon_y + \nu\varepsilon_x) \\ \tau_{xy} = 0 \end{cases} \tag{12}$$

The case of homogeneous plane stress is characterized by the fact that there is no residual stress field and all the local stresses have the same value.

With this, we obtain:

$$\begin{cases} \Sigma_1^e = \sigma_x \\ \Sigma_2^e = \sigma_y \end{cases} \tag{13}$$

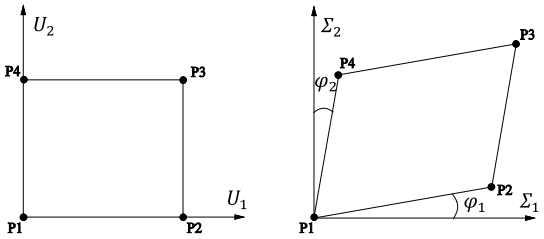

Fig. 5 Transformation relationship

Consider four points in the shakedown displacement load domain (Fig. 5).
For P2:

$$\begin{cases} U_1 = \alpha_{SD} U_1^0 \\ U_2 = 0 \end{cases} \Longrightarrow \begin{cases} \varepsilon_x = U_1^0 / L \\ \varepsilon_y = 0 \end{cases} \Longrightarrow \begin{cases} \sigma_x = \frac{E\varepsilon_x}{1-\nu^2} \\ \sigma_y = \frac{\nu E \varepsilon_x}{1-\nu^2} = \nu \sigma_x \end{cases} \tag{14}$$

Therefore, the point P2 in the shakedown macroscopic stress domain has the value:

$$\begin{cases} \Sigma_1 = \alpha_{SD} \Sigma_1^e \\ \Sigma_2 = \alpha_{SD} \nu \Sigma_1^e \end{cases} \tag{15}$$

After transformation, P2 in the local displacement domain rotated through an angle φ_1 in the macroscopic stress domain:

$$\varphi_1 = \arctan \frac{\Sigma_2}{\Sigma_1} = \arctan(\nu) \tag{16}$$

Similarly, for P4:

$$\begin{cases} \Sigma_1 = \alpha_{SD} \nu \Sigma_2^e \\ \Sigma_2 = \alpha_{SD} \Sigma_2^e \end{cases} \tag{17}$$

The rotated angle φ_2 is:

$$\varphi_2 = \arctan \frac{\Sigma_1}{\Sigma_2} = \arctan(\nu) \tag{18}$$

According to the constitutive law (12), we may obtain the macroscopic elastic stress for P3 as:

$$\begin{cases} \Sigma_1^{e*} = \frac{E}{1-\nu^2}(\varepsilon_x - \nu \varepsilon_y) \\ \Sigma_2^{e*} = \frac{E}{1-\nu^2}(\nu \varepsilon_x - \varepsilon_y) \end{cases} \tag{19}$$

Also the angle φ^* between the X-axis and a line from the origin to P3 is:

$$\varphi^* = \arctan \frac{\Sigma_2^*}{\Sigma_1^*} \tag{20}$$

Table 1 The positions of points in different domains

Points	Displacement load domain		Stress load domain	
P1	0	0	0	0
P2	αU_1^0	0	$\alpha \Sigma_1^e$	$\alpha \nu \Sigma_1^e$
P3	αU_1^0	αU_2^0	$\alpha \Sigma_1^{e*}$	$\alpha \Sigma_1^{e*}$
P4	0	αU_2^0	$\alpha \nu \Sigma_2^e$	$\alpha \Sigma_2^e$

Note: α could be the safety factors for elastic, alternating plasticity, shakedown or limit state

The positions of load vertexes in different domains are listed in Table 1.

For composite materials, we need to keep in mind that the macroscopic stress is obtained basing on the particular case of homogenization theory by using strain approach. Since the average of the residual stresses equals to zero, the macroscopic stress at different states can be defined as:

- Elastic state: $\Sigma_{EL} = \alpha_{EL} \Sigma^e$
- Shakedown state: $\Sigma_{SD} = \alpha_{SD} \Sigma^e$
- Limit state: $\Sigma_{LM} = \alpha_{LM} \Sigma^e$
- Alternating plasticity state: $\Sigma_{AP} = \alpha_{AP} \Sigma^e$

A numerical example will be illustrated in Sect. 4.2.

3 Numerical Solution

The implementation of lower bound direct methods mainly involves two numerical tools: finite element method and large scale nonlinear optimization method.

Any discretized version of lower bound direct methods preserves the relevant bounding properties only if the following conditions are satisfied simultaneously: (i) the solution of the purely elastic response is exact; (ii) the residual stress field satisfies pointwise the homogeneous equilibrium equations; (iii) the yield condition is satisfied in each point of the considered material.

The existence of these bounding properties was the reason why many authors used the finite element stress method with a discretization of the stress field. Moreover, since the lower bound direct methods is formulated in static quantities, it is meaningful to discretize the stress field rather than the displacement field. However, most of the available finite element codes are based on displacement formulations. On the other hand, it is very difficult to preserve in this case the bounding properties. Especially the first condition can hardly be satisfied, if other than particular structures are studied. Thus, to use the proposed method with commercial codes, we prefer here the displacement method. In this case all the well-known displacement element formulations can be used. For that purpose it is necessary to transform the statical equations from their local form into the equivalent weak form.

3.1 Non-conforming Finite Element Discretization

The accuracy of a finite element analysis can be improved by using higher order elements. For instance, an 8 node element can be replaced with a 20 node element, which costs more computer time and storage. Wilson et al. [48] introduced non-conforming elements by including additional incompatible displacement modes, which increase the basic accuracy still using a simple (first order) element and avoid the "shear locking" numerical problem [36, 38].

The scale of the optimization problem is mainly determined by the number of elements and the used element type. Therefore non-conforming element is adopted here. Comparative study using different element types is presented in Sect. 4.1.

In terms of the principle of virtual work, the external virtual work is equal to the internal virtual work, when equilibrated forces and stresses undergo unrelated but consistent displacements and strains:

$$\int_V \left\{\varepsilon^*\right\}^T \left\{\alpha \boldsymbol{\sigma}^E + \bar{\boldsymbol{\rho}}\right\} \mathrm{d}V = \int_{\partial V} \left\{\boldsymbol{\delta}^*\right\}^T \left\{\boldsymbol{p}^*\right\} \mathrm{d}S + \int_V \left\{\boldsymbol{\delta}^*\right\}^T \left\{\boldsymbol{f}^*\right\} \mathrm{d}V \tag{21}$$

Here, $\boldsymbol{\varepsilon}^*$ is the virtual strain, and $\boldsymbol{\delta}^*$ is the virtual displacement. These discretizations have to be carried out for both the purely elastic stress field $\boldsymbol{\sigma}^E$ and the residual stress field $\bar{\boldsymbol{\rho}}$.

Let u, v and w be displacements in the x, y and z-directions, respectively, then:

$$\begin{Bmatrix} u \\ v \\ w \end{Bmatrix} = \sum_{i=1}^{8} N_i \begin{Bmatrix} u_i \\ v_i \\ w_i \end{Bmatrix} + \begin{bmatrix} P_1 & P_2 & P_3 & 0 & 0 & 0 & 0 & 0 & 0 \\ 0 & 0 & 0 & P_1 & P_2 & P_3 & 0 & 0 & 0 \\ 0 & 0 & 0 & 0 & 0 & 0 & P_1 & P_2 & P_3 \end{bmatrix} \{a\} \tag{22}$$

Here, N_i is the shape function, $N_i = \frac{1}{8}(1 + rr_i)(1 + ss_i)(1 + tt_i)$; r, s, t are natural coordinates, and r_i, s_i, t_i are the values of the natural coordinates of node i. $P_1 = 1 - r^2$, $P_2 = 1 - s^2$ and $P_3 = 1 - t^2$. One important feature is that P_1, P_2 and P_3 are zero at eight nodes, which maintains the displacement compatibility at nodes. $\{a\}$ is the vector of additional degrees of freedom.

$$\{a\} = \{a_1\ a_2\ a_3\ a_4\ a_5\ a_6\ a_7\ a_8\ a_9\}^T$$

The element stiffness matrix is defined as follows:

$$\begin{aligned} \boldsymbol{K}^e &= \int_{V_e} \boldsymbol{B}^T \boldsymbol{D}^{-1} \boldsymbol{B}\, \mathrm{d}x\, \mathrm{d}y\, \mathrm{d}z = \int_{-1}^{1}\int_{-1}^{1}\int_{-1}^{1} \boldsymbol{B}^T \boldsymbol{D}^{-1} \boldsymbol{B} |\boldsymbol{J}|\, \mathrm{d}r\, \mathrm{d}s\, \mathrm{d}t \\ &= \sum_{i=1}^{ngl1}\sum_{j=1}^{ngl2}\sum_{k=1}^{ngl3} |\boldsymbol{J}| \boldsymbol{B}^T \boldsymbol{D}^{-1} \boldsymbol{B} w_r^i w_s^j w_t^k \end{aligned} \tag{23}$$

Here, $\boldsymbol{B}$ is the strain matrix, computed from the derivatives of shape functions; $\boldsymbol{D}$ is the fourth-order tensor of elastic modulus; $|\boldsymbol{J}|$ is the determinant of the Jacobian matrix, which is evaluated at the centre of the element [22], i.e. $r = s = t = 0$; w

are weighting factors; $ngl1$, $ngl2$, $ngl3$ are the number of Gauss points along r, s, t directions, respectively. Using Gauss quadrature, the $2 \times 2 \times 2$ scheme has found to be adequate. The dimension of element stiffness matrix is 33×33, instead of 24×24 for standard 8 node finite element. For 20-node solid element, the stiffness matrix can be evaluated using $3 \times 3 \times 3$ Gauss points. However, a reduced 14 points integration rule is also used, since this rule gives the same accuracy with less computational effort [22].

In a similar way, the residual stress can be discretized as follows (see e.g. [28]):

$$\begin{aligned}\int_{V_e} \boldsymbol{B}^T\{\bar{\boldsymbol{\rho}}\}\,\mathrm{d}V &= \int_{-1}^{1}\int_{-1}^{1}\int_{-1}^{1} \boldsymbol{B}^T\{\bar{\boldsymbol{\rho}}\}|J|\,\mathrm{d}r\,\mathrm{d}s\,\mathrm{d}t \\ &= \sum_{i=1}^{ngl1}\sum_{j=1}^{ngl2}\sum_{k=1}^{ngl3} |J|\boldsymbol{B}^T\{\bar{\boldsymbol{\rho}}\} w_r^i w_s^j w_t^k \end{aligned} \tag{24}$$

The weighting factors $w_r = w_s = w_t = 1$, when using 2 Gauss points at each axis direction. Therefore, we obtain:

$$[\boldsymbol{C}]^e = \int_{-1}^{1}\int_{-1}^{1}\int_{-1}^{1} \boldsymbol{B}^T = \sum_{m=1}^{NGE} |J| \begin{bmatrix} \boldsymbol{B}_O{}^T \\ \boldsymbol{B}_A{}^T \end{bmatrix} = \sum_{n=1}^{NGE} \left[\boldsymbol{C}_m^e\right] \tag{25}$$

NGE is the total number of Gauss points in each element: $NGE = ngl1 \times ngl2 \times ngl3 = 8$. For the whole system,

$$[\boldsymbol{C}] = \sum_{n=1}^{NE}\sum_{m=1}^{NGE} |J|\boldsymbol{B}^T = \sum_{n=1}^{NE}[\boldsymbol{C}]^e = \sum_{n=1}^{NE} \begin{bmatrix} \boldsymbol{C}_O{}^e \\ \boldsymbol{C}_A{}^e \end{bmatrix} = \begin{bmatrix} \boldsymbol{C}_O \\ \boldsymbol{C}_A \end{bmatrix} \tag{26}$$

NE is the total number of elements. The equilibrium matrix $[\boldsymbol{C}]$ is composed of two parts: $[\boldsymbol{C}_O]$, with the dimension $3NK \times 6NGS$ and the additional matrix $[\boldsymbol{C}_A]$, with the dimension $9NE \times 6NGS$, corresponding to the extra shape function of non-conforming finite element.

Finally, the shakedown problem can be formulated as the following mathematical problem:

$$\begin{aligned} &\max \alpha \\ &\begin{cases} [\boldsymbol{C}]\{\bar{\boldsymbol{\rho}}\} = 0 \\ F\left[\alpha\boldsymbol{\sigma}_i^e(P_k) + \bar{\boldsymbol{\rho}}_i, \sigma_{Yi}\right] \le 0 \\ i \in [1, NGS],\ k \in \left[1, 2^n\right] \end{cases} \end{aligned} \tag{27}$$

Here, $\bar{\boldsymbol{\rho}}$ is the time-independent periodic residual stress field; F is the von-Mises yield condition; NGS is the number of Gauss points of the considered representative element; n is the number of independent loads; $[\boldsymbol{C}]$ is the constant equilibrium matrix, uniquely defined by the discretized representative volume element with respect to boundary conditions; σ_{Yi} is the yield stress; P_k is the load vertex.

3.2 Interior Point Method

The static shakedown problem is finally reduced to a large-scale nonlinear optimization problem after discretization by using finite elements. Nowadays, different methods are developed to solve large-scale nonlinear optimization problems [16, 17], such as sequential quadratic programming (SQP), augmented Lagrangian method and interior point method. Correspondingly, different software packages are available. Here, we focus on the interior-point-method-based software packages IPDCA and IPOPT.

IPDCA (Interior Point with DC regularization Algorithm), is a C-programming package, using quasi-definite matrix techniques [1], which is specially designed for shakedown and limit analysis, and characterized by high speed and large scale number of variables [27, 28].

IPOPT (Interior Point Optimizer) is an open source software package for large-scale nonlinear optimization [44]. It implements an interior-point line-search filter method. However, the algorithm is only trying to find the local minimizer of the problem [43]. For non-convex problems, many stationary points may exist. As a matter of fact, the static shakedown problem is convex, and thus any local minimizer is also global minimizer as well. IPOPT is designed to solve the general mathematical optimization forms:

$$\begin{aligned} &\min f(x) \\ &\text{s.t.} \quad c_L \le c(x) \le c_U \\ &\qquad x_L \le x \le x_U \end{aligned} \tag{28}$$

Note that the equality constraints can be formulated by setting $c_L = c_U$. To simplify the notation, the following problem formulation is considered:

$$\begin{aligned} &\min f(x) \\ &\text{s.t.} \quad c(x) = 0, \quad i = 1, \ldots, m \\ &\qquad x \ge 0 \end{aligned} \tag{29}$$

where $f : R^n \to R$, and $c : R^n \to R^m$ are twice continuously differentiable functions. As an interior point (or barrier) method, the proposed algorithm computes solutions for a sequence of barrier problems, with the barrier parameter $\mu > 0$.

$$\begin{aligned} \min \quad & \varphi_\mu(x) := f(x) - \mu \sum_{i=1}^{n} \log(x_i) \\ \text{s.t.} \quad & c(x) = 0 \end{aligned} \tag{30}$$

The KKT conditions for (30) are:

$$\begin{aligned} \nabla \varphi_\mu(x) + \lambda \nabla c(x) &= 0 \\ c(x) &= 0 \end{aligned} \tag{31}$$

Solving this system directly by a Newton-type method leads to a so-called primal method, which treats only the primal variables x and the multipliers λ. However, the term $\nabla\varphi_\mu(x)$ includes components μ/x_i. It indicates, that system (31) is not defined at the optimal solution x^* of system (29) with bound $x^*_{(i)} = 0$, i.e. an optimal solution will be in the interior of the region defined by $x \geq 0$.

The amount of influence of barrier term relies on the size of μ. Under certain conditions, the optimal solution $x^*(\mu)$ of system (31) converges to x^* of the original system (29): As $x_i \to 0$, $\log(x_i) \to \infty$; As $\mu \to 0$, $x^*(\mu) \to x^*$.

Instead of using this primal approach, dual variables z are introduced: $z_i = \mu/x_i$. Therefore, the KKT conditions (31) are equivalent to the perturbed KKT conditions or primal-dual equations [42]:

$$\begin{aligned} \nabla f(x) + \lambda \nabla c(x) &= 0 \\ c(x) &= 0 \\ XZe - \mu e &= 0 \end{aligned} \tag{32}$$

where $X = \mathrm{Diag}(x)$, $Z = \mathrm{Diag}(z)$ and $e = (1, \ldots, 1)^T$. Note, that Eqs. (32) for $\mu = 0$ together with $(x \geq 0,\ z \geq 0)$ are KKT conditions for original system (36). The optimality error for the above barrier problem is defined as:

$$E_\mu(x, \lambda, z) = \max\left\{ \frac{\|\nabla f(x) + \lambda \nabla c(x)\|_\infty}{s_d}, \left\|c(x)\right\|_\infty, \frac{\|XZe - \mu e\|_\infty}{s_c} \right\} \tag{33}$$

s_d and s_c are scaling factors, under the definition:

$$s_d = \max\left\{ s_{\max}, \frac{\|\lambda\|_1 + \|z\|_1}{m+n} \right\} \Big/ s_{\max}, \qquad s_c = \max\left\{ s_{\max}, \frac{\|z\|_1}{n} \right\} \Big/ s_{\max} \tag{34}$$

$s_{\max}$ is a fixed number, in IPOPT $s_{\max} = 100$. Let $E_0 = (x,\ \lambda,\ ,z)$ denote the optimality error for the original problem. The overall algorithm terminates if an approximate solution satisfies:

$$E_\mu\left(\tilde{x}^*, \tilde{\lambda}^*, \tilde{z}^*\right) \leq \theta_{tol} \tag{35}$$

θ_{tol} is the user provided convergence tolerance. In order to solve the barrier problem for a given fixed value μ_j, a Newton method is applied to nonlinear systems of equation (32):

$$\begin{bmatrix} W_k & A_k & -I \\ A_k^T & 0 & 0 \\ Z_k & 0 & X_k \end{bmatrix} \begin{pmatrix} d_k^x \\ d_k^\lambda \\ d_k^z \end{pmatrix} = - \begin{pmatrix} \nabla f(x_k) + A_k \lambda_k - z_k \\ c(x) \\ X_k Z_k e - \mu_j e \end{pmatrix} \tag{36}$$

Here $A_k := \nabla c(x_k)$; $W_k := \nabla_x(\nabla f(x_k) + A_k) = \nabla^2_{xx} L(x_k, \lambda_k, z_k)$; $L(x, \lambda, z) := f(x) + c(x)^T\lambda - z$; $d_k^x := x_{k+1} - x_k$; $d_k^\lambda := \lambda_{k+1} - \lambda_k$; $d_k^z := z_{k+1} - z_k$.

Reformulating Eqs. (36) into a symmetric system:

$$\begin{cases} W_k d_k^x + A_k d_k^\lambda - I d_k^z = -(\nabla f(x_k) + A_k \lambda_k - z_k) \\ A_k^T d_k^x = -c(x_k) \\ Z_k d_k^x + X_k d_k^z = -(X_k Z_k e - \mu_j e) \end{cases}$$

$$\Longrightarrow \quad \begin{cases} d_k^z = \mu_j X_k^{-1} e - X_k^{-1} Z_k d_k^x - z_k \\ (W_k + X_k^{-1} Z_k) d_k^x + A_k d_k^\lambda = -(\nabla f(x_k) - \mu_j X_k^{-1} e + A_k \lambda_k) \end{cases}$$

$$\Longrightarrow \quad \begin{bmatrix} W_k + \Sigma_k & A_k \\ A_k^T & 0 \end{bmatrix} \begin{pmatrix} d_k^x \\ d_k^\lambda \end{pmatrix} = - \begin{pmatrix} \nabla \varphi_{\mu j}(x_k) + A_k \lambda_k \\ c(x) \end{pmatrix} \tag{37}$$

Here $\nabla \varphi_{\mu j}(x_k) = \nabla f(x_k) - \mu_j X_k^{-1} e$; $\Sigma_k = X_k^{-1} Z_k$.

In order to avoid a singularity or ill-conditioned problem, the iteration matrix is modified by adding a diagonal correction, i.e. regularization:

$$\begin{bmatrix} W_k + \Sigma_k + \delta_w I & A_k \\ A_k^T & -\delta_c I \end{bmatrix} \begin{pmatrix} d_k^x \\ d_k^\lambda \end{pmatrix} = - \begin{pmatrix} \nabla \varphi_{\mu j}(x_k) + A_k \lambda_k \\ c(x) \end{pmatrix} \tag{38}$$

δ_w and δ_c are two scalars, called "numeric damping coefficient". These choices for each iteration can be determined by Algorithm IC (Inertia Correction) [44]. The next iteration is then determined by:

$$\begin{aligned} x_{k+1} &:= x_k + \alpha_k d_k^x \\ \lambda_{k+1} &:= \lambda_k + \alpha_k d_k^\lambda \\ z_{k+1} &:= z_k + \alpha_k^z d_k^z \end{aligned} \tag{39}$$

α_k is primal step length; α_k^z is dual step length.

From the above description, one may observe, that either the Newton method or the damped Newton method uses the first and second derivatives (gradient and Hessian) to find the stationary point. Meanwhile, IPOPT also offers an option to approximate the Hessian of the Lagrangian by a limited-memory quasi-Newton method (L-BFGS) [7]. L-BFGS stands for "limited memory BFGS", which uses the Broyden-Fletcher-Goldfarb-Shanno update to approximate the Hessian matrix. That is, by using quasi-Newton method, the Hessian matrix of second derivatives of function does not need to be computed, which can be updated by analyzing successive gradient vectors instead.

4 Results and Discussion

To show the validity of the proposed methods, several numerical results are presented. The input data for the optimization procedure are obtained from customized ANSYS and Matlab, and the optimization is carried out with IPOPT.

Table 2 Material properties Al/Al_2O_3

	E (GPa)	ν	σ_Y (MPa)
Matrix (Al)	70	0.3	80
Fiber (Al_2O_3)	370	0.3	2000

4.1 Comparison of Different Elements

To show the advantage of non-conforming element, we tested the limit analysis of MMCs by step-by-step method using the following element types: (a) 8-node brick element with bilinear shape function (LSF); (b) 8-node brick element with extra shape function (ESF), i.e. non-conforming element; (c) 20-node brick element with quadratic shape function. Square pattern of periodicity (Fig. 8, Left) under plane strain condition is considered and subjected to the uniaxial stress Σ_{11}. Material properties is shown in Table 2, with the assumption that each phase is isotropic and elastic-perfectly plastic.

Using an 8-node solid element with a bilinear shape function, we can observe that in the limit uniaxial stress Σ_{11} is extremely large (Fig. 6). However, an 8-node solid element with extra shape function produces reasonable results, similar to the 20-node solid element. Because 8-node element with bilinear shape functions can not represent flexural response.Therefore, the key point of the non-conforming element is to add quadratic terms on the basis of linear shape function.

4.2 Illustration of Transformation

The transformation given in Sect. 2.1 is illustrated by considering a thin plate with square pattern (Fig. 8, Left). The side of RVE is 100 mm, the width is 2 mm and the fiber radius is 15 mm. Material model is the same as in Sect. 4.1. It is subjected to two independent displacement loadings: $U_1^0 = U_0$; $U_2^0 = U_0$. The elastic and

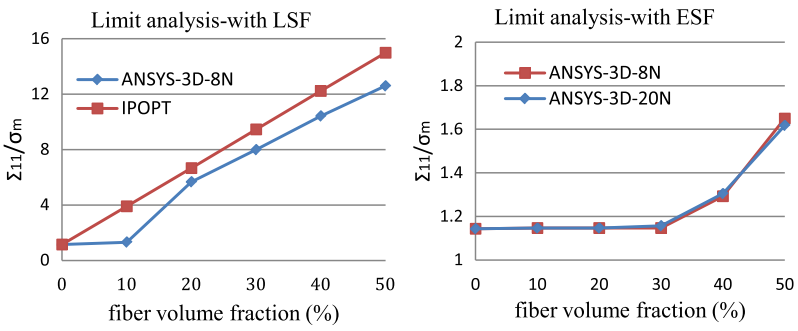

Fig. 6 Limit state of macroscopic stress with fiber volume fraction

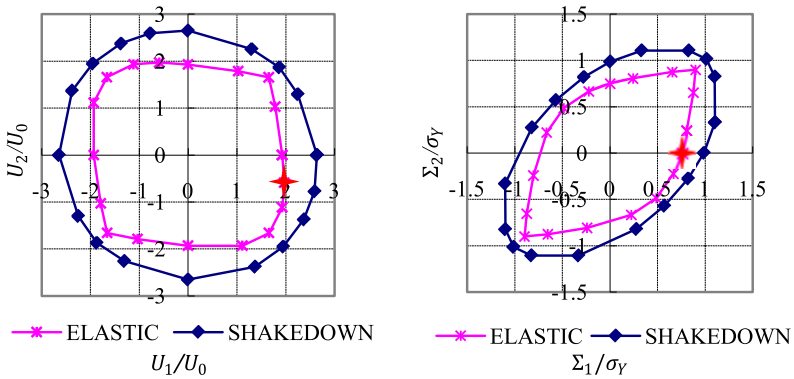

Fig. 7 Transformation between two scales

Table 3 Characteristic angle for uniaxial macroscopic stress under plane strain conditions

η %	φ^* [15]	φ (this work)	Σ_{11}	Σ_{22}	U_1^e/U_1^0	U_2^e/U_2^0
0	−23.20	−23.20	28.281	0	0.1838	−0.0788
10	−22.89	−22.88	31.918	0	0.1843	−0.0778
20	−22.34	−22.33	36.613	0	0.1850	−0.0760
30	−21.61	−21.58	42.642	0	0.1860	−0.0736
40	−20.80	−20.74	50.259	0	0.1870	−0.0708
50	−20.05	−19.99	59.718	0	0.1880	−0.0684

shakedown domains are normally scaled (Fig. 7). Benchmark U_0 is 0.02 mm and σ_Y is the yield stress of the matrix.

According to Eq. (16) in Sect. 2.3, the characteristic angle here is $\varphi = -16.65°$ and the elastic and shakedown safety factors are: $\alpha_{EL} = 2.06$ and $\alpha_{SD} = 2.71$.

For the same pattern and material properties, but under plane strain conditions, the change of characteristic angles φ in terms of the fiber volume fraction is shown in Table 3.

4.3 Fiber Distribution and Volume Fraction

The influence of fiber distribution and fiber volume fraction is investigated under plane strain condition (Fig. 8). The dimensions of RVEs are given in Table 4. They are subjected to two independent displacement loadings, $U_1^0 = U_2^0 = U_0 =$ 0.02 mm.

Figure 9 presents the admissible displacement domain (left side) and the corresponding transformed macroscopic stress domain (right side) for periodic composites under plane strain case. The fiber ratio is 40 %. From top to bottom are square,

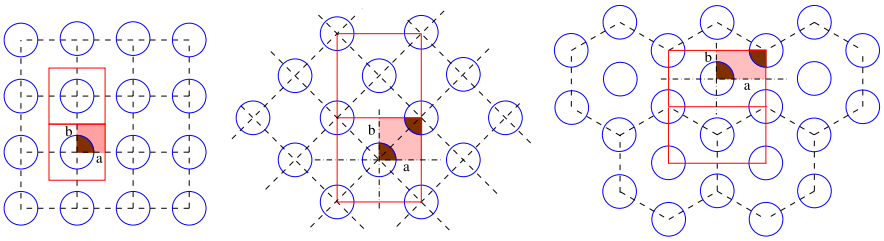

Fig. 8 Fiber distribution: (*Left*) Square pattern (SQ); (*Middle*) Rotated square pattern (TS); (*Right*) Hexagonal pattern (HEX)

Table 4 Dimensions of RVEs

Dimension of whole RVE	Square pattern	Rotated pattern	Hexagonal pattern
2a/mm	100	100	131.607
2b/mm	100	100	75.984

rotated square and hexagonal pattern, respectively. Note that, the quadratic and rotated composites are anisotropic. We use the transformation described in Sect. 2.3 to obtain stresses along the principal direction. After transformation, the macroscopic stress domain of hexagonal pattern also becomes symmetric in the principal directions. It satisfies the reality that the unidirectional continuous fiber with hexagonal periodicity is approximately isotropic in transverse direction.

Figure 10 shows the variation of the macroscopic limit stress in one axial direction with fiber volume fraction. For square pattern, the axial limit stress increases remarkably from around 35 %. For hexagonal pattern, the axial limit stress increases stably from 10 % to 50 %. While for the rotated pattern, the axial limit stress varies quite slightly, i.e. the fiber volume fraction has almost no influence on the macroscopic performance.

Figure 11 shows that the square pattern has the biggest macroscopic stress domain when the fiber volume fraction is 50 %. In macroscopic view, choose which kind of fiber pattern depends on the external loading.

In principle, the square pattern and rotated square pattern are the same. However, the loading domains, either in local level or global level, are different. It illustrates that periodic composites with square pattern is essentially not transversely isotropic, although in the traditional micromechanics of laminate they are treated as such [13].

4.4 Homogenized Elastic Material Properties

The homogenized elastic properties are determined for fiber reinforced composite given in Sect. 4.3. For square pattern and rotated square pattern, the characteristic angles φ_1 and φ_2 should equal to each other because of the geometric symmetry. It

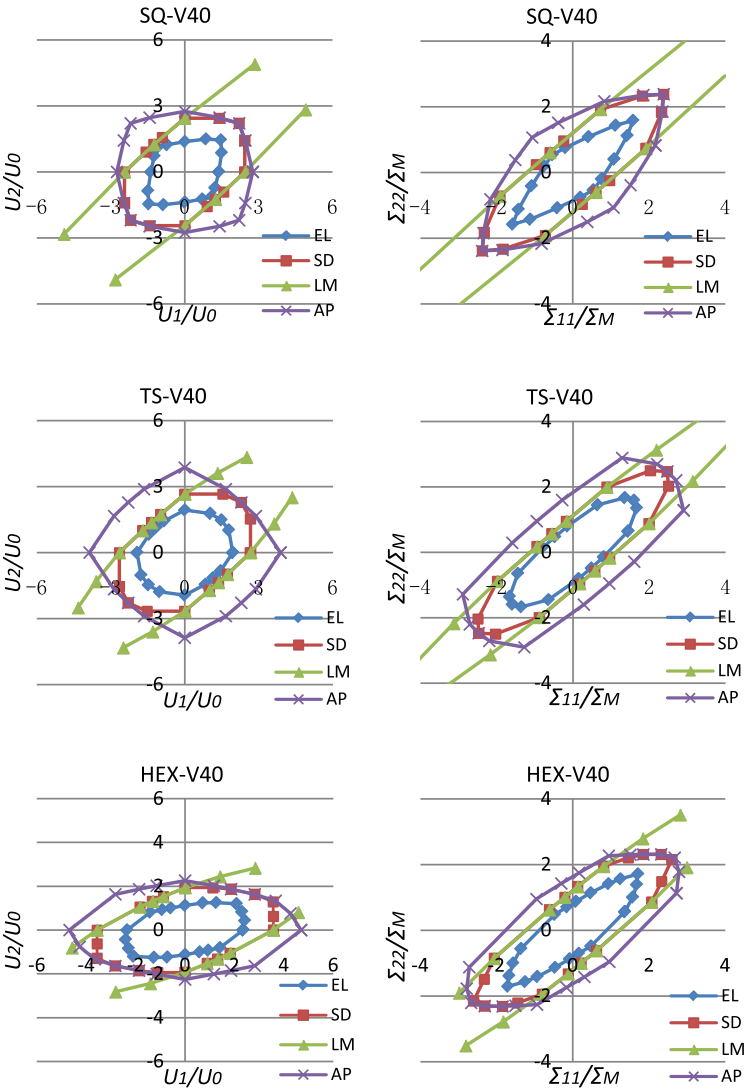

Fig. 9 Admissible displacement domain (*Left*) and related maximal macroscopic stress domain (*Right*) for periodic composites with different fiber pattern

is also verified in our numerical calculation. The unit cell of hexagonal distributed periodic composites is not symmetric. The characteristic angles at two directions are different. However, in macroscopic view, the homogenized material properties for all three patterns should be the same, in restrict words, that same in X and Y directions. According to the former methods, the homogenized transverse Young's modulus (Fig. 12) and Poisson ratios (Fig. 13) of different patterns with variation of fiber volume fraction can be obtained.

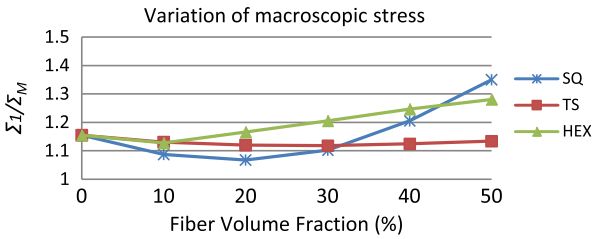

Fig. 10 Axial macroscopic limit stress

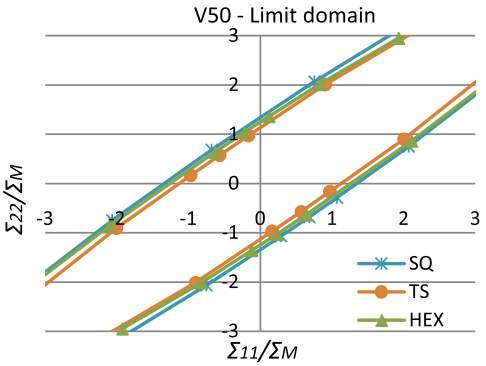

Fig. 11 Macroscopic limit stress domain for different patterns

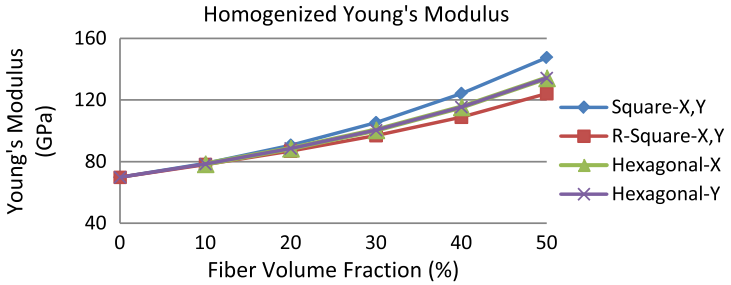

Fig. 12 Homogenized Young's modulus

Figure 12 presents the homogenized transverse Young's modulus for the three patterns. Generally, with the increment of fiber ratio, the transverse modulus increases, and among three patterns, the square one increased a little stronger than other two.

Their Poisson ratios are assumed the same value 0.3. Figure 13 presents the difference among three patterns. For the hexagonal pattern, with the variation of fiber volume fraction, Poisson's ratio is almost constant, while for the square pattern, it decreases, and for the rotated square pattern, it increases slightly.

From Fig. 12 and Fig. 13 we may conclude, that the fiber distributed pattern affects the transversely effective material properties. And after the transformation,

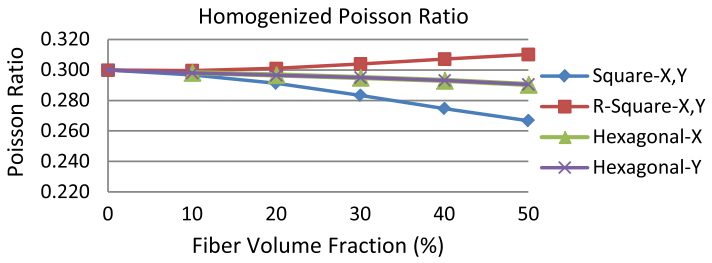

Fig. 13 Homogenized Poisson ratio

the hexagonal pattern shows the transversely isotropic characteristics on the macroscopic level.

4.5 Homogenized Plastic Material Properties

Based on the homogenization theory and mechanical constitute law, we may give a prediction of the effective elastic material properties of the composites. The biggest difficulty consists in how to define the plastic material properties, such as yield strength. During numerical simulation, we observed that the yielding process can be regarded as three states: firstly, it begins to yield, then the debonding of the interface, finally, the ductile phase exhibits overall plastic flow. By combination of lower bound direct methods and homogenization technique, the yield strength of periodic composites can be defined in three states [11, 18]:

1. Onset of plasticity: $\Sigma_{YEL} = \alpha_{EL}\Sigma_V$
2. Shakedown state: $\Sigma_{YSD} = \alpha_{SD}\Sigma_V$
3. Limit state: $\Sigma_{YLM} = \alpha_{LM}\Sigma_V$

Here, Σ_{YEL}, Σ_{YSD} and Σ_{YLM} are the yield strengths corresponding to purely elastic, shakedown and limit states, respectively; Σ_V is the macroscopic equivalent stress. Admissible macroscopic stress domains from beginning of plasticity to the limit state are obtained with the help of homogenization theory. Since three states are defined, for a uniaxial macroscopic stress Σ_1 ($\Sigma_2 = \Sigma_3 = 0$), we therefore get even for the elastic-perfectly matrix a "structural hardening" effect, due to the microscopic inhomogeneous stress distribution in the composite.

The stress components Σ_{ij} depend on the orientation of the coordinate system. Nevertheless, there are certain invariants associated with every tensor which are independent of the coordinate system. By solving the characteristic equation, we may obtain three principal stresses. For plane stress case, Σ_3 is zero. Therefore, yield curve fitting is carried out only in plane. This is one of the reasons, that why the yield criterion for sheets are developed a lot. For plane strain case, or general stress state, the principal stresses are distributed in the space.

Numerous anisotropic yield criteria have been developed and tested for anisotropic plastic deformation [3, 4, 30]. The simplest, however, is the quadratic Hill yield criterion [21], which is a straightforward extension of the von Mises yield criterion. It has the form:

$$F(\sigma_{22}-\sigma_{33})^2+G(\sigma_{33}-\sigma_{11})^2+H(\sigma_{11}-\sigma_{22})^2 +2\left(L\sigma_{23}^2+M\sigma_{31}^2+N\sigma_{12}^2\right)-1=0 \tag{40}$$

Here F, G, H, L, M, N are constants that have to be determined by experiments. The expressions of these parameters are defined as:

$$\begin{aligned} F&=\frac{1}{2}\left(\frac{1}{Y^2}+\frac{1}{Z^2}+\frac{1}{X^2}\right), \qquad G=\frac{1}{2}\left(\frac{1}{Z^2}+\frac{1}{X^2}+\frac{1}{Y^2}\right),\\ H&=\frac{1}{2}\left(\frac{1}{X^2}+\frac{1}{Y^2}+\frac{1}{Z^2}\right)\\ L&=\frac{1}{2P^2}, \qquad M=\frac{1}{2S^2}, \qquad N=\frac{1}{2T^2} \end{aligned} \tag{41}$$

Here X, Y, Z are the normal yield stress with respect to the axes of anisotropy in 1, 2 and 3 directions; P, S, T are the shear yield stresses in 23, 13 and 12 directions, respectively. By choosing the reference system in principle stress directions, we get:

$$F(\sigma_2-\sigma_3)^2+G(\sigma_3-\sigma_1)^2+H(\sigma_1-\sigma_2)^2-1=0 \tag{42}$$

Under the assumption, that the investigated material is isotropic in transverse direction, i.e. $F=G$. As defined above, X and Z are the tensile equivalent stress in and along the normal to the sheet plane, respectively. This implies:

$$X^2+\frac{H}{F}X^2=\frac{1}{F} \quad \Rightarrow \quad X=\frac{1}{\sqrt{F+H}} \tag{43}$$

$$2Z^2=\frac{1}{F} \quad \Rightarrow \quad Z=\frac{1}{\sqrt{2F}} \tag{44}$$

From (43) and (44):

$$\left(\frac{Z}{X}\right)^2=\frac{F+H}{2F} \quad \Rightarrow \quad \frac{H}{F}=2\left(\frac{Z}{X}\right)^2-1 \tag{45}$$

Substitute (44) and (45) into (42), we may obtain the criterion in terms of the equivalent stresses:

$$(\sigma_2-\sigma_3)^2+(\sigma_3-\sigma_1)^2+(\sigma_1-\sigma_2)^2\left[2\left(\frac{Z}{X}\right)^2-1\right]=2Z^2 \tag{46}$$

According to the associated flow rule, we have:

$$\varepsilon_i^p = \lambda \frac{\partial f}{\partial \sigma_i} \quad \Rightarrow \quad \frac{\mathrm{d}\varepsilon_i^p}{\mathrm{d}\lambda} = \frac{\partial f}{\partial \sigma_i} \tag{47}$$

For plane stress $\sigma_3 = 0$, which gives:

$$\begin{aligned} \frac{\mathrm{d}\varepsilon_1^p}{\mathrm{d}\lambda} &= \frac{\partial f}{\partial \sigma_1} = 2\sigma_1 + 2(\sigma_1 - \sigma_2)\left[2\left(\frac{Z}{X}\right)^2 - 1\right] \\ \frac{\mathrm{d}\varepsilon_2^p}{\mathrm{d}\lambda} &= \frac{\partial f}{\partial \sigma_2} = 2\sigma_2 - 2(\sigma_1 - \sigma_2)\left[2\left(\frac{Z}{X}^2\right) - 1\right] \\ \frac{\mathrm{d}\varepsilon_3^p}{\mathrm{d}\lambda} &= \frac{\partial f}{\partial \sigma_3} = -2(\sigma_1 + \sigma_2) \end{aligned} \tag{48}$$

Import the R-value [23] which is a measure of the plastic anisotropy of a rolled metal sheet. Let R_0 and R_{90} are the ratio of the in-plane and out-of plane plastic strains under uniaxial stress σ_1 and σ_2, respectively:

$$\begin{aligned} R_0 &= \frac{\mathrm{d}\varepsilon_2^p}{\mathrm{d}\varepsilon_3^p} = 2\left(\frac{Z}{X}\right)^2 - 1 \\ R_{90} &= \frac{\mathrm{d}\varepsilon_1^p}{\mathrm{d}\varepsilon_3^p} = 2\left(\frac{Z}{X}\right)^2 - 1 \end{aligned} \tag{49}$$

Thus,

$$R = R_0 = R_{90} = 2\left(\frac{Z}{X}\right)^2 - 1 \tag{50}$$

Substitute Eq. (50) into (46), we have:

$$\sigma_1^2 + \sigma_2^2 - \left(\frac{R+1}{2}\right)\sigma_1\sigma_2 = X^2 \tag{51}$$

From mathematical point of view, Eq. (51) represents an ellipse by a 45 degrees rotation of a canonical ellipse with the centre (0, 0). Assume that the semimajor and semiminor are a and b, respectively. Take composites with square pattern fiber volume fraction 7.07 % as an illustrative example, and with the dimension as reported in Sect. 4.1. Material parameters of two phases, as well as homogenized parameters are shown in Table 5. The macroscopic admissible domain of the composites, transformed in principal stress directions, is shown in Fig. 14, where the bounds of the elastic (EL), limit (LM) and shakedown (SD) domains are represented. Based on least-square method, Hill_1 and Hill_2 are fitted yield surface according to the limit and shakedown domain, respectively.

Hill_1: with R-value 1.0194, which means, it can be treated as von Mises yield criterion approximately. Hill_2: with R-value 1.3204. The other related parameters are shown in Table 5.

Table 5 Parameters by yield surface fitting

	R	*a*	*b*	*X*	*Z*	*F*	*H*
Hill_1	1.0194	381.13	218.64	268.20	269.50	6.8842e-6	7.0177e-6
Hill_2	1.3204	328.65	172.24	215.75	232.39	9.2583e-6	1.2225e-5

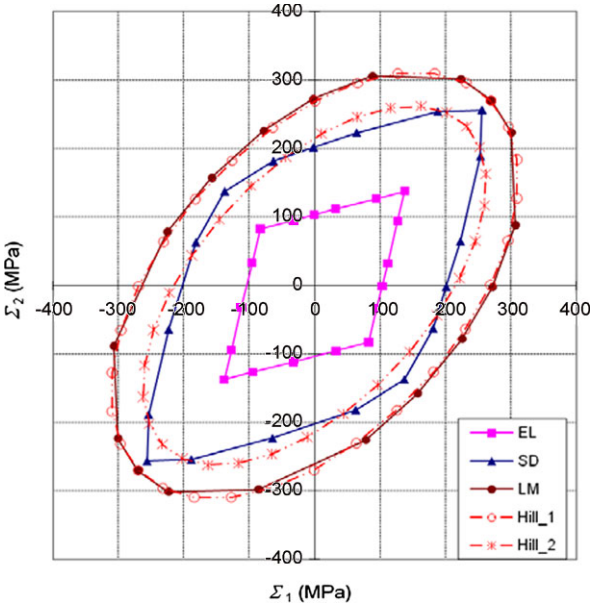

Fig. 14 Admissible macroscopic stress domain and yield surface fitting

Table 6 Homogenized material parameters

Material property	Matrix	Fiber	Homogenized
Young's modulus (GPa)	2.1	210	174.52
Poisson ratio	0.3	0.2	0.2966
Yield strength (MPa)	280	140	269.50

If we fit the yield surface with von Mises yield criterion ($R = 1$) according to macroscopic stress under limit state, the homogenized elastic and plastic properties of periodic composite material are shown in Table 6.

We note that the yield surface fitting according to shakedown domain is only suitable for a specific loading domain.

5 Conclusion

This paper shows how the lower bound shakedown analysis combined with homogenization theory can be used to determine safe loading domains for composites and how to calculate global homogenized material parameters. We conclude that a three-dimensional non-conforming element will fit for the direct methods with the same accuracy as second order element but with much less computational cost. The yield surface fitting according to shakedown domain is only suitable for arbitrarily chosen but specific loading domains.

References

1. Akoa, F., Hachemi, A., Le Thi Hai An, Mouhtamid, S., Tao, P.D.: Application of lower bound direct method to engineering structures. Special Issue of J. Global Optim. **37**(4), 609–630 (2007)
2. Andrianov, I., Awrejcewicz, J., Manevitch, L.I.: Asymptotical Mechanics of Thin-Walled Structures. Springer, Berlin (2004)
3. Banabic, D., Bunge, H.-J., Pöhlandt, K., Tekkaya, A.E.: Formability of Metallic Materials. Springer, New York (2000)
4. Banabic, D., Kuwabara, T., Balan, T., Comsa, D.S.: An anisotropic yield criterion for sheet metals. J. Mater. Process. Technol. **157–158**, 462–465 (2004)
5. Belytschko, T.: Plane stress shakedown analysis by finite elements. Int. J. Mech. Sci. **14**, 619–625 (1972)
6. Bourgeois, S., Magoariec, H., Débordes, O.: A direct method for determination of effective strength domains for periodic elastic-plastic media. In: Weichert, D., Ponter, A. (eds.) Limit States of Materials and Structures, pp. 179–190 (2009)
7. Byrd, R.H., Lu, P.H., Nocedal, J., Zhu, C.Y.: A limited memory algorithm for bound constrained optimization. SIAM J. Sci. Stat. Comput. **16**(5), 1190–1208 (1995)
8. Carvelli, V.: Shakedown analysis of unidirectional fiber reinforced metal matrix composites. Comput. Mater. Sci. **31**, 24–32 (2004)
9. Carvelli, V., Maier, G., Taliercio, A.: Shakedown analysis of periodic heterogeneous materials by a kinematic approach. J. Mech. Eng. **50**(4), 229–240 (1999)
10. Carvelli, V., Taliercio, A.: A micromechanical model for the analysis of unidirectional elastoplastic composites subjected to 3d stresses. Mech. Res. Commun. **26**(5), 547–553 (1999)
11. Chen, M., Zhang, L.L., Weichert, D., Tang, W.C.: Shakedown and limit analysis of periodic composites. Proc. Appl. Math. Mech. **9**(1), 415–416 (2009)
12. Débordes, O.: Homogenization computations in the elastic or plastic collapse range applications to unidirectional composites and perforated sheets. In: Proceedings of the 4th International Symposium Innovative Numerical Methods in Engineering, Computational Mechanics Publications, pp. 453–458 (1986)
13. Daniel, I.M., Ishai, O.: Engineering Mechanics of Composite Materials, 2nd edn. Oxford University Press, London (2006)
14. Döbert, C., Mahnken, R., Stein, E.: Numerical simulations of interface debonding with a combined damage/friction constitutive model. Comput. Mech. **25**, 456–467 (2000)
15. Du, Z.-Z., McMeeking, R.M., Schmauder, S.: Transverse yielding and matrix flow past the fibers in metal matrix composites. Mech. Mater. **21**, 159–167 (1995)
16. Forsgren, A., Gill, P.E., Wright, M.H.: Interior methods for nonlinear optimization. SIAM Rev. **44**(4), 525–597 (2002)
17. Gould, N.I.M., Orban, D., Toint, P.L.: Numerical methods for large-scale nonlinear optimization. Technical report, Library and Information Services, CCLRC Rutherford Appleton Laboratory (2004)

18. Hachemi, A., Chen, M., Weichert, D.: Plastic design of composites by direct methods. In: Simos, T.E., Psihoyios, G., Tsitouras, Ch. (eds.) Numerical Analysis and Applied Mathematics, International Conference, pp. 319–323 (2009)
19. Hachemi, A., Mouthamid, S., Weichert, D.: Progress in shakedown analysis with applications to composites. Arch. Appl. Mech. **74**, 762–772 (2005)
20. Hachemi, A., Weichert, D.: On the problem of interfacial damage in fibre-reinforced composites under variable loads. Mech. Res. Commun. **32**, 15–23 (2005)
21. Hill, R.: A theory of yielding and plastic flow of anisotropic solids. Proc. R. Soc. A **193**, 281–297 (1948)
22. Krishnamoorthy, C.S.: Finite Element Analysis: Theory and Programming, 2nd edn. Tata McGraw-Hill, Naveen Shahdara (2007)
23. Lankford, W.T., Snyder, S.C., Bausher, J.A.: New criteria for predicting the press performance of deep drawing sheets. Trans. Am. Soc. Mech. Eng. **42**, 1197–1205 (1950)
24. Magoariec, H.: Adaptation élastoplastique et homogénéisation périodique. PhD thesis, France: Mecanique Solides, Université de la Méditerranée—Aix Marseille II (2003)
25. Magoariec, H., Bourgeois, S., Débordes, O.: Elastic plastic shakedown of 3d periodic heterogenous media: a direct numerical approach. Int. J. Plast. **20**, 1655–1675 (2004)
26. Michael, J.C., Moulinec, H., Suquet, P.: Effective properties of composite materials with periodic microstructure: a computational approach. Comput. Methods Appl. Math. **172**, 109–143 (1999)
27. Mouhtamid, S.: Anwendung direkter Methoden zur industriellen Berechnung von Grenzlasten mechanischer Komponeten. PhD thesis, Germany: Institut für Allgemeine Mechanik, RWTH-Aachen (2008)
28. Nguyen, A.D.:: Lower-bound shakedown analysis of pavements by using the interior point method. PhD thesis, Germany: Institut für Allgemeine Mechanik, RWTH-Aachen (2007)
29. Pelissou, C., Baccou, J., Monerie, Y., Perales, F.: Determination of the size of the representative volume element for random quasi-brittle composites. Int. J. Solids Struct. **46**, 2842–2855 (2009)
30. Plunkett, B., Cazacu, O., Barlat, F.: Orthotropic yield criteria for description of the anisotropy in tension and compression of sheet metals. Int. J. Plast. **24**, 847–866 (2008)
31. Ponter, A.R.S., Leckie, F.A.: Bounding properties of metal-matrix composites subjected to cyclic thermal loading. J. Mech. Phys. Solids **46**, 697–717 (1998)
32. Ponter, A.R.S., Leckie, F.A.: On the behaviour of metal matrix composites subjected to cyclic thermal loading. J. Mech. Phys. Solids **46**, 2183–2199 (1998)
33. Schwabe, F.: Einspieluntersuchungen von Verbundwerkstoffen mit periodischer Mikrostruktur. PhD thesis, Institut für Allgemeine Mechanik, RWTH-Aachen (2000)
34. Shan, Z.H., Gokhale, A.M.: Representative volume element for non-uniform micro-structure. Comput. Mater. Sci. **24**, 361–379 (2002)
35. Sun, C.T., Vaidya, R.S.: Prediction of composite properties from a representative volume element. Compos. Sci. Technol. **56**, 171–179 (1996)
36. Sun, E.Q.: Shear locking and hourglassing in Msc Nastran, Abaqus and Ansys.in Msc software users meeting (2006)
37. Suquet, P.: Plasticité et homogénéisation. PhD thesis, France: Université Pierre et Marie Curie (1982)
38. Taiebat, H.H., Carter, J.P.: Three-dimensional non-conforming elements. Technical report, The University of Sydney, Department of Civil Engineering (2001)
39. Taliercio, A.: Lower and upper bounds to the macroscopic strength domain of a fiber-reinforced composite material. Int. J. Plast. **8**(6), 741–762 (1992)
40. Taliercio, A.: Generalized plane strain finite element model for the analysis of elastoplastic composites. Int. J. Solids Struct. **42**, 2842–2855 (2005)
41. Taliercio, A.: Macroscopic strength estimates for metal matrix composites embedding a ductile interphase. Int. J. Solids Struct. **44**, 7213–7238 (2007)
42. Wächter, A.: An interior point algorithm for large-scale nonlinear optimization with applications in process engineering. PhD thesis, Pennsylvania: Chemical Engineering, Carnegie

Mellon University (2002)
43. Wächter, A.: Short tutorial: getting started with ipopt in 90 minutes. Technical report, IBM Research Report (2009)
44. Wächter, A., Biegler, L.T.: On the implementation of a primal-dual interior-point filter line-search algorithm for large-scale nonlinear programming. Math. Program. **106**(1), 25–57 (2006)
45. Weichert, D., Hachemi, A.: Influence of geometrical nonlinearities on the shakedown of damaged structures. Int. J. Plast. **14**(9), 891–907 (1999)
46. Weichert, D., Hachemi, A., Schwabe, F.: Shakedown analysis of composites. Mech. Res. Commun. **26**(3), 309–318 (1999)
47. Weichert, D., Hachemi, A., Schwabe, F.: Application of shakedown analysis to the plastic design of composites. Arch. Appl. Mech. **69**, 623–633 (1999)
48. Wilson, E.L., Taylor, R.L., Doherty, W.P., Ghaboussi, J.: Incompatible displacement models. In: Fenves, S.J. (ed.) Numerical and Computer Methods in Structural Mechanics, pp. 43–57 (1973)
49. You, J.-H., Kim, B.Y., Miskiewicz, M.: Shakedown analysis of fiber-reinforced copper matrix composites by direct and incremental approaches. Mech. Mater. **41**(7), 857–867 (2009)
50. Zahl, D.B., Schmauder, S.: Transverse strength of continuous fiber metal matrix composites. Comput. Mater. Sci. **3**, 293–299 (1994)

An Upper Bound Algorithm for Limit and Shakedown Analysis of Bounded Linearly Kinematic Hardening Structures

Phu Tinh Phạm and Manfred Staat

Abstract The paper develops a new FEM based algorithm for shakedown analysis of structures made of elastic plastic bounded linearly kinematic hardening material. The hardening effect is simulated by using a two-surface plastic model to bound the Melan-Prager model. The initial yield surface can translate inside the bounding surface, without changing its shape and size. The translated yield surface may touch the bounding surface and ratcheting may occur with clear benefit of hardening. Or it may not touch the bounding surface, alternating plasticity may occur and there is no effect of hardening. The direct calculation of plastic limit and shakedown bounds is considered as a nonlinear programming problem. The upper bound of the shakedown load is obtained as the minimum of the plastic dissipation function, which is based on the von Mises yield criterion.

1 Introduction

The main business of structural engineers is to design structures safely, economically and efficiently. Elastic analysis does not fully exploit the capacity of structures made of ductile materials. Direct plastic analysis, also called limit analysis, finds the ultimate strength capacity (static collapse) with the assumption that the applied loads on the structure are time-independent and proportional. Actually, applied loads are often neither monotonic nor proportional, such as wind loads on buildings, traffic loads on bridges, waves on offshore oil-rigs, cyclic loads on machine parts, internal pressure in pipes, varying thermal loads, etc. Then the structure may fail by fatigue or unserviceability before reaching its ultimate strength capacity. Shakedown analysis is used to define the load bounds for design checks against low cycle fatigue and incremental plastic collapse. From the engineering point of view, a structure

P.T. Phạm · M. Staat (✉)
Campus Jülich, Institute of Bioengineering, Aachen University of Applied Sciences
Heinrich-Mußmann-Str. 1, 52428 Jülich, Germany
e-mail: m.staat@fh-aachen.de
url: http://www.biomechanik.fh-aachen.de/

P.T. Phạm
e-mail: phamphutinh@yahoo.com

G. Saxcé et al. (eds.), *Limit State of Materials and Structures*,
DOI 10.1007/978-94-007-5425-6_4,

which is designed based on the shakedown limit is safer than if based on the plastic collapse limit.

For a perfectly plastic material the first shakedown theorem was formulated by Bleich [1], the static theorem was extended by Melan [9], and the kinematic shakedown theorem was stated by Koiter [5]. There have been many studies on shakedown for elastic perfectly plastic material so far.

For more realistic materials, resulting in more economic and efficient structures, the hardening effect should be taken into account. Among hardening models, the isotropic hardening law is generally not reasonable in situations where structures are subjected to cyclic loading, it does not account for the Bauschinger effect, and rejects the possibility of incremental plasticity. The unbounded kinematic hardening model has already been used by Melan [10] and later by Prager [14]. It cannot define the plastic collapse and also incremental plasticity, but only low cycle fatigue. Introducing a bounding surface in Melan-Prager's model a two-surface model of plasticity is achieved which appears to be most basic, suitable and simple for shakedown analysis. Many researchers have investigated the benefit of hardening, using either analytical methods, such as Bodoville and de Saxcé [2, 3], or numerical methods based on the lower bound theorem, such as Weichert and Groß-Weege [22], Staat and Heitzer [6, 7, 16], Stein and Zhang [18–20, 23], Makrodimopoulos and Bisbos [8], etc.

Nguyễn Q.S. [11], Phạm Đ.C. [12, 13] have presented upper bound shakedown theorems in hardening plasticity for both static and kinematic approaches. This paper develops a FEM based upper bound algorithm to investigate the influence of hardening on ratcheting by a direct plastic method, using a simple two-surface model of plasticity with a fixed bounding surface. The initial yield surface can translate inside the bounding surface, so that: (1) it always stays inside the bounding surface, or (2) its centre cannot move outside the back stress surface. As the two-surface model is only based on yield stress σ_y and ultimate strength σ_u, so it does not depend on the hardening curve, consequently it is a model of linearly kinematic hardening.

2 Bounded Kinematic Hardening Model

2.1 Unbounded Kinematic Hardening Model

The original Melan-Prager model is characterized by an unbounded translation of the loading surface in the multi-axial stress space, see Fig. 1.

According to the von Mises yield condition, the initial yield surface is defined as

$$f(\boldsymbol{\sigma}) = F[\boldsymbol{\sigma}] - \sigma_y^2 = 0 \tag{1}$$

and the subsequent or translated surface is defined as

$$f(\boldsymbol{\sigma}, \boldsymbol{\pi}) = F[\boldsymbol{\sigma} - \boldsymbol{\pi}] - \sigma_y^2 = 0, \tag{2}$$

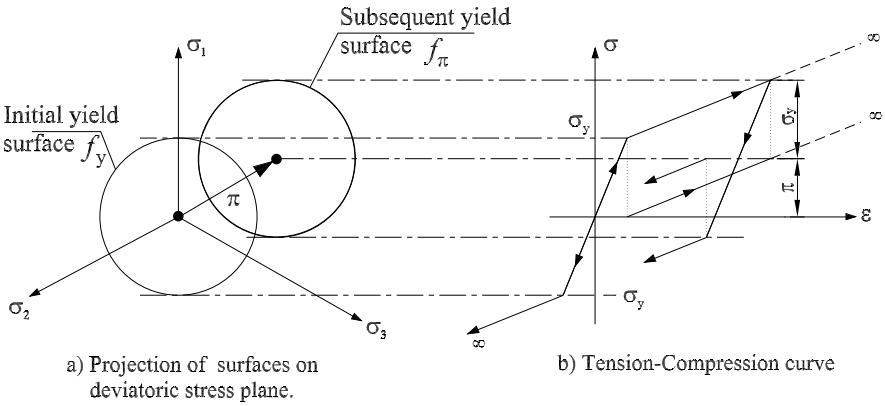

Fig. 1 A model for unbounded kinematic hardening

where $\boldsymbol{\pi}$ is called *back stress*, $\pi = (\sigma_u - \sigma_y)$, and

$$\dot{\boldsymbol{\pi}} = \frac{2}{3} C \dot{\varepsilon}^p, \tag{3}$$

where C is a material constant, and with the associated plastic flow

$$\dot{\varepsilon}^p = \dot{\lambda} \frac{\partial f}{\partial \boldsymbol{\sigma}}. \tag{4}$$

For the unbounded kinematic hardening model, the initial yield surface translates without constraint, in other words, the ultimate strength σ_u is infinite and so this model is not realistic and not suitable for limit analysis. In addition, the structure made of unbounded kinematic materials can fail only by alternating plasticity (LCF), i.e. it is impossible for such a structure to be involved in incremental plastic collapse, while the alternating limit with the kinematical hardening model seems not to be essentially different from the perfectly plastic model, cf. Gokhfeld and Cherniavsky [4], Stein and Huang [17].

2.2 Bounded Kinematic Hardening Model

In the so-called bounded kinematic hardening model of two-surface plasticity the initial yield surface translates with a constraint, so that it cannot move outside the bounding surface f_u (see Fig. 2).

The initial surface is defined in Eq. (1), and the subsequent surface is defined in Eq. (2). The subsequent surface may or may not touch the bounding surface. It is bounded in one of two following ways.

– It always stays inside a bounding surface, expressed by the following condition

$$F[\boldsymbol{\sigma}] \le \sigma_u^2. \tag{5a}$$

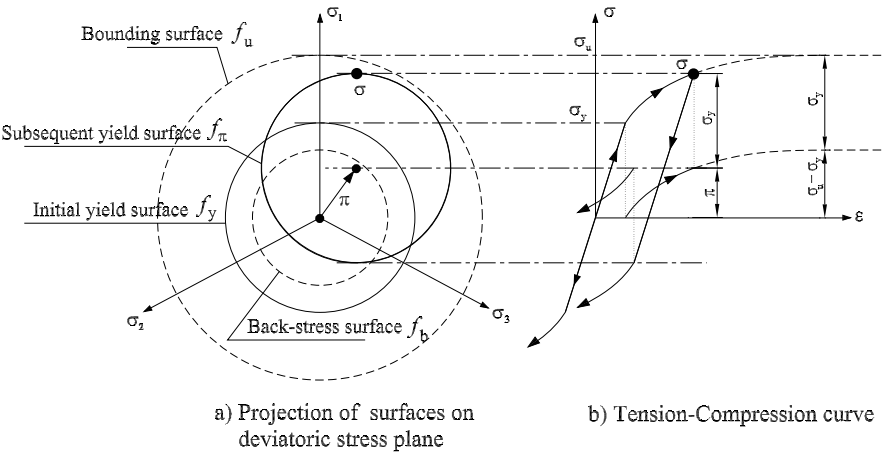

Fig. 2 A two-surface model for bounded kinematic hardening

– Its centre cannot move outside the back stress surface f_b, expressed by the following condition

$$F[\boldsymbol{\pi}] \le (\sigma_u - \sigma_y)^2. \tag{5b}$$

Intuitively, from Fig. 2, we can see that conditions (5a) and (5b) are exactly the same, which is easily proven.

Firstly, we show that (5a) leads to (5b). From triangle inequality:

$$\sqrt{F[\boldsymbol{\sigma}]} = \sqrt{F\big[(\boldsymbol{\sigma}-\boldsymbol{\pi})+\boldsymbol{\pi}\big]} \le \sqrt{F[\boldsymbol{\sigma}-\boldsymbol{\pi}]} + \sqrt{F[\boldsymbol{\pi}]} \le \sigma_y + (\sigma_u - \sigma_y) = \sigma_u \tag{6}$$

then

$$\begin{cases} \sqrt{F[\boldsymbol{\sigma}-\boldsymbol{\pi}]} = \sigma_y, & \text{(for the appearance of plastic deformation), and} \\ \sqrt{F[\boldsymbol{\pi}]} \le (\sigma_u - \sigma_y) \quad \Rightarrow \quad F[\boldsymbol{\pi}] \le (\sigma_u - \sigma_y)^2. & \text{(Q.E.D.)} \end{cases} \tag{7}$$

Secondly, we show that (5b) leads to (5a).

We choose $\boldsymbol{\pi} = (\frac{\sigma_u - \sigma_y}{\sigma_u})\boldsymbol{\sigma}$ so that $\boldsymbol{\sigma} - \boldsymbol{\pi} = \frac{\sigma_y}{\sigma_u}\boldsymbol{\sigma}$. Then for any $\boldsymbol{\sigma}$ satisfying $F[\boldsymbol{\sigma}] \le \sigma_u^2$ we find:

$$F[\boldsymbol{\pi}] = F\left[\frac{\sigma_u - \sigma_y}{\sigma_u}\boldsymbol{\sigma}\right] = \left(\frac{\sigma_u - \sigma_y}{\sigma_u}\right)^2 F[\boldsymbol{\sigma}] \le (\sigma_u - \sigma_y)^2 \tag{8}$$

and

$$F[\boldsymbol{\sigma}-\boldsymbol{\pi}] = F\left[\frac{\sigma_y}{\sigma_u}\boldsymbol{\sigma}\right] = \left(\frac{\sigma_y}{\sigma_u}\right)^2 F[\boldsymbol{\sigma}] \le \sigma_y^2 \quad \Rightarrow \quad F[\boldsymbol{\sigma}] \le \sigma_u^2. \quad \text{(Q.E.D.)} \tag{9}$$

Heitzer, Staat [6] have proven that if $\sigma_u \ge 2\sigma_y$ then shakedown limit of bounded kinematic hardening structures is equal to that of an unbounded kinematic harden-

ing structure. Gokhfeld and Cherniavsky [4] also stated that the problem of alternating plasticity can be solved directly by using a fictitious elastic field $\boldsymbol{\sigma}^E$. It is due to the fact that the plastic fatigue limit is determined by the condition that anywhere in the structure, the maximum magnitude of fictitious equivalent (von Mises) elastic stress cannot exceed two times the yield limit of the material. Moreover, the Bauschinger effect in metals leads to an evolution of initial yield surface within the range of $2\sigma_y$.

3 Upper Bound Algorithm for Limit and Shakedown Analysis

3.1 Statement of the Problem

Based on Koiter's kinematic theorem, the upper bound of shakedown load multiplier in normalized form is the solution of following nonlinear programming problem

$$\alpha_{sd} = \min_{\dot{\boldsymbol{\varepsilon}}^p} \int_0^T \int_V D^p\left(\dot{\boldsymbol{\varepsilon}}^p\right) dV\, dt \qquad \text{(a)}$$

$$\text{s.t.:} \quad \begin{cases} \Delta\boldsymbol{\varepsilon}^p = \displaystyle\int_0^T \dot{\boldsymbol{\varepsilon}}^p dt & \text{(b)} \\ \operatorname{tr}(\dot{\boldsymbol{\varepsilon}}^p) = 0 & \text{(c)} \\ \Delta\boldsymbol{\varepsilon}^p = \dfrac{1}{2}(\nabla\mathbf{u} + (\nabla\mathbf{u})^T) \quad \text{in } V & \text{(d)} \\ \mathbf{u} = \mathbf{0} \quad \text{on } \partial V_u & \text{(e)} \\ \displaystyle\int_0^T \int_V \boldsymbol{\sigma}^E(\mathbf{x}, t) : \dot{\boldsymbol{\varepsilon}}^p dV dt = 1 & \text{(g)} \end{cases} \qquad (10)$$

where (10b) is the definition of plastic strain accumulation over a cycle. $\Delta\boldsymbol{\varepsilon}^p$ must satisfy the kinematic compatibility conditions (10d) and (10e). Constraint (10c) is the incompressibility condition and (10g) is the normalized constraint of external energy.

For perfect plasticity, the plastic dissipation function according to the von Mises yield criterion in the form of strain rate is

$$D^p\left(\dot{\boldsymbol{\varepsilon}}^p\right) = \sqrt{2}k_v\sqrt{J_2(\dot{\boldsymbol{\varepsilon}}^p)} = \sqrt{\frac{2}{3}}\sigma_y \left\|\dot{\boldsymbol{\varepsilon}}^p\right\|, \qquad (11)$$

where the constant $k_v = \sigma_y/\sqrt{3}$ is the yield stress in pure shear and $J_2(\dot{\boldsymbol{\varepsilon}}^p)$ is the second invariant of the strain rate tensor.

For bounded kinematic hardening the plastic dissipation function is [8]

$$\int_0^T \int_V D^p\left(\dot{\boldsymbol{\varepsilon}}^p\right) dV\, dt = \int_0^T \int_V \sqrt{\frac{2}{3}}\sigma_y \left\| \dot{\boldsymbol{\varepsilon}}^p \right\| dV\, dt + \int_V \sqrt{\frac{2}{3}}(\sigma_u - \sigma_y) \left\| \Delta \boldsymbol{\varepsilon}^p \right\| dV. \tag{12}$$

The second term on the right hand side of Eq. (12) is the effect of hardening, represented by the translation of yield surface. If structures fail in alternating plasticity mode, closed cycles of plastic rates must be considered, $\Delta \boldsymbol{\varepsilon}^p = 0$, then Eq. (12) becomes Eq. (11), so there is no difference between perfectly plastic and kinematic hardening if LCF occurs.

3.2 Numerical Formulation

To solve Eq. (10), we will transform the integration into a summation, by discretization of time and space. By load domain discretization the integration over a certain time interval $t[0, T]$ is transformed into summation over $k = \overline{1, m}$, where k is a load vertex, $m = 2^n$, n is number of variable loads. By finite element discretization, the integration over entire structure V is transformed into the numerical integration for $i = \overline{1, NG}$, where i is a Gaussian point with weight residual w_i, and NG is total Gaussian points in the structure. With these discretizations, the limit and shakedown analysis is reduced to checking the restrictions only at all load vertices m and all Gaussian points NG instead of checking for entire load domain $\mathscr{L}$ and whole structure V. The numerical form of Eq. (10) can be written as

$$\alpha_{sd}^{blkh} = \min_{\dot{\boldsymbol{\varepsilon}}^p} \left\{ \sqrt{\frac{2}{3}}\sigma_y \sum_{k=1}^{m} \sum_{i=1}^{NG} \sqrt{w_i^2 \boldsymbol{\varepsilon}_{ik}^T \mathbf{D} \boldsymbol{\varepsilon}_{ik} + w_i^2 \varepsilon_0^2} + \sqrt{\frac{2}{3}}(\sigma_u - \sigma_y) \sum_{i=1}^{NG} \sqrt{w_i^2 \sum_{k=1}^{m} \boldsymbol{\varepsilon}_{ik}^T \mathbf{D} \sum_{k=1}^{m} \boldsymbol{\varepsilon}_{ik} + w_i^2 \varepsilon_0^2} \right\} \quad \text{(a)}$$

$$\text{s.t.:} \begin{cases} \sum_{k=1}^{m} \boldsymbol{\varepsilon}_{ik} = \mathbf{B}_i \mathbf{u}, \quad \forall i = \overline{1, NG} & \text{(b)} \\ \mathbf{D}_M \boldsymbol{\varepsilon}_{ik} = \mathbf{0}, \quad \forall i = \overline{1, NG}, \quad \forall k = \overline{1, m} & \text{(c)} \\ \sum_{k=1}^{m} \sum_{i=1}^{NG} w_i \boldsymbol{\varepsilon}_{ik}^T \boldsymbol{\sigma}_{ik}^E = 1 & \text{(d)} \end{cases} \tag{13}$$

where α_{sd}^{blkh} denotes the shakedown multiplier in bounded linearly kinematic hardening. If the second term in the objective function (13a) is omitted, consequently

α_{sd}^{blkh} becomes α_{sd}^{pp}, which denotes the shakedown multiplier in perfect plasticity. $\boldsymbol{\varepsilon}_{ik}$ is strain vector, corresponding to load vertex k, at Gaussian point i

$$\begin{aligned}\boldsymbol{\varepsilon}_{ik} &= \left[\varepsilon_{11}^{ik} \quad \varepsilon_{22}^{ik} \quad \varepsilon_{33}^{ik} \quad 2\varepsilon_{12}^{ik} \quad 2\varepsilon_{23}^{ik} \quad 2\varepsilon_{13}^{ik}\right]^T \\ &= \left[\varepsilon_{11}^{ik} \quad \varepsilon_{22}^{ik} \quad \varepsilon_{33}^{ik} \quad \gamma_{12}^{ik} \quad \gamma_{23}^{ik} \quad \gamma_{13}^{ik}\right].^T \end{aligned} \tag{14}$$

$\boldsymbol{\sigma}_{ik}^{E}$ is fictitious elastic stress vector corresponding to load vertex k, at Gaussian point i, $\mathbf{u}$ is the nodal displacement vector, $\mathbf{B}_i$ is deformation matrix, ε_0 is small number to avoid singularity. $\mathbf{D}$ and $\mathbf{D}_M$ are square matrices of the form

$$\mathbf{D} = Diag\left[1 \quad 1 \quad 1 \quad \tfrac{1}{2} \quad \tfrac{1}{2} \quad \tfrac{1}{2}\right], \qquad \mathbf{D}_M = \begin{bmatrix} 1 & 1 & 1 & 0 & 0 & 0 \\ 1 & 1 & 1 & 0 & 0 & 0 \\ 1 & 1 & 1 & 0 & 0 & 0 \\ 0 & 0 & 0 & 0 & 0 & 0 \\ 0 & 0 & 0 & 0 & 0 & 0 \\ 0 & 0 & 0 & 0 & 0 & 0 \end{bmatrix}. \tag{15}$$

For the sake of simplicity, we define some new quantities as

$$\mathbf{e}_{ik} = w_i \mathbf{D}^{1/2} \boldsymbol{\varepsilon}_{ik}, \quad \mathbf{t}_{ik} = \mathbf{D}^{-1/2} \boldsymbol{\sigma}_{ik}^{E}, \quad \hat{\mathbf{B}}_i = w_i \mathbf{D}^{1/2} \mathbf{B}_i. \tag{16}$$

Then (13) becomes

$$\alpha_{sd}^{blkh} = \sqrt{\frac{2}{3}}\sigma_y \min_{\dot{\mathbf{e}}_{ik}} \left\{ \sum_{k=1}^{m} \sum_{i=1}^{NG} \sqrt{\mathbf{e}_{ik}^T \mathbf{e}_{ik} + \varepsilon^2} + a \sum_{i=1}^{NG} \sqrt{\sum_{k=1}^{m} \mathbf{e}_{ik}^T \sum_{k=1}^{m} \mathbf{e}_{ik} + \varepsilon^2} \right\} \quad \text{(a)}$$

$$\text{s.t.:} \quad \begin{cases} \sum_{k=1}^{m} \mathbf{e}_{ik} = \hat{\mathbf{B}}_i \mathbf{u}, \quad \forall i = \overline{1, NG} & \text{(b)} \\ \frac{1}{3}\mathbf{D}_M \mathbf{e}_{ik} = \mathbf{0}, \quad \forall i = \overline{1, NG}, \quad \forall k = \overline{1, m} & \text{(c)} \\ \sum_{k=1}^{m} \sum_{i=1}^{NG} \mathbf{e}_{ik}^T \mathbf{t}_{ik} = 1 & \text{(d)} \end{cases} \tag{17}$$

where

$$a = (\sigma_u - \sigma_y)/\sigma_y. \tag{18}$$

Using penalty function method to eliminate the compatibility constraint (17b) and incompressibility constraint (17c) the penalty function $\tilde{F}_P$ is written as

$$\begin{aligned}\tilde{F}_P = \sum_{i=1}^{NG}\Bigg\{ &\sum_{k=1}^{m}\sqrt{\mathbf{e}_{ik}^T\mathbf{e}_{ik}+\varepsilon^2} + a\sqrt{\sum_{k=1}^{m}\mathbf{e}_{ik}^T\sum_{k=1}^{m}\mathbf{e}_{ik}+\varepsilon^2} \\ &+ \frac{c}{2}\sum_{k=1}^{m}\mathbf{e}_{ik}^T\mathbf{D}_M\mathbf{e}_{ik} + \frac{c}{2}\left(\sum_{k=1}^{m}\mathbf{e}_{ik}-\hat{\mathbf{B}}_i\mathbf{u}\right)^T\left(\sum_{k=1}^{m}\mathbf{e}_{ik}-\hat{\mathbf{B}}_i\mathbf{u}\right)\Bigg\} \qquad (19)\\ \text{s.t.:}\quad &\sum_{k=1}^{m}\sum_{i=1}^{NG}\mathbf{e}_{ik}^T\mathbf{t}_{ik}=1,\end{aligned}$$

where c is a penalty parameter such that $c \gg 1$. For the sake of simplicity c is chosen to be constant at every Gaussian point.

Using Lagrange multiplier method to eliminate the normalized constraint (17d) the Lagrange function F_{PL} is written as

$$F_{PL} = \tilde{F}_P + \alpha\left(\sum_{i=1}^{NG}\sum_{k=1}^{m}\mathbf{e}_{ik}^T\mathbf{t}_{ik} - 1\right), \qquad (20)$$

where α is the Lagrange multiplier.

To find the minimum of F_{PL} we write the Karush-Kuhn-Tucker condition for Eq. (20). Then using Newton-Raphson method to solve the KKT condition, we obtain the Newton directions $d\mathbf{u}$ and $d\mathbf{e}_{ik}$.

Algorithm

- Step 1: Initialize displacement and strain vectors $\mathbf{u}^0$ and $\mathbf{e}^0$ such that the normalized condition (17d) is satisfied:

$$\sum_{i=1}^{NG}\sum_{k=1}^{m}\mathbf{t}_{ik}^T\mathbf{e}_{ik}^0 = 1.$$

- Step 2: Calculate $d\mathbf{u}, d\mathbf{e}_{ik}, (\alpha + d\alpha)$ from current values of $\mathbf{u}, \mathbf{e}$.
  Calculate $d\mathbf{u}$

$$d\mathbf{u} = d\mathbf{u}_1 + (\alpha + d\alpha)d\mathbf{u}_2, \qquad (21)$$

where

$$\begin{cases}(d\mathbf{u})_1 = -\mathbf{u} + \tilde{\mathbf{S}}^{-1}\tilde{\mathbf{f}}_1 & \text{(a)}\\ (d\mathbf{u})_2 = \tilde{\mathbf{S}}^{-1}\tilde{\mathbf{f}}_2 & \text{(b)}\end{cases} \qquad (22)$$

$$\begin{cases} \tilde{\mathbf{S}} = \sum_{i=1}^{NG} \hat{\mathbf{B}}_i^T \tilde{\mathbf{E}}_i \hat{\mathbf{B}}_i, & \text{(a)} \\ \tilde{\mathbf{f}}_1 = \sum_{i=1}^{NG} \hat{\mathbf{B}}_i^T \tilde{\mathbf{E}}_i \sum_{k=1}^{m} \mathbf{e}_{ik} \\ \quad - \sum_{i=1}^{NG} \hat{\mathbf{B}}_i^T \mathbf{Q}_i^{-1} \sum_{k=1}^{m} \tilde{\mathbf{M}}_{ik}^{-1} \left(a \sum_{k=1}^{m} \mathbf{e}_{ik} \sqrt{\mathbf{e}_{ik}^T \mathbf{e}_{ik} + \varepsilon^2} \right. \\ \quad \left. + \mathbf{e}_{ik} \sqrt{\sum_{k=1}^{m} \mathbf{e}_{ik}^T \sum_{k=1}^{m} \mathbf{e}_{ik} + \varepsilon^2} \right) \\ \quad - \sum_{i=1}^{NG} \hat{\mathbf{B}}_i^T \mathbf{Q}_i^{-1} \sum_{k=1}^{m} \tilde{\mathbf{M}}_{ik}^{-1} c b_{ik} \mathbf{D}_M \mathbf{e}_{ik}, & \text{(b)} \\ \tilde{\mathbf{f}}_2 = - \sum_{i=1}^{NG} \hat{\mathbf{B}}_i^T \mathbf{Q}_i^{-1} \sum_{k=1}^{m} \tilde{\mathbf{M}}_{ik}^{-1} \mathbf{t}_{ik} b_{ik}, & \text{(c)} \end{cases} \tag{23}$$

$$\tilde{\mathbf{E}}_i = \left(\mathbf{I}_i - c \mathbf{Q}_i^{-1} \sum_{k=1}^{m} b_{ik} \tilde{\mathbf{M}}_{ik}^{-1} \right), \tag{24}$$

$$\mathbf{Q}_i = \mathbf{I}_i + \sum_{k=1}^{m} \tilde{\mathbf{M}}_{ik}^{-1} \mathbf{N}_{ik}, \tag{25}$$

$$\tilde{\mathbf{M}}_{ik} \approx \left(\sqrt{\sum_{k=1}^{m} \mathbf{e}_{ik}^T \sum_{k=1}^{m} \mathbf{e}_{ik} + \varepsilon^2} \mathbf{I}_{ik} + c b_{ik} \mathbf{D}_M \right), \tag{26}$$

$$\mathbf{N}_{ik} \approx \left(a \sqrt{\mathbf{e}_{ik}^T \mathbf{e}_{ik} + \varepsilon^2} + c b_{ik} \right) \mathbf{I}_{ik}, \tag{27}$$

$$b_{ik} = \sqrt{\sum_{k=1}^{m} \mathbf{e}_{ik}^T \sum_{k=1}^{m} \mathbf{e}_{ik} + \varepsilon^2} \sqrt{\mathbf{e}_{ik}^T \mathbf{e}_{ik} + \varepsilon^2}. \tag{28}$$

Calculate $d\mathbf{e}_{ik}$

$$d\mathbf{e}_{ik} = (d\mathbf{e}_{ik})_1 + (\alpha + d\alpha)(d\mathbf{e}_{ik})_2, \tag{29}$$

where

$$\begin{cases} (d\mathbf{e}_{ik})_1 = \left(\tilde{\mathbf{M}}_{ik}^{-1} \mathbf{N}_{ik} \mathbf{Q}_i^{-1} \sum_{k=1}^{m} \tilde{\mathbf{M}}_{ik}^{-1} - \tilde{\mathbf{M}}_{ik}^{-1} \right) \boldsymbol{\beta}_1, & \text{(a)} \\ (d\mathbf{e}_{ik})_2 = \left(\tilde{\mathbf{M}}_{ik}^{-1} \mathbf{N}_{ik} \mathbf{Q}_i^{-1} \sum_{k=1}^{m} \tilde{\mathbf{M}}_{ik}^{-1} - \tilde{\mathbf{M}}_{ik}^{-1} \right) \boldsymbol{\beta}_2, & \text{(b)} \end{cases} \tag{30}$$

$$\begin{cases} \boldsymbol{\beta}_1 = a\sum_{k=1}^{m}\mathbf{e}_{ik}\sqrt{\mathbf{e}_{ik}^T\mathbf{e}_{ik}+\varepsilon^2} + \mathbf{e}_{ik}\sqrt{\sum_{k=1}^{m}\mathbf{e}_{ik}^T\sum_{k=1}^{m}\mathbf{e}_{ik}+\varepsilon^2} \\ \qquad + c\mathbf{D}_M\mathbf{e}_{ik}b_{ik} + c\left(\sum_{k=1}^{m}\mathbf{e}_{ik} - \hat{\mathbf{B}}_i\mathbf{u}\right)b_{ik} - cb_{ik}\hat{\mathbf{B}}_i d\mathbf{u}_1, \quad \text{(a)} \\ \boldsymbol{\beta}_2 = (\mathbf{t}_{ik} - c\hat{\mathbf{B}}_i d\mathbf{u}_2). \quad \text{(b)} \end{cases} \tag{31}$$

Calculate $(\alpha + d\alpha)$

$$\begin{aligned}(\alpha + d\alpha) &= \frac{1 - \sum_{i=1}^{NG}\sum_{k=1}^{m}\mathbf{t}_{ik}^T(\mathbf{e}_{ik} + (d\mathbf{e}_{ik})_1)}{\sum_{i=1}^{NG}\sum_{k=1}^{m}\mathbf{t}_{ik}^T(d\mathbf{e}_{ik})_2} \\ &= -\frac{\sum_{i=1}^{NG}\sum_{k=1}^{m}\mathbf{t}_{ik}^T(d\mathbf{e}_{ik})_1}{\sum_{i=1}^{NG}\sum_{k=1}^{m}\mathbf{t}_{ik}^T(d\mathbf{e}_{ik})_2}.\end{aligned} \tag{32}$$

- Step 3: Perform a line search to find λ_u such that

$$\lambda_u = \min F_P(\mathbf{u} + \lambda d\mathbf{u}, \mathbf{e} + \lambda d\mathbf{e}). \tag{33}$$

Update displacement, strain as:

$$\begin{aligned} &\mathbf{u} = \mathbf{u} + \lambda_u d\mathbf{u}, && \text{(a)} \\ &\mathbf{e}_{ik} = \mathbf{e}_{ik} + \lambda_u d\mathbf{e}_{ik}. && \text{(b)} \end{aligned} \tag{34}$$

- Step 4: Check convergence criteria: if they are all satisfied, then go to step 5, otherwise go to step 2.
- Step 5: Stop.

4 Validations

In this section, we validate our theory and algorithm by analyzing some examples, which are available in literature. For shakedown analysis, the results are verified by

$$\begin{cases} \alpha_{sd}^{blkh} = \alpha_{sd}^{pp}, & \text{for } \sigma_u = \sigma_y \\ \alpha_{sd}^{pp} \le \alpha_{sd}^{blkh} \le (\sigma_u/\sigma_y)\alpha_{sd}^{pp}, & \text{for } \sigma_y < \sigma_u \le 2\sigma_y \end{cases}$$

4.1 Thin Plate Under Tension and Temperature

4.1.1 Problem Definitions

This problem has been investigated in [6], using a numerical approach based on the lower bound shakedown theorem.

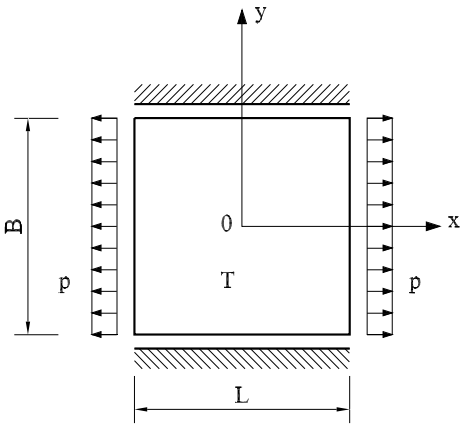

Fig. 3 Thin plate under tension and temperature

Geometry: The square plate has the dimensions: $B \times L = 400 \times 400$ mm^2, simply supported at two opposite sides, see Fig. 3.

Material: Young's modulus: $E = 2.1 \cdot 10^5$ N/mm^2, yield stress: $\sigma_y = 160$ N/mm^2, hardening effect (ultimate strength): $\sigma_u/\sigma_y = 1.5$ for bounded hardening, and $\sigma_u/\sigma_y \geq 2$ for unbounded hardening, Poisson's ratio: $\nu = 0.3$, coefficient of thermal expansion: $\alpha_t = 10^{-5}$ K^{-1}.

Loads: Uniform distributed tension p(N/mm) applied on the lateral sides, and uniform distributed temperature T(°C) in the plate, these loads vary in the domain: $p \in [0, p_0], T \in [0, T_0]$, where p_0 and T_0 is the elastic analytical solution for pure tension and pure temperature, respectively. See details in [6].

$$p_0 = \frac{1}{\sqrt{1-\nu+\nu^2}}\sigma_y, \qquad T_0 = \frac{1}{E\alpha_t}\sigma_y. \tag{35}$$

FEM model: Using sixteen 8-node-2D elements with 2×2 Gaussian points whichever to analyze a quarter of the structure. The structure is considered as plane stress problem.

4.1.2 Numerical Results

The results presented in Fig. 4, are close to the results from the work of Heitzer and Staat [6].

4.2 Tension-Torsion Experiment

4.2.1 Problem Definitions

A steel hollow section bar is subjected to tension force N and torsional moment M. This problem has been investigated by Heitzer, Staat by both experiment and FE analysis, see [7, 16].

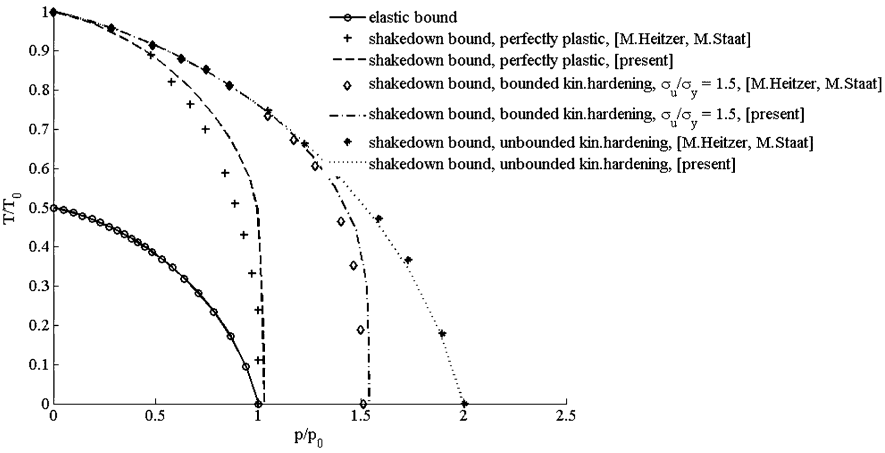

Fig. 4 Interaction diagram for elastic and shakedown limits of thin plate under tension and temperature, normalized by p_0 and T_0 in formula (34)

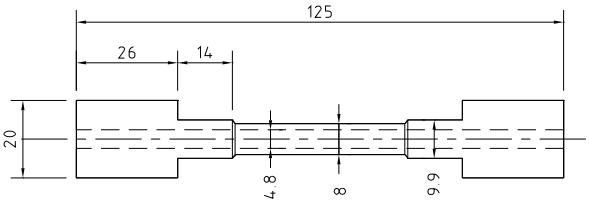

Fig. 5 Tension torsion specimen

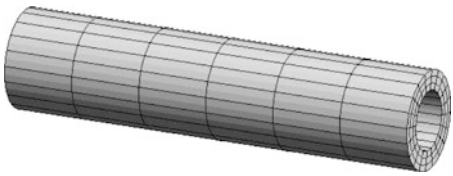

Fig. 6 FEM mesh of tension–torsion experiment

Geometry: the structure of the test specimen is described in Fig. 5.

Material: Young's modulus: $E = 2.07 \cdot 10^5$ N/mm^2, yield stress: $\sigma_y = 485$ N/mm^2, ultimate strength: $\sigma_u = 631$ N/mm^2, $\sigma_u/\sigma_y = 1.3$, Poisson's ratio: $\nu = 0.3$.

Loads: There are four cases of load domains considered: (a) constant torsion and cyclic tension with nonzero mean stress, M: dead load, $N \in [0, 1]$, (b) constant torsion and cyclic tension with zero mean stress, M: dead load, $N \in [-1, 1]$, (c) constant tension and cyclic torsion with zero mean stress, N: dead load, $M \in [-1, 1]$, and (d) both tension and torsion are cyclic loads, fully reversed, $N \in [-1, 1]$, $M \in [-1, 1]$.

FEM model: To reduce the computing time we use 360 20-node-3D elements to model only the critical thinner part of the structure, Fig. 6. This simplification does not affect the result.

4.2.2 Results

- *Analytical solutions:* the analytical solutions for this structure has been obtained in [7, 16] and is presented hereafter:

Elastic analysis

For pure torsion and axial symmetry, the normal stress vanishes and only shear stress $\tau(r) = \sigma_{\theta z}$ occurs. The stress for constant moment M at the radius r is calculated as:

$$\sigma_{\theta z}(r) = \tau(r) = \frac{2M}{\pi(r_a^4 - r_i^4)} r. \tag{36}$$

The maximum shear stress occurs at the outer radius. For $r_a = 4$ mm and $r_i = 2.4$ mm then:

$$\tau_{\max} = \tau(r_a) = \frac{2M}{\pi(r_a^4 - r_i^4)} r_a = \frac{M}{87.5}\ 1/\text{mm}^3. \tag{37}$$

With the equivalent von Mises stress $\sigma_{eq} = \sqrt{3}\tau_{\max}$ the structure starts yielding at:

$$M_{el} = 87.5\ \text{mm}^3 \frac{\sigma_y}{\sqrt{3}} = 87.5 \frac{485}{\sqrt{3}}\ \text{N mm} = 24501.3\ \text{N mm}. \tag{38}$$

Limit analysis

The pure tension capacity is easily calculated.

– for perfectly plastic material:

$$N_{\lim}^{pp} = N_{pl} = \pi\left(r_a^2 - r_i^2\right)\sigma_y = 3.14\left(4^2 - 2.4^2\right)485\ \text{N} = 15602\ \text{N}. \tag{39}$$

– for bounded linearly kinematic hardening material:

$$N_{\lim}^{blkh} = (\sigma_u/\sigma_y) N_{\lim}^{pp} = 1.3 \cdot 15602\ \text{N} = 20282.6\ \text{N}. \tag{40}$$

Pure torsion capacity:

– for perfectly plastic material: $M_{\lim}^{pp}$ is obtained from elastic moment M_{el} with plastic limit factor η_{pl}

$$M_{\lim}^{pp} = M_{pl} = \eta_{pl} M_{el} = 1.2 \cdot 24501.3\ \text{N mm} = 29401.56\ \text{N mm}, \tag{41}$$

where M_{el} is calculated in formula (38) and

$$\eta_{pl} = \frac{4}{3} \cdot \frac{1 - (d/D)^3}{1 - (d/D)^4} = \frac{4}{3} \cdot \frac{1 - (4.8/8)^3}{1 - (4.8/8)^4} = 1.20098. \tag{42}$$

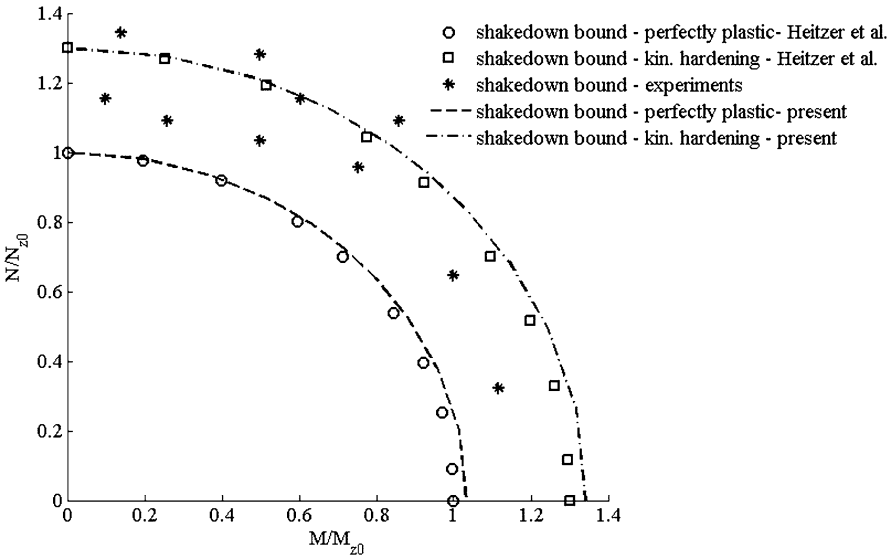

Fig. 7a Shakedown interaction diagram for load domain (a), normalized by $N_{z0} = 15.602$ kN and $M_{z0} = 27.98$ N m

– for bounded linearly kinematic hardening material:

$$M_{\lim}^{blkh} = (\sigma_u/\sigma_y) M_{\lim}^{pp} = 1.3 \cdot 29401.56 \text{ N mm} = 38222.0 \text{ N mm}. \tag{43}$$

- *Numerical solutions:* Interaction diagrams are plotted in Figs. 7a, 7b, 7c and 7d, corresponding to load domains (a) to (d). In the Fig. 7a, for the reason of comparison, the shakedown bounds are normalized by $N_{z0} = 15.602$ kN and $M_{z0} = 27.98$ N m, taken from [7, 16]. In the Fig. 7b to 7d, the shakedown bounds are normalized by analytical solutions of pure tension $N_{\lim}^{pp} = 15.602$ kN and pure torsion $M_{\lim}^{pp} = 29401.56$ N mm.

5 Conclusions

A new upper bound algorithm for shakedown analysis of elastic plastic bounded linearly kinematic hardening structures has been developed. The results are very close to those in literature. In the present model the shakedown limit does not depend on the hardening curve, but on the initial yield stress σ_y and ultimate strength σ_u. If $\sigma_u = \sigma_y$, then the bounding surface coincides with the initial yield surface, we have the elastic perfectly plastic model. If $\sigma_u \geq 2\sigma_y$ we have the unbounded kinematic hardening model.

Let α_{el}, α_{sd}^{pp}, and α_{sd}^{blkh} denote respectively elastic limit, shakedown limit for elastic perfectly plastic, and shakedown limit for bounded kinematic hardening ma-

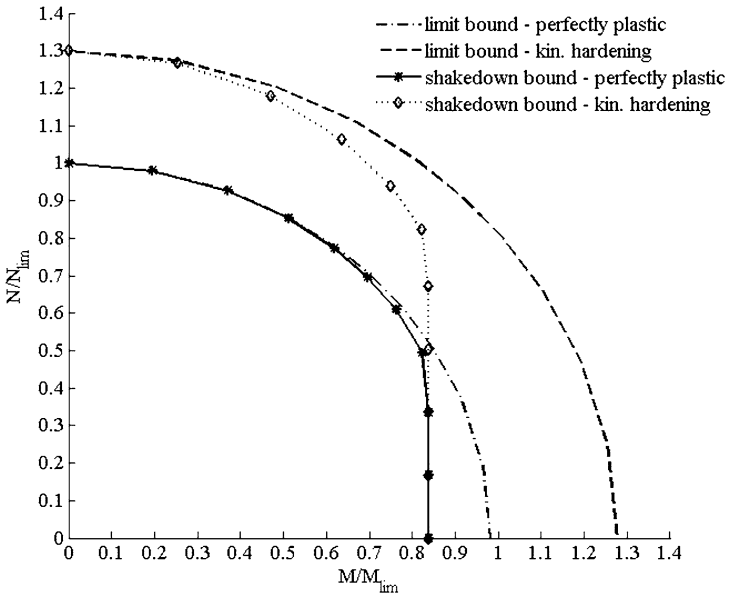

Fig. 7b Limit and Shakedown interaction diagram for load domain (b), normalized by $N_{\text{lim}}^{pp} = 15.6$ kN and $M_{\text{lim}}^{pp} = 29.4$ N m

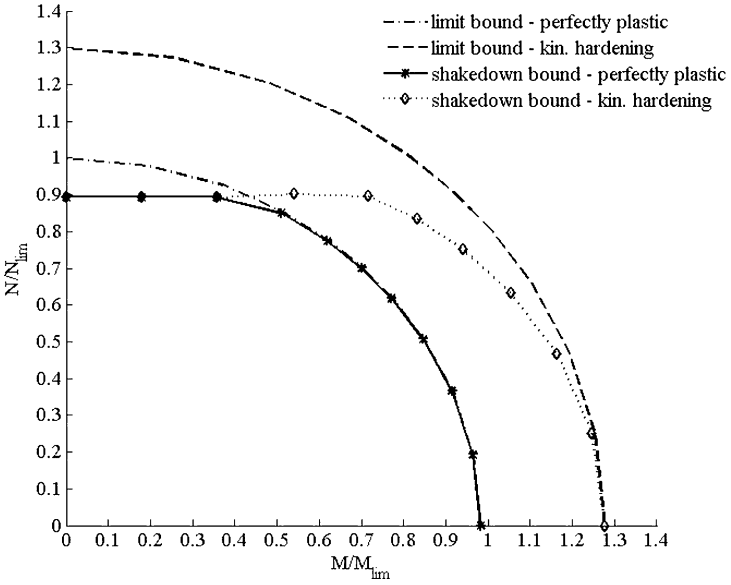

Fig. 7c Limit and Shakedown interaction diagram for load domain (c), normalized by $N_{\text{lim}} = 15.6$ kN and $M_{\text{lim}} = 29.4$ N m

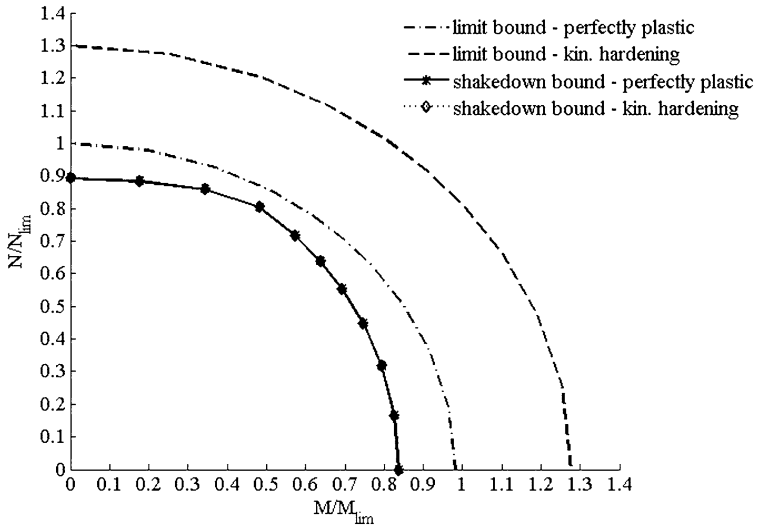

Fig. 7d Limit and Shakedown interaction diagram for load domain (d), normalized by $N_{\text{lim}} = 15.6$ kN and $M_{\text{lim}} = 29.4$ N m

terial, then:

$$\alpha_{sd}^{pp} \leq \alpha_{sd}^{blkh} \leq \frac{\sigma_u}{\sigma_y}\alpha_{sd}^{pp} \leq 2\alpha_{el}.$$

The left equality occurs if the translated surface is inside the bounding surface, the middle equality occurs if the translated surface is fixed on the bounding surface, otherwise, for inequalities, the translated surface moves on the bounding surface. The last equality occurs when yield surface translates unboundedly.

If the structure shakes down in the alternating plasticity mode, then there is no difference between perfectly plastic and kinematic hardening models.

Acknowledgements The work of Phú Tình Phạm has been supported by the Ministry of Education and Training of Vietnam (MOET) through the 322 project, and Aachen University of Applied Sciences, Germany.

References

1. Bleich: Über die Bemessung statisch unbestimmter Stahltragwerke unter Berücksichtigung des elastisch-plastischen Verhaltens des Baustoffes. Bauingenieur **19/20**, 261–266 (1932)
2. Bodovillé, G., de Saxcé, G.: Plasticity with non-linear kinematic hardening—modelling and shakedown analysis by the bipotential approach. Eur. J. Mech. A, Solids **20**, 99–112 (2001)
3. Bouby, C., de Saxcé, G., Tritsch, J.-B.: A comparison between analytical calculations of the shakedown load by the bipotential approach and step-by-step computations for elastoplastic materials with nonlinear kinematic hardening. Int. J. Solids Struct. **43**, 2670–2692 (2006)
4. Gokhfeld, D.A., Cherniavsky, O.F.: Limit Analysis of Structures at Thermal Cycling. Sijthoff & Noordhoff, Amsterdam (1980)

5. Koiter, W.T.: General theorems of elastic–plastic solids. In: Sneddon, J.N., Hill, R. (eds.) Progress in Solid Mechanics, vol. 1, pp. 67–221. North-Holland, Amsterdam (1960)
6. Heitzer, M., Staat, M.: Basic reduction technique for limit and shakedown problems. In: Staat, M., Heitzer, M. (eds.) Numerical Methods for Limit and Shakedown Analysis—Deterministic and Probabilistic Problems. NIC Series, vol. 15. John von Neumann Institute for Computing, Jülich (2003). http://www.fz-juelich.de/nic-series/volume15/nic-series-band15.pdf
7. Heitzer, M., Staat, M., Reiners, H., Schubert, F.: Shakedown and ratcheting under tension–torsion loadings—analysis and experiments. Nucl. Eng. Des. **225**, 11–26 (2003). doi:10.1016/S0029-5493(03)00134-1
8. Makrodimopoulos, A., Bisbos, C.: Shakedown analysis of plane stress problems via SOCP. In: Staat, M., Heitzer, M. (eds.) Numerical Methods for Limit and Shakedown Analysis—Deterministic and Probabilistic Problems. NIC Series, vol. 15. John von Neumann Institute for Computing, Jülich (2003). http://www.fz-juelich.de/nic-series/volume15/nic-series-band15.pdf
9. Melan, E.: Theorie statisch unbestimmter Systeme aus ideal plastischem Baustoff. Sitzber. Akad. Wiss. Wien IIa **145**, 195–218 (1936)
10. Melan, E.: Zur Plastizität des räumlichen Kontinuums. Ing.-Arch. **8**, 116–126 (1938)
11. Nguyễn, Q.S.: On shakedown analysis in hardening. J. Mech. Phys. Solids **51**, 101–125 (2003)
12. Phạm, Đ.C.: Shakedown static and kinematic theorems for elastic-plastic limited linear kinematic-hardening solids. Eur. J. Mech. A, Solids **24**, 35–45 (2005)
13. Phạm, Đ.C.: Shakedown theory for elastic plastic kinematic hardening bodies. Int. J. Plast. **23**, 1240–1259 (2007)
14. Prager, W.: A new method of analyzing stress and strain in work hardening plastic solids. J. Appl. Mech. **23**, 493–496 (1956)
15. Staat, M., Heitzer, M.: LISA—a European project for FEM-based limit and shakedown analysis. Nucl. Eng. Des. **206**(2–3), 151–166 (2001). doi:10.1016/S0029-5493(00)00415-5
16. Staat, M., Heitzer, M.: The restricted influence of kinematic hardening on shakedown loads. In: Proceedings of WCCM V, 5th World Congress on Computational Mechanics, Vienna, Austria, July 7–12 (2002). http://opus.bibliothek.fh-aachen.de/opus/volltexte/2005/79/
17. Stein, E., Huang, Y.J.: Shakedown for systems of kinematic hardening materials. In: Mróz, Z., Weichert, D., Doroz, S. (eds.) Inelastic Behaviour of Structures Under Variables Loads, pp. 33–50. Kluwer Academic, Norwell (1995)
18. Stein, E., Zhang, G.: Theoretical and numerical shakedown analysis for kinematic hardening materials. Computational plasticity. Fundamentals and applications. In: Owen, D.R.J., Oñate, E., Hinton, E. (eds.) Proc. 3rd Conf. on Computational Plasticity, Barcelona, Spain, 6–10th April, pp. 1–26. Pineridge, Swansea (1992)
19. Stein, E., Zhang, G., König, J.A.: Shakedown with nonlinear strain hardening including structural computation using finite element method. Int. J. Plast. **8**, 1–31 (1992)
20. Stein, E., Zhang, G., Mahnken, R.: Shakedown analysis for perfectly plastic and kinematic hardening materials. In: Stein, E. (ed.) Progress in Computational Analysis of Inelastic Structures, pp. 175–244. Springer, Wien (1993)
21. Vũ, Đ.K.: Dual limit and shakedown analysis of structures. PhD Thesis, Université de Liège, Belgium (2001)
22. Weichert, D., Groß-Weege, J.: The numerical assessment of elastic-plastic sheets under variable mechanical and thermal loads using a simplified two-surface yield condition. Int. J. Mech. Sci. **30**, 757–767 (1988)
23. Zhang, G.: Einspielen und dessen numerische Behandlung von Flächentragwerken aus ideal plastischem bzw. kinematisch verfestigendem material. Ph.D. Thesis, Universität Hannover, Germany (1991)

An Edge-Based Smoothed Finite Element Method for Primal-Dual Shakedown Analysis of Structures Under Uncertainties

Thanh Ngọc Trân and Manfred Staat

Abstract This paper deals with the application of a new algorithm of probabilistic limit and shakedown analysis for 2D structures, in which the loading and strength of the material are to be considered as random variables. The procedure involves a deterministic shakedown analysis for each probabilistic iteration, which is based on the primal-dual approach and the edge-based smoothed finite element method (ES-FEM). The limit state function separating the safe and failure regions is defined directly as the difference between the obtained shakedown load factor and the current load factor. A Sequential Quadratic Programming (SQP) is implemented for finding the design point. Sensitivity analyses are performed numerically from a mathematical model and the probability of failure is calculated by the First Order Reliability Method. Because of use of constant smoothing functions in the ES-FEM, only one Gaussian point is required for each smoothing domain ensuring that the total number of variables in the resulting optimization problem is kept to a minimum compared with standard finite element formulation. Numerical examples are presented to show the validity and effectiveness of the present method.

1 Introduction

Recent trends consider the combination of the limit state analysis with the probabilistic approach to safety as a promising point of view, in order to take rational decisions in structural design. For limit state analysis, it has been recognized that the plastic collapse limit and the shakedown limit have to be accounted in an advanced

T.N. Trân
Chair of Mechanics and Robotics, University of Duisburg-Essen, 47057 Duisburg, Germany
e-mail: thanh.tran@uni-due.de

M. Staat (✉)
Campus Jülich, Institute of Bioengineering, Aachen University of Applied Sciences,
Heinrich-Mußmann-Str. 1, 52428 Jülich, Germany
e-mail: m.staat@fh-aachen.de
url: http://www.fh-aachen.de/biomechanik.html

G. Saxcé et al. (eds.), *Limit State of Materials and Structures*,
DOI 10.1007/978-94-007-5425-6_5,

approach since they define the real limit states of structures. Handling with such kind of problems, well-known direct plasticity methods such as limit and shakedown analysis becomes a powerful and effective tool. The upper bound shakedown analysis is based on Koiter's kinematic theorem to determine the minimum load factor for non-shakedown, see e.g. [9, 15]. The strategy of computation is initiated from the unsafe region to calculate the exterior approximation of the shakedown load domain by supposing a kinematically admissible failure mechanism. On the contrary, the lower bound shakedown analysis is based on Melan's static theorem, and the strategy of computation is begun from the safe region by supposing a statically admissible stress field to determine the maximum load factor for shakedown, see e.g. [2, 4]. Duality between these two bounds was proved by the flow rule including two main points: (1) the strain rate vector is proportional to the gradient of the yield function and (2) the plastic multiplier can be non-negative only at points where the yield function equals to zero.

In fact, no established design standard is able to definitely exclude any occurrence of structural malfunctions. All that can be successfully done is to recognize that both strength of the material and loading have an essential random nature, that therefore they are described as random variables or processes, and to keep the probability that such malfunctions occur as small as possible. Structural reliability analysis deals with these random variables in a rational way. An effective method of structural reliability analysis is probabilistic limit and shakedown analyses, which is based on the direct computation of the load-carrying capacity or the safety margin. Most important, this approach makes the problem time-invariant and therefore reduces considerably the needs for uncertain technological input data and computing costs.

The submitted contribution based on a new algorithm of probabilistic limit and shakedown analysis for 2D structures, in which the loading and strength of the material are to be considered as random variables. The procedure involves a deterministic shakedown analysis for each probabilistic iteration, which is based on the primal-dual approach and the edge-based smoothed finite element method (ES-FEM). The limit state function separating the safe and failure regions is defined directly as the difference between the obtained shakedown load factor and the current load factor. A Sequential Quadratic Programming (SQP) is implemented for finding the design point. Sensitivity analyses are performed numerically from a mathematical model and the probability of failure is calculated by the First Order Reliability Method. Because of use of constant smoothing functions in the ES-FEM, only one Gaussian point is required for each smoothing domain ensuring that the total number of variables in the resulting optimization problem is kept to a minimum compared with standard finite element formulation.

2 The Formulation of the ES-FEM

In engineering practice, the 3-node linear triangular element (FEM-T3) and the 4-node linear quadrilateral element (FEM-Q4) are preferred by many engineers due

to their simplicity, robustness, lesser demand on the smoothness of the solution, and efficiency of adaptive mesh refinements for solutions of desired accuracy. However, the FEM models using FEM-T3 or FEM-Q4 elements still possess inherent drawbacks such as the overestimation of the system stiffness matrix which leads to poor accuracy of the solution and they are subjected to locking effects for incompressible materials. Moreover, mesh distortion due to large deformations may lead to a severe convergence problem of the analysis.

In order to avoid these drawbacks, Liu et al. [5] have combined the strain smoothing technique used in meshfree methods with the FEM to formulate a so-called smoothed finite element method (S-FEM or CS-FEM). In the S-FEM, they subdivide each FE element into smoothing cells and do not use the compatible strain fields. The strain field is projected (smoothed) onto a constant field or set of constant fields based on local smoothing cells (domains) and the domain integration becomes integration along the boundary of the domain. The derivatives of the shape functions are not used to calculate the strain matrix, which accordingly reduces the requirements on the smoothness of the shape functions.

Very recently, Liu et al. [6] also proposed an edge-based smoothed finite element method (ES-FEM) for static, free and forced vibration analyses of solid 2D mechanics problems using triangular elements (T3). Intensive numerical results have demonstrated that ES-FEM possesses the following excellent properties: (1) ES-FEM-T3 is much more accurate than the FEM using linear triangular elements (FEM-T3) and often found even more accurate than those of the FEM using quadrilateral elements (FEM-Q4) with the same sets of nodes; (2) there are no spurious non-zeros energy modes found and hence the method is also temporally stable and works well for vibration analysis and (3) no penalty parameter is used and the computational efficiency is much better than the FEM using the same sets of elements. The ES-FEM was then extended successfully to primal-dual limit and shakedown analysis of structures made of elastic-perfectly plastic material [11].

Suppose that the entire problem domain is discretized by finite elements. In the ES-FEM, the compatible strains $\boldsymbol{\varepsilon} = \nabla_s \mathbf{u}$ are smoothed over local smoothing domains $\Omega^{(k)}$ associated with edges of the elements by the following operation

$$\tilde{\boldsymbol{\varepsilon}}_k = \int_{\Omega^{(k)}} \boldsymbol{\varepsilon}(\mathbf{x}) \Phi_k(\mathbf{x}) d\Omega = \int_{\Omega^{(k)}} \nabla_s \mathbf{u}(\mathbf{x}) \Phi_k(\mathbf{x}) d\Omega, \tag{1}$$

where $\Phi_k(\mathbf{x})$ is a given smoothing function that satisfies the unity property

$$\int_{\Omega^{(k)}} \Phi_k(\mathbf{x}) d\Omega = 1. \tag{2}$$

The local smoothing domains $\Omega^{(k)}$ are constructed based on edges of elements such that they cover the entire problem domain $\Omega = \bigcup_{k=1}^{N_e} \Omega^{(k)}$ and $\Omega^{(i)} \cap \Omega^{(j)} = \emptyset$ for $i \neq j$, in which N_e is the total number of edges (sides) in the entire problem domain. If triangular elements are used, the smoothing domain $\Omega^{(k)}$ associated with

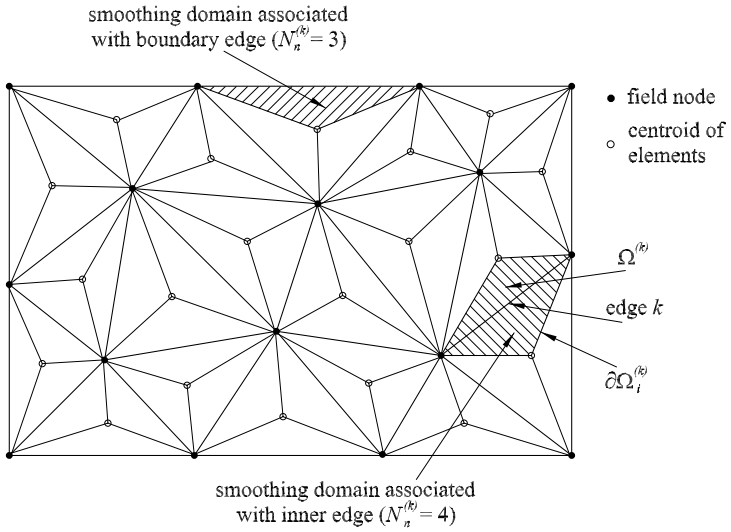

Fig. 1 Division of domain into triangular elements and smoothing cells $\Omega^{(k)}$ connected to edge k of triangular elements

edge k is created by connecting two endpoints of the edge to two centroids of two adjacent elements, see Fig. 1. For the mesh consisting of n-sided polygonal elements, the construction of smoothing domains is straightforward.

Using the constant smoothing function

$$\Phi_k(\mathbf{x}) = \begin{cases} 1/A^{(k)}, & \mathbf{x} \in \Omega^{(k)}, \\ 0, & \mathbf{x} \notin \Omega^{(k)}, \end{cases} \tag{3}$$

where $A^{(k)}$ is the area of the smoothing domain $\Omega^{(k)}$, the smoothed strains $\tilde{\boldsymbol{\varepsilon}}_k$ in (1) and therefore the stresses are constant in the smoothing domain. Let $\mathbf{x}_k$ stand for $\mathbf{x} \in \Omega^{(k)}$. In terms of nodal displacement vectors $\mathbf{d}_I$, the smoothing strains can be written as

$$\tilde{\boldsymbol{\varepsilon}}_k = \sum_{I=1}^{N_n^{(k)}} \tilde{\mathbf{B}}_I(\mathbf{x}_k)\mathbf{d}_I, \tag{4}$$

where $N_n^{(k)}$ is the total number of nodes of elements containing the common edge k. For inner edges (see Fig. 1) $N_n^{(k)} = 4$, for boundary edges $N_n^{(k)} = 3$. $\tilde{\mathbf{B}}_I(\mathbf{x}_k)$ is the smoothed strain matrix on the domain $\Omega^{(k)}$ which is calculated numerically by an assembly process similarly as in the standard FEM

$$\tilde{\mathbf{B}}_I(\mathbf{x}_k) = \frac{1}{A^{(k)}} \sum_{j=1}^{N_e^{(k)}} \frac{1}{3} A_e^{(j)} \mathbf{B}_j, \tag{5}$$

in which $N_e^{(k)}$, $A_e^{(j)}$, $\mathbf{B}_j$ are the number of elements, the area and the strain matrix of the jth element around the edge k, respectively. For inner edges (see Fig. 1) $N_e^{(k)} = 2$, for boundary edges $N_e^{(k)} = 1$. The matrix $\mathbf{B}_j$ is exactly the strain matrix of the T3 element in the standard FEM. When linear elements are used, the entries of $\mathbf{B}_j$ and therefore of $\tilde{\mathbf{B}}_I(\mathbf{x}_k)$ are also constants.

In general, the smoothed strain matrix for 2-dimensional problems consisting of n-sided polygonal elements can be calculated as follows

$$\tilde{\mathbf{B}}_I(\mathbf{x}_k) = \begin{bmatrix} \tilde{b}_{Ix}(\mathbf{x}_k) & 0 \\ 0 & \tilde{b}_{Iy}(\mathbf{x}_k) \\ \tilde{b}_{Iy}(\mathbf{x}_k) & \tilde{b}_{Ix}(\mathbf{x}_k) \end{bmatrix}, \tag{6}$$

in which

$$\tilde{b}_{Ih}(\mathbf{x}_k) = \frac{1}{A^{(k)}} \sum_{i=1}^{N_s} N_I\left(\mathbf{x}_i^{GP}\right) n_{ih}^{(k)} l_i^{(k)}, \quad (h = x, y), \tag{7}$$

where N_s is the total number of the boundary segments $\partial\Omega_i^{(k)}$ of the domain $\Omega^{(k)}$, $N_I(\mathbf{x}_i^{GP})$ is the shape function value at Gaussian point (midpoint) $\mathbf{x}_i^{GP}$ on $\partial\Omega_i^{(k)}$ and $n_{ih}^{(k)}$, $l_i^{(k)}$ are the outward unit normal and the length of boundary segment $\partial\Omega_i^{(k)}$.

The smoothed domain stiffness matrix is then calculated by

$$\tilde{\mathbf{K}}_{(k)} = \int_{\Omega^{(k)}} \tilde{\mathbf{B}}_I^T \mathbf{E} \tilde{\mathbf{B}}_I d\Omega = A^{(k)} \tilde{\mathbf{B}}_I^T \mathbf{E} \tilde{\mathbf{B}}_I, \tag{8}$$

where $\mathbf{E}$ is the matrix of elastic material constants. The global stiffness matrix $\tilde{\mathbf{K}}$ is then assembled over all domain stiffness matrices $\tilde{\mathbf{K}}_{(k)}$ by a similar process as in the FEM.

3 A Primal-Dual Shakedown Algorithm Based on the ES-FEM

Let us restrict ourselves to the case of homogeneous material, where the yield limit σ_y is the same at every point of the structure. Then we always can write $\sigma_y = Y\sigma_0$ where σ_0 is a constant reference value and Y is a random variable. Consider a convex polyhedral load domain $\mathscr{L}$ and a special loading path consisting of all load vertices $\hat{P}_i$ $(i = 1, \ldots, m)$ of $\mathscr{L}$. According to Koiter's theorem, the upper bound shakedown limit, which is the smaller one of the low cycle fatigue limit and the ratcheting limit, may be found by the following minimization

$$\alpha^+ = \min \sum_{i=1}^{m} \int_{\Omega} D^p(\dot{\tilde{\boldsymbol{\varepsilon}}}_{ik}) d\Omega \qquad \text{(a)}$$

$$\text{s.t.:} \begin{cases} \Delta\dot{\tilde{\boldsymbol{\varepsilon}}}_k = \sum_{i=1}^{m} \dot{\tilde{\boldsymbol{\varepsilon}}}_{ik} = \nabla_s(\Delta\dot{\mathbf{u}}_k), \quad \text{in } \Omega & \text{(b)} \\ \Delta\dot{\mathbf{u}}_k = 0, \quad \text{on } \partial\Omega_u & \text{(c)} \\ \mathbf{D}_v \dot{\tilde{\boldsymbol{\varepsilon}}}_{ik} = \mathbf{0}, & \text{(d)} \\ \sum_{i=1}^{m} \int_{\Omega} \dot{\tilde{\boldsymbol{\varepsilon}}}_{ik}^T \boldsymbol{\sigma}_k^E(x, \hat{P}_i) d\Omega = 1, & \text{(e)} \end{cases} \tag{9}$$

in which $D^p(\dot{\tilde{\boldsymbol{\varepsilon}}}_{ik})$ is the plastic dissipation power per unit domain, $\boldsymbol{\sigma}^E$ is the fictitious elastic stress vector, $\Delta\dot{\tilde{\boldsymbol{\varepsilon}}}$ is the vector of accumulated strain rates over a load cycle and $\dot{\mathbf{u}}$ is the vector of nodal velocities. The fictitious elastic stress vector $\boldsymbol{\sigma}^E$ and the starting value of the strain rate vector $\dot{\tilde{\boldsymbol{\varepsilon}}}_{ik}$ are calculated by solving the global system of equations with the global stiffness matrix $\tilde{\mathbf{K}}$ derived from Eq. (8). The third constraint (Eq. (9d)) ensures that the incompressibility condition is satisfied on all smoothing domains $\Omega^{(k)}$ and at all load vertices i. For plane strain problems, $\mathbf{D}_v$ assumes the form

$$\mathbf{D}_v = \begin{bmatrix} 1 & 1 & 0 \\ 1 & 1 & 0 \\ 0 & 0 & 0 \end{bmatrix}. \tag{10}$$

It is noted that only the first row in Eq. (9d) is necessary to ensure the incompressibility. However, we write $\mathbf{D}_v$ as a square matrix since it will help to formulate our optimization procedure conveniently, for example in Eq. (14). By discretizing the entire problem domain into smoothing domains, applying the strain smoothing technique described in Sect. 2 and introducing some new notations such as

$$\dot{\mathbf{e}}_{ik} = A^{(k)} \mathbf{D}^{1/2} \dot{\tilde{\varepsilon}}_{ik}, \qquad \mathbf{t}_{ik} = \mathbf{D}^{-1/2} \sigma_{ik}^E, \qquad \hat{\mathbf{B}}_k = A^{(k)} \mathbf{D}^{1/2} \tilde{\mathbf{B}}_k, \tag{11}$$

we obtain a simplified version for the upper bound shakedown analysis (primal problem)

$$\alpha^+ = \min \sum_{i=1}^{m} \sum_{k=1}^{N_e} \sqrt{\frac{2}{3}} Y \sigma_0 \sqrt{\dot{\mathbf{e}}_{ik}^T \dot{\mathbf{e}}_{ik} + \varepsilon_0^2} \qquad \text{(a)}$$

$$\text{s.t.:} \begin{cases} \sum_{i=1}^{m} \dot{\mathbf{e}}_{ik} - \hat{\mathbf{B}}_k \dot{\mathbf{u}} = \mathbf{0}, \quad \forall k = \overline{1, N_e} & \text{(b)} \\ \mathbf{D}_v \dot{\mathbf{e}}_{ik} = \mathbf{0}, \quad \forall k = \overline{1, N_e}, \ \forall i = \overline{1, m} & \text{(c)} \\ \sum_{i=1}^{m} \sum_{k=1}^{N_e} \dot{\mathbf{e}}_{ik}^T \mathbf{t}_{ik} - 1 = 0, & \text{(d)} \end{cases} \tag{12}$$

where ε_0^2 is a small positive number to ensure the objective function to be differentiable everywhere. It has been proved that the numerical result is not sensitive to ε_0^2 if it is smaller than 10^{-14} [14]. $\mathbf{D}$ is a diagonal square matrix and has the following form for two-dimensional problems

$$\mathbf{D} = diag\left[1 \quad 1 \quad \tfrac{1}{2}\right]. \tag{13}$$

Note that the second constraint in (9) is omitted here since it will be automatically fulfilled by the shape functions. The Lagrangian associated with the primal problem (12) can be written as follows

$$L = \sum_{k=1}^{N_e}\left\{\sum_{i=1}^{m}\sqrt{\frac{2}{3}}Y\sigma_0\sqrt{\dot{\mathbf{e}}_{ik}^T\dot{\mathbf{e}}_{ik}+\varepsilon_0^2} - \sum_{i=1}^{m}\boldsymbol{\gamma}_{ik}^T\mathbf{D}_v\dot{\mathbf{e}}_{ik} - \boldsymbol{\beta}_k^T\left(\sum_{i=1}^{m}\dot{\mathbf{e}}_{ik} - \hat{\mathbf{B}}_k\dot{\mathbf{u}}\right)\right\}$$
$$-\alpha\left(\sum_{k=1}^{N_e}\sum_{i=1}^{m}\dot{\mathbf{e}}_{ik}^T\mathbf{t}_{ik} - 1\right), \tag{14}$$

where $\boldsymbol{\gamma}_{ik}$, $\boldsymbol{\beta}_k$, α are Lagrange multipliers. The dual problem of (12) which can be proved by dual theory takes the form [14]

$$\begin{aligned} &\alpha^- = \max\alpha && \text{(a)}\\ &\text{s.t.:}\quad \begin{cases} \|\boldsymbol{\gamma}_{ik} + \boldsymbol{\beta}_k + \alpha\mathbf{t}_{ik}\| \le \sqrt{\frac{2}{3}}Y\sigma_0, & \text{(b)}\\ \sum_{k=1}^{N_e}\hat{\mathbf{B}}_k^T\boldsymbol{\beta}_k = \mathbf{0}. & \text{(c)} \end{cases} \end{aligned} \tag{15}$$

The form (15) is also exactly the discretized form of the lower bound shakedown limit which is formulated by Melan's static theorem. Since the stresses are constant in each smoothing domain, the two constraints in (15) are satisfied at all points in the entire problem domain. It follows that the lower bound shakedown limit obtained in (15) dual to the upper bound obtained in (12), for $\varepsilon_0^2 \to 0$, will have a strict bounding characteristic. It is noted that when $m = 1$, the formulations (12) and (15) reduce to those of limit analysis.

Dealing with the nonlinear constrained optimization problem (12), an iterative primal-dual algorithm is developed to calculate simultaneously the upper bound and lower bound of the shakedown limit. Details of this iterative algorithm can be found in [11].

4 Probabilistic Algorithm

Denote by $\mathbf{X} = (X_1, X_1, \ldots, X_n)$ an n-dimensional random vector characterizing uncertainties in the structure and load parameters. The limit state function $g(\mathbf{x}) = 0$,

which is based on the comparison of a structural resistance (threshold) and loading, defines the limit state hyper-surface ∂S which separates the failure region $S = \{\mathbf{x}|g(\mathbf{x}) < 0\}$ from the safe region. The probability of failure P_f is the probability that $g(\mathbf{X})$ is non-positive, i.e.

$$P_f = P\big(g(\mathbf{X}) \leq 0\big) = \int_S f_X(\mathbf{x})dx, \tag{16}$$

where $f_X(\mathbf{x})$ is the n-dimensional joint probability density function. In general, it is not possible to calculate P_f analytically since the form of the limit state surface is very complex. Therefore, approximation approaches should be used. In the First-Order Reliability Method (FORM), an approximation to the probability of failure is obtained by linearizing the limit state function at the "design point" (the most likely failure point or β_{HL}-point). This is the point on the limit state surface that is nearest to the origin in the space of standard normal random variables. The failure probability P_f is thus approximated by

$$P_f = \Phi(-\beta_{HL}) = \frac{1}{\sqrt{2\pi}} \int_{-\infty}^{-\beta_{HL}} e^{-0.5z^2} dz, \tag{17}$$

where $\beta_{HL} = \|\mathbf{u}^*\|$, $\Phi(.)$ is the standard normal cumulative distribution function and $\mathbf{u}^*$ is found from a nonlinear constrained optimization problem as follows

$$\begin{aligned} &\text{minimize:} \quad f(\mathbf{u}) = \frac{1}{2}\|\mathbf{u}\|^2 \\ &\text{s.t.} \qquad\quad g(\mathbf{u}) \leq 0. \end{aligned} \tag{18}$$

The main computational task for a reliability analysis problem is to locate the design point $\mathbf{u}^*$, i.e. to solve the optimization problem (18). Staat and Heitzer [8], Heitzer and Staat [3] and Bjerager [1] got good results in probabilistic limit analyses with a simple gradient search algorithm, which is based on a linearization of the limit state function at each step. However, this algorithm is only guaranteed to converge towards a locally most likely failure point in each sequence of points on the failure surface if the safe region is quasi-convex or concave. A more general algorithm is the Sequential Quadratic Programming (SQP). This method has proved to be suitable for tasks in the area of the reliability theory [7]. Details of an SQP method stabilized by a simple line search procedure subject to a suitable merit function for solving the optimization problem (18) can be found in [10]. Details of the definition of the limit state function and its gradients can be found in [12].

5 Validations

In the following, a number of examples are presented to demonstrate the capabilities of the proposed algorithm. In all cases, structures are made of elastic-perfectly plastic material and the 3-node triangular elements (FEM-T3) are applied for structural discretization.

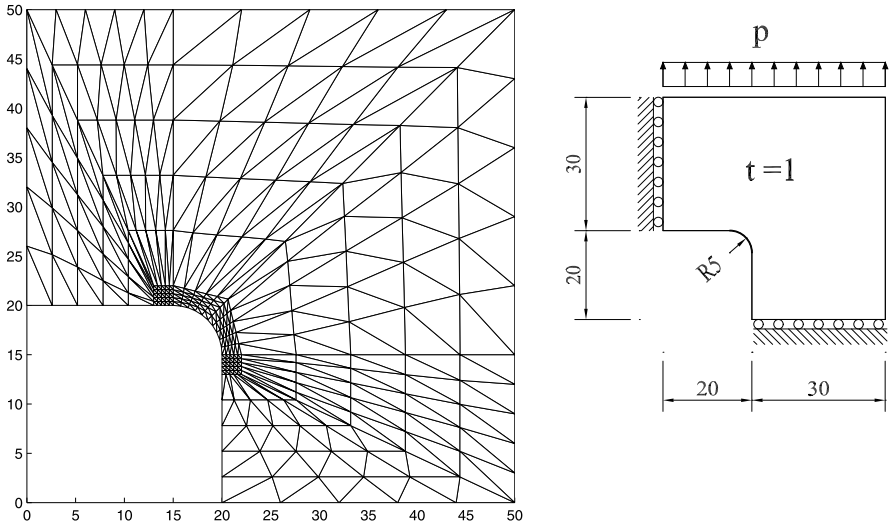

Fig. 2 FE-mesh and geometrical dimensions of square plate in mm

5.1 Square Plate with a Hole

The first example concerns a square plate with central hole as shown in Fig. 2b. The plate is subjected to a pressure p which can vary within a range $p \in [0, p_{\max}]$. The geometrical data and material properties are chosen as those used in [14]: $E = 200$ GPa, $\nu = 0.3$, $\sigma_y = 10$ MPa. Both plane strain and plane stress hypotheses are analyzed using 500 T3 elements as shown in Fig. 2a.

If both material strength and load (stress) random variables are supposed to be normally distributed with means μ_r, μ_s and standard deviations σ_r, σ_s respectively, then the analytical reliability index may be given [8]

$$\beta_{HL} = \frac{(1-\alpha)\mu_r - \mu_s}{\sqrt{(1-\alpha)^2\sigma_r^2 + \sigma_s^2}} \tag{19}$$

where $\alpha = p_{\lim}/\sigma_y$ is the load factor. From the deterministic numerical analysis [13], we got the limit load factor $\alpha = 0.5573$ and the shakedown load factor $\alpha = 0.3626$ for the case of plane stress. For plane strain, they are 0.6895 and 0.4331, respectively.

The numerical probabilities of failure for limit and shakedown analysis and for both plane stress and plane strain cases are presented in Tables 1 and 2, compared with the semi-analytical solutions, which are calculated by substituting α in (19). Both random variables have the same standard deviations $\sigma_{r,s} = 0.1\mu_{r,s}$. The present solutions are very close to the semi-analytical ones for both cases. It is

Table 1 Failure probabilities for normal distributions, plane stress

Limit analysis			Shakedown analysis		
μ_s/μ_r	P_f (anal.)	P_f (num.)	μ_s/μ_r	P_f (anal.)	P_f (num.)
0.20	7.975E-10	7.901E-10	0.10	1.460E-12	1.005E-12
0.25	2.439E-07	2.327E-07	0.15	3.015E-08	2.793E-08
0.30	2.398E-05	2.366E-05	0.20	4.308E-05	4.119E-05
0.35	8.163E-04	8.134E-04	0.25	5.285E-03	5.091E-03
0.40	1.092E-02	1.088E-02	0.30	9.173E-02	9.089E-02
0.45	6.707E-02	6.702E-02	0.35	4.013E-01	3.985E-01
0.50	2.220E-01	2.214E-01	0.3626	5.000E-01	5.017E-01
0.55	4.629E-01	4.622E-01	0.40	7.558E-01	7.584E-01
0.5573	5.000E-01	5.086E-01	0.45	9.348E-01	9.371E-01
0.6	6.989E-01	6.999E-01	0.50	9.869E-01	9.873E-01
0.65	8.605E-01	8.612E-01	0.55	9.978E-01	9.979E-01
0.70	9.446E-01	9.453E-01	0.60	9.996E-01	9.996E-01
0.75	9.804E-01	9.808E-01	0.65	9.999E-01	9.999E-01

Table 2 Failure probabilities for normal distributions, plane strain

Limit analysis			Shakedown analysis		
μ_s/μ_r	P_f (anal.)	P_f (num.)	μ_s/μ_r	P_f (anal.)	P_f (num.)
0.25	1.034E-09	9.981E-10	0.15	3.274E-10	2.898E-10
0.30	1.110E-07	1.003E-07	0.20	5.138E-07	4.983E-07
0.35	5.652E-06	5.434E-06	0.25	1.254E-04	1.009E-04
0.40	1.407E-04	1.248E-04	0.30	5.763E-03	5.537E-03
0.45	1.814E-03	1.594E-03	0.35	6.781E-02	6.483E-02
0.50	1.304E-02	1.217E-02	0.40	2.872E-01	2.567E-01
0.55	5.687E-02	5.606E-02	0.4331	5.000E-01	5.045E-01
0.6	1.637E-01	1.589E-01	0.45	6.066E-01	6.101E-01
0.65	3.384E-01	3.328E-01	0.50	8.441E-01	8.483E-01
0.6895	5.000E-01	5.071E-01	0.55	9.525E-01	9.537E-01
0.70	5.426E-01	5.467E-01	0.60	9.879E-01	9.881E-01
0.80	8.523E-01	8.571E-01	0.65	9.973E-01	9.974E-01
0.90	9.683E-01	9.689E-01	0.7	9.994E-01	9.994E-01
1.00	9.947E-01	9.948E-01	0.75	9.999E-01	9.999E-01

worth to note that the shakedown probabilities of failure are considerably smaller than those of limit analysis. Thus, the loading conditions should be considered carefully when assessing the load-carrying capacity of the structure.

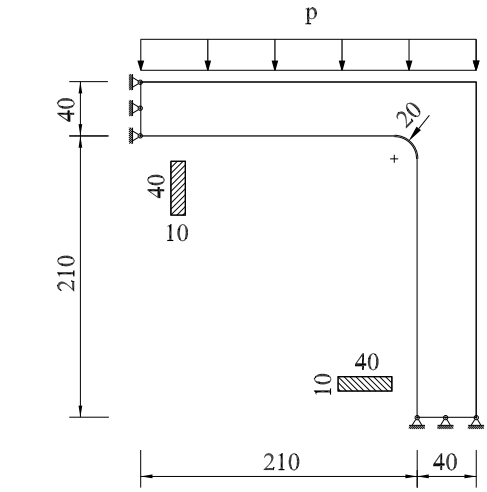

(a)

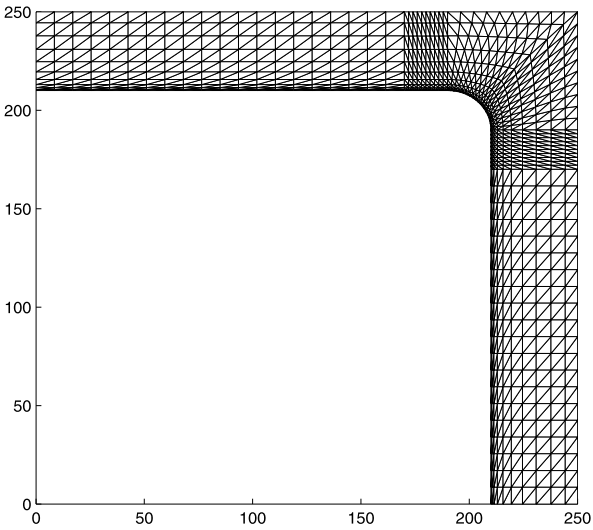

(b)

Fig. 3 FE-mesh and geometrical dimensions of simple frame in mm

5.2 Simple Frame

In the second example, we consider a simple frame subjected to a load as shown in Fig. 3a. Two different boundary conditions are considered: (a) only the horizontal displacement on the left boundary is free and (b) both vertical and horizontal displacements on both boundaries are fixed. The load domain, geometrical data and material properties are chosen analogously as: $p \in [0, p_{\max}]$, $E = 2 \cdot 10^5$ GPa,

Table 3 Failure probabilities for normal distributions, case (a)

Limit analysis			Shakedown analysis		
μ_s/μ_r	P_f (anal.)	P_f (num.)	μ_s/μ_r	P_f (anal.)	P_f (num.)
0.30	5.666E-10	3.898E-10	0.30	1.175E-09	1.022E-09
0.40	9.008E-07	8.322E-07	0.40	1.883E-06	1.447E-06
0.50	2.072E-04	2.014E-04	0.50	3.959E-04	3.670E-04
0.60	8.593E-03	8.187E-03	0.60	1.422E-02	1.211E-02
0.70	8.995E-02	8.637E-02	0.70	1.271E-01	1.165E-01
0.80	3.421E-01	3.223E-01	0.80	4.199E-01	4.087E-01
0.8474	5.000E-01	5.051E-01	0.8232	5.000E-01	5.034E-01
0.85	5.086E-01	5.112E-01	0.85	5.896E-01	5.907E-01
0.90	6.648E-01	6.693E-01	0.90	7.355E-01	7.365E-01
1.00	8.778E-01	8.791E-01	1.00	9.139E-01	9.146E-01
1.10	9.655E-01	9.659E-01	1.10	9.780E-01	9.787E-01
1.20	9.918E-01	9.919E-01	1.20	9.952E-01	9.954E-01
1.30	9.982E-01	9.982E-01	1.30	9.990E-01	9.990E-01
1.40	9.996E-01	9.996E-01	1.40	9.998E-01	9.998E-01

$\nu = 0.3$, $\sigma_y = 10$ MPa. The frame is discretized by 1600 T3 elements as shown in Fig. 3b.

For case (a), numerical deterministic analyses lead to the limit load factor $\alpha = 0.8474$ and the shakedown load factor $\alpha = 0.8232$. For case (b), they are 1.3487 and 0.9187, respectively. Numerical probabilities of failure for limit and shakedown analyses for normal distributions are presented in Tables 3 and 4, compared with corresponding semi-analytical solutions by (19). Both random variables have standard deviations $\sigma_{r,s} = 0.1\mu_{r,s}$. The numerical error results only from reliability analysis. It is shown that the present numerical results are very close to the exact ones, even in the case of very small probabilities.

6 Conclusions

The paper has presented the application of a numerical procedure for probabilistic limit and shakedown analyses of 2D structures made of elastic-perfectly plastic materials using a novel ES-FEM. The procedure involves a deterministic limit and shakedown analysis for each probabilistic iteration, which is based on the primal-dual approach and the use of the von Mises yield criterion. A mesh of three-node linear triangular elements and constant smoothing functions are used to construct the ES-FEM formulation. The probabilistic formulation considers the loading and the material strength as random variables. A nonlinear optimization was implemented, which is based on the Sequential Quadratic Programming for finding the design

Table 4 Failure probabilities for normal distributions, case (b)

Limit analysis			Shakedown analysis		
μ_s/μ_r	P_f (anal.)	P_f (num.)	μ_s/μ_r	P_f (anal.)	P_f (num.)
0.50	1.814E-09	1.032E-09	0.30	7.676E-11	4.232E-11
0.60	1.968E-07	1.247E-07	0.40	1.130E-07	9.998E-08
0.70	9.815E-06	9.511E-06	0.50	3.126E-05	2.364E-05
0.80	2.334E-04	2.102E-04	0.60	1.839E-03	1.352E-03
0.90	2.826E-03	2.579E-03	0.70	2.914E-02	2.674E-02
1.00	1.891E-02	1.772E-02	0.80	1.649E-01	1.466E-01
1.10	7.650E-02	7.604E-02	0.90	4.422E-01	4.467E-01
1.20	2.051E-01	2.001E-01	0.9187	5.000E-01	5.023E-01
1.30	3.974E-01	3.921E-01	0.95	5.936E-01	5.976E-01
1.3487	5.000E-01	5.021E-01	1.00	7.253E-01	7.261E-01
1.35	5.027E-01	5.046E-01	1.10	8.971E-01	8.977E-01
1.40	6.041E-01	6.051E-01	1.20	9.687E-01	9.691E-01
1.50	7.734E-01	7.738E-01	1.30	9.917E-01	9.920E-01
1.60	8.851E-01	8.857E-01	1.40	9.980E-01	9.981E-01
1.70	9.473E-01	9.475E-01	1.50	9.995E-01	9.995E-01

point and the probabilities of failure were calculated by FORM. Numerical examples were tested demonstrating that the proposed method appears to be powerful and effective for evaluating of the probabilities of failure of 2D structures. The extension for 3D structures using the face-based smoothed finite element method (FS-FEM) is straightforward.

References

1. Bjerager, P.: Plastic systems reliability by LP and FORM. Comput. Struct. **31**(2), 187–196 (1989)
2. Heitzer, M., Staat, M.: FEM-computation of load carrying capacity of highly loaded passive components by direct methods. Nucl. Eng. Des. **193(3)**, 349–358 (1999)
3. Heitzer, M., Staat, M.: Reliability analysis of elasto-plastic structures under variable loads. In: Maier, G., Weichert, D. (eds.) Inelastic Analysis of Structures Under Variable Loads: Theory and Engineering Applications, pp. 269–288. Kluwer Academic, Dordrecht (2000)
4. Krabbenhoft, K., Damkilde, L.: A general non-linear optimization algorithm for lower bound limit analysis. Int. J. Numer. Methods Eng. **56**(2), 165–184 (2003)
5. Liu, G.R., Dai, K.Y., Nguyen, T.T.: A smoothed finite element for mechanics problems. Comput. Mech. **39**(6), 859–877 (2007)
6. Liu, G.R., Nguyen-Thoi, T., Lam, K.Y.: An edge-based smoothed finite element method (ES-FEM) for static, free and forced vibration analyses of solids. J. Sound Vib. **320**(4–5), 1100–1130 (2009)
7. Rackwitz, R.: Zuverlässigkeit und Lasten im Konstruktiven Ingenieurbau. Course Notes, Technische Universität, München (1993–2004)

8. Staat, M., Heitzer, M.: Probabilistic limit and shakedown problems. In: Staat, M., Heitzer, M. (eds.) Numerical Methods for Limit and Shakedown Analysis, Deterministic and Probabilistic Problems, NIC–Series, vol. 15, pp. 217–268. John von Neumann Institute for Computing, Jülich (2003). http://www.fz-juelich.de/nic-series/volume15/nic-series-band15.pdf
9. Tran, T.N., Kreißig, R., Vu, D.K., Staat, M.: Upper bound limit and shakedown analysis of shells using the exact Ilyushin yield surface. Comput. Struct. **86**(17–18), 1683–1695 (2008)
10. Tran, T.N., Kreißig, R., Staat, M.: Probabilistic limit and shakedown analysis of thin shells. Struct. Saf. **31**(1), 1–18 (2009)
11. Tran, T.N., Liu, G.R., Nguyen-Xuan, H., Nguyen-Thoi, T.: An edge-based smoothed finite element method for primal-dual shakedown analysis of structures. Int. J. Numer. Methods Eng. **82**(7), 917–938 (2010)
12. Tran, T.N., Liu, G.R.: Probabilistic primal-dual shakedown analysis of structures using the edge-based smoothed finite element method. Int. J. Numer. Methods Eng. (2012, submitted)
13. Tran, T.N., Staat, M.: Shakedown analysis of two dimensional structures by an edge-based smoothed finite element method. In: ECCM 2010, IV European Conference on Computational Mechanics, Paris, France, May 16–21 (2010). http://www.eccm2010.org/complet/fullpaper_1042.pdf
14. Vu, D.K.: Dual limit and shakedown analysis of structures. Dissertation, Université de Liège, Belgium (2001)
15. Yan, A.M., Nguyen-Dang, H.: Kinematical shakedown analysis with temperature-dependent yield stress. Int. J. Numer. Methods Eng. **50**(5), 1145–1168 (2001)

Interior-Point Method for Lower Bound Shakedown Analysis of von Mises-Type Materials

J.-W. Simon and D. Weichert

Abstract The lower bound shakedown theorem for the determination of shakedown loading factors leads to nonlinear convex optimization problems. For their solution, the use of interior-point methods has become common practice. In this paper, an extended formulation of the interior-point method for shakedown analysis is presented for von Mises-type materials. The formulation is generalized for the case of arbitrary finite numbers of loading cases. Numerical details of the algorithm are given and the described methodology is illustrated by a numerical example.

1 Introduction

The design of engineering structures and components requires reliable predictions of whether or not the system is capable of resisting to the given thermo-mechanical loading. In case that the loads are varying with time, two different methods can be used for this.

In the conventional step-by-step methods, the loading path is divided into sufficiently small loading steps and a full analysis of the evolution of stresses and strains is carried out for each step. Besides the question of running time, the most obvious disadvantage of these methods is the fact that the exact knowledge of the complete loading history is essential for the calculation, which is not realistic in many cases.

This disadvantage can be overcome by the use of *direct methods* [20, 25, 52, 53], where the loading path is not necessarily given but only its bounding envelope. The basement of direct methods is constituted by the theorems of Koiter [19] and Melan [28, 29]. In the present work, only the statical approach by Melan is used, which gives a lower bound of the loading factor. From practical point of view, the determination of the lower bound is of special interest because it leads in principle to conservative solutions.

J.-W. Simon (✉) · D. Weichert
Institute of General Mechanics, RWTH Aachen University, Templergraben 64, 52056 Aachen, Germany
e-mail: simon@iam.rwth-aachen.de

D. Weichert
e-mail: weichert@iam.rwth-aachen.de

G. Saxcé et al. (eds.), *Limit State of Materials and Structures*,
DOI 10.1007/978-94-007-5425-6_6,

Melan's theorem leads to nonlinear optimization problems, which has handicapped the use of direct methods in the past, due to the lack of appropriate numerical tools. However, the fast advancement in computer technology in recent years has allowed for the development of efficient numerical methods in this field.

In the present work, we focus on the widely used *interior-point method* [13, 14, 37, 54]. Commonly used codes based on interior-point methods are IPOPT [48–50], LOQO [9, 17, 44] and KNITRO [12, 51]. Comparative studies can be found in e.g. [10, 32, 48] and a valuable commented overview of existing optimization codes is given in [31]. In addition, in the last years the program MOSEK [7, 8] came into the picture of direct methods and has been applied for both (piecewise) linear and second-order conic problems, e.g. [11, 16, 22, 26, 36, 43] at least for reference solutions.

All of the above mentioned programs have already proven their abilities and robustness. Nonetheless, independent interior-point algorithms have been developed by several authors, e.g. [2, 18, 21, 23, 34, 35, 46, 47]. Compared to the above mentioned general codes, these algorithms are distinguished by problem-taylored solution strategies. Especially in the application to direct methods this is highly relevant because of the usually high number of variables and subsidiary conditions.

In [40–42] an alternative interior-point algorithm has been presented, focusing on both the reduction of running time on the one hand side and robustness on the other one. This is achieved by tayloring the formulation of the problem as well as the solution procedure to the specific problem of shakedown analysis for von Mises-type materials. In this paper, the underlying theory of this algorithm is presented, where the formulation is extended for the general case of arbitrary finite numbers of loading cases. Here, focus is laid on a closed-form and consistent presentation. Moreover, some numerical aspects are investigated, which are used to guarantee convergence of the algorithm.

2 The Statical Shakedown Theorem

In this paper, the statical shakedown approach by Melan [28, 29] is used to determine the shakedown factor α_{SD}, which is the maximum loading factor α such that the system does neither fail due to instantaneous or incremental plastic collapse nor due to alternating plasticity.

Melan's shakedown theorem states that shakedown occurs if one can find a loading factor $\alpha > 1$ and a time-independent residual stress field $\bar{\boldsymbol{\rho}}$ whose superposition with all possible elastic stress fields $\alpha \boldsymbol{\sigma}^E$ within the associated loading domain Ω satisfies the yield condition $F \leq 0$ at any time t and in any point $\boldsymbol{x} \in V$ of the volume V of the structure.

This theorem can be expressed as an optimization problem for the loading factor α, which can be used for the determination of the shakedown factor α_{SD}.

$$(\mathscr{P}_{Melan}) \qquad \max \alpha$$

$$\int_V \delta \boldsymbol{\varepsilon}^E : \bar{\boldsymbol{\rho}}\, dV = 0 \tag{1a}$$

$$F\left(\alpha \boldsymbol{\sigma}^E + \bar{\boldsymbol{\rho}}; \sigma_Y\right) \leq 0 \tag{1b}$$

In the following subsections, the subsidiary conditions Eqs. (1a) and (1b) will be further investigated.

2.1 Discretization of the Residual Stress Field

As already stated above, the total stresses $\boldsymbol{\sigma}$ are decomposed into the residual stress field $\bar{\boldsymbol{\rho}}$ which is induced by the evolution of plastic deformation and the purely elastic stress field $\boldsymbol{\sigma}^E$ which would occur in a purely elastic reference body under the same conditions and loading.

$$\boldsymbol{\sigma} = \boldsymbol{\sigma}^E + \bar{\boldsymbol{\rho}} \tag{2}$$

The condition (1a) ensures that the residual stress field $\bar{\boldsymbol{\rho}}$ is self-equilibrated. This is necessary, because the external loading is in equilibrium with the elastic reference stress field $\boldsymbol{\sigma}^E$ solely.

Using the Finite Element Method (FEM), the elastic displacement field $\boldsymbol{u}^E$ is expressed by appropriate shape functions $\boldsymbol{N}$ and the vector of nodal displacements $\boldsymbol{u}_K^E$. In analogy, we express the virtual elastic displacement field $\delta \boldsymbol{u}^E$ by the same shape functions $\boldsymbol{N}$ and the vector of nodal virtual displacements $\delta \boldsymbol{u}_K^E$.

$$\boldsymbol{u}^E = \boldsymbol{N} \cdot \boldsymbol{u}_K^E \quad \text{and} \quad \delta \boldsymbol{u}^E = \boldsymbol{N} \cdot \delta \boldsymbol{u}_K^E \tag{3}$$

According to Eq. (3), the elastic strain field $\boldsymbol{\varepsilon}^E$ and the virtual elastic strain field $\delta \boldsymbol{\varepsilon}^E$ can be expressed by $\boldsymbol{u}_K^E$ and $\delta \boldsymbol{u}_K^E$, respectively, introducing the differentiation matrix $\boldsymbol{B}$.

$$\boldsymbol{\varepsilon}^E = \frac{1}{2}\left(\nabla \boldsymbol{u}^E + \boldsymbol{u}^E \nabla\right) = \boldsymbol{B} \cdot \boldsymbol{u}_K^E \tag{4}$$

$$\delta \boldsymbol{\varepsilon}^E = \frac{1}{2}\left(\nabla \delta \boldsymbol{u}^E + \delta \boldsymbol{u}^E \nabla\right) = \boldsymbol{B} \cdot \delta \boldsymbol{u}_K^E \tag{5}$$

Substituting Eq. (4) into Eq. (1a) reads:

$$\int_V \delta \boldsymbol{\varepsilon}^E : \bar{\boldsymbol{\rho}}\, dV = \delta \boldsymbol{u}_K^E \cdot \int_V \boldsymbol{B}(\boldsymbol{x}) : \bar{\boldsymbol{\rho}}\, dV \stackrel{!}{=} 0 \quad \Longrightarrow \quad \int_V \boldsymbol{B}(\boldsymbol{x}) : \bar{\boldsymbol{\rho}}\, dV \stackrel{!}{=} \boldsymbol{0} \tag{6}$$

Using the Gauss method, the integration in Eq. (6) is carried out numerically. The residual stresses $\bar{\boldsymbol{\rho}}_r$ are then evaluated in the Gaussian points GP. The weighting factors, the matrix $\boldsymbol{B}$ and the Jacobian of each element are merged into the equilibrium

matrices $\mathbb{C}_r$, which leads to the following formulation.

$$\int_V \boldsymbol{B}(\boldsymbol{x}) : \bar{\boldsymbol{\rho}}\, dV =: \sum_{r=1}^{NG} \mathbb{C}_r \cdot \bar{\boldsymbol{\rho}}_r \stackrel{!}{=} \mathbf{0} \tag{7}$$

As can be seen in Eq. (7), the given derivation converts Eq. (1a) into a system of linear equations for the residual stresses $\bar{\boldsymbol{\rho}}_r$ in the Gaussian points. The equilibrium matrices $\mathbb{C}_r \in \mathbb{R}^{m_E \times 6}$ depend only on the geometry of the system and the applied element type and take into account the kinematical boundary conditions. Their dimension is $m_E = 3NK - NBC$, where NK is the total number of nodes and NBC the number of kinematical boundary conditions.

2.2 Description of the Loading Domain

The given loads P_ℓ, $\ell \in [1, NL]$, span a convex polyhedral loading domain Ω with $NC = 2^{NL}$ corners in the NL-dimensional loading space. Each of the loads varies independently in the range described by the factors μ_ℓ^- and μ_ℓ^+.

$$\mu_\ell^- P_0 \leq P_\ell \leq \mu_\ell^+ P_0 \tag{8}$$

The loading domain Ω can thereby be expressed as follows.

$$\Omega = \left\{ P(\boldsymbol{x}, t) \;\middle|\; P(\boldsymbol{x}, t) = \sum_{\ell=1}^{NL} \mu_\ell(t) P_0(\boldsymbol{x}),\ \forall \mu_\ell \in \left[\mu_\ell^-; \mu_\ell^+\right] \right\} \tag{9}$$

As shown in [20], it is sufficient to only consider the corners of the loading domain in order to ensure that the system will shake down for all possible loading paths contained within Ω. The time-dependence of $\boldsymbol{\sigma}^E$ can thus be expressed as a dependence of the considered corner $j \in [1, NC]$ of the loading domain. Thereby, the optimization problem is transformed into the following one.

$$(\mathscr{P}_{NC}) \qquad \alpha_{SD} = \max \alpha$$

$$\sum_{r=1}^{NG} \mathbb{C}_r \cdot \bar{\boldsymbol{\rho}}_r = \mathbf{0} \tag{10a}$$

$$\forall r \in [1, NG],\ \forall j \in [1, NC]:$$

$$F\left(\alpha \boldsymbol{\sigma}_r^{E,j} + \bar{\boldsymbol{\rho}}_r, \sigma_{Y,r}\right) \leq 0 \tag{10b}$$

In order to solve the optimization problem $(\mathscr{P}_{NC})$, it is necessary to express the elastic stresses $\boldsymbol{\sigma}_r^{E,j}$ in the considered corner j in dependence of the elastic stresses $\boldsymbol{\sigma}_{r,l}^E$ as a result of the loading case l, which can be computed by standard

FEM software. This is done by introducing matrices $\boldsymbol{U} \in \mathbb{R}^{NC \times NL}$ with entries U_{jl}, where $j \in [1, NC]$ and $l \in [1, NL]$.

$$\boldsymbol{\sigma}_r^{E,j} = \sum_{l=0}^{NL} U_{jl} \boldsymbol{\sigma}_{r,l}^E \tag{11}$$

Thereby, each row of the matrices $\boldsymbol{U}$ represents the coordinates of one corner of the loading domain in the NL-dimensional loading space—scaled with the load P_0. Thus, the introduction of $\boldsymbol{U}$ requires the definition of the corners of the loading domain with the given factors μ_i^- and μ_i^+ as introduced in Eq. (8).

Note, that this formulation holds for both mechanical and thermal loading, as long as all material parameters are considered as temperature-independent. Once the elastic reference stress field is computed, it is irrelevant by which loading type it has been induced. The loading domain Ω then contains the domain of mechanical loading Ω_M as well as the domain of thermal loading Ω_T, as introduced in [40].

2.3 The von Mises Yield Criterion

For the case of one- and two-dimensional loading spaces, the following transformations have been already investigated in [1, 2, 18]. For the sake of a generalized and consistent formulation, we extend these derivations for the case of arbitrary finite numbers NL.

The yield condition Eq. (1b) has to be satisfied for all Gaussian points $r \in [1, NG]$ and all corners of the loading domain $j \in [1, NC]$. In order to allow for the use of different materials in the structure the yield stress $\sigma_{Y,r}$ can be independently attributed to each Gaussian point r.

$$\forall r \in [1, NG],\ \forall j \in [1, NC]: \quad F\left(\alpha \boldsymbol{\sigma}_r^{E,j} + \bar{\boldsymbol{\rho}}_r; \sigma_{Y,r}\right) \leq 0 \tag{12}$$

In this work, the von Mises yield criterion is used.

$$\begin{aligned} F\left(\boldsymbol{\sigma}_r^j; \sigma_{Y,r}\right) = &\left(\sigma_{r,1}^j - \sigma_{r,2}^j\right)^2 + \left(\sigma_{r,2}^j - \sigma_{r,3}^j\right)^2 + \left(\sigma_{r,3}^j - \sigma_{r,1}^j\right)^2 \\ &+ 6\left(\sigma_{r,4}^j\right)^2 + 6\left(\sigma_{r,5}^j\right)^2 + 6\left(\sigma_{r,6}^j\right)^2 - 2\sigma_{Y,r}^2 \end{aligned} \tag{13}$$

We introduce the transformation matrix $\boldsymbol{T}$ and the variables $\boldsymbol{p}_r^j$.

$$\boldsymbol{\sigma}_r^j = \boldsymbol{T} \cdot \boldsymbol{p}_r^j, \quad \text{where} \quad \boldsymbol{T} = \frac{1}{2\sqrt{6}} \begin{pmatrix} \sqrt{6} & \sqrt{6} & \sqrt{6} & & & \\ -\sqrt{6} & \sqrt{6} & \sqrt{6} & & & \\ -\sqrt{6} & -\sqrt{6} & \sqrt{6} & & & \\ & & & 2 & & \\ & & & & 2 & \\ & & & & & 2 \end{pmatrix} \tag{14}$$

Then, the yield condition Eq. (13) can be expressed with $\boldsymbol{p}_r^j$.

$$F\left(\boldsymbol{p}_r^j;\sigma_{Y,r}\right) = \left(p_{r,1}^j\right)^2 + \left(p_{r,2}^j\right)^2 + \left(p_{r,1}^j + p_{r,2}^j\right)^2 + 6\left(p_{r,4}^j\right)^2 + 6\left(p_{r,5}^j\right)^2 + 6\left(p_{r,6}^j\right)^2 - 2\sigma_{Y,r}^2 \tag{15}$$

The third component $p_{r,3}^j$ of the vector $\boldsymbol{p}_r^j$ does not enter the yield condition in this form. Thus, it is extracted from the problem, reducing the dimensions of the vectors from six of $\boldsymbol{p}_r^j$ to five of $\bar{\boldsymbol{p}}_r^j$.

$$\bar{\boldsymbol{p}}_r^j = \begin{pmatrix} \bar{p}_{r,1}^j \\ \bar{p}_{r,2}^j \\ \bar{p}_{r,3}^j \\ \bar{p}_{r,4}^j \\ \bar{p}_{r,5}^j \end{pmatrix} = \begin{pmatrix} p_{r,1}^j \\ p_{r,2}^j \\ p_{r,4}^j \\ p_{r,5}^j \\ p_{r,6}^j \end{pmatrix} \quad \text{and} \quad v_r^j = p_{r,3}^j \tag{16}$$

The extracted values $v_r^j = p_{r,3}^j$ of all Gaussian points $r \in [1, NG]$ are merged into the vector $\boldsymbol{v}^j = v_r^j \boldsymbol{e}_r$.

$$\boldsymbol{v}^j = \begin{pmatrix} v_1^j \\ \vdots \\ v_r^j \\ \vdots \\ v_{NG}^j \end{pmatrix} = \begin{pmatrix} p_{1,3}^j \\ \vdots \\ p_{r,3}^j \\ \vdots \\ p_{NG,3}^j \end{pmatrix} \in \mathbb{R}^{NG} \tag{17}$$

Introducing the matrix $\boldsymbol{L}^T$, the yield function can be expressed by the Euclidean vector norm of the vector $\boldsymbol{u}_r^j = \boldsymbol{L}^T \cdot \bar{\boldsymbol{p}}_r^j$.

$$F\left(\boldsymbol{u}_r^j;\sigma_{Y,r}\right) = \left\|\boldsymbol{L}^T \cdot \bar{\boldsymbol{p}}_r^j\right\|^2 - 2\sigma_{Y,r}^2 = \left\|\boldsymbol{u}_r^j\right\|^2 - 2\sigma_{Y,r}^2 \tag{18a}$$

where

$$\boldsymbol{L}^T = \frac{1}{\sqrt{2}} \begin{pmatrix} 2 & \frac{1}{\sqrt{3}} & & & \\ & & \sqrt{2} & & \\ & & & \sqrt{2} & \\ & & & & \sqrt{2} \end{pmatrix} \tag{18b}$$

These transformations lead to a compact formulation of the yield condition, as one can see from Eq. (18a). Moreover, the yield criterion is expressed in only five variable components for each corner of the loading domain and for each Gaussian point instead of six components as in Eq. (13).

According to the new formulation of the yield condition in the variables $\boldsymbol{u}_r^j$, the condition (7) for the residual stresses has to be transformed as well.

$$\sum_{r=1}^{NG} \mathbb{C}_r \cdot \bar{\boldsymbol{\rho}}_r = \sum_{r=1}^{NG} \mathbb{C}_r \cdot \left(\boldsymbol{\sigma}_r^j - \alpha \boldsymbol{\sigma}_r^{E,j}\right) \stackrel{!}{=} \mathbf{0} \tag{19}$$

Thereby, the time-independence of the residual stresses is not accounted for anymore and thus has to be re-injected into the problem. The fact that $\bar{\boldsymbol{\rho}}$ is constant with time implies that it is independent of the considered corner j of the loading domain. Thereby, the stresses in the different corners of the loading domain can be linked to each other.

$$\bar{\boldsymbol{\rho}}_r = \boldsymbol{\sigma}_r^j - \alpha \boldsymbol{\sigma}_r^{E,j} = const(j) = \boldsymbol{\sigma}_r^{j+1} - \alpha \boldsymbol{\sigma}_r^{E,j+1} \tag{20a}$$

$$\boldsymbol{\sigma}_r^{j+1} = \boldsymbol{\sigma}_r^j - \alpha\left(\boldsymbol{\sigma}_r^{E,j} - \boldsymbol{\sigma}_r^{E,j+1}\right), \quad \forall j \in [1, NC-1] \tag{20b}$$

With Eq. (20b) it is clear that the condition (19) is satisfied for all possible j if there exists at least one j which satisfies it. Thus, Eq. (19) is rewritten for one arbitrarily chosen corner of the loading domain $j = 1$.

$$\sum_{r=1}^{NG} \mathbb{C}_r \cdot \left(\boldsymbol{\sigma}_r^1 - \alpha \boldsymbol{\sigma}_r^{E,1}\right) \stackrel{!}{=} \mathbf{0} \tag{21}$$

Recalling Eq. (14), we substitute the stresses $\boldsymbol{\sigma}_r^1$ from Eq. (21), where $\bar{\boldsymbol{T}} \in \mathbb{R}^{5\times 6}$ denotes the matrix $\boldsymbol{T}$ without the third column $\boldsymbol{T}_3 \in \mathbb{R}^6$.

$$\begin{aligned}\sum_{r=1}^{NG} \mathbb{C}_r \cdot \left(\boldsymbol{\sigma}_r^1 - \alpha \boldsymbol{\sigma}_r^{E,1}\right) &= \sum_{r=1}^{NG} \mathbb{C}_r \cdot \left[\left(\bar{\boldsymbol{T}} \cdot \bar{\boldsymbol{p}}_r^1 + v_r^1 \boldsymbol{T}_3\right) - \alpha \boldsymbol{\sigma}_r^{E,1}\right] \\ &= \sum_{r=1}^{NG} \left[\mathbb{C}_r \cdot \bar{\boldsymbol{T}} \cdot \boldsymbol{L}^{-T} \cdot \boldsymbol{u}_r^1 + v_r^1 \mathbb{C}_r \cdot \boldsymbol{T}_3 - \alpha \mathbb{C}_r \cdot \boldsymbol{\sigma}_r^{E,1}\right] \end{aligned} \tag{22}$$

We introduce the vectors $\boldsymbol{u}^1$ and $\boldsymbol{b}$ as well as the matrices $\tilde{\boldsymbol{A}}$ and $\tilde{\boldsymbol{B}}$.

$$\boldsymbol{u}^1 = \left[\boldsymbol{u}_1^1, \ldots, \boldsymbol{u}_r^1, \ldots, \boldsymbol{u}_{NG}^1\right]^T \in \mathbb{R}^{5NG} \tag{23}$$

$$\boldsymbol{b} = \sum_{r=1}^{NG} \mathbb{C}_r \cdot \boldsymbol{\sigma}_r^{E,1} \in \mathbb{R}^{m_E} \tag{24}$$

$$\tilde{\boldsymbol{A}} = \left[\mathbb{C}_1 \cdot \bar{\boldsymbol{T}} \cdot \boldsymbol{L}^{-T} | \ldots | \mathbb{C}_r \cdot \bar{\boldsymbol{T}} \cdot \boldsymbol{L}^{-T} | \ldots | \mathbb{C}_{NG} \cdot \bar{\boldsymbol{T}} \cdot \boldsymbol{L}^{-T}\right] \in \mathbb{R}^{m_E \times 5NG} \tag{25}$$

$$\tilde{\boldsymbol{B}} = \left[\mathbb{C}_1 \cdot \boldsymbol{T}_3 | \ldots | \mathbb{C}_r \cdot \boldsymbol{T}_3 | \ldots | \mathbb{C}_{NG} \cdot \boldsymbol{T}_3\right] \in \mathbb{R}^{m_E \times NG} \tag{26}$$

Thereby, we can rewrite Eq. (22) as follows.

$$\sum_{r=1}^{NG} \mathbb{C}_r \cdot \left(\boldsymbol{\sigma}_r^1 - \alpha \boldsymbol{\sigma}_r^{E,1}\right) = \tilde{\boldsymbol{A}} \cdot \boldsymbol{u}^1 + \tilde{\boldsymbol{B}} \cdot \boldsymbol{v}^1 - \alpha \boldsymbol{b} \stackrel{!}{=} \boldsymbol{0} \tag{27}$$

For a consistent formulation, Eq. (20b) has to be expressed in the variables $\boldsymbol{u}_r^j$ and v_r^j as well. Therefore, the stresses $\boldsymbol{\sigma}_r^j$ are substituted using Eq. (14).

$$\boldsymbol{p}_r^{j+1} = \boldsymbol{p}_r^j - \alpha \boldsymbol{T}^{-1} \cdot \left(\boldsymbol{\sigma}_r^{E,j} - \boldsymbol{\sigma}_r^{E,j+1}\right) \tag{28}$$

The third component is separated from this equation. Here, $\boldsymbol{T}_3^{-1}$ denotes the third row of the matrix $\boldsymbol{T}^{-1}$.

$$\boldsymbol{u}_r^{j+1} = \boldsymbol{u}_r^j - \alpha \boldsymbol{L}^T \cdot \bar{\boldsymbol{T}}^{-1} \cdot \left(\boldsymbol{\sigma}_r^{E,j} - \boldsymbol{\sigma}_r^{E,j+1}\right) \tag{29}$$

$$v_r^{j+1} = v_r^j - \alpha \boldsymbol{T}_3^{-1} \cdot \left(\boldsymbol{\sigma}_r^{E,j} - \boldsymbol{\sigma}_r^{E,j+1}\right) \tag{30}$$

Using Eqs. (18a), (27), (29) and (30) together with the definition of $(\mathscr{P}_{Melan})$, the optimization problem can be represented in the following formulation $(\mathscr{P}_{Melan})^*$.

$$(\mathscr{P}_{Melan})^* \qquad \max \alpha$$

$$\tilde{\boldsymbol{A}} \cdot \boldsymbol{u}^1 + \tilde{\boldsymbol{B}} \cdot \boldsymbol{v}^1 - \alpha \boldsymbol{b} = \boldsymbol{0} \tag{31a}$$

$$\forall r \in [1, NG],\ \forall j \in [1, NC-1]:$$

$$\boldsymbol{u}_r^{j+1} = \boldsymbol{u}_r^j - \alpha \boldsymbol{L}^T \cdot \bar{\boldsymbol{T}}^{-1} \cdot \left(\boldsymbol{\sigma}_r^{E,j} - \boldsymbol{\sigma}_r^{E,j+1}\right) \tag{31b}$$

$$v_r^{j+1} = v_r^j - \alpha \boldsymbol{T}_3^{-1} \cdot \left(\boldsymbol{\sigma}_r^{E,j} - \boldsymbol{\sigma}_r^{E,j+1}\right) \tag{31c}$$

$$\left\|\boldsymbol{u}_r^j\right\|_2^2 - 2\sigma_{Y,r}^2 \leq 0, \quad \forall r \in [1, NG],\ \forall j \in [1, NC] \tag{31d}$$

Since for $j > 1$ the variables $\boldsymbol{v}^j$ occur only in the condition (31c) and are therefore independent of any of the other variables, this condition can be removed from the optimization process. However, once the values $\boldsymbol{v}^1$ are determined by solving the optimization problem, it can be used to compute the $\boldsymbol{v}^j$. For the sake of simplicity, we denote $\boldsymbol{v} := \boldsymbol{v}^1$ and omit the upper index in the following.

Moreover, we abbreviate $\boldsymbol{\gamma}_r^j$ in Eq. (31b) and achieve the generalized formulation of the optimization problem.

$$(\mathscr{P}_{IPDCA}) \qquad \max \alpha$$

$$\tilde{\boldsymbol{A}} \cdot \boldsymbol{u}^1 + \tilde{\boldsymbol{B}} \cdot \boldsymbol{v} - \alpha \boldsymbol{b} = \boldsymbol{0} \tag{32a}$$

$$\boldsymbol{u}_r^{j+1} = \boldsymbol{u}_r^j - \alpha \boldsymbol{\gamma}_r^j, \quad \forall r \in [1, NG],\ \forall j \in [1, NC-1] \tag{32b}$$

$$\left\|\boldsymbol{u}_r^j\right\|_2^2 - 2\sigma_{Y,r}^2 \leq 0, \quad \forall r \in [1, NG],\ \forall j \in [1, NC] \tag{32c}$$

where:

$$\boldsymbol{\gamma}_r^j = \boldsymbol{L}^T \cdot \bar{\boldsymbol{T}}^{-1} \cdot \left(\boldsymbol{\sigma}_r^{E,j} - \boldsymbol{\sigma}_r^{E,j+1}\right) \tag{32d}$$

2.4 Condensation of the Optimization Problem

The solution vector of the problem ($\mathscr{P}_{IPDCA}$) consists of the ($5NG \cdot NC$) unknowns $\boldsymbol{u}_r^j$, the NG unknowns $\boldsymbol{v}$ and the shakedown factor α. Thus, the total number of variables is ($5NG \cdot NC + NG + 1$).

The number of equality constraints from Eq. (32a) and Eq. (32b) is increased by the presented transformations to the total amount of ($m_E + 5NG \cdot (NC - 1)$), whereas the number of inequality constraints (32c) remains unchanged $m_I = NG \cdot NC$.

This formulation can be condensed through expressing the variables $\boldsymbol{u}_r^{j+1}$ in dependence of $\boldsymbol{u}_r^1$ in the first corner of the loading domain instead of the dependence of the previous corner $\boldsymbol{u}_r^j$. As before, it is an arbitrary choice which of the corners of the loading domain is considered to be the first one, $j = 1$.

$$\begin{aligned} &\forall r \in [1, NG],\ \forall j \in [1, NC-1]: \\ &\boldsymbol{u}_r^{j+1} = \boldsymbol{u}_r^1 - \alpha \boldsymbol{L}^T \cdot \bar{\boldsymbol{T}}^{-1} \cdot \left(\boldsymbol{\sigma}_r^{E,1} - \boldsymbol{\sigma}_r^{E,j+1}\right) \end{aligned} \tag{33}$$

Since for $j > 1$ the variables $\boldsymbol{u}_r^j$ occur only in Eq. (32c) and Eq. (33) but not in Eq. (32a), they can be removed from the optimization process by substituting Eq. (33) into Eq. (32c). However, once the values $\boldsymbol{u}_r^1$ are determined by solving the optimization problem, Eq. (33) can be used to compute the $\boldsymbol{u}_r^j$. For the sake of simplicity, we denote $\boldsymbol{u}_r := \boldsymbol{u}_r^1$ and omit the upper index in the following.

The optimization problem can thereby be expressed as follows:

$$(\mathscr{P}_{IPDCA})^* \qquad \min f(\boldsymbol{x}) = -\alpha$$

$$\tilde{\boldsymbol{A}} \cdot \boldsymbol{u} + \tilde{\boldsymbol{B}} \cdot \boldsymbol{v} - \alpha \boldsymbol{b} = \boldsymbol{0} \tag{34a}$$

$$\forall r \in [1, NG],\ \forall j \in [1, NC]:$$

$$\left\| \boldsymbol{u}_r - \alpha \boldsymbol{a}_r^j \right\|_2^2 - 2\sigma_{Y,r}^2 \leq 0 \tag{34b}$$

where:

$$\boldsymbol{a}_r^j = \boldsymbol{L}^T \cdot \bar{\boldsymbol{T}}^{-1} \cdot \left(\boldsymbol{\sigma}_r^{E,1} - \boldsymbol{\sigma}_r^{E,j}\right) \in \mathbb{R}^5 \tag{34c}$$

$$\boldsymbol{x} = [\boldsymbol{u}_1, \ldots, \boldsymbol{u}_r, \ldots, \boldsymbol{u}_{NG}, \boldsymbol{v}, \alpha]^T \in \mathbb{R}^{6NG+1} \tag{34d}$$

This reformulation leads to a reduction of the dimension of the problem. In particular, the number of unknowns is reduced to $n = 6NG + 1$. Moreover, the number

of equality constraints is reduced to m_E, whereas the number of inequality constraints remains unchanged m_I. Furthermore, the condensation of the optimization problem can be used for a more efficient solution strategy, later on, as proposed in [42].

3 Solution of the Optimization Problem by Interior-Point Method

For the purpose of clarity of the presentation, the problem $(\mathscr{P}_{IPDCA})^*$ is rewritten in the following form.

$$
\begin{aligned}
(\mathscr{P}_{IP}) \qquad & \min f(\boldsymbol{x}) = -\alpha \\
& \boldsymbol{A} \cdot \boldsymbol{x} = \boldsymbol{0} && \text{(35a)} \\
& \boldsymbol{c}_I(\boldsymbol{x}) \geq \boldsymbol{0} && \text{(35b)} \\
& \boldsymbol{x} \in \mathbb{R}^n && \text{(35c)}
\end{aligned}
$$

where:

$$
\boldsymbol{A} = \left[\tilde{\boldsymbol{A}} | \tilde{\boldsymbol{B}} | -\boldsymbol{b}\right] \in \mathbb{R}^{m_E \times n} \tag{35d}
$$

$$
\boldsymbol{c}_I(\boldsymbol{x}) = 2\sigma_{Y,r}^2 - \left\| \boldsymbol{u}_r - \alpha \boldsymbol{a}_r^j \right\|_2^2 \in \mathbb{R}^{m_I} \tag{35e}
$$

The objective function $f(\boldsymbol{x})$ is linear and therefore both convex and concave at the same time. The equality constraints (35a) are affine linear, whereas the inequality constraints (35b) are nonlinear but concave. Thus, the optimization problem $(\mathscr{P}_{IP})$ is nonlinear convex. In addition, it is regular because the Slater condition is satisfied by definition. For the solution of nonlinear convex optimization problems, the interior-point method has already proven to be efficient, see e.g. the references given in Sect. 1.

3.1 Introduction of the Barrier Function

The subsidiary conditions define a feasible region for the solution candidates of the optimization problem. The starting point is chosen to be inside of the feasible region. Then, the key idea of the interior-point method consists of the introduction of barriers, which preclude the solution candidate from leaving the interior region of feasible solutions in the course of the iteration procedure.

The objective function is perturbed by these barrier terms such that the function value increases the closer the solution tends towards the boundary. The barrier terms are weighted by the barrier parameter μ which tends to zero during the iteration.

Before the barriers are introduced, the subsidiary conditions are reformulated. The inequality constraints (35b) are converted into equality constraints through the introduction of nonnegative slack variables $\boldsymbol{w} \in \mathbb{R}_+^{m_I}$.

$$\boldsymbol{c}_I(\boldsymbol{x}) \geq \boldsymbol{0} \quad \longrightarrow \quad \boldsymbol{c}_I(\boldsymbol{x}) - \boldsymbol{w} = \boldsymbol{0} \quad \wedge \quad \boldsymbol{w} \geq \boldsymbol{0} \tag{36}$$

In addition, split variables $\boldsymbol{y}$ and $\boldsymbol{z}$ are introduced, because otherwise the unboundedness of the free variable $\boldsymbol{x}$ in Eq. (35c) would lead to instabilities as shown in e.g. [30, 45].

$$\boldsymbol{x} \in \mathbb{R}^n \quad \longrightarrow \quad \boldsymbol{x} - \boldsymbol{y} + \boldsymbol{z} = \boldsymbol{0} \quad \wedge \quad \boldsymbol{y} \geq \boldsymbol{0}, \boldsymbol{z} \geq \boldsymbol{0} \tag{37}$$

For these reformulated constraints (36) and (37), we introduce logarithmic barrier terms into the objective function. The slack and split variables lead to the following barrier objective function $f_\mu(\boldsymbol{x}, \boldsymbol{y}, \boldsymbol{z}, \boldsymbol{w})$.

$$f_\mu(\boldsymbol{x}, \boldsymbol{y}, \boldsymbol{z}, \boldsymbol{w}) = f(\boldsymbol{x}) - \mu \left[\sum_{i=1}^{n} \log(y_i) + \sum_{i=1}^{n} \log(z_i) + \sum_{j=1}^{m_I} \log(w_j) \right] \tag{38}$$

The resulting optimization problem taking into account the barrier terms is expressed in $(\mathscr{P}_\mu)$.

$$(\mathscr{P}_\mu) \qquad \min f_\mu(\boldsymbol{x}, \boldsymbol{y}, \boldsymbol{z}, \boldsymbol{w}) = -\alpha - \mu \left[\sum_{i=1}^{n} \log(y_i) + \sum_{i=1}^{n} \log(z_i) + \sum_{j=1}^{m_I} \log(w_j) \right]$$

$$\boldsymbol{A} \cdot \boldsymbol{x} = \boldsymbol{0} \tag{39a}$$

$$\boldsymbol{c}_I(\boldsymbol{x}) - \boldsymbol{w} = \boldsymbol{0} \tag{39b}$$

$$\boldsymbol{x} - \boldsymbol{y} + \boldsymbol{z} = \boldsymbol{0} \tag{39c}$$

$$\boldsymbol{w} > \boldsymbol{0}, \ \boldsymbol{y} > \boldsymbol{0}, \ \boldsymbol{z} > \boldsymbol{0} \tag{39d}$$

Note, that the use of logarithmic barrier terms Eq. (38) forces the slack and the split variables to be strictly positive.

3.2 The Karush-Kuhn-Tucker Conditions

For regular convex optimization problems, the Karush-Kuhn-Tucker (KKT) optimality conditions [24] are both necessary and sufficient. The KKT state that a solution is optimal if and only if the Lagrange function $\mathscr{L}$ possesses a saddle point, $\nabla \mathscr{L} = \boldsymbol{0}$ in all variables. The Lagrangian of the problem $(\mathscr{P}_\mu)$ is given by the following formula, where $\boldsymbol{\lambda}_E \in \mathbb{R}^{m_E}$, $\boldsymbol{\lambda}_I \in \mathbb{R}_+^{m_I}$ and $\boldsymbol{s} \in \mathbb{R}_+^n$ are Lagrange multipliers.

Since $\boldsymbol{\lambda}_I$ as well as $\boldsymbol{s}$ are linked to the initial inequality constraints they have to be nonnegative, whereas the sign of $\boldsymbol{\lambda}_E$ is arbitrary.

$$\mathscr{L} = f_\mu(\boldsymbol{x}, \boldsymbol{y}, \boldsymbol{z}, \boldsymbol{w}) - \boldsymbol{\lambda}_E \cdot (\boldsymbol{A} \cdot \boldsymbol{x}) - \boldsymbol{\lambda}_I \cdot \big(\boldsymbol{c}_I(\boldsymbol{x}) - \boldsymbol{w}\big) - \boldsymbol{s} \cdot (\boldsymbol{x} - \boldsymbol{y} + \boldsymbol{z}) \tag{40}$$

The saddle point condition leads to the following system of equations (KKT_μ):

$$(KKT_\mu) \qquad \nabla_x \mathscr{L} = \nabla_x f(\boldsymbol{x}) - \boldsymbol{A}^T \cdot \boldsymbol{\lambda}_E - \boldsymbol{C}_I^T(\boldsymbol{x}) \cdot \boldsymbol{\lambda}_I - \boldsymbol{s} = \boldsymbol{0} \tag{41a}$$

$$\nabla_y \mathscr{L} = -\mu \boldsymbol{Y}^{-1} \cdot \boldsymbol{e} + \boldsymbol{s} = \boldsymbol{0} \tag{41b}$$

$$\nabla_z \mathscr{L} = -\mu \boldsymbol{Z}^{-1} \cdot \boldsymbol{e} - \boldsymbol{s} = \boldsymbol{0} \tag{41c}$$

$$\nabla_w \mathscr{L} = -\mu \boldsymbol{W}^{-1} \cdot \boldsymbol{e} + \boldsymbol{\lambda}_I = \boldsymbol{0} \tag{41d}$$

$$\nabla_{\lambda_E} \mathscr{L} = -(\boldsymbol{A} \cdot \boldsymbol{x}) = \boldsymbol{0} \tag{41e}$$

$$\nabla_{\lambda_I} \mathscr{L} = -\big(\boldsymbol{c}_I(\boldsymbol{x}) - \boldsymbol{w}\big) = \boldsymbol{0} \tag{41f}$$

$$\nabla_s \mathscr{L} = -(\boldsymbol{x} - \boldsymbol{y} + \boldsymbol{z}) = \boldsymbol{0} \tag{41g}$$

where:

$$\boldsymbol{C}_I(\boldsymbol{x}) = \boldsymbol{c}_I(\boldsymbol{x}) \nabla_x \in \mathbb{R}^{m_I \times n}$$

Here and in the following, we denote the vector $\boldsymbol{e} = [1, 1, \ldots, 1]^T$ in proper dimension and the matrices $\boldsymbol{Y} = diag(y_i) \in \mathbb{R}^{n \times n}$, $\boldsymbol{Z} = diag(z_i) \in \mathbb{R}^{n \times n}$ and $\boldsymbol{W} = diag(w_j) \in \mathbb{R}^{m_I \times m_I}$. As proposed in [1], we introduce the new variable $\boldsymbol{r}$ and the according diagonal matrix $\boldsymbol{R} = diag(r_i)$ in order to ensure consistency during the iteration process.

$$\boldsymbol{r} = -\boldsymbol{s} \tag{42}$$

Since both variables $\boldsymbol{r}$ and $\boldsymbol{s}$ are non-negative by definition, they are thereby forced to be sequences tending to zero during the iteration. Furthermore, defining $\boldsymbol{S} = diag(s_i)$ and $\boldsymbol{\Lambda}_I = diag(\lambda_{I,j})$, the three Eqs. (41b)–(41d) are rearranged and multiplied by the matrixes $\boldsymbol{Y}$, $\boldsymbol{Z}$ and $\boldsymbol{W}$, respectively.

$$-\mu \boldsymbol{e} + \boldsymbol{Y} \cdot \boldsymbol{S} \cdot \boldsymbol{e} = \boldsymbol{0} \tag{43a}$$

$$-\mu \boldsymbol{e} + \boldsymbol{Z} \cdot \boldsymbol{R} \cdot \boldsymbol{e} = \boldsymbol{0} \tag{43b}$$

$$-\mu \boldsymbol{e} + \boldsymbol{W} \cdot \boldsymbol{\Lambda}_I \cdot \boldsymbol{e} = \boldsymbol{0} \tag{43c}$$

Merging all variables of the problem into the vector $\boldsymbol{\Pi} = [\boldsymbol{x}, \boldsymbol{y}, \boldsymbol{z}, \boldsymbol{w}, \boldsymbol{\lambda}_E, \boldsymbol{\lambda}_I, \boldsymbol{s}, \boldsymbol{r}]^T$, the resulting system of optimality constraints can be expressed by the func-

tion $\boldsymbol{F}_\mu(\boldsymbol{\Pi})$.

$$\boldsymbol{F}_\mu(\boldsymbol{\Pi}) = -\nabla\mathscr{L} = -\begin{pmatrix} -\nabla_x f(\boldsymbol{x}) + \boldsymbol{A}^T \cdot \boldsymbol{\lambda}_E + \boldsymbol{C}_I^T(\boldsymbol{x}) \cdot \boldsymbol{\lambda}_I + \boldsymbol{s} \\ \mu\boldsymbol{e} - \boldsymbol{Y} \cdot \boldsymbol{S} \cdot \boldsymbol{e} \\ \mu\boldsymbol{e} - \boldsymbol{Z} \cdot \boldsymbol{R} \cdot \boldsymbol{e} \\ \mu\boldsymbol{e} - \boldsymbol{W} \cdot \boldsymbol{\Lambda}_I \cdot \boldsymbol{e} \\ \boldsymbol{A} \cdot \boldsymbol{x} \\ \boldsymbol{c}_I(\boldsymbol{x}) - \boldsymbol{w} \\ \boldsymbol{x} - \boldsymbol{y} + \boldsymbol{z} \\ \boldsymbol{r} + \boldsymbol{s} \end{pmatrix} = \boldsymbol{0} \tag{44}$$

3.3 Solution of the Nonlinear Equation System

The optimality condition (44) constitutes a system of nonlinear equations, which is solved by use of Newton's method for a fixed value of the barrier parameter μ in each iteration step. The variables $\boldsymbol{\Pi}_{k+1}$ of the subsequent iteration step $k+1$ are computed from the variables $\boldsymbol{\Pi}_k$ of the previous one k and the step values $\Delta\boldsymbol{\Pi}_k$.

$$\boldsymbol{\Pi}_{k+1} = \boldsymbol{\Pi}_k + \boldsymbol{\Upsilon}_k \cdot \Delta\boldsymbol{\Pi}_k \tag{45}$$

Here, $\boldsymbol{\Upsilon}_k$ denotes a diagonal matrix of damping factors which might be necessary for the convergence of the algorithm. The meaning and construction of appropriate damping factors will be explained later. However, the step values $\Delta\boldsymbol{\Pi}_k$ are computed as solution of the following system of linearized equations.

$$\boldsymbol{J}(\boldsymbol{\Pi}_k) \cdot \Delta\boldsymbol{\Pi}_k = -\boldsymbol{F}_\mu(\boldsymbol{\Pi}_k) \tag{46}$$

where:

$$\boldsymbol{J}(\boldsymbol{\Pi}_k) = \boldsymbol{F}_\mu(\boldsymbol{\Pi})\nabla_{\boldsymbol{\Pi}}|_{\boldsymbol{\Pi}=\boldsymbol{\Pi}_k}$$

The Jacobian $\boldsymbol{J}(\boldsymbol{\Pi})$ of the function $\boldsymbol{F}_\mu(\boldsymbol{\Pi})$ as defined in Eq. (44) can be expressed as follows, where the subscription with k will be omitted in the following for the sake of clarity of the presentation.

$$\boldsymbol{J}(\boldsymbol{\Pi}) = \begin{pmatrix} \nabla_x^2\mathscr{L} & \boldsymbol{0} & \boldsymbol{0} & \boldsymbol{0} & -\boldsymbol{A}^T & -\boldsymbol{C}_I^T(\boldsymbol{x}) & -\boldsymbol{I}_n & \boldsymbol{0} \\ \boldsymbol{0} & \boldsymbol{S} & \boldsymbol{0} & \boldsymbol{0} & \boldsymbol{0} & \boldsymbol{0} & \boldsymbol{Y} & \boldsymbol{0} \\ \boldsymbol{0} & \boldsymbol{0} & \boldsymbol{R} & \boldsymbol{0} & \boldsymbol{0} & \boldsymbol{0} & \boldsymbol{0} & \boldsymbol{Z} \\ \boldsymbol{0} & \boldsymbol{0} & \boldsymbol{0} & \boldsymbol{\Lambda}_I & \boldsymbol{0} & \boldsymbol{W} & \boldsymbol{0} & \boldsymbol{0} \\ -\boldsymbol{A} & \boldsymbol{0} & \boldsymbol{0} & \boldsymbol{0} & \boldsymbol{0} & \boldsymbol{0} & \boldsymbol{0} & \boldsymbol{0} \\ -\boldsymbol{C}_I(\boldsymbol{x}) & \boldsymbol{0} & \boldsymbol{0} & \boldsymbol{I}_{m_I} & \boldsymbol{0} & \boldsymbol{0} & \boldsymbol{0} & \boldsymbol{0} \\ -\boldsymbol{I}_n & \boldsymbol{I}_n & -\boldsymbol{I}_n & \boldsymbol{0} & \boldsymbol{0} & \boldsymbol{0} & \boldsymbol{0} & \boldsymbol{0} \\ \boldsymbol{0} & \boldsymbol{0} & \boldsymbol{0} & \boldsymbol{0} & \boldsymbol{0} & \boldsymbol{0} & -\boldsymbol{I}_n & -\boldsymbol{I}_n \end{pmatrix} \tag{47}$$

Recalling the definition of the Lagrangian $\mathscr{L}$ in Eq. (40) and its first derivative $\nabla_x \mathscr{L}$ with respect to $\boldsymbol{x}$ from Eq. (41a) and considering that the objective function $f(\boldsymbol{x})$ is linear, the second derivative $\nabla_x^2 \mathscr{L}$ can be expressed as follows.

$$\nabla_x^2 \mathscr{L} = -\nabla_x^2 \big(\boldsymbol{c}_I(\boldsymbol{x}) \cdot \boldsymbol{\lambda}_I\big) = -\sum_{k=1}^{m_I} \big(\nabla_x^2 c_{I,k}(\boldsymbol{x})\big) \lambda_{I,k} =: \boldsymbol{Q}_I(\boldsymbol{\lambda}_I) \tag{48}$$

With Eqs. (44) and (46)–(48) the linearized system to be solved is clearly defined. It will now be condensed by successive elimination of those equations which include only invertible matrixes. The following variables are eliminated by substitution.

$$\Delta \boldsymbol{s} = -\boldsymbol{E}_1 \cdot \boldsymbol{b}_1 - \boldsymbol{E}_1 \cdot \Delta \boldsymbol{x} \tag{49}$$

$$\Delta \boldsymbol{y} = \mu \boldsymbol{S}^{-1} \cdot \boldsymbol{e} - \boldsymbol{y} - \boldsymbol{Y} \cdot \boldsymbol{S}^{-1} \cdot \Delta \boldsymbol{s} \tag{50}$$

$$\Delta \boldsymbol{r} = -\boldsymbol{r} - \boldsymbol{s} - \Delta \boldsymbol{s} \tag{51}$$

$$\Delta \boldsymbol{z} = \mu \boldsymbol{R}^{-1} \cdot \boldsymbol{e} - \boldsymbol{z} - \boldsymbol{Z} \cdot \boldsymbol{R}^{-1} \cdot \Delta \boldsymbol{r} \tag{52}$$

$$\Delta \boldsymbol{w} = \mu \boldsymbol{\Lambda}_I^{-1} \cdot \boldsymbol{e} - \boldsymbol{w} - \boldsymbol{E}_2 \cdot \Delta \boldsymbol{\lambda}_I \tag{53}$$

where:

$$\boldsymbol{b}_1 = \boldsymbol{x} + \boldsymbol{z} + \mu \big(\boldsymbol{R}^{-1} - \boldsymbol{S}^{-1}\big) \cdot \boldsymbol{e} + \boldsymbol{R}^{-1} \cdot \boldsymbol{Z} \cdot \boldsymbol{s}$$

$$\boldsymbol{E}_1 = \big(\boldsymbol{S}^{-1} \cdot \boldsymbol{Y} + \boldsymbol{R}^{-1} \cdot \boldsymbol{Z}\big)^{-1}$$

$$\boldsymbol{E}_2 = \boldsymbol{W} \cdot \boldsymbol{\Lambda}_I^{-1}$$

The resulting condensed system is given by Eq. (54).

$$\begin{pmatrix} -(\boldsymbol{Q}_I(\boldsymbol{\lambda}_I) + \boldsymbol{E}_1) & \boldsymbol{A}^T & \boldsymbol{C}_I^T(\boldsymbol{x}) \\ \boldsymbol{A} & \boldsymbol{0} & \boldsymbol{0} \\ \boldsymbol{C}_I(\boldsymbol{x}) & \boldsymbol{0} & \boldsymbol{E}_2 \end{pmatrix} \cdot \begin{pmatrix} \Delta \boldsymbol{x} \\ \Delta \boldsymbol{\lambda}_E \\ \Delta \boldsymbol{\lambda}_I \end{pmatrix} = \begin{pmatrix} \boldsymbol{d}_1 \\ \boldsymbol{d}_2 \\ \boldsymbol{d}_3 \end{pmatrix} \tag{54}$$

The right hand side values of this system are as follows.

$$\boldsymbol{d}_1 = \nabla_x f(\boldsymbol{x}) - \boldsymbol{A}^T \cdot \boldsymbol{\lambda}_E - \boldsymbol{C}_I^T(\boldsymbol{x}) \cdot \boldsymbol{\lambda}_I - \boldsymbol{s} + \boldsymbol{E}_1 \cdot \boldsymbol{b}_1 \tag{55a}$$

$$\boldsymbol{d}_2 = -\boldsymbol{A} \cdot \boldsymbol{x} \tag{55b}$$

$$\boldsymbol{d}_3 = -\boldsymbol{c}_I(\boldsymbol{x}) + \mu \boldsymbol{\Lambda}_I^{-1} \cdot \boldsymbol{e} \tag{55c}$$

4 Numerical Aspects

The new algorithm based on the improved formulation has already been briefly presented in [41], and some numerical aspects have been discussed in [40]. Here, we recapitulate some of these and add some new details.

The algorithm's mode of operation is illustrated in Fig. 1. As one can see, there exist two different iterations:

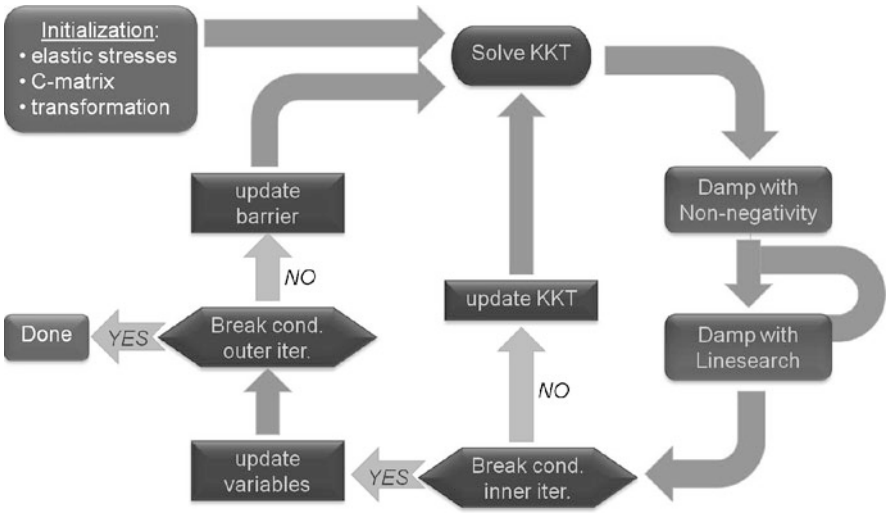

Fig. 1 Sketch of algorithm's mode of operation

- The ***outer iteration*** is the major loop in Fig. 1, where in each iteration step the barrier parameter μ is reduced in accordance with the update-rule. Thereby, during the outer iteration process, μ is a sequence tending to zero.
- The ***inner iteration*** is the minor loop in Fig. 1, which ensures that the approximate solution of the linearized system is in the close proximity of the exact solution, such that the KKT conditions are satisfied sufficiently accurate.

Since the full Newton step $\Delta \boldsymbol{\Pi}$ computed from Eq. (46) may happen to be too large, it has to be damped in these cases. This is done by a linesearch procedure, which actually is a third iteration within the outer and the inner one.

4.1 Starting Point Strategy

The choice of an admissible starting point is a critical issue when using interior-point methods. Fortunately, this does not hold for our specific problem because any solution vector $\boldsymbol{x}$ representing a stress state within the elastic limit domain is admissible. Thus, we compute the initial solution vector $\boldsymbol{x}_0$ from the elastic limit stresses. In order to stay inside of the strict interior of the elastic domain, these values are multiplied by the constant factor $\alpha_0 = 0.995$.

$$\boldsymbol{x}_0 = \boldsymbol{x}(\boldsymbol{\sigma} = \alpha_0 \boldsymbol{\sigma}_{el}) \tag{56}$$

With this choice for the initial solution vector, the condition (41e) is satisfied *a priori*. The other variables can be fitted such that the remaining conditions (41a)–(41g) are satisfied as well. Note, that one of the variables can be chosen arbitrarily.

Moreover, the condition (42) can not be satisfied by any choice of positive $\boldsymbol{r}_0$ and $\boldsymbol{s}_0$. This condition is necessary to enforce $\boldsymbol{r}$ and $\boldsymbol{s}$ to be sequences tending to zero during the iteration, though. Except of this, the starting point $\boldsymbol{\Pi}_0$ is feasible.

4.2 Solution of the System of Linearized Equations

When trying to solve the system Eq. (59), from numerical point of view there arise two critical issues linked to the question of definiteness of the coefficient matrix. The upper left block $(\boldsymbol{Q}_I(\boldsymbol{\lambda}_I) + \boldsymbol{E}_1)$ needs be positive definite in order to use a Cholesky-like factorization. In case that it is not positive definite, one possibility is the primal regularization, where perturbation terms are introduced to ensure positive definiteness, e.g. [17, 38, 39]. In the former formulation with IPDCA the decomposition of the objective function into a difference of convex functions (DC) acts like a certain primal regularization. The basics of the DC-approach can be followed in [4–6].

However, we will show in the following that primal regularization is not necessary for the specific class of optimization problems resulting from shakedown analysis under the mentioned circumstances. To do so, we recall the definition equation (48) of the matrix $\boldsymbol{Q}_I(\boldsymbol{\lambda}_I)$.

$$\boldsymbol{Q}_I(\boldsymbol{\lambda}_I) = -\sum_{k=1}^{m_I} \left(\nabla_x^2 c_{I,k}(\boldsymbol{x})\right) \lambda_{I,k} \tag{57}$$

Since all the inequality constraints $c_{I,k}(\boldsymbol{x})$ are concave, their Hessians $\nabla_x^2 c_{I,k}(\boldsymbol{x})$ are negative semidefinite by definition. The same holds when multiplying with $\lambda_{I,k}$ because the Lagrange multipliers linked to inequality constraints have to be non-negative. Thus, the matrix $\boldsymbol{Q}_I(\boldsymbol{\lambda}_I)$ is positive semidefinite. Since $\boldsymbol{E}_1$ is a diagonal matrix of only positive values, their sum $(\boldsymbol{Q}_I(\boldsymbol{\lambda}_I) + \boldsymbol{E}_1)$ has to be positive definite in any case. Thus, the primal regularization is not necessary.

The other issue to consider concerns the zero block in the 2-2-component. In general, the zero values on the diagonal of the matrix can lead to numerical instabilities. These instabilities can be avoided by use of dual regularization, as proposed in [1, 2] on the basis of e.g. [17, 38, 39]. There, a diagonal matrix with positive perturbations $\delta \boldsymbol{I}_{m_E}$ is added to the 2-2-component such that the system is stabilized. Note, that the convergence properties of the iterative process may be affected by this perturbation. As an option in the solution strategy, we have implemented an alternative approach as well. On the basis of the condensed formulation $(\mathscr{P}_{IPDCA})^*$, the system of linear equations (54) can be further reduced. For this purpose, we eliminate the third row and column of the coefficient matrix by substitution of $\Delta\boldsymbol{\lambda}_I$.

$$\Delta\boldsymbol{\lambda}_I = \boldsymbol{E}_2^{-1} \cdot (\boldsymbol{d}_3 - \boldsymbol{C}_I \cdot \Delta\boldsymbol{x}) \tag{58}$$

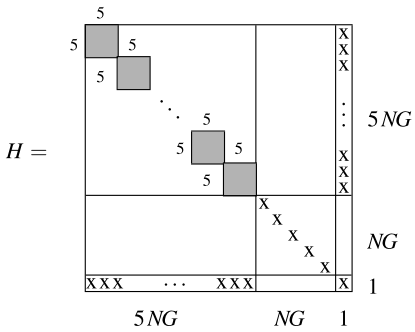

Fig. 2 Sparsity pattern of the matrix $\boldsymbol{H}$

The reduced system after substituting Eq. (58) into the first row reads as follows.

$$\begin{pmatrix} -\boldsymbol{H} & \boldsymbol{A}^T \\ \boldsymbol{A} & \boldsymbol{0} \end{pmatrix} \cdot \begin{pmatrix} \Delta \boldsymbol{x} \\ \Delta \boldsymbol{\lambda}_E \end{pmatrix} = \begin{pmatrix} \bar{\boldsymbol{d}}_1 \\ \boldsymbol{d}_2 \end{pmatrix} \tag{59}$$

where:

$$\boldsymbol{H} = \boldsymbol{Q}_I + \boldsymbol{E}_1 + \boldsymbol{C}_I^T \cdot \boldsymbol{E}_2^{-1} \cdot \boldsymbol{C}_I$$
$$\bar{\boldsymbol{d}}_1 = \boldsymbol{d}_1 - \boldsymbol{C}_I^T \cdot \boldsymbol{E}_2^{-1} \cdot \boldsymbol{d}_3$$

Note, that the matrix $\boldsymbol{C}_I^T \cdot \boldsymbol{E}_2^{-1} \cdot \boldsymbol{C}_I$ has a quadratic form and therefore is positive definite by definition. Thus, the matrix $\boldsymbol{H}$ is positive definite as well, following the reasoning on $(\boldsymbol{Q}_I(\boldsymbol{\lambda}_I) + \boldsymbol{E}_1)$ from above. Furthermore, we investigate the specific sparsity pattern of the matrix $\boldsymbol{H}$ as shown in Fig. 2.

In the range $i \in [1, 5NG]$ denoted by $\boldsymbol{H}_u$ in the following, all entries surround the diagonal block-wise in 5×5 blocks, whereas $\boldsymbol{H}_v$ in the range $i \in [5NG, 6NG]$ is diagonal. Denoting the last column in the range $i \in [1, 5NG]$ by $\boldsymbol{h}$ and the entry in the last column and last row by H_α, the matrix $\boldsymbol{H}$ can be presented as follows.

$$\boldsymbol{H} = \begin{pmatrix} \boldsymbol{H}_u & \boldsymbol{0} & \boldsymbol{h} \\ \boldsymbol{0} & \boldsymbol{H}_v & \boldsymbol{0} \\ \boldsymbol{h}^T & \boldsymbol{0} & H_\alpha \end{pmatrix}, \qquad \boldsymbol{H}_v \in \mathbb{R}^{NG \times NG} : diag \tag{60}$$

The shown sparsity pattern of $\boldsymbol{H}$ can be used to further reduce the system (59) by splitting of the solution vector $\Delta \boldsymbol{x}$, the right hand side vector $\bar{\boldsymbol{d}}_1$ and the matrix $\boldsymbol{A}$.

$$\Delta \boldsymbol{x} = \begin{pmatrix} \Delta \boldsymbol{u} \\ \Delta \boldsymbol{v} \\ \Delta \alpha \end{pmatrix}, \qquad \bar{\boldsymbol{d}}_1 = \begin{pmatrix} \bar{\boldsymbol{d}}_1^u \\ \bar{\boldsymbol{d}}_1^v \\ \bar{\boldsymbol{d}}_1^\alpha \end{pmatrix}, \qquad \boldsymbol{A} = [\boldsymbol{A}_u | \boldsymbol{A}_v | \boldsymbol{a}_\alpha], \qquad \boldsymbol{A}^T = \begin{pmatrix} \boldsymbol{A}_u^T \\ \boldsymbol{A}_v^T \\ \boldsymbol{a}_\alpha^T \end{pmatrix} \tag{61}$$

Using Eq. (60) and Eq. (61) the variable $\Delta \boldsymbol{v}$ can be eliminated.

$$\Delta \boldsymbol{v} = -\boldsymbol{H}_v^{-1} \cdot \left(\bar{\boldsymbol{d}}_1^v - \boldsymbol{A}_v^T \cdot \Delta \boldsymbol{\lambda}_E \right) \tag{62}$$

Finally, the following system of linear equations has to be solved.

$$\begin{pmatrix} -\boldsymbol{H}_u & -\boldsymbol{h} & \boldsymbol{A}_u^T \\ -\boldsymbol{h}^T & -H_\alpha & \boldsymbol{a}_\alpha^T \\ \boldsymbol{A}_u & \boldsymbol{a}_\alpha & \boldsymbol{K} \end{pmatrix} \cdot \begin{pmatrix} \Delta \boldsymbol{u} \\ \Delta \alpha \\ \Delta \boldsymbol{\lambda}_E \end{pmatrix} = \begin{pmatrix} \bar{\boldsymbol{d}}_1^u \\ \bar{\boldsymbol{d}}_1^\alpha \\ \bar{\boldsymbol{d}}_2 \end{pmatrix} \tag{63}$$

where:

$$\boldsymbol{K} = \boldsymbol{A}_v \cdot \boldsymbol{H}_v^{-1} \cdot \boldsymbol{A}_v^T$$
$$\bar{\boldsymbol{d}}_2 = \boldsymbol{d}_2 + \boldsymbol{A}_v \cdot \boldsymbol{H}_v^{-1} \cdot \bar{\boldsymbol{d}}_1^v$$

It has to be mentioned that the matrix $\boldsymbol{K}$ is still symmetric and positive definite. Unfortunately, depending on the structure of $\boldsymbol{A}_v$ and thus problem-dependent it may happen that $\boldsymbol{K}$ appears to be relatively dense. Although the coefficient matrix of the system (63) will remain sparse in total, the density of $\boldsymbol{K}$ might lead to a less efficient solution procedure. On the other hand the dimension of the problem is reduced which has a positive influence. Moreover, this disadvantage as a result of the relative density of $\boldsymbol{K}$ is accepted for the advantage that no regularization is necessary at all. In [42] the described reduction has been shown to lead to a remarkable decrease of running time. Nevertheless, in some other cases there appeared problems in the solution of the equation system due to the possible bad conditioning of the coefficient matrix. However, when using this optional new approach, the system of linear equations (63) is solved by use of the NAG-library [33]. In particular, the solver *nag_sparse_sym_chol_sol (f11jcc)* is used which takes into account both the symmetry and the sparsity of the coefficient matrix using an incomplete Cholesky preconditioning.

4.3 Damping of the Newton Step

The full Newton step $\Delta \boldsymbol{\Pi}$ computed from Eq. (46) may happen to be too large in the sense that one or more of the Lagrange multipliers, the slack or the split variables become negative. Since these have to be nonnegative by definition, the Newton step is damped in these cases.

For this reason, the damping factors α_i are introduced, which are merged into the diagonal matrix $\boldsymbol{\Upsilon}_k$ in Eq. (45). In principle, damping factors can be defined for each of the variables separately. Nonetheless, it is common practice in linear and nonlinear programs to use two different values α_P for the primal variables $\boldsymbol{\Pi}_P = [\boldsymbol{x}, \boldsymbol{y}, \boldsymbol{z}, \boldsymbol{w}]^T$ and α_D for the dual variables $\boldsymbol{\Pi}_D = [\boldsymbol{\lambda}_E, \boldsymbol{\lambda}_I, \boldsymbol{s}, \boldsymbol{r}]^T$. The two according sets of enforced nonnegative variables are denoted by $\boldsymbol{\Pi}_P^* = [\boldsymbol{y}, \boldsymbol{z}, \boldsymbol{w}]^T$ and $\boldsymbol{\Pi}_D^* = [\boldsymbol{\lambda}_I, \boldsymbol{s}, \boldsymbol{r}]^T$.

$$\tilde{\alpha}_P = \max\left\{\bar{\alpha} \middle| \boldsymbol{\Pi}_P^* + \bar{\alpha} \Delta \boldsymbol{\Pi}_P^* \geq \boldsymbol{0};\ \boldsymbol{\Pi}_P^* = [\boldsymbol{y}, \boldsymbol{z}, \boldsymbol{w}]^T\right\} \tag{64a}$$

$$\tilde{\alpha}_D = \max\left\{\bar{\alpha} \middle| \boldsymbol{\Pi}_D^* + \bar{\alpha} \Delta \boldsymbol{\Pi}_D^* \geq \boldsymbol{0};\ \boldsymbol{\Pi}_D^* = [\boldsymbol{\lambda}_I, \boldsymbol{s}, \boldsymbol{r}]^T\right\} \tag{64b}$$

In order to prevent hitting the boundary, these values are multiplied by the constant factor $\alpha_0 = 0.99995$.

Damping of the Newton step with the nonnegativity condition may still not be sufficient, because it is possible that the resulting step values do not lead to a descent direction in both the infeasibilities and the objective function. In order to ensure that the computed direction is a decreasing one, the following merit function $\Phi_{\mu,\nu}$ is introduced for a linesearch procedure. The term in squared brackets [.] is optional but should be used in order to avoid the Maratos effect [27].

$$\Phi_{\mu,\nu}(\boldsymbol{\Pi}) = f_\mu(\boldsymbol{x}, \boldsymbol{y}, z, \boldsymbol{w}) + \frac{\nu}{2} \left\| \begin{pmatrix} \boldsymbol{A} \cdot \boldsymbol{x} \\ \boldsymbol{c}_I(\boldsymbol{x}) - \boldsymbol{w} \\ \boldsymbol{x} - \boldsymbol{y} + z \end{pmatrix} \right\|_2^2 + \left[(\boldsymbol{A} \cdot \boldsymbol{x}) \cdot \boldsymbol{\lambda}_E \right] \tag{65}$$

Here, ν denotes the penalty parameter, which is updated if necessary in each iteration step before the linesearch starts.

With help of the linesearch, the supplementary damping factor α_T is determined. Starting from the initial value 1, the factor α_T is halved as often as is necessary such that the Armijo condition (66) is satisfied. As proposed in e.g. [51], this reduction is carried out in dependence of the primal values only. For the Armijo-factor we set $\beta = 10^{-3}$.

$$\Phi_{\mu,\nu}(\boldsymbol{\Pi} + \bar{\alpha} \Delta \boldsymbol{\Pi}) \leq \Phi_{\mu,\nu}(\boldsymbol{\Pi}) + \beta \bar{\alpha} \Phi'_{\mu,\nu}(\boldsymbol{\Pi}; \Delta \boldsymbol{\Pi}) \tag{66}$$

where:

$$\bar{\alpha} = \alpha_T \alpha_0 \tilde{\alpha}_P$$

Once the value α_T is determined, the total damping factors can be calculated.

$$\alpha_P = \alpha_T \alpha_0 \tilde{\alpha}_P, \qquad \alpha_D = \alpha_T \alpha_0 \tilde{\alpha}_D \tag{67}$$

Concerning the penalty parameter ν, we use the new update-rule equation (70), which has been recently developed in [42]. It is based on the necessary condition of a decreasing direction, $\Phi'(\boldsymbol{\Pi}; \Delta \boldsymbol{\Pi}) < 0$. Here and in the following the subscription with μ and ν will be omitted for the sake of clarity of the presentation. The total differential $\Phi'(\boldsymbol{\Pi}; \Delta \boldsymbol{\Pi})$ can be expressed as follows.

$$\Phi'(\boldsymbol{\Pi}; \Delta \boldsymbol{\Pi}) = \Phi'_f(\boldsymbol{\Pi}; \Delta \boldsymbol{\Pi}) + \nu \Phi'_{feas}(\boldsymbol{\Pi}; \Delta \boldsymbol{\Pi}) \tag{68a}$$

where:

$$\begin{aligned} \Phi'_f(\boldsymbol{\Pi}; \Delta \boldsymbol{\Pi}) = \nabla_x f \cdot \Delta \boldsymbol{x} - \mu \left[\boldsymbol{Y}^{-1} \cdot \Delta \boldsymbol{y} + \boldsymbol{Z}^{-1} \cdot \Delta z + \boldsymbol{W}^{-1} \cdot \Delta \boldsymbol{w} \right] \\ - \left[\left(\boldsymbol{A}^T \cdot \boldsymbol{\lambda}_E \right) \cdot \boldsymbol{x} + (\boldsymbol{A} \cdot \boldsymbol{x}) \cdot \boldsymbol{\lambda}_E \right] \end{aligned} \tag{68b}$$

and:

$$\begin{aligned} \Phi'_{feas}(\boldsymbol{\Pi}; \Delta \boldsymbol{\Pi}) = (\boldsymbol{A} \cdot \boldsymbol{x}) \cdot (\boldsymbol{A} \cdot \Delta \boldsymbol{x}) + (\boldsymbol{c} - \boldsymbol{w}) \cdot \boldsymbol{C} \cdot \Delta \boldsymbol{x} - (\boldsymbol{c} - \boldsymbol{w}) \cdot \Delta \boldsymbol{w} \\ + (\boldsymbol{x} - \boldsymbol{y} + z) \cdot (\Delta \boldsymbol{x} - \Delta \boldsymbol{y} + \Delta z) \end{aligned} \tag{68c}$$

Substituting the analytical expressions for the step values into Eq. (68c) one gets:

$$\Phi'_{feas} = -\left[(\boldsymbol{A}\cdot\boldsymbol{x})^2 + (\boldsymbol{c}-\boldsymbol{w})^2 + (\boldsymbol{x}-\boldsymbol{y}+\boldsymbol{z})^2\right] \tag{69}$$

With Eq. (69) it is clear that Φ'_{feas} is negative in any case. Thus, the following update-rule is sufficient to guarantee $\Phi'(\boldsymbol{\Pi}_k; \Delta\boldsymbol{\Pi}_k) < 0$.

$$\mathsf{IF}\left(\nu_{k-1} < -\gamma_\nu \frac{\Phi'_f}{\Phi'_{feas}}\right): \qquad \nu_k = -\gamma_\nu \frac{\Phi'_f}{\Phi'_{feas}} \tag{70}$$

The factor $\gamma_\nu = 10$ is chosen to avoid problems due to numeric inaccuracy.

4.4 Break Conditions

In general, break conditions in interior-point algorithms have the form $\|\boldsymbol{F}\| \leq \varepsilon$, where formulations differ in the used norm, the choice of the tolerances ε and ε_μ and in the applied scaling.

Scaling should be used to make the convergence criteria reasonable. However, calculation of scaling factors from the actual step values takes computation time. As a balance between practicality and scale invariance, we follow [51] and calculate the scaling factors only once from the values of the starting point, which is denoted by the subindex $(.)_0$.

The break condition of the inner iteration has to ensure proximity of the linearized solution to the exact solution for the fixed barrier parameter μ and is given by Eqs. (71a)–(71h).

$$\left\|\nabla_x f(\boldsymbol{x}) - \boldsymbol{A}^T\cdot\boldsymbol{\lambda}_E - \boldsymbol{C}_I^T(\boldsymbol{x})\cdot\boldsymbol{\lambda}_I - \boldsymbol{s}\right\|_\infty \leq \max\left\{1; \left\|\nabla_x f(\boldsymbol{x})\right\|_\infty\right\}\varepsilon_\mu^{opt} = \varepsilon_\mu^{opt} \tag{71a}$$

$$\|\mu\boldsymbol{e} - \boldsymbol{Y}\cdot\boldsymbol{S}\cdot\boldsymbol{e}\|_\infty \leq \max\left\{1; \left\|\nabla_x f(\boldsymbol{x})\right\|_\infty\right\}\varepsilon_\mu^{opt} = \varepsilon_\mu^{opt} \tag{71b}$$

$$\|\mu\boldsymbol{e} - \boldsymbol{Z}\cdot\boldsymbol{R}\cdot\boldsymbol{e}\|_\infty \leq \max\left\{1; \left\|\nabla_x f(\boldsymbol{x})\right\|_\infty\right\}\varepsilon_\mu^{opt} = \varepsilon_\mu^{opt} \tag{71c}$$

$$\|\mu\boldsymbol{e} - \boldsymbol{W}\cdot\boldsymbol{\Lambda}_I\cdot\boldsymbol{e}\|_\infty \leq \max\left\{1; \left\|\nabla_x f(\boldsymbol{x})\right\|_\infty\right\}\varepsilon_\mu^{opt} = \varepsilon_\mu^{opt} \tag{71d}$$

$$\|\boldsymbol{A}\cdot\boldsymbol{x}\|_\infty \leq \max\left\{1; \|\boldsymbol{A}\cdot\boldsymbol{x}_0\|_\infty\right\}\varepsilon_\mu^{feas} \tag{71e}$$

$$\left\|\boldsymbol{c}_I(\boldsymbol{x}) - \boldsymbol{w}\right\|_\infty \leq \max\left\{1; \left\|\boldsymbol{c}_I(\boldsymbol{x}_0) - \boldsymbol{w}_0\right\|_\infty\right\}\varepsilon_\mu^{feas} \tag{71f}$$

$$\|\boldsymbol{x} - \boldsymbol{y} + \boldsymbol{z}\|_\infty \leq \max\left\{1;\, \|\boldsymbol{x}_0 - \boldsymbol{y}_0 + \boldsymbol{z}_0\|_\infty\right\} \varepsilon_\mu^{feas} \tag{71g}$$

$$\|\boldsymbol{r} + \boldsymbol{s}\|_\infty \leq \max\left\{1;\, \|\boldsymbol{r}_0 + \boldsymbol{s}_0\|_\infty\right\} \varepsilon_\mu^{feas} \tag{71h}$$

For the tolerances of the inner iteration we use:

$$\varepsilon_\mu^{opt} = \max\left\{\theta\mu;\, \varepsilon^{opt} - \mu\right\} \tag{72a}$$

$$\varepsilon_\mu^{feas} = \max\left\{\theta\mu;\, \varepsilon^{feas}\right\} \tag{72b}$$

By setting $\mu = 0$ in both the conditions and the tolerances, a consistent formulation of break conditions is used for the outer iteration. In addition, the scaled fractional change of the objective is introduced as an additional convergence criterion for the outer iteration, as proposed in [15].

$$\frac{|f(\boldsymbol{x}^{k+1}) - f(\boldsymbol{x}^k)|}{1 + |f(\boldsymbol{x}^k)|} \leq \varepsilon^{obj} \tag{73}$$

The tolerances are set to the following values: $\varepsilon^{opt} = \varepsilon^{feas} = \varepsilon^{obj} = 10^{-6}$ and $\theta = 1$.

4.5 Update-Rule of the Barrier Parameter

Once the inner iteration has converged, the barrier parameter has to be updated. We modify the update-rule given in [3], which takes into account the distance from the solution, in order to fit it to the break conditions (71a)–(71h).

$$\begin{aligned}
&\text{IF } (\bar{\mu}_i < 0.1\mu_k): \ \text{if } \left(\mu_k < 10^{-4}\right): && \mu_{k+1} = \min\left\{0.85\mu_k;\, 10 \cdot (0.85)^{k+2\sigma}\, \bar{\mu}_o\right\} \\
&\qquad\qquad \text{else:} && \mu_{k+1} = \min\left\{0.85\mu_k;\, 10 \cdot (0.85)^{k+\sigma}\, \bar{\mu}_o\right\} \\
&\text{ELSE:} && \mu_{k+1} = \min\left\{0.95\mu_k;\, 10 \cdot (0.95)^{k}\, \bar{\mu}_o\right\} \\
&\text{where:} && \bar{\mu}_i = \frac{1}{\theta} \max\left\{\textit{scaled infeasibility}(\mu)\right\} \quad \text{and} \quad \bar{\mu}_o = \bar{\mu}_i|_{\mu=0}
\end{aligned} \tag{74}$$

The left hand side values in Eqs. (71a)–(71h) are the infeasibilities of the current iteration step. Thus, the maximum scaled infeasibility can be taken from the computation of the inner and outer break conditions, respectively. As suggested in [3] we use $\sigma = 5$.

5 Numerical Example

The described algorithm is applied to a pipe-junction with an angle of 60° between the main pipe and the nozzle, Fig. 3. The pipe-junction is made of steel, and it is

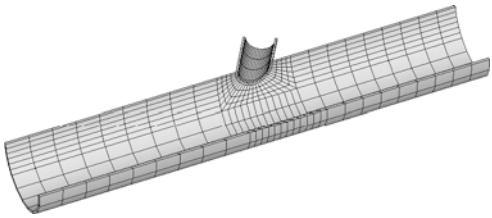

Fig. 3 FEM-model and mesh

Table 1 Characteristic dimensions of pipe-junction

	Length [mm]	Inner radius [mm]	Thickness [mm]
Pipe	600.00	53.55	3.6
Nozzle	157.15	18.60	2.6

Table 2 Thermal and mechanical characteristics

Young's modulus [MPa]	2.1×10^5
Yield stress [MPa]	235
Poisson's ratio	0.3
Density [kg/m^3]	7.85×10^3
Thermal conductivity [W/(m·K)]	48
Specific heat capacity [J/(kg·K)]	470
Coefficient of thermal expansion	1.2×10^{-5}
Transfer coefficient at boundary [W/(m^2·K)]	200
Transfer coefficient in pipe [W/(m^2·K)]	1200

subjected to internal pressure and temperature loading, which vary independently. Due to the symmetry it is sufficient to consider only one half of the system. The left end of the tube is clamped, whereas the right end is fixed only in longitudinal direction of the tube. The nozzle is assumed to be closed without any restriction on the displacements. The geometrical and mechanical characteristics are given in Tables 1 and 2, respectively.

For the finite element analysis, the software package ANSYS is used. In particular, we use the isoparametric solid elements (square with 8 nodes) *solid70* for the thermal analysis and *solid45* for the structural analysis. The mesh consists of 510 elements and 1136 nodes and is shown in Fig. 3.

The results of the finite element analysis are presented in Figs. 4 and 5. In particular, the equivalent stresses resulting from the temperature load and from the internal pressure are shown. Using the described algorithm, the shakedown loading factors for different angles φ in the two-dimensional loading space are computed. The resulting domain is presented in Fig. 6 and the according numerical values are given in Table 3. Note, that in Fig. 6 the value for $\varphi \approx 61.6°$ is plotted additionally, which represents the intersection point between two different regions, which are both defined by the alternating plasticity criterion.

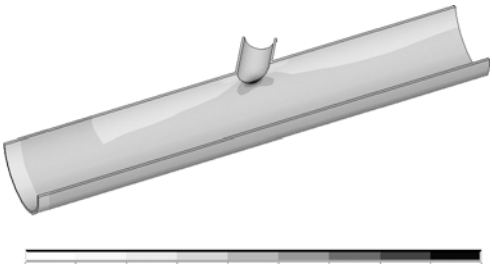

Fig. 4 Equivalent stresses due to temperature load

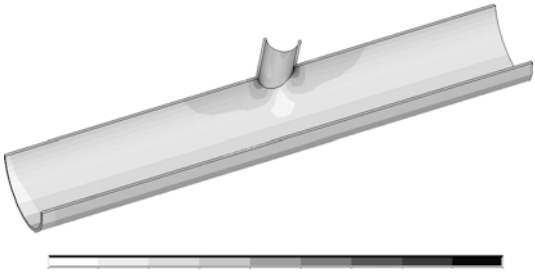

Fig. 5 Equivalent stresses due to internal pressure

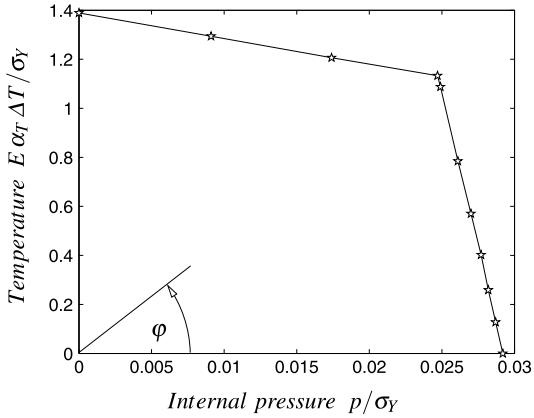

Fig. 6 Result of shakedown analysis

Table 3 Numeric result of shakedown analysis

φ	0°	10°	20°	30°	40°	50°	60°	70°	80°	90°
p/σ_Y	0.0292	0.0287	0.0282	0.0277	0.0270	0.0261	0.0249	0.0174	0.0091	0
$E\alpha_T\Delta T/\sigma_Y$	0	0.1276	0.2589	0.4023	0.5705	0.7847	1.0874	1.2066	1.2939	1.3891

6 Conclusion

We have presented a method to compute the shakedown factors of structures subjected to varying thermal and mechanical loadings using the lower bound approach.

The formulation has been generalized for the case of arbitrary finite numbers of loading cases. Furthermore, an improved formulation has been derived for the special case of von Mises materials. The described method has been successfully implemented into an interior-point algorithm and the relevant numerical details have been presented. Finally, the efficiency of the algorithm is illustrated by a practical example.

Acknowledgements We wish to thank David Huet, who carried out the structural part of the FEA during his student project work.

References

1. Akoa, F.B.: Approches de points intérieurs et de la programmation DC en optimisation non convexe. PhD thesis, Institut National des Sciences Appliquées de Rouen (2007)
2. Akoa, F.B., Hachemi, A., An, L.T.H., Mouhtamid, S., Tao, P.D.: Application of lower bound direct method to engineering structures. J. Glob. Optim. **37**(4), 609–630 (2007)
3. Akrotirianakis, I., Rustem, B.: A primal-dual interior point algorithm with an exact and differentiable merit function for general nonlinear programming problems. Technical Report 98-09, Department of Computing, Imperial College of Science, Technology and Medicine, 180 Queen's Gate, London SW7 2BZ, UK (1999)
4. An, L.T.H., Tao, P.D.: Solving a class of linearly constrained indefinite quadratic problems by DC algorithms. J. Glob. Optim. **11**, 253–285 (1997)
5. An, L.T.H., Tao, P.D.: The DC (difference of convex functions) programming and DCA revisited with DC models of real world nonconvex optimization problems. Ann. Oper. Res. **133**, 23–46 (2005)
6. An, L.T.H., Tao, P.D., Muu, L.D.: A combined DC optimization—ellipsoidal branch-and-bound algorithm for solving nonconvex quadratic programming problems. J. Comb. Optim. **2**, 9–28 (1998)
7. Andersen, E.D., Jensen, B., Jensen, J., Sandvik, R., Worsøe, U.: MOSEK Version 6. Technical Report TR–2009–3, MOSEK (2009)
8. Andersen, E.D., Roos, C., Terlaky, T.: On implementing a primal-dual interior-point method for conic quadratic optimization. Math. Program. **95**(2), 249–277 (2003)
9. Benson, H.Y., Shanno, D.F., Vanderbei, R.J.: Interior-point methods for nonconvex nonlinear programming: filter methods and merit functions. Technical Report ORFE-00-06, Operations Research and Financial Engineering, Princeton University (2001)
10. Benson, H.Y., Shanno, D.F., Vanderbei, R.J.: A comparative study of large-scale nonlinear optimization algorithms. Technical Report ORFE-01-04, Operations Research and Financial Engineering, Princeton University (2002)
11. Bisbos, C.D., Makrodimopoulos, A., Pardalos, P.M.: Second-order cone programming approaches to static shakedown analysis in steel plasticity. Optim. Methods Softw. **20**(1), 25–52 (2005)
12. Byrd, R.H., Hribar, M.E., Nocedal, J.: An interior point algorithm for large-scale nonlinear programming. SIAM J. Optim. **9**(4), 877–900 (2000)
13. El-Bakry, A.S., Tapia, R.A., Tsuchiya, T., Zhang, Y.: On the formulation and theory of the Newton interior-point method for nonlinear programming. J. Optim. Theory Appl. **89**, 507–541 (1996)
14. Forsgren, A., Gill, P.E., Wright, M.H.: Interior methods for nonlinear optimization. SIAM Rev. **44**(4), 525–597 (2002)
15. Gajulapalli, R.S., Lasdon, L.S.: Computational experience with a safeguarded barrier algorithm for sparse nonlinear programming. Comput. Optim. Appl. **19**, 107–120 (2001)

16. Garcea, G., Leonetti, L.: Numerical methods for the evaluation of the shakedown and limit loads. In: Contribution on Conference ESMC2009, Lisbon, Portugal (2009)
17. Griva, I., Shanno, D.F., Vanderbei, R.J., Benson, H.Y.: Global convergence analysis of a primal-dual interior-point method for nonlinear programming. Algorithmic Oper. Res. **3**(1), 12–19 (2008)
18. Hachemi, A., An, L.T.H., Mouhtamid, S., Tao, P.D.: Large-scale nonlinear programming and lower bound direct method in engineering applications. In: An, L.T.H., Tao, P.D. (eds.) Modelling, Computation and Optimization in Information Systems and Management Sciences, pp. 299–310. Hermes Science, London (2004)
19. Koiter, W.T.: General theorems for elastic-plastic solids. In: Sneddon, I.N., Hill, R. (eds.) Progress in Solid Mechanics, pp. 165–221. North-Holland, Amsterdam (1960)
20. König, J.A.: Shakedown of Elastic-Plastic Structures. Elsevier, Amsterdam (1987)
21. Krabbenhøft, K., Damkilde, L.: A general nonlinear optimization algorithm for lower bound limit analysis. Int. J. Numer. Methods Eng. **56**, 165–184 (2003)
22. Krabbenhøft, K., Lyamin, A.V., Sloan, S.W.: Formulation and solution of some plasticity problems as conic programs. Int. J. Solids Struct. **44**, 1533–1549 (2007)
23. Krabbenhøft, K., Lyamin, A.V., Sloan, S.W., Wriggers, P.: An interior-point algorithm for elastoplasticity. Int. J. Numer. Methods Eng. **69**, 592–626 (2007)
24. Kuhn, H.W., Tucker, A.W.: Nonlinear programming. In: Neyman, J. (ed.) Second Berkeley Symposium on Mathematical Statistics and Probability, pp. 481–492. University of California Press, Berkeley (1950)
25. Maier, G., Pastor, J., Ponter, A.R.S., Weichert, D.: Direct methods of limit and shakedown analysis. In: de Borst, R., Mang, H.A. (eds.) Comprehensive Structural Integrity—Fracture of Materials from Nano to Macro, Numerical and Computational Methods, vol. 3, pp. 637–684. Elsevier, Amsterdam (2003)
26. Makrodimopoulos, A.: Computational formulation of shakedown analysis as a conic quadratic optimization problem. Mech. Res. Commun. **33**, 72–83 (2006)
27. Maratos, N.: Exact penalty function algorithms for finite dimensional and control optimization problems. PhD thesis, University of London, London, UK (1978)
28. Melan, E.: Der Spannungszustand eines "Mises-Hencky'schen" Kontinuums bei veränderlicher Belastung. Sitzungsber. Akad. Wiss. Wien, Math.-Naturwiss. Kl., Abt. IIa **147**, 73–87 (1938)
29. Melan, E.: Zur Plastizität des räumlichen Kontinuums. Ing.-Arch. **9**, 116–126 (1938)
30. Mészáros, C.: On free variables in interior point methods. Optim. Methods Softw. **9**, 121–139 (1998)
31. Mittelmann, H.: Decision Tree for Optimization Software (2010). http://plato.asu.edu/guide.thml
32. Morales, J.L., Nocedal, J., Waltz, R.W., Lie, G., Goux, J.-P.: Assessing the potential of interior methods for nonlinear optimization. In: Biegler, L.T., Ghattas, O., Heinkenschloss, M., van Bloemen Waander, B. (eds.) Large-Scale PDE-Constrained Optimization. Lecture Notes in Computational Science and Engineering, vol. 30, pp. 167–183. Springer, Berlin (2003)
33. The Numerical Algorithms Group Limited: NAG C Library Manual. NAG (2005)
34. Pastor, F., Loute, E.: Limit analysis decomposition and finite element mixed method. J. Comput. Appl. Math. **234**(7), 2213–2221 (2010)
35. Pastor, F., Loute, E., Pastor, J., Trillat, M.: Mixed method and convex optimization for limit analysis of homogeneous Gurson materials: a kinematic approach. Eur. J. Mech. A, Solids **28**, 25–35 (2009)
36. Pastor, F., Thoré, Ph., Loute, E., Pastor, J., Trillat, M.: Convex optimization and limit analysis: application to Gurson and porous Drucker-Prager materials. Eng. Fract. Mech. **75**, 1367–1383 (2008)
37. Potra, F.A., Wright, S.J.: Interior-point methods. J. Comput. Appl. Math. **124**, 281–302 (2000)
38. Saunders, M.A.: Cholesky-based methods for sparse least squares: the benefits of regularization. In: Adams, L., Nazareth, J.L. (eds.) Linear and Nonlinear Conjugate Gradient-Related Methods, pp. 92–100. SIAM, Philadelphia (1996)

39. Saunders, M.A., Tomlin, J.A.: Solving regularized linear programs using barrier methods and KKT systems. Technical Report SOL 96-4, Dept. of Operations Research, Stanford University, Stanford, CA 94305, USA (1996)
40. Simon, J.-W., Chen, M., Weichert, D.: Shakedown analysis combined with the problem of heat conduction. In: Proc. ASME 2010 Pressure Vessels & Piping Conference (2010)
41. Simon, J.-W., Weichert, D.: An improved interior-point algorithm for large-scale shakedown analysis. In: PAMM Proc. Appl. Math. Mech., vol. 2010 (2010)
42. Simon, J.-W., Weichert, D.: Interior-point method for the computation of shakedown loads for engineering systems. In: Proc. ASME 2010 10th Biennial Conference on Engineering Systems Design and Analysis (2010)
43. Trillat, M., Pastor, J.: Limit analysis and Gurson's model. Eur. J. Mech. A, Solids **24**, 800–819 (2005)
44. Vanderbei, R.J.: LOQO: An interior point code for quadratic programming. Optim. Methods Softw. **11–12**, 451–484 (1999)
45. Vanderbei, R.J., Carpenter, T.J.: Symmetric indefinite systems for interior point methods. Math. Program. **58**, 1–32 (1993)
46. Vu, D.K., Staat, M.: Analysis of pressure equipment by application of the primal-dual theory of shakedown. Commun. Numer. Methods Eng. **23**(3), 213–225 (2007)
47. Vu, D.K., Yan, A.M., Nguyen-Dang, H.: A primal-dual algorithm for shakedown analysis of structures. Comput. Methods Appl. Mech. Eng. **193**, 4663–4674 (2004)
48. Wächter, A.: An interior point algorithm for large-scale nonlinear optimization with applications in process engineering. PhD thesis, Carnegie Mellon University, Pittsburgh, Pennsylvania (2002)
49. Wächter, A., Biegler, L.T.: Line-search filter methods for nonlinear programming: Motivation and global convergence. SIAM J. Optim. **16**(1), 1–31 (2005)
50. Wächter, A., Biegler, L.T.: On the implementation of an interior-point filter line-search algorithm for large-scale nonlinear programming. Math. Program. **106**(1), 25–57 (2006)
51. Waltz, R.A., Morales, J.L., Nocedal, J., Orban, D.: An interior algorithm for nonlinear optimization that combines line search and trust region steps. Math. Program. **107**(3), 391–408 (2006)
52. Weichert, D., Maier, G.: Inelastic Analysis of Structures Under Variable Repeated Loads. Kluwer Academic, Dordrecht (2000)
53. Weichert, D., Ponter, A.R.S.: Limit States of Materials and Structures. Springer, Wien (2009)
54. Wright, M.H.: The interior-point revolution in optimization: History, recent developments and lasting consequences. Bull. Am. Math. Soc. **42**(1), 39–56 (2004)

Numerical Analysis of Nonholonomic Elastoplastic Frames by Mathematical Programming

Konstantinos V. Spiliopoulos and Theodoros N. Patsios

Abstract The strength as well as the ductility of a structure may be estimated by performing an elastoplastic analysis. In such an analysis structural loading is incrementally applied through a proportional loading factor in accordance to a predefined loading pattern. During this process we have continuous plasticizations of various parts of the structure. For a more accurate description of the physical process, possible deplasticizations should also be taken into account. Thus a nonholonomic material behavior should be followed. In this work such an analysis is performed in an efficient way. The basis of the approach is the formulation of the incremental problem as a convex parametric quadratic programming (PQP) problem between two successive plastic hinges. The solution of this problem is done by assuming a fictitious load factor which establishes a search direction for the next plasticization. The true load factor is established when the plastic hinge that is closest to open really opens. An example of application, which serves as benchmark, is also included.

1 Introduction

The capacity of a structure beyond its elastic limits may be estimated by performing a step-by-step elastoplastic analysis. During this process the loading is applied sequentially with consecutive parts of the structure being plasticized. Between two plasticizations an elastic analysis is performed. Thus a series of elastic analyses is carried out before reaching either a limit load state or a predefined load state. In this way, one may have a good estimate of the structure's strength as well as of its ductility. The above described procedure is called holonomic plasticity.

A more realistic material behavior is to take into account any local unloading (plastic unstressing) in the course of the analysis. This approach, which is much more involved computationally, is called nonholonomic plasticity.

K.V. Spiliopoulos (✉) · T.N. Patsios
Department of Civil Engineering, Institute of Structural Analysis & Antiseismic Research, National Technical University of Athens, Zografou Campus, Zografos 157-80, Athens, Greece
e-mail: kvspilio@central.ntua.gr

T.N. Patsios
e-mail: tpatsios@central.ntua.gr

G. Saxcé et al. (eds.), *Limit State of Materials and Structures*,
DOI 10.1007/978-94-007-5425-6_7,

Maier [1] was the first to show that mathematical programming (MP) and especially parametric quadratic programming (PQP) provides a unified formalism for the problem of elastoplastic analysis with the load factor being the parameter of the program. In this work holonomic plasticity has been addressed. The alternative formulation as a parametric complementarity problem (PLCP) has also been given by Maier [2]. The framework for this problem is linear programming (LP) with the Simplex method employed for its solution (de Donato and Maier [3]). Smith [4] extended this approach to nonholonomic plasticity proposing a numerical solution based on the Simplex method that restricts the variables that enter the basis. The methodology was applied to a simple frame. In an attempt to produce a PLCP based general purpose computer program for nonholonomic plasticity Franchi and Cohn [5] and Kaneko [6] proposed a rather involved algorithm. PLCP based solutions of problems with a softening material behavior have also appeared recently (Tangaramvong and Tin-Loi [7, 8]).

Besides the compact MP formulation of an elastoplastic problem, all the above PLCP based solutions generally involve a large number of variables and constraints (Tin-Loi and Wong [9]). At the same time computer implementation of these algorithms is quite difficult. Thus an alternative approach, the direct stiffness method has almost exclusively been used. This is based on the displacement method and whenever a plasticization occurs, an elastic prediction—plastic correction takes place by re-formulating and re-decomposing the stiffness matrix. Re-formulation and re-decomposition, must also take place if nonholonomicity is considered. These two tasks increase the computational time quite considerably.

The present work presents a methodology that was proposed by Spiliopoulos and Patsios [10]. The main ingredient of the procedure is to cast the problem in the form of an incremental PQP and solve it directly in this form. A numerical strategy was developed that employs a fictitious load factor and solves the resulting QP program by standard algorithms (e.g. Goldfarb and Idnani [11]). The solution of the fictitious program will automatically detect a possible unstressing and, at the same time, it establishes a solution direction which searches for the formation of the next plastic hinge which is closest to open. When it opens, the load factor receives its true value.

The approach appears to be numerically stable and very fast. Although it may be formulated either with respect to a displacement based or a force based MP, the force based one is preferred, due to the less number of unknowns and to the accurate way that equilibrium is expressed through this method. An approach (Spiliopoulos [12]) may be used to automatically establish this equilibrium both with respect to the hyperstatic forces and the applied loading.

2 Problem Formulation

Let a frame, whose material is elastic-perfectly plastic, be subjected to a loading pattern which changes in a proportional way:

$$\mathbf{P} = \mathbf{P}_{in} + \gamma \cdot \mathbf{r}_P \tag{1}$$

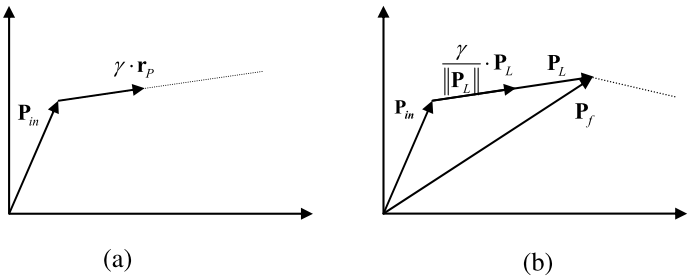

Fig. 1 Proportional loading: (**a**) limit load analysis, (**b**) prescribed loading analysis

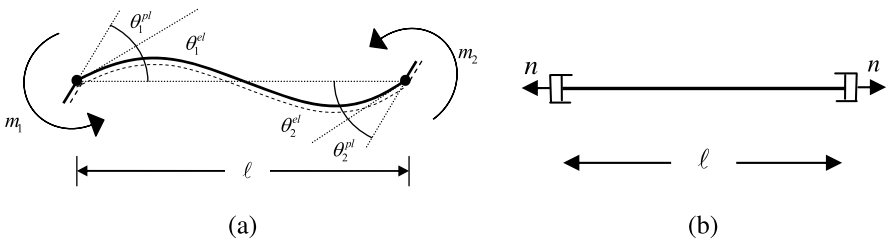

Fig. 2 (**a**) Rotations and moments, (**b**) plastic axial deformations and axial force

where bold letters represent vectors and matrices, $\mathbf{P}_{in}$ represents an initial load state, γ is a proportional load factor and $\mathbf{r}_p$ is the unit vector along the direction of the loading pattern (Fig. 1). This vector is always known either in limit or prescribed loading analysis. If the final loading state in the prescribed loading case is given by $\mathbf{P}_f$ then $\mathbf{r}_P = (1/\|\mathbf{P}_L\|) \cdot \mathbf{P}_L$, with $\mathbf{P}_\mathrm{L} = \mathbf{P}_\mathrm{f} - \mathbf{P}_\mathrm{in}$.

If we consider plasticity to be lumped at the two ends of a member, we may decompose the rotations and the axial deformations into elastic and plastic components (Fig. 2).

The elastic rotations are related to the moments through the flexibility matrix:

$$\begin{Bmatrix} \theta_1^{el} \\ \theta_2^{el} \end{Bmatrix} = \frac{\ell}{6EI} \cdot \begin{bmatrix} 2 & 1 \\ 1 & 2 \end{bmatrix} \cdot \begin{Bmatrix} m_1 \\ m_2 \end{Bmatrix} \tag{2}$$

At the same time the two elastic axial deformations at the two ends are given by:

$$\delta_{1,2}^{el} = n\ell/EA \tag{3}$$

where ℓ, EI and EA are the member's length, bending and axial stiffness respectively.

By grouping all the bending and axial deformations of all the critical sections of the structure one may write:

$$\begin{Bmatrix} \boldsymbol{\theta}^{el} = \mathbf{F}_m \cdot \mathbf{m} \\ \boldsymbol{\delta}^{el} = \mathbf{F}_n \cdot \mathbf{n} \end{Bmatrix} \rightarrow \begin{Bmatrix} \boldsymbol{\theta}^{el} \\ \boldsymbol{\delta}^{el} \end{Bmatrix} = \left[\begin{array}{c|c} \mathbf{F}_m & \emptyset \\ \hline \emptyset & \mathbf{F}_n \end{array}\right] \cdot \begin{Bmatrix} \mathbf{m} \\ \mathbf{n} \end{Bmatrix} \rightarrow \mathbf{q}^{el} = \bar{\mathbf{F}} \cdot \mathbf{Q} \tag{4}$$

where $\mathbf{F}_m$ and $\mathbf{F}_n$ are the block-diagonal bending flexibility and axial flexibility matrices respectively. $\mathbf{Q}$ are the stress resultant pairs (m, n) at each critical section.

A plastic hinge opens if any of these pairs touch an interaction surface. This surface may be written for rectangular sections:

$$\frac{|m|}{m_*} + \left(\frac{n}{n_*}\right)^2 = 1 \tag{5}$$

where m_*, n_* are the section's bending and axial plastic capacities.

The above yield surface is doubly symmetric with respect to the four quadrants with ordinates (m/m_*), (n/n_*). We may use a finite set of ζ linear equations to approximate it. So we may write:

$$f(m, n) = (\pm)s_1 \cdot \frac{m}{m_*} + (\pm)s_2 \cdot \frac{n}{n_*} - 1 = 0 \tag{6}$$

There are ζ distinct couples of (s_1, s_2).

The simplest linearization consists of four lines ($\zeta = 1$) and we will call it "$M + N = 1$", whereas the AISC criterion [13] consists of 8 lines ($\zeta = 2$).

Due to the nonlinear nature of the problem, the solution will be acquired incrementally.

Let us suppose we have completed the incremental step $k - 1$. If we apply the next increment of loading the structure will respond with increments of moments and axial forces. Thus by grouping all the moments and axial forces of the structure one may write for the increment k:

$$\left\{\begin{array}{c} \mathbf{m}_k = \mathbf{m}_{k-1} + \Delta\mathbf{m} \\ \mathbf{n}_k = \mathbf{n}_{k-1} + \Delta\mathbf{n} \end{array}\right\} \rightarrow \mathbf{Q}_k = \mathbf{Q}_{k-1} + \Delta\mathbf{Q} \tag{7}$$

where $\Delta\mathbf{Q}$ denotes the increments of the force vector.

In the framework of the force method of analysis one may write these increments as:

$$\left\{\begin{array}{c} \Delta\mathbf{m} = \mathbf{B}_m \cdot \Delta\mathbf{p} + (\Delta\gamma_k) \cdot \mathbf{B}_{o,m} \cdot \mathbf{r}_p \\ \Delta\mathbf{n} = \mathbf{B}_n \cdot \Delta\mathbf{p} + (\Delta\gamma_k) \cdot \mathbf{B}_{o,n} \cdot \mathbf{r}_p \end{array}\right\} \rightarrow \Delta\mathbf{Q} = \bar{\mathbf{B}} \cdot \Delta\mathbf{p} + \Delta\gamma_k \cdot \bar{\mathbf{B}}_o \cdot \mathbf{r}_p \tag{8}$$

where

$$\bar{\mathbf{B}} = \left[\frac{\mathbf{B}_m}{\mathbf{B}_n}\right], \qquad \bar{\mathbf{B}}_o = \left[\frac{\mathbf{B}_{o,m}}{\mathbf{B}_{o,n}}\right]$$

The first terms of the above equations are due to the indeterminacy of the structure, with $\mathbf{p}$ being a set of hyperstatic forces which is called statical basis. These forces may be found by introducing cuts around the structure so that it is made statically determinate.

The second terms are due to the equilibrium with the increments of the applied loading which is expressed through the increment of the loading factor $\Delta\gamma$.

Using an equivalent piecewise linear form (i.e. Eq. (6)) of the yield surface (5), we may write the plastic counterparts of the rotation and the axial deformation at a critical section i:

$$\Delta \mathbf{q}_i^{pl} = \begin{bmatrix} \Delta\theta_i^{pl} \\ \Delta\delta_i^{pl} \end{bmatrix} = \Delta\lambda_i \cdot \frac{\partial f}{\partial \mathbf{Q}_i} = \Delta\lambda_i \cdot \begin{bmatrix} s_1/m_{*i} \\ s_2/n_{*i} \end{bmatrix} \tag{9}$$

Thus the vector of the total deformations of the critical sections of the structure may now be written as:

$$\Delta \mathbf{q} = \Delta \mathbf{q}^{el} + \Delta \mathbf{q}^{pl} \tag{10}$$

From the principle of static kinematic duality (SKD), the conjugate to the hyperstatic forces discontinuities at the cuts induced around the structure are related through $\bar{\mathbf{B}}^T$. If we close these cuts we may write down the compatibility conditions:

$$\bar{\mathbf{B}}^T \cdot \Delta \mathbf{q} = \mathbf{0} \tag{11}$$

The condition of static admissibility states that the total generalized force $\mathbf{Q}_k = \mathbf{Q}_{k-1} + \Delta\mathbf{Q}$ at the step k stays within the yield surface. With the complementarity condition holding between $\Delta\lambda_i$ and the section's generalized potential which marks the distance from a yield plane, Eqs. (7)–(11), with also the use of (4) lead to the solution of the following PQP program:

$$\begin{aligned} &\text{Minimize} \quad z(\Delta\mathbf{p}) = \frac{1}{2} \cdot \Delta\mathbf{p}^T \cdot \left(\bar{\mathbf{B}}^T \cdot \bar{\mathbf{F}} \cdot \bar{\mathbf{B}}\right) \cdot \Delta\mathbf{p} + \Delta\gamma_k \cdot \left(\bar{\mathbf{B}}^T \cdot \bar{\mathbf{F}} \cdot \bar{\mathbf{B}}_o \cdot \mathbf{r}_p\right)^T \cdot \Delta\mathbf{p} \\ &\text{Subject to:} \quad \left(\bar{\mathbf{N}}^T \cdot \bar{\mathbf{B}}\right) \cdot \Delta\mathbf{p} \le \mathbf{e} - \bar{\mathbf{N}}^T \cdot \mathbf{Q}_{k-1} - \Delta\gamma_k \cdot \left(\bar{\mathbf{N}}^T \cdot \bar{\mathbf{B}}_o \cdot \mathbf{r}_p\right) \end{aligned} \tag{12}$$

where $\bar{\mathbf{N}}$ contains the different coefficients of the left-hand side of the constraints of (6). It may be written in the form [10]:

$$\bar{\mathbf{N}} = \left[\overbrace{\left[\bar{\mathbf{N}}_{\mathrm{I}} \,\middle|\, \bar{\mathbf{N}}_{\mathrm{II}} \,\middle|\, \bar{\mathbf{N}}_{\mathrm{III}} \,\middle|\, \bar{\mathbf{N}}_{\mathrm{IV}}\right]}^{(s_{11}, s_{21})} \vdots \overbrace{\left[\bar{\mathbf{N}}_{\mathrm{I}} \,\middle|\, \bar{\mathbf{N}}_{\mathrm{II}} \,\middle|\, \bar{\mathbf{N}}_{\mathrm{III}} \,\middle|\, \bar{\mathbf{N}}_{\mathrm{IV}}\right]}^{(s_{12}, s_{22})} \vdots \cdots \vdots \overbrace{\left[\bar{\mathbf{N}}_{\mathrm{I}} \,\middle|\, \bar{\mathbf{N}}_{\mathrm{II}} \,\middle|\, \bar{\mathbf{N}}_{\mathrm{III}} \,\middle|\, \bar{\mathbf{N}}_{\mathrm{IV}}\right]}^{(s_{1\zeta}, s_{2\zeta})} \right]$$

with the various submatrices given by:

$$\bar{\mathbf{N}}_{\mathrm{I}} = \left[\begin{array}{c:c} s_1 \cdot [diag(\mathbf{m}_*^+)]^{-1} & \emptyset \\ \hdashline \emptyset & s_2 \cdot [diag(\mathbf{n}_*^+)]^{-1} \end{array} \right]$$

$$\bar{\mathbf{N}}_{\mathrm{II}} = \left[\begin{array}{c:c} s_1 \cdot [diag(\mathbf{m}_*^+)]^{-1} & \emptyset \\ \hdashline \emptyset & s_2 \cdot [-diag(\mathbf{n}_*^-)]^{-1} \end{array} \right]$$

$$\bar{\mathbf{N}}_{\mathrm{III}} = \left[\begin{array}{c:c} s_1 \cdot [-diag(\mathbf{m}_*^-)]^{-1} & \emptyset \\ \hdashline \emptyset & s_2 \cdot [diag(\mathbf{n}_*^+)]^{-1} \end{array} \right]$$

$$\bar{\mathbf{N}}_{\mathrm{IV}} = \left[\begin{array}{c:c} s_1 \cdot [-diag(\mathbf{m}_*^-)]^{-1} & \emptyset \\ \hdashline \emptyset & s_2 \cdot [-diag(\mathbf{n}_*^-)]^{-1} \end{array} \right]$$

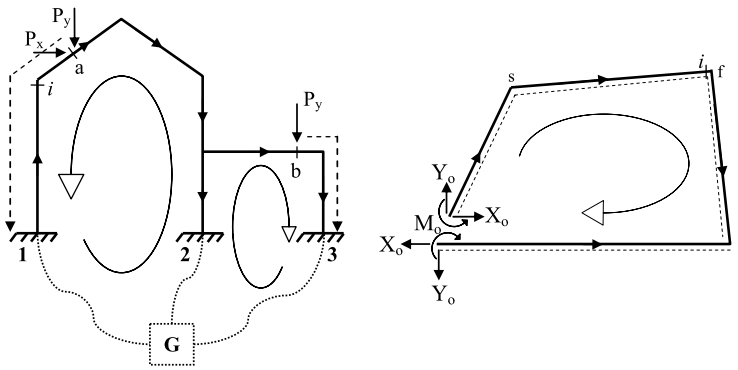

Fig. 3 (**a**) Graph representation, a cycle basis and shortest path cantilevers, (**b**) Self-equilibrating system of forces

where the diagonal matrices $\mathbf{m}_*$ and $\mathbf{n}_*$ contain the bending and axial capacities of the critical sections of the frame, with the superscripts $\pm$ denoting the corresponding ones in tension or compression.

We may have ζ couples of $(s_1, s_2) = \{(s_{11}, s_{21}), (s_{12}, s_{22}), \ldots, (s_{1\zeta}, s_{2\zeta})\}$, depending on the number of yield planes considered for a particular yield criterion. For the simple "$M + N = 1$" criterion $\zeta = 1$, $s_{11} = s_{21} = 1$, whereas for the AISC criterion $\zeta = 2$, $s_{11} = 8/9$, $s_{21} = 1$, $s_{12} = 1$, $s_{22} = 1/2$.

The solution of this program will be discussed analytically in Sect. 4.

Once the optimum solution of (12) is obtained, its Lagrange multipliers provides us with the various $\Delta\lambda_i$.

3 Methodology to Obtain Equilibrium Matrices

3.1 Construction of $\bar{\mathbf{B}}$

It is recalled that this matrix has to do with the indeterminacy of the structure. This may be accomplished using an algorithm that was originally presented by Spiliopoulos [12]. It is based on the graph representation of a frame. One may see such a graph in Fig. 3. In this graph the ground is represented by an extra node and extra additional members connecting each foundation node with this ground node. This algorithm selects a set of independent cycles using a minimum path technique from graph theory and the fact that the number of these cycles that constitutes a cycle basis is known and equal to $\mu - \nu + 1$ where μ, ν are the total number of members and nodes that compose the graph.

For the compactness of the present work the algorithm is briefly presented here. It is based on giving to each member of the graph an initial value of its "length"

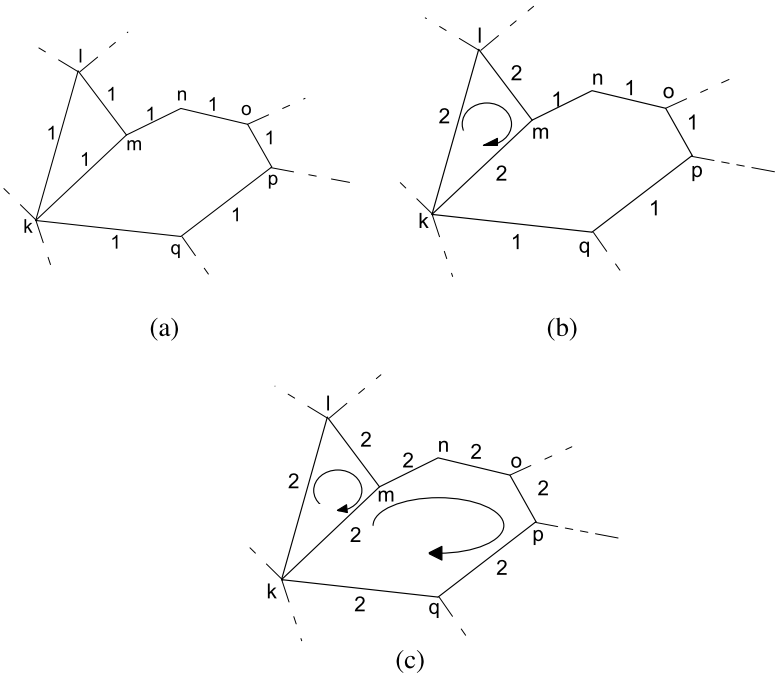

Fig. 4 Formation of a cycle basis

equal to 1. Of course this length has nothing to do with its Euclidean length but rather refers to an existence of a member between two nodes.

The procedure then starts from the node that is incident to the maximum number of members. Each of these members are chosen as generator members and the minimum path between its ends is found not by traveling along the member but going around it. This minimum path together with the generator member forms a cycle which is a candidate to enter the cycle basis. It will enter the basis only if the following admissibility rule is satisfied:

"The length of the path is less than 2* (nodes along the path-1)"

If this rule is satisfied it means that the cycle is independent from the ones already found, enters the basis and at the same time to all the members of the cycle we give the value of 2. This last action guarantees that this particular cycle will not enter the cycle again.

The procedure may be understood if we consider the cycle formation in a sub graph extracted from a main graph (Fig. 4(a)). Staring from the node k, we may pick up the member km as a generator member. Then the cycle $klmk$ is selected and the lengths of the members of the cycle take the value of 2 (Fig. 4(b)). Then a next member, e.g. mn may be selected to serve as a generator member and a next cycle may be selected to enter the cycle basis (Fig. 4(c)). There can be cases of complicated graphs where this simple procedure may break down and leave

some cycles unidentified. There are remedies, however, to overcome this problem [12].

If we make a cut at each cycle one may establish a pair of two unknown forces X_o, Y_o along the x and y directions and an unknown bending moment M_o at the point of the cut, with coordinates x_o and y_o. These may be considered as the three hyperstatic quantities of the cycle (Fig. 3(b)). The bending moment as well as the axial force at a critical section i may be shown to be:

$$\begin{Bmatrix} m_i \\ n_i \end{Bmatrix} = (\pm) \begin{bmatrix} (y_0 - y_i) & (x_i - x_0) & -1 \\ -\cos\varphi & -\sin\varphi & 0 \end{bmatrix} \cdot \begin{bmatrix} X_0 \\ Y_0 \\ M_0 \end{bmatrix} \tag{13}$$

with:

$$\cos\varphi = \frac{x_f - x_s}{\sqrt{(x_f - x_s)^2 + (y_f - y_s)^2}} \quad \text{and} \quad \sin\varphi = \frac{y_f - y_s}{\sqrt{(x_f - x_s)^2 + (y_f - y_s)^2}}$$

with (x_s, y_s) and (x_f, y_f) being the coordinates of the two ends of the member that the critical section i belongs to. The positive or the negative sign of the parenthesis in (13) depends on whether the mesh orientation coincides or not with the mesh orientation. By filling in the appropriate positions, the matrix $\bar{\mathbf{B}}$ may be formed.

3.2 *Construction of* $\bar{\mathbf{B}}_\mathbf{0}$

The minimum path technique may be also used to substantiate equilibrium with respect to the applied loading, which is considered concentrated. Thus one may establish the quickest way to the ground of the load through the use of a cantilever which may be formed between the point of application of the load and the ground (Fig. 3(a)). Thus the following equation may be written:

$$\begin{Bmatrix} m_i \\ n_i \end{Bmatrix} = (\pm) \begin{bmatrix} (x_a - x_i) & (y_a - y_i) \\ \cos\varphi & -\sin\varphi \end{bmatrix} \cdot \begin{bmatrix} P_x \\ P_y \end{bmatrix} \tag{14}$$

where (x_a, y_a) are the coordinates of the point of application of the concentrated load. The sign of the parenthesis is positive if the direction of the member, that a particular cross section i belongs to, coincides with the direction of the cantilever.

4 Numerical Solution of the PQP Program

The following numerical steps that have been suggested in [10], will be briefly described here:

Beginning of the incremental procedure with $\gamma = 0$ and $k = 1$

1. Suppose a "fictitious" small initial value for $\Delta\gamma_k = \rho$ (see Fig. 6)

2. Solve the resulting QP program (12) and obtain a "fictitious" set of increments of the hyperstatic forces $\Delta\tilde{\mathbf{p}}$ and a set of fictitious increments of the generalized plastic displacements $\Delta\tilde{\mathbf{q}}^{pl}$ through the Lagrange multipliers of the optimal solution $\Delta\tilde{\lambda}_i$. Any efficient algorithm [11] may be used.
3. A first correction to the fictitious set of the hyperstatic forces and the length of the plastic vectors is made:

$$\Delta\mathbf{p}' = \frac{1}{\rho}\cdot\Delta\tilde{\mathbf{p}} \quad \text{and} \quad \Delta\boldsymbol{\lambda}' = \frac{1}{\rho}\cdot\Delta\tilde{\boldsymbol{\lambda}} \quad \rightarrow \quad \Delta\mathbf{q}_i'^{pl} = \Delta\lambda_i'\cdot\begin{bmatrix} s_1/m_{*i} \\ s_2/n_{*i}\end{bmatrix} \tag{15}$$

4. Fictitious increments of bending and axial forces are evaluated using (8):

$$\Delta\mathbf{Q}' = \bar{\mathbf{B}}\cdot\Delta\mathbf{p}' + \bar{\mathbf{B}}_o\cdot\mathbf{r}_p$$

   In this way, a search direction $\Delta\mathbf{Q}_i'$, for each critical section is established. It is this direction that will determine the next possible plasticization at the intersection with one of the yield planes (Fig. 5(a))
5. Find the correct $\Delta\gamma_k$ as the minimum $\Delta\gamma_{i,k}$ among the non-active constraints that produces a new plastic hinge (Fig. 5(a)):

$$\Delta\gamma_{i,k} = \frac{(\alpha_i\cdot n_{i,k-1}+\beta_i) - m_{i,k-1}}{\Delta m_i' - \alpha_i\cdot\Delta n_i'} \tag{16}$$

   where $i = 1, 2, \ldots N_c$, with N_c being the total number of critical sections. The parameters (a_i, β_i) may be evaluated with the aid of (6) and turn out to be:

$$\alpha_i = -\frac{s_2}{s_1}\cdot\frac{m_{*,i}}{n_{*,i}} \quad \text{and} \quad \beta_i = \frac{m_{*,i}}{s_1}$$

   A search is made for each critical section for all the possible intersections with the yield planes for all the four quadrants. The minimum positive among all numbers one may get using (16), is the sought $\Delta\gamma_{i,k}$.
6. Find the increments of the bending moments, axial forces and plastic displacements as:

$$\Delta\mathbf{m} = \Delta\gamma_k\cdot\Delta\mathbf{m}', \quad \Delta\mathbf{n} = \Delta\gamma_k\cdot\Delta\mathbf{n}', \quad \Delta\mathbf{q}^{pl} = \Delta\gamma_k\cdot\Delta\mathbf{q}'^{pl} \tag{17}$$

7. The load factor, the various static and kinematic variables may be now updated:

$$\begin{aligned}
&\gamma_k = \gamma_{k-1} + \Delta\gamma_k \\
&\left.\begin{aligned}\mathbf{m}_k &= \mathbf{m}_{k-1} + \Delta\mathbf{m} \\ \mathbf{n}_k &= \mathbf{n}_{k-1} + \Delta\mathbf{n}\end{aligned}\right\} \quad \mapsto \quad \mathbf{Q}_k \\
&\left.\begin{aligned}\boldsymbol{\theta}_k^{el} &= \mathbf{F}_m\cdot\mathbf{m}_k \\ \boldsymbol{\delta}_k^{el} &= \mathbf{F}_n\cdot\mathbf{n}_k\end{aligned}\right\} \quad \mapsto \quad \mathbf{q}_k^{el} = \bar{\mathbf{F}}\cdot\mathbf{Q}_k \\
&\mathbf{q}_k^{pl} = \mathbf{q}_{k-1}^{pl} + \Delta\mathbf{q}^{pl} \\
&\mathbf{q}_k = \mathbf{q}_k^{el} + \mathbf{q}_k^{pl}
\end{aligned} \tag{18}$$

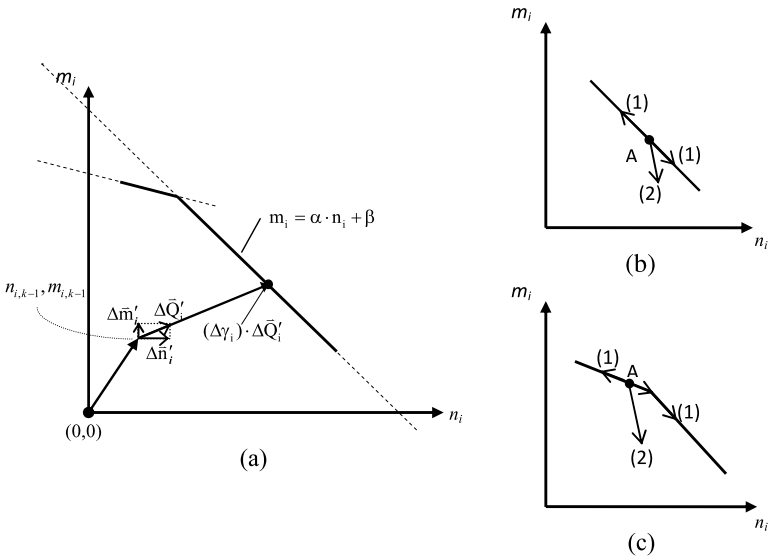

Fig. 5 (**a**) Search direction and plasticization from elastic state, (**b**) Further plasticization (1) or unloading (2)

The displacements at the points of the load application may be found from SKD:

$$\mathbf{u}_k = \bar{\mathbf{B}}_0^T \cdot \mathbf{q}_k$$

8. Return to step 1 and repeat the process for $k = k + 1$, until either
   i. No solution of the QP may be found, meaning a collapse state has been reached and if it were for a limit analysis case γ_k is the limit load factor, or
   ii. For a prescribed loading the process stops if (i) has not occurred and $|\gamma_k - \|P_L\|| \leq \rho$, meaning we have reached the end of the specific loading case.

If we have an already plasticized critical section, the algorithm automatically detects at the beginning of the incremental step whether we are going to move along the directions (1) (Fig. 5(b) or (c)), meaning we get further plasticization, or move along the directions (2), meaning we have plastic unloading. Moving along either the direction (1) or (2) depends on whether the corresponding Lagrange multiplier of the active constraint becomes positive or zero, respectively.

There is always going to be one active constraint for a particular critical section. Even in the case of Fig. 5(c) when further plasticization continues along a neighboring constraint the previously active one now becomes inactive. In the very unlikely case when the search direction meets the point of intersection of the two constraints, then two nonzero Lagrange multipliers $\Delta\lambda_i$ will appear, rendering both the constraints active. Thus, because of (9), two plastic vectors will appear. Each of them is perpendicular to the corresponding plane. In this case the plastic deformation will be the composition of these two vectors.

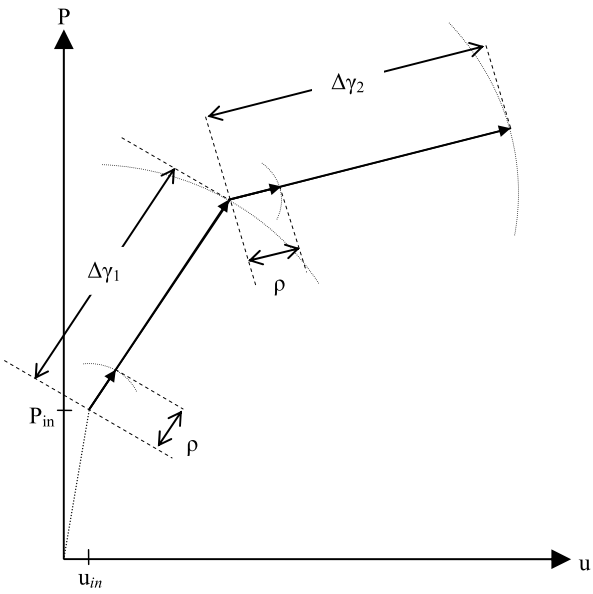

Fig. 6 Search direction with fictitious (ρ), and true incremental load factors ($\Delta\gamma$)

A physical interpretation of the fictitious load factor that is used at the beginning of the incremental step is to find a feasible direction on which the prospective solution lies taking into account all the previous plasticization that have occurred before the current incremental step. The true length of the step is then found on the demand to capture the next plasticization. The procedure may be depicted for two steps on a force-displacement diagram of the Fig. 6.

5 Numerical Example

The numerical example has been chosen in order to demonstrate the efficiency of the approach. This example was found difficult to converge when using standard commercial packages that use the direct stiffness as the solution method [14, 15].

The structure is a three-storey one-bay frame shown in Fig. 7. The original frame has appeared with Imperial units [16] which herein have been converted to SI.

This frame was experimentally tested by Yarimci [17] and the results of the experiments have been taken from [16]. The members of the frame were assigned mechanical properties, which are shown in Table 1, so that they match the ones that were measured. A pure bending behavior was considered for the beams.

The loading scenario is the following: First the vertical loads were applied up to their final values that may be seen in Fig. 7 and then the horizontal loads were proportionally increased from zero. These loads were applied up to a certain value, then unloading of the structure took place, following a reversed loading and then reloading up to zeros so that a full cycle of loading was completed.

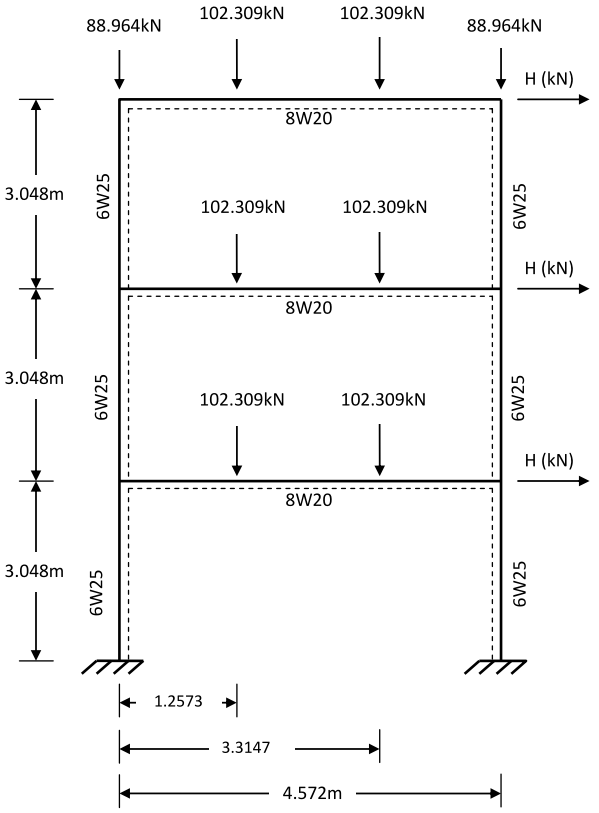

Fig. 7 Geometry of the analyzed frame

Table 1 Mechanical properties used for the analysis

Section	E (kN/m^2)	I (m^4)	m_* (kNm)	n_* (kN)
8W20	2×10^8	2.90×10^{-5}	76.83	∞
6W25	2×10^8	2.68×10^{-5}	83.61	1015

Three different constitutive relations were considered: (a) a pure bending behavior (to all the members a big value for n_* was given as input), (b) a moment/axial interaction using the "$M + N = 1$" criterion and (c) a moment/axial interaction using the AISC LRFD criterion [13].

For all the three different cases of constitutive modeling, the numerical application of loading, unloading and reloading tried to follow the experiment that was performed [16].

Results of the three analyses are shown in Fig. 8.

One may see that the pure bending behavior simulates better the loading part of the cycle. This supports the assumption that for low rise buildings moment/axial force interaction need not be considered. The residual bending moment diagram at the end of the load cycle may be seen in Fig. 9.

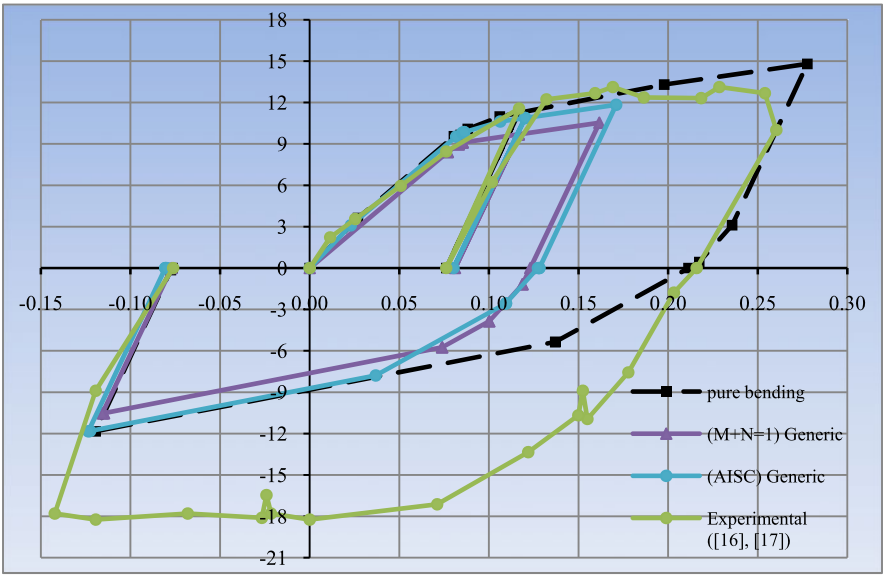

Fig. 8 Horizontal load in kN (*vertical axis*) vs. Roof Displacement in m (*horizontal axis*)

Fig. 9 Bending moment distribution at the end of the load cycle under pure bending

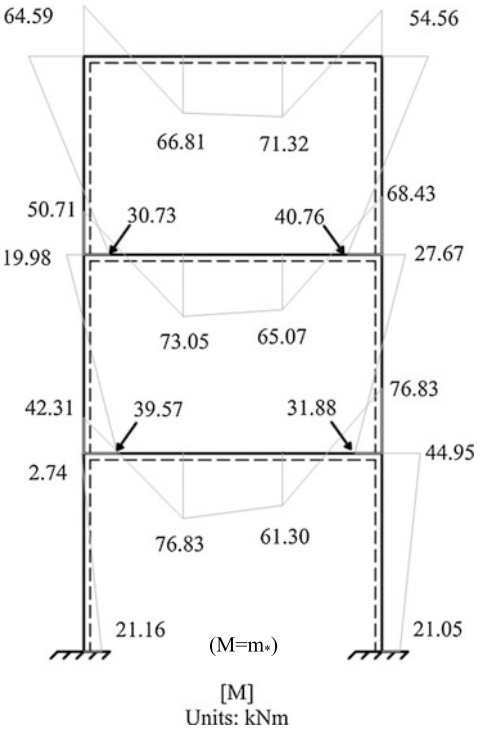

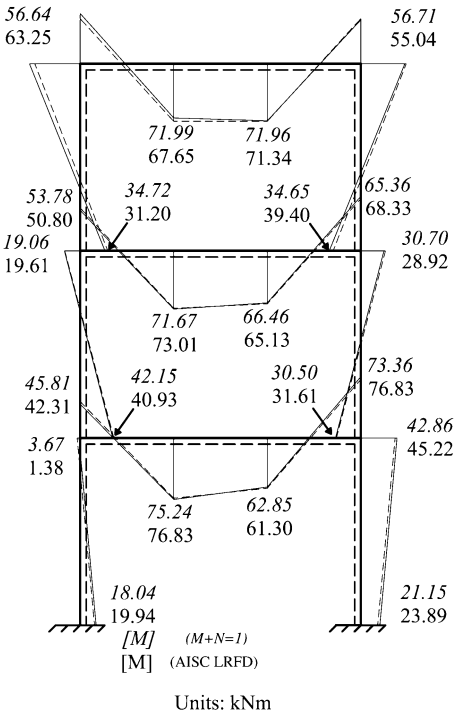

Fig. 10 Bending moment distributions at the end of the cycle under bending and axial force interactions

Although the conditions of the experiment are not known in great detail, it seems that, under the assumptions of an elastic-perfectly plastic material and first order theory, the analytical results underestimate, in terms of the load, the unloading part of the cycle.

On the other hand, when moment/axial force interaction under any of the two criteria is considered, the hysteresis loop shrinks. This supports the fact of the reduced ductility of a frame in the presence of axial forces.

In Figs. 10 & 11 one may see the residual bending moment and axial force distributions at the end of the loading cycle for the two criteria.

5.1 Computational Considerations

The fictitious factor ρ is the basis of the presented method. In this way we may have the conversion of the PQP problem to a QP one. It is a pure number and in order to capture all the events, one has to use a small value. In all the examples that were tried, a value of 10^{-3} or 10^{-4} has proved to be sufficient.

6 Conclusions

The nonholonomic elastoplastic analysis is performed with the aid of the force method of analysis. The framework of the exposed method is mathematical pro-

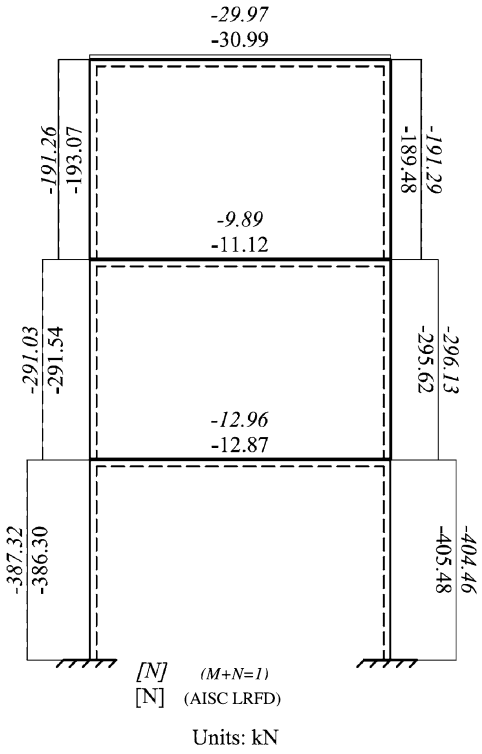

Fig. 11 Axial force distributions at the end of the cycle under bending and axial force interactions

gramming with a strategy to convert the resulting program which is originally a parametric quadratic program to a pure quadratic program.

As demonstrated from the presented example and also from other examples that were tested [10] the method proves to be a very stable and robust numerical procedure.

It is also computationally efficient because the only matrix that needs to be formed and decomposed once and for all is the flexibility matrix. The quadratic program is solved only once at the beginning of each incremental step and the step length that determines the next plasticization is determined automatically without the need to perform unnecessary intermediate elastic steps that have fixed length as is the case in any computer program that has the direct stiffness method as the basis for its formulation. No elastic prediction-plastic correction and no reformulation or re-decomposition of any matrix, as it would be the case for the stiffness matrix in a direct stiffness method, is needed. This operation, which is well known to be quite time consuming, is also avoided in the case of plastic unstressing since this information is contained directly inside the solution of the quadratic program and no extra work needs to be done. Thus from comparisons that have been made with the orthodox time stepping direct stiffness methods it has proved to be much more reliable and efficient [10].

The method although is certainly a step-by-step procedure it may be classified as a direct method as it is formulated within mathematical programming. These methods are known to be better suited than the direct stiffness method based ones if one seeks for a limit state of a structure. It is hoped that such methods will also be used more and more in the future as they seem to be a better alternative, even for a historical deformation analysis of a structure.

References

1. Maier, G.: A quadratic programming approach for certain classes of non linear structural problems. Meccanica **3**, 121–130 (1968)
2. Maier, G.: A matrix structural theory of piecewise linear elastoplasticity with interacting yield planes. Meccanica **5**, 54–66 (1970)
3. De Donato, O., Maier, G.: Historical deformation analysis of elastoplastic structures as a parametric linear complementarity problem. Meccanica **11**, 166–171 (1976)
4. Smith, D.L.: The Wolf-Markowitz algorithm for nonholonomic elastolpastic analysis. Eng. Struct. **1**, 8–16 (1978)
5. Franchi, A., Cohn, M.Z.: Computer analysis of elastic-plastic structures. Comput. Methods Appl. Mech. Eng. **21**, 271–294 (1980)
6. Kaneko, I.: Complete solutions for a class of elastic-plastic structures. Comput. Methods Appl. Mech. Eng. **21**, 193–209 (1980)
7. Tangaramvong, S., Tin-Loi, F.: Limit analysis of strain softening steel frames under pure bending. J. Constr. Steel Res. **63**, 1151–1159 (2007)
8. Tangaramvong, S., Tin-Loi, F.: A complementarity approach for elastoplastic analysis of strain softening frames under combined bending and axial force. Eng. Struct. **29**, 742–753 (2007)
9. Tin-Loi, F., Wong, M.B.: Nonholonomic computer analysis of elastoplastic frames. Comput. Methods Appl. Mech. Eng. **72**, 351–364 (1989)
10. Spiliopoulos, K.V., Patsios, T.N.: An efficient mathematical programming method for the elastoplastic analysis of frames. Eng. Struct. **32**, 1199–1214 (2010)
11. Golfarb, D., Idnani, A.: A numerically stable dual method for solving strictly convex quadratic programs. Math. Program. **27**, 1–33 (1983)
12. Spiliopoulos, K.V.: On the automation of the force method in the optimal plastic design of frames. Comput. Methods Appl. Mech. Eng. **141**, 141–156 (1997)
13. American Institute of Steel Construction: Load and Resistance Factor Design Specification for Structural Steel Buildings, Chicago, 2nd edn. (1993)
14. SAP2000: ver. 14.1.0 User's manual. CSI Inc. (2010)
15. ABAQUS: ver. 6.8-1 User's manual. SIMULIA Inc. (2009)
16. Toma, S., Chen, W.-F., White, D.W.: A selection of calibration frames in North America for second-order inelastic analysis. Eng. Struct. **17**, 104–112 (1995)
17. Yarimci, E.: Incremental inelastic analysis of framed structures and some experimental verifications. PhD dissertation, Department of Civil Engineering, Lehigh University, Bethlehem, PA (1966)

Inelastic Behavior of a Two-Bar System with Temperature-Dependent Elastic Modulus Under Cyclic Thermomechanical Loadings

Abdelbacet Oueslati, Géry de Saxcé, and Simon Hasbroucq

Abstract This paper is concerned with the elastic plastic response of a two-bar system with temperature-dependent elastic coefficients under cyclic thermomechanical loadings. Such materials are characterized by lack of results concerning the asymptotic behaviors and conditions for shakedown occurrence. This study shows that the considered simple structure is sufficiently complex to experience different periodic long term behaviors as in classical elastoplasticity. In order to understand how Melan-Koiter method works for such materials, the evolution of the structure's response until the stabilization of the plastic strain ('shakedown') or the asymptotic dissipative behavior ('alternating plasticity' or 'ratcheting') is analytically addressed and the Bree diagram is then constructed. The main result of this work is that the residual stress and strain fields are time-dependent even when shakedown occurs. Incidently, we proved that Halphen's conjecture (Halphen in C. R. Méc. 33:617–621, 2005) giving a sufficient condition for shakedown occurrence is not a necessary condition. Finally, numerical results performed by an incremental finite element procedure are presented.

1 Introduction

The phenomenon of fatigue of solids is deeply related to the inelastic asymptotic behaviors of structures subjected to cyclic loads in the sense that the prediction of the lifetime of structures requires the knowledge of the possible stabilized state (shakedown, alternating plasticity or ratcheting) and the use of an appropriate damage criterion. More precisely, elastic shakedown occurs if the plastic strain stabilizes

A. Oueslati (✉) · G. de Saxcé · S. Hasbroucq
Laboratoire de Mécanique de Lille – CNRS UMR 8107, Université de Lille 1, 59655 Villeneuve d'Ascq cedex, France
e-mail: abdelbacet.oueslati@univ-lille1.fr

G. de Saxcé
e-mail: gery.desaxce@univ-lille1.fr

S. Hasbroucq
e-mail: simon.hasbroucq@ed.univ-lille1.fr

G. Saxcé et al. (eds.), *Limit State of Materials and Structures*,
DOI 10.1007/978-94-007-5425-6_8,

after transient phase and the response of the structure becomes purely elastic. In this case the failure of the structure could happens after a great number of cycles (several hundreds of thousands even several million, for metallic materials); it is the high-cycle fatigue (or polycyclic fatigue) [1]. Alternating plasticity arises when the response of the structure converges to hysteresis loop, leading to a stabilized cycle of plastic strain. The structure may fail with a relatively low number of cycles; it is the low-cycle fatigue or the oligocyclic fatigue. As the energy dissipated by cycle (or plastic deformation cumulated by cycle) tends towards a constant value, it can be used as indicator of the severity of the damage induced by the cyclic loads [1]. Finally, ratcheting occurs if a constant increment of plastic strain is developed at every cycle during the loading history and consequently the structure will collapse by plastic strain accumulation (incremental collapse).

The study of the long-term steady responses of inelastic solids is a challenging topic for both theoretical aspects and industrial applications. Most of work concerns shakedown in the sense of establishing path-independent necessary and sufficient conditions for convergence to an asymptotic elastic response. Since the pioneering works of Bleich [2], Melan [3, 4] and Koiter [5], many extensions of the static and kinematic shakedown theorems to diverse and complicated constitutive material behaviors have been derived. Without being exhaustive, one may mention the extensions of Melan-Koiter shakedown theorems to hardening plasticity, materials with temperature-dependent yield function, dynamic plasticity, damaged and cracked bodies, non-associated plasticity, poro-plasticity, gradient plasticity, contact with friction, shape memory alloy structures, etc. However, in a recent work, Pham [6] showed that actually shakedown theorems, in Melan-Koiter path-independent spirit, have been extended successfully only for certain cases. Undoubtedly, the most accomplished extension concerns diverse hardening laws. It is already known that the unlimited linear kinematic hardening allows only to predict alternating plasticity collapse. The limited linear hardening one predicts an alternating and incremental plasticity collapse: the ultimate yield strength determines the unbounded incremental collapse pattern and the initial yield stress is responsible for the bounded cyclic plasticity occurrence [7]. It seems that nonlinear kinematic hardening appears the more realistic hardening model, however because of its non-associated flow law, no general shakedown or limit analysis theorems could be derived. It is worth noting that for such materials with non-associative constitutive models, the bipotential approach, based on a possible generalization of Fenchel's inequality, allows the recovery of the flow rule normality in a weak form of an implicit relation [8].

Classical Melan-Koiter shakedown theorems and their extensions rest on the assumption that elastic modulus are independent of the temperature. This is reasonable for thermal loading of low amplitude. However, in many industrial domains, for example in boilers of nuclear power plants or in chemical plants and airplane/automotive motors, the structural elements are subjected to thermal cycles of large amplitude in such way that the dependence of the elastic coefficients with respect to the temperature cannot be neglected. The case for which the yield stress depends on the temperature is well understood [9, 10] and many numerical algorithms where proposed for its study [11]. However, when the compliance elastic

tensor is temperature-dependent, the question of convergence of the elastic plastic evolution to a periodic asymptotic state remains open. Recently, Halphen [12] established the differential inclusion governing the evolution of the residual stress field for material with temperature-elastic coefficients but no solutions were derived. To our best knowledge, only one static shakedown theorem in this field was proposed by König [13]. Nevertheless, a key point in the proposed proof is questionable and not convincing.

In the present work we study analytically and numerically the elastic plastic evolution of a simple mechanical system in order to characterize the stabilized asymptotic states. The primary motivation is the extension of the Melan-Koiter shakedown theorems to materials with temperature-dependent coefficients.

2 Evolution of the Residual Stress Field

This section presents the differential inclusion governing the stress field evolution for elastic perfectly plastic materials with temperature-dependent elastic coefficients and derived in [12].

Consider an elastic perfectly plastic material occupying a volume Ω of the space with a smooth boundary $\partial\Omega$. The elastic coefficients are temperature-dependent. This solid Ω is loaded by given body forces $\mathbf{F}_v(t)$ in Ω, a prescribed displacement $\mathbf{u}^d(t)$ on Γ_u, surface tractions $\mathbf{T}^d(t)$ on Γ_T ($\Gamma_u \cup \Gamma_T = \partial\Omega$, $\Gamma_u \cap \Gamma_T = \emptyset$) and a temperature variation $\theta(t)$.

Let $(\boldsymbol{\sigma}(t), \boldsymbol{\varepsilon}(t), \mathbf{u}(t))$ denote the quasistatic elastic-plastic response to the path loading and let $(\boldsymbol{\sigma}^E(t), \boldsymbol{\varepsilon}^E(t), \mathbf{u}^E(t))$ be the fictitious purely thermo-elastic response under the same thermomechanical loads.

Within the framework of the infinitesimal transformation, the strain field is additively split into elastic, thermal and plastic parts

$$\boldsymbol{\varepsilon}(t) = \boldsymbol{\varepsilon}^e(t) + \boldsymbol{\varepsilon}^\theta(t) + \boldsymbol{\varepsilon}^p(t) \tag{1}$$

where elastic strains are related to the stresses through Hooke's law $\boldsymbol{\varepsilon}^e(t) = \mathbf{S}(\theta(t)) : \boldsymbol{\sigma}(t)$ ($\mathbf{S}$ is the fourth order elastic compliance tensor) and the thermal strain is given for isotropic behavior by $\boldsymbol{\varepsilon}^\theta(t) = \alpha\,\theta(t)\,\mathbf{I}$ (α is the coefficient of linear thermal expansion and $\mathbf{I}$ denotes the identity tensor).

The associated flow rule ensures that plastic strain rate obeys to the normality law

$$\dot{\boldsymbol{\varepsilon}}^p = \dot{\lambda}\frac{\partial f}{\partial \boldsymbol{\sigma}}\big(\boldsymbol{\sigma}, \theta(t)\big), \quad \dot{\lambda} \geq 0,\ \dot{\lambda} f = 0 \tag{2}$$

where $f(\boldsymbol{\sigma}, \theta)$ stands for the plasticity yield function and $\dot{\lambda}$ denotes the plastic multiplier.

By definition, the residual stress field is given by

$$\boldsymbol{\rho}(t) = \boldsymbol{\sigma}(t) - \boldsymbol{\sigma}^E(t) \tag{3}$$

Notice that $\boldsymbol{\rho}$ is the stress field subsisting in the structure after complete elastic unloading of Ω.

In the same manner, one can introduce the residual strain field as follows

$$\boldsymbol{\eta}(t) = \boldsymbol{\varepsilon}(t) - \boldsymbol{\varepsilon}^E(t) = \mathbf{S}\big(\theta(t)\big) : \boldsymbol{\rho}(t) + \boldsymbol{\varepsilon}^p(t) = \boldsymbol{\eta}^e(t) + \boldsymbol{\varepsilon}^p(t) \tag{4}$$

where $\boldsymbol{\eta}^e(t)$ is called the elastic residual strain field.

From the virtual power principle one gets

$$\int_\Omega (\boldsymbol{\sigma} - \widetilde{\boldsymbol{\sigma}}) : \dot{\boldsymbol{\varepsilon}} d\Omega = \int_\Omega (\boldsymbol{\sigma} - \widetilde{\boldsymbol{\sigma}}) : \dot{\boldsymbol{\varepsilon}}^E d\Omega \widetilde{\boldsymbol{\sigma}} \tag{5}$$

for any plastically admissible stress tensor $\widetilde{\boldsymbol{\sigma}}$.

Using relation (4) it becomes

$$\int_\Omega (\boldsymbol{\sigma} - \widetilde{\boldsymbol{\sigma}}) : \left(\frac{d}{dt}\big(\mathbf{S}(\theta) : \boldsymbol{\sigma}\big) + \dot{\boldsymbol{\varepsilon}}^p \right) d\Omega = \int_\Omega (\boldsymbol{\sigma} - \widetilde{\boldsymbol{\sigma}}) : \left(\frac{d}{dt}\big(\mathbf{S}(\theta) : \boldsymbol{\sigma}^E\big) \right) d\Omega \tag{6}$$

By use of the normality rule (2) we have

$$\int_\Omega (\boldsymbol{\sigma} - \widetilde{\boldsymbol{\sigma}}) : \left(\frac{d}{dt}\big(\mathbf{S}(\theta) : \boldsymbol{\sigma}\big) \right) d\Omega \leq \int_\Omega (\boldsymbol{\sigma} - \widetilde{\boldsymbol{\sigma}}) : \left(\frac{d}{dt}\big(\mathbf{S}(\theta) : \boldsymbol{\sigma}^E\big) \right) d\Omega \tag{7}$$

In the convex analysis theory, the last inequality (7) is equivalent to

$$-\frac{d}{dt}\big(\mathbf{S}\big(\theta(t)\big) : \boldsymbol{\sigma}(t)\big) \in \partial \psi_{K(t)}\big(\boldsymbol{\sigma}(t)\big) - \frac{d}{dt}\big(\mathbf{S}\big(\theta(t)\big) : \boldsymbol{\sigma}^{\boldsymbol{E}}(t)\big) \tag{8}$$

where $\partial \psi_{K(t)}(\sigma)$ is the subgradient at the point $\boldsymbol{\sigma}$ of the indicator function $\psi_{K(t)}$ of the convex set $K(t)$ of statically and plastically admissible fields at time t, with respect of the following scalar product of two second order tensor fields $\langle \mathbf{a} : \mathbf{b} \rangle = \int_\Omega \mathbf{a} : \mathbf{b}\, d\Omega$.

By introducing the residual stress field $\boldsymbol{\rho}$ we may write

$$-\frac{d}{dt}\big(\mathbf{S}\big(\theta(t)\big) : \boldsymbol{\rho}(t)\big) \in \partial \psi_{K^0(t)}\big(\boldsymbol{\rho}(t)\big) \tag{9}$$

in which $K^0(t) = K(t) - \boldsymbol{\sigma}^E$ denotes the convex of the residual stress field $\widetilde{\boldsymbol{\rho}}$, such that $\boldsymbol{\sigma}^E + \widetilde{\boldsymbol{\rho}}$ is statically and plastically admissible at time t.

Compared to the case when the elastic coefficients are constant there are two modifications: (i) the scalar product which is used is not defined by the elastic energy and (ii) the elastic compliance appears in Eq. (9). No rigorous mathematical study concerning the solutions of this differential inclusion is available in the literature.

Concerning the asymptotic behavior and basing on the relation Eq. (9), Halphen [14] proposed the following conjecture giving sufficient condition for shakedown:

Fig. 1 The two-bar problem

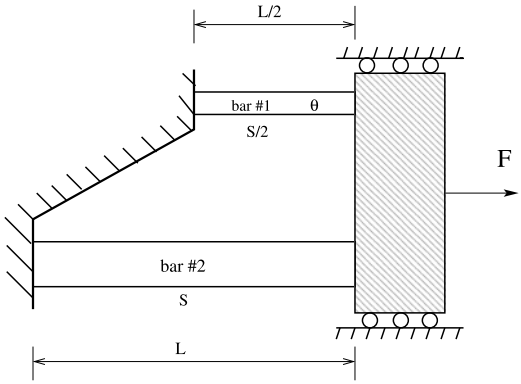

If there exists a residual stress field $\overline{\boldsymbol{\rho}}(t)$*, a scalar* $m > 1$ *such that*

- $\overline{\boldsymbol{\eta}}^e = \mathbf{S}(\theta(t)) : \overline{\boldsymbol{\rho}}(t)$ *is time independent and*
- $f(m\,\boldsymbol{\sigma}(t)) = f(m(\boldsymbol{\sigma}^E(t) + \overline{\boldsymbol{\rho}}(t))) \leq 0$

anywhere and at any time t*, then shakedown occurs for any initial condition.*

These proposed conditions were checked through elementary numerical examples [14, 15].

3 Description of the Problem

Consider a simple mechanical system composed of two parallel bars of cross-sections S and $S/2$ and lengths L and $L/2$ as shown in Fig. 1. The bars are built-in at one extremity and linked to a rigid bloc at the other one so that the assemblage is constraint to deform only in the horizontal direction. The bars are made of an elastic perfectly plastic material. The elastic coefficients are taken constant except the Young modulus E_1 and the yield stress σ_{y1} of bar ♯1 which depend on the temperature as follows

$$E_1(\theta) = E_0 - \lambda\theta \tag{10}$$

$$\sigma_{y1}(\theta) = \sigma_{y0} - \lambda_2\theta \tag{11}$$

where λ and λ_2 are material constants and θ is the temperature field.

Young's modulus and the yield stress of bar ♯2 are given by $E_2 = E_0$ and $\sigma_{y2} = \sigma_{y0}$ respectively.

This structure is subjected to a constant force F applied to the rigid support, bar ♯1 next heated and cooled according a cyclic temperature variation within $[\theta_0, \theta_0 + \Delta\tau]$ (Fig. 2) while bar ♯2 is maintained at a constant temperature θ_0. Without loss of generality and for seek of simplicity we suppose that $\theta_0 = 0$.

The study of the problem is carried out within the framework of the infinitesimal transformation. Furthermore, we assume that the initial state coincides with a null strain.

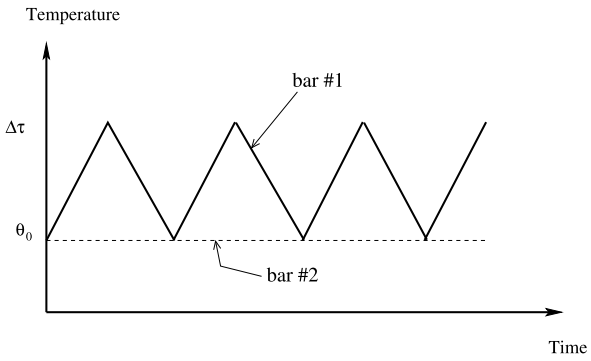

Fig. 2 Cyclic thermal load

The rigid bloc imposes the same axial displacement for the bars which results in the following relation

$$\varepsilon_1 = 2\varepsilon_2 \tag{12}$$

where ε_1 and ε_2 are the axial strain components in the bar ♯1 and bar ♯2 respectively.

By use of Hooke's law, Eq. (12) becomes

$$\frac{\sigma_1}{E_1(\theta)} + \varepsilon_1^p + \alpha\theta = 2\frac{\sigma_2}{E_2} + 2\varepsilon_2^p \tag{13}$$

where σ_1 and σ_2 are the stresses, ε_1^p and ε_2^p are the plastic strain in the bars, α is the coefficient of linear thermal expansion and θ is the temperature variation.

The equilibrium of the mechanical system writes

$$\frac{\sigma_1}{2} + \sigma_2 = \frac{F}{S} \tag{14}$$

Equations (13), (14) allows a complete investigation of all possible structure's responses.

At any instant, the stresses σ_1 and σ_2 are given by

$$\begin{cases} \sigma_1 = \left(1 + \dfrac{1}{1 - \frac{\lambda\theta}{E_0}}\right)^{-1} \left[2\dfrac{F}{S} - \alpha E_0\theta + 2E_0\left(\varepsilon_2^P - \dfrac{\varepsilon_1^P}{2}\right)\right] \\ \sigma_2 = \left(1 + \dfrac{1}{1 - \frac{\lambda\theta}{E_0}}\right)^{-1} \left[\dfrac{\frac{F}{S}}{1 - \frac{\lambda\theta}{E_0}} + \dfrac{\alpha E_0\theta}{2} - E_0\left(\varepsilon_2^P - \dfrac{\varepsilon_1^P}{2}\right)\right] \end{cases} \tag{15}$$

It is useful to introduce the stress $\sigma_T = \frac{E_0\alpha\Delta\tau}{2}$ associated to the temperature variation, the mechanical stress $\sigma_A = \frac{F}{S}$ and the non dimensional constants $A = \frac{\lambda\sigma_{y0}}{\alpha E_0^2}$ and $B = \frac{\lambda_2}{E_0\alpha}$. We shall adopt the classical Bree (or Miller) diagram representation with axis σ_A/σ_{y0} and σ_T/σ_{y0}.

Table 1 Elastic response

	Middle of a cycle	End of a cycle
ε_1^P	0	0
σ_1	$\frac{(\sigma_A-\sigma_T)(1-2A\frac{\sigma_T}{\sigma_{y0}})}{1-A\frac{\sigma_T}{\sigma_{y0}}}$	σ_A
ε_2^P	0	0
σ_2	$\frac{(\sigma_A+\sigma_T-2A(\frac{\sigma_T}{\sigma_{y0}})^2\sigma_{y0})}{2-2A\frac{\sigma_T}{\sigma_{y0}}}$	$\frac{\sigma_A}{2}$

4 Asymptotic Responses

Depending on the amplitude of the given loads, the two-bar system exhibit the four known long-term behaviors, namely purely elastic response, shakedown, alternating plasticity and incremental collapse.

4.1 Elastic Behavior

For sufficiently small external loads, the bars are in an elastic state. The stresses are easily obtained from Eqs. (15) by setting $\varepsilon_i^p = 0$ $(i = 1, 2)$

$$\begin{cases} \sigma_1 = \left(1 + \dfrac{1}{1 - \frac{\lambda\theta}{E_0}}\right)^{-1} (2\sigma_A - \alpha E_0 \theta) \\ \sigma_2 = \left(1 + \dfrac{1}{1 - \frac{\lambda\theta}{E_0}}\right)^{-1} \left[\dfrac{\sigma_A}{1 - \frac{\lambda\theta}{E_0}} + \dfrac{\alpha E_0 \theta}{2}\right] \end{cases} \tag{16}$$

The limiting values of stresses corresponding to the middle and the end of cycles for which respectively $\theta = \Delta\tau$ and $\theta = 0$ are summarized in Table 1.

Plastic strains appear in the structure as soon as stresses reach the yield limits. This may arise in different cases: $\sigma_1 \geq -\sigma_{y1}$ and $\sigma_2 \leq \sigma_{y2}$ at the middle of the cycle or $\sigma_1 \leq \sigma_{y1}$ at the end of the first cycle

$$(\sigma_A - \sigma_T)\left(1 - 2A\frac{\sigma_T}{\sigma_{y0}}\right) \geq -\sigma_{y0}\left(1 - A\frac{\sigma_T}{\sigma_{y0}}\right)\left(1 - 2B\frac{\sigma_T}{\sigma_{y0}}\right) \tag{17}$$

$$\sigma_A + \sigma_T - 2A\left(\frac{\sigma_T}{\sigma_{y0}}\right)^2 \sigma_{y0} \leq 2\sigma_{y0}\left(1 - A\frac{\sigma_T}{\sigma_{y0}}\right) \tag{18}$$

$$\sigma_A \leq \sigma_{y0} \tag{19}$$

Inequalities (17), (18), (19) define the elastic domain in the Bree diagram as shown in Fig. 3 for some values given in Table 10.

Note that for $A = 0$ and $B = 0$, the classical conditions corresponding to constant Young's moduli are found.

Table 2 Shakedown (SD1)

	Middle of a cycle	End of a cycle
ε_1^P	$\frac{2(\sigma_{y0}-(1+A+2B)\sigma_T+2A(1+B)\frac{\sigma_T^2}{\sigma_{y0}}+\sigma_A(1-A\frac{\sigma_T}{\sigma_{y0}}))}{E_0(1-A\frac{\sigma_T}{\sigma_{y0}})}$	
σ_1	$-\sigma_{y0}+2B\sigma_T$	$-\frac{\sigma_{y0}-(1+A+2B)\sigma_T+2A(1+B)\frac{\sigma_T^2}{\sigma_{y0}}}{(1-2A\frac{\sigma_T}{\sigma_{y0}})}$
ε_2^P	0	0
σ_2	$\frac{1}{2}(\sigma_{y0}+2\sigma_A-2B\sigma_T)$	$-\frac{\sigma_{y0}-(1+A+2B)\sigma_T+2A(1+B)\frac{\sigma_T^2}{\sigma_{y0}}+2\sigma_A(1-2A\frac{\sigma_T}{\sigma_{y0}})}{2(1-2A\frac{\sigma_T}{\sigma_{y0}})}$

4.2 Shakedown

Shakedown occurs if the plastic strain stabilizes after transient phase and the response of the structure becomes purely elastic. In other words, there is shakedown if the dissipated plastic energy remains bounded. The failure of the structure could happens after a great number of cycles (several hundreds of thousands even several million, for metallic materials): it is the polycyclic fatigue [1].

For the problem under consideration, different modes of shakedown are possible.

4.2.1 First Shakedown Mode (SD1)

Shakedown may arise if bar ♯1 develops some plastic strains during the first cycle (at the middle of the cycle) and then, if the loadings σ_A and σ_T are not too high, the structure has an elastic behavior. Thus after the first cycle, the plastic strain in bar ♯1 remains constant and the bar ♯2 evolves elastically.

These conditions are ensured by writing

$$\sigma_1 < -\sigma_{y1} \tag{20}$$

$$(\sigma_A - \sigma_T)\left(1 - 2A\frac{\sigma_T}{\sigma_{y0}}\right) \leq -\sigma_{y0}\left(1 - A\frac{\sigma_T}{\sigma_{y0}}\right)\left(1 - 2B\frac{\sigma_T}{\sigma_{y0}}\right) \tag{21}$$

and

$$\sigma_T \leq \frac{1+3A+2B-\sqrt{1-10A+9A^2+4B-4AB+4B^2}}{4(A+AB)}\sigma_{y0} \tag{22}$$

The set of inequations (20), (21), (22) permit one to draw the first shakedown domain $(SD1)$ in the Bree diagram, cf. Fig. 3.

The limiting states of stresses and plastic strains are reported in Table 2.

Table 3 Shakedown (SD2)

	Middle of a cycle	End of a cycle
ε_1^P	0	0
σ_1	$2(\sigma_A - \sigma_{y0})$	$-\frac{2\sigma_{y0}-(1+2A)\sigma_T+2A\frac{\sigma_T^2}{\sigma_{y0}}-2\sigma_A(1-A\frac{\sigma_T}{\sigma_{y0}})}{(1-2A\frac{\sigma_T}{\sigma_{y0}})}$
ε_2^P	$-\frac{2\sigma_{y0}-\sigma_A-\sigma_T(1+2A)+2A\frac{\sigma_T^2}{\sigma_{y0}}}{E_0(1-2A\frac{\sigma_T}{\sigma_{y0}})}$	
σ_2	σ_{y0}	$\frac{2\sigma_{y0}-(1+2A(1+\frac{\sigma_A}{\sigma_{y0}}))\sigma_T+2A\frac{\sigma_T^2}{\sigma_{y0}}}{2(1-2A\frac{\sigma_T}{\sigma_{y0}})}$

4.2.2 Second Shakedown Mode (SD2)

Now bar ♯2 develops plastic strain during the first cycle (middle of the first cycle) and then, the structure has an elastic behavior during the subsequent cycles.

The first condition writes

$$-2\sigma_{y0} + (1+2A)\sigma_T - 2A\frac{\sigma_T^2}{\sigma_{y0}} \geq -\sigma_A \tag{23}$$

Table 3 summarizes the stress and plastic strain field at the middle and the end of cycles.

The boundary of this shakedown domain is obtained by setting that bar ♯1 does not reach the yield stress in compression at the middle of the cycle and in tensile at the end of cycle:

$$\sigma_{y0} + 2B\sigma_T \leq 2\sigma_A \tag{24}$$

$$-\frac{3\sigma_{y0} - (1+4A)\sigma_T + 2A\frac{\sigma_T^2}{\sigma_{y0}}}{1 - A\frac{\sigma_T}{\sigma_{y0}}} \geq 2\sigma_A \tag{25}$$

The second shakedown domain $(SD2)$ is depicted in Bree diagram in Fig. 3.

4.2.3 Third Shakedown Mode (SD3)

Bar ♯1 develops plastic strain at the end of the first cycle when $\sigma_A \geq \sigma_{y0}$ while the two bars evolve elastically during the remainder of cycle. In Table 4, the limiting states are reported.

In order to obtain the limit of the domain called (SD3) in Fig. 3, we must write that the stress in bar ♯2 is less than the yield limit at the middle of cycles:

$$-\frac{3\sigma_{y0} - (1+4A)\sigma_T + 2A\frac{\sigma_T^2}{\sigma_{y0}}}{1 - A\frac{\sigma_T}{\sigma_{y0}}} \geq 2\sigma_A \tag{26}$$

Notice that this new condition is the same as (25).

Table 4 Shakedown (SD3)

	Middle of a cycle	End of a cycle
ε_1^P	$\frac{2(\sigma_A-\sigma_{y0})}{E_0}$	$\frac{2(\sigma_A-\sigma_{y0})}{E_0}$
σ_1	$\frac{(\sigma_{y0}-\sigma_T)(1-2A\frac{\sigma_T}{\sigma_{y0}})}{1-A\frac{\sigma_T}{\sigma_{y0}}}$	σ_{y0}
ε_2^P	0	0
σ_2	$\frac{2\sigma_A(1-A\frac{\sigma_T}{\sigma_{y0}})+(\sigma_T-\sigma_{y0})(1-2A\frac{\sigma_T}{\sigma_{y0}})}{2(1-A\frac{\sigma_T}{\sigma_{y0}})}$	$\frac{1}{2}(2\sigma_A-\sigma_{y0})$

Table 5 Shakedown (SD4)

	Middle of a cycle	End of a cycle
ε_1^P	$2\varepsilon_2^P+\varepsilon_1^P(SD1)$	$2\varepsilon_2^P+\varepsilon_1^P(SD1)$
σ_1	$-\sigma_{y0}+2B\sigma_T$	$-\frac{\sigma_{y0}-(1+A+2B)\sigma_T+2A(1+B)\frac{\sigma_T^2}{\sigma_{y0}}}{(1-2A\frac{\sigma_T}{\sigma_{y0}})}$
ε_2^P	$\frac{A((1+2B)\sigma_{y0}-2\sigma_A)(2\sigma_A-\sigma_y)+B(2(1+B)\sigma_A-(1+4B)\sigma_{y0})}{2BE_0(A+B-2A\frac{\sigma_A}{\sigma_{y0}})}$	
σ_2	$\frac{1}{2}(\sigma_{y0}+2\sigma_A-2B\sigma_T)$	$-\frac{\sigma_{y0}-(1+A+2B)\sigma_T+2A(1+B)\frac{\sigma_T^2}{\sigma_{y0}}+2\sigma_A(1-2A\frac{\sigma_T}{\sigma_{y0}})}{2(1-2A\frac{\sigma_T}{\sigma_{y0}})}$

4.2.4 Fourth Shakedown Mode (SD4)

For certain amplitude of mechanical and thermal loads, it may happen that before reaching the middle of the first cycle, some plastic strain is generated in bar ♯2 and then plastic strains cease developing in bar ♯2 during the second part of the cycle. Because of the stress yield decreasing with the temperature, the bar ♯1 develops plastic strain ε_1^p until the middle of the cycle and, after that, behaves elastically during the thermal unloading until the end of the cycle and during all next loads. In this shakedown domain referred to us by $(SD4)$ both bars shake down.

Limiting values of stress and plastic strain fields are given in Table 5.

The limit of this domain is obtained when bar ♯1 reaches the yield stress at the end of a cycle:

$$\sigma_T \leq \frac{1+3A+2B-\sqrt{1-10A+9A^2+4B-4AB+4B^2}}{4(A+AB)}\sigma_{y0} \qquad (27)$$

4.3 Alternating Plasticity

Alternating plasticity occurs when the response of the structure converges to hysteresis loop, leading to a stabilized cycle of plastic strain. In others words, plastic strains evolve during the cycle, but at the end of the cycle, they reach their initial

Table 6 Alternating plasticity (P1)

	Middle of a cycle	End of a cycle
ε_1^P	$\varepsilon_1^P(SD1)$	$\frac{2(\sigma_A-\sigma_{y0})}{E_0}$
σ_1	$-\sigma_{y0}+2B\sigma_T$	σ_{y0}
ε_2^P	0	0
σ_2	$\frac{1}{2}(\sigma_{y0}+2\sigma_A-2B\sigma_T)$	$\frac{1}{2}(2\sigma_A-\sigma_{y0})$

values. The structure may fail with a relatively low number of cycles, it is the low-cycle fatigue or the oligocyclic fatigue. As the energy dissipated by cycle (or plastic deformation cumulated by cycle) tends towards a constant value, it can be used as indicator of the severity of the damage induced by the cyclic loads [1].

4.3.1 First Alternating Plasticity Mode (P1)

Alternating plasticity arises if bar ♯1 undergoes some plastic strains at the middle and the end of the cycle in compression and traction respectively while bar ♯2 is any time in an elastic state. The limiting values of stresses and plastic strains are given in Table 6.

The amplitude of the limiting plastic strain loop is given by

$$\Delta\varepsilon_1^p=\varepsilon_{1max}^p-\varepsilon_{1min}^p=-\frac{4\sigma_{y0}-2(1+3A+2B)\sigma_T+4A(1+B)\frac{\sigma_T^2}{\sigma_{y0}}}{\left(1-2A\frac{\sigma_T}{\sigma_{y0}}\right)E_0} \tag{28}$$

and the mean value reads

$$\begin{aligned}\varepsilon_{1m}^p&=\frac{1}{2}\left(\varepsilon_{1max}^p+\varepsilon_{1min}^p\right)\\&=\frac{2\sigma_A\left(1-2A\frac{\sigma_T}{\sigma_{y0}}\right)-(1-A+2B)\sigma_T+2A(1+B)\frac{\sigma_T^2}{\sigma_{y0}}}{\left(1-2A\frac{\sigma_T}{\sigma_{y0}}\right)E_0}\end{aligned} \tag{29}$$

The domain (P1) is plotted in Fig. 3.

4.3.2 Second Alternating Plasticity Mode (P2)

As for the case of the forth shakedown case ($SD4$), bar ♯2 shakes down after developing some plastic strain ε_2^p before reaching the middle of cycles. On the contrary, in bar ♯1 plastic strains are developed at the middle and at the end of the cycles giving rise to hysteresis loop. Therefore, bar ♯1 and the whole system are in a reversed plasticity state.

The limiting states are reported in Table 7.

Notice that the only difference with the domain (P1) is that the bar ♯2 has developed some plastic strains during the first cycle.

Table 7 Alternating plasticity (P2)

	Middle of a cycle	End of a cycle
ε_1^P	$\varepsilon_1^P(SD1)$	$\frac{2(\sigma_A-\sigma_{y0})}{E_0}$
σ_1	$-\sigma_{y0}+2B\sigma_T$	σ_{y0}
ε_2^P	$\varepsilon_2^P(SD4)$	$\varepsilon_2^P(SD4)$
σ_2	$\frac{1}{2}(\sigma_{y0}+2\sigma_A-2B\sigma_T)$	$\frac{1}{2}(2\sigma_A-\sigma_{y0})$

Table 8 Ratcheting

	Middle of a cycle	End of a cycle
ε_1^P	$\varepsilon_1^{P0}+2(n-1)\varepsilon_{inc}^P$	$\varepsilon_1^{P0}+2n\varepsilon_{inc}^P$
σ_1	$2(\sigma_A-\sigma_{y0})$	σ_{y0}
ε_2^P	$\varepsilon_2^{P0}+(n-1)\varepsilon_{inc}^P$	$\varepsilon_2^{P0}+(n-1)\varepsilon_{inc}^P$
σ_2	σ_{y0}	$\frac{1}{2}(2\sigma_A-\sigma_{y0})$

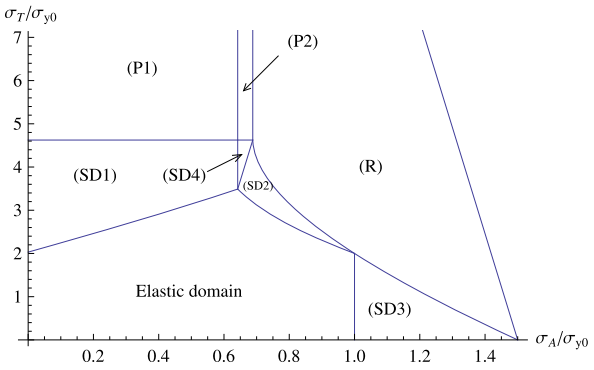

Fig. 3 Bree diagram of the two-bar system

4.4 Ratcheting (R)

When the load is high enough, stresses in both bars may reach the yield limits and a constant increment of plastic strain is developed at every cycle. The structure will collapse by plastic strain accumulation (incremental collapse).

The stresses and the plastic strain are given in Table 8 where

$$\varepsilon_{inc}^P=-\frac{3\sigma_{y0}-(1+4A)\sigma_T+2A\frac{\sigma_T^2}{\sigma_{y0}}-2\sigma_A\left(1-A\frac{\sigma_T}{\sigma_{y0}}\right)}{\left(1-2A\frac{\sigma_T}{\sigma_{y0}}\right)E_0}$$

It is worth noting that the starting values ε_1^{P0} and ε_2^{P0} depend on the initial load and the previous domain, see Fig. 3. For example, if $\sigma_A \geq \sigma_{y0}$ therefore $\varepsilon_1^{P0} = \varepsilon_1^P(SD3)$ and $\varepsilon_2^{P0}=0$.

4.5 Collapse

The structure will collapse if $\sigma_1 > \sigma_{y1}$ and $\sigma_2 > \sigma_{y2}$. This can happen when the temperature is very high. It is found that the first condition is more severe than the second one and consequently the condition for collapse reads

$$\sigma_1 > \sigma_{y1} \quad \Leftrightarrow \quad 2(\sigma_A - \sigma_{y0}) > \sigma_{y0} - B\sigma_T \tag{30}$$

5 Residual Stress and Strain Fields

Here, we focus our attention on the evolution of the residual stress and strain fields. As already mentioned in Sect. 1, the residual stresses are given by

$$\boldsymbol{\rho}(x,t) = \boldsymbol{\sigma}(x,t) - \boldsymbol{\sigma}^E(x,t)$$

Recall that in the classical case, Melan-Koiter shakedown theorems ensure that $\boldsymbol{\rho}$ is time-independent.

For the two-bar truss, closed-form expression of $\boldsymbol{\rho}$ can be easily obtained basing upon Eqs. (15), (16)

$$\begin{cases} \rho_1 = 2E_0\left(1 + \dfrac{1}{1 - \frac{\lambda\theta}{E_0}}\right)^{-1}\left(\varepsilon_2^P - \dfrac{\varepsilon_1^P}{2}\right) \\ \rho_2 = E_0\left(1 + \dfrac{1}{1 - \frac{\lambda\theta}{E_0}}\right)^{-1}\left(\varepsilon_2^P - \dfrac{\varepsilon_1^P}{2}\right) \end{cases} \tag{31}$$

It is obvious from Eq. (31) that even when shakedown occurs (plastic strains of the two bars are constant), the residual stress field varies with respect to the temperature because of the presence of the temperature θ in the analytic expressions of ρ_i, $i \in \{1, 2\}$.

Let us know examine the evolution of the elastic residual strain field given by the following relation

$$\boldsymbol{\eta}^e(x,t) = \mathbf{S}(x,t) : \boldsymbol{\rho}(x,t)$$

where $\mathbf{S}$ is the compliance tensor.

For the problem under consideration, one obtains

$$\begin{cases} \eta_1^e = \dfrac{2}{2 - \frac{\lambda\theta}{E_0}}\left(\varepsilon_2^P - \dfrac{\varepsilon_1^P}{2}\right) \\ \eta_2^e = \left(1 + \dfrac{1}{1 - \frac{\lambda\theta}{E_0}}\right)^{-1}\left(\varepsilon_2^P - \dfrac{\varepsilon_1^P}{2}\right) \end{cases} \tag{32}$$

Observe that neither η_1^e nor η_2^e is time-independent even for shakedown.

Table 9 Elastic response with initial residual stresses

	Middle of a cycle	End of a cycle
ε_1^P	$\varepsilon_1^P(0)$	$\varepsilon_1^P(0)$
σ_1	$\frac{(\sigma_A-\sigma_T-\rho_1(0))(1-2A\frac{\sigma_T}{\sigma_{y0}})}{1-A\frac{\sigma_T}{\sigma_{y0}}}$	$\sigma_A-\rho_1(0)$
ε_2^P	$\varepsilon_2^P(0)$	$\varepsilon_2^P(0)$
σ_2	$\frac{(\sigma_A+\sigma_T-2A(\frac{\sigma_T}{\sigma_{y0}})^2\sigma_{y0})-2\rho_2(0)(1-2A\frac{\sigma_T}{\sigma_{y0}})}{2-2A\frac{\sigma_T}{\sigma_{y0}}}$	$\frac{\sigma_A}{2}-\rho_2(0)$

6 Influence of the Initial State

Let us examine the influence of the initial state on the response of the structure. We suppose that at time $t=0$ there exist nonvanishing plastic strains $\varepsilon_1^p(0)$ and $\varepsilon_2^p(0)$ in bar ♯1 and bar ♯2 respectively. The correspondent initial residual stress field induced in the mechanical system are given by

$$\rho_1(0)=\frac{E_0}{2}\left(2\varepsilon_2^p(0)-\varepsilon_1^p(0)\right) \tag{33}$$

$$\rho_2(0)=-\frac{E_0}{4}\left(2\varepsilon_2^p(0)-\varepsilon_1^p(0)\right) \tag{34}$$

Notice those residual stresses must be plastically admissible:

$$-\sigma_{1y}(0)=-\sigma_0\le\rho_1(0)\le\sigma_{1y}(0)=\sigma_0 \tag{35}$$

$$-\sigma_{y2}=-\sigma_0\le\rho_2(0)\le\sigma_{y2}=\sigma_0 \tag{36}$$

The method of solution is the same as the one in the previous section.

The elastic domain is of course modified and Table 9 resumes the limiting values of stresses with initial residual stresses.

The elastic zone is defined by the same conditions (17), (18), (19) but with the apparition of the residual stresses:

$$\left(\sigma_A-\sigma_T-\rho_1(0)\right)\left(1-2A\frac{\sigma_T}{\sigma_{y0}}\right)\ge-\sigma_{y0}\left(1-A\frac{\sigma_T}{\sigma_{y0}}\right)\left(1-2B\frac{\sigma_T}{\sigma_{y0}}\right)$$

$$\sigma_A+\sigma_T-2A\left(\frac{\sigma_T}{\sigma_{y0}}\right)^2\sigma_{y0}-2\rho_2(0)\left(1-2A\frac{\sigma_T}{\sigma_{y0}}\right)\le2\sigma_{y0}\left(1-A\frac{\sigma_T}{\sigma_{y0}}\right)$$

$$\sigma_A-\rho_1(0)\le\sigma_{y0}$$

We must notice that for certain values of the residual stresses some shakedown domains disappear from the Bree diagram. More precisely, for $\rho_1(0)\ge\frac{\sigma_{y0}}{2}$, the domain $(SD3)$ does not exist in the diagram, and for

$$\rho_1(0)\le\frac{A(-2+B)+B(1+2B)-B\sqrt{9A^2+(1+2B)^2-2A(5+2B)}}{4A(1+B)}\sigma_{y0}$$

Table 10 Characteristics of the bars

Cross-section area S (m^2)	1×10^{-5}
Length of the bar ♯1 (cm)	10
E_0 (Pa)	2.1×10^{11}
ν	0.3
α ($°C^{-1}$)	1.17×10^{-5}
σ_{y0} (MPa)	200
λ (MPa)	320
λ_2 (MPa)	0.2

then the domains $(SD2)$ and $(SD4)$ disappear. Furthermore, the presence of the initial plastic strains does not change the curves's shapes which define the shakedown, ratcheting and alternating plasticity zones. It only introduces additional constant terms in the limiting values of stresses and in the plastic strains expressions.

It is important to underline that the residual stresses and residual strains are again time-dependent when shakedown occurs.

7 Numerical Study

In this section, numerical results performed by incremental finite element procedure are presented. Two numerical simulations are carried out over a number of loading cycles by the software ABAQUS and stored separately: (i) full elastic-plastic analysis under the thermo-mechanical path loading and (ii) purely elastic results under the same loads. The status of the response (shakedown or ratcheting or alternating plasticity) is numerically checked by observing the evolution of the plastic strain tensor $\boldsymbol{\varepsilon}^p(t)$ in the whole structure and its cumulative value $\int_0^t \boldsymbol{\varepsilon}^p(s)ds$. Besides, the residual stress field $\boldsymbol{\rho}(t)$ is simply computed at Gauss-points by the relation $\boldsymbol{\rho}(t) = \boldsymbol{\sigma}(t) - \boldsymbol{\sigma}^E(t)$ and the elastic residual strain field is obtained by $\boldsymbol{\eta}^e(t) = \boldsymbol{\varepsilon}(t) - \boldsymbol{\varepsilon}^E(t) - \boldsymbol{\varepsilon}^p(t)$.

Each bar is modeled by one truss/bar element T2D2T of uniform cross-section bounded by two nodes. The geometric and mechanical characteristics of the trusses are given in Table 10.

First, we were interested to reproduce numerically the Bree diagram plotted in Fig. 3. To this end, several computations were carried out in the following manner: one maintains constant the mechanical load F and increases gradually the amplitude of the thermal load until the response changes the status. Graphically this corresponds to run within the Bree diagram in Fig. 3 along a vertical path. It is checked that numerical bounds of different domains lie exactly on the analytical curves.

Figure 4 illustrates the time-evolution of the stress plastic strain field ε_1^p in bar ♯1 for shakedown (SD1) ($F = 2000$ N, $\Delta\tau = 280$ °C), reverse plasticity (P1) ($F = 2000$ N, $\Delta\tau = 350$ °C) and ratcheting ($F = 4300$ N, $\Delta\tau = 150$ °C). These diagrams evolution are typical of the three mentioned classical asymptotic behaviors.

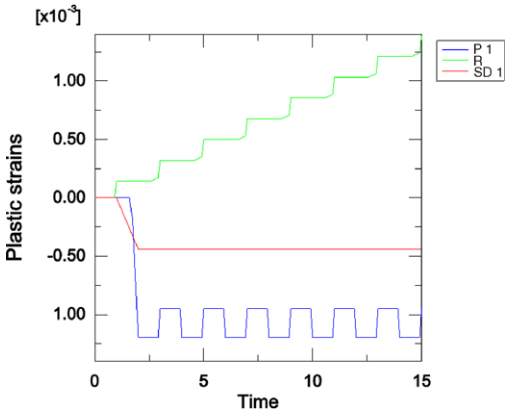

Fig. 4 Evolution of the plastic strains ε_1^P in bar ♯1

Let us focus our attention now to the zones $(SD4)$ and $(P2)$. Time-evolution of the plastic strains in the bars for an arbitrary points in $(DS4)$ domain ($F = 2600$ N, $\Delta\tau = 310$ °C) and in $P2$ ($F = 2600$ N, $\Delta\tau = 335$ °C) are reported in Fig. 5. It can be observed that in $(SD2)$ the plastic strains stabilize in both bars while in domain $(P2)$ bar ♯1 adapts to the loads and the plastic strain in bar ♯2 is cyclic. Observe also that in both cases, plastic strain ε_1^p is generated before the middle of the first cycle. This scenario was suggested in analytical analysis.

In Fig. 6, we display the time evolution of the elastic residual strain $\boldsymbol{\eta}^e$ of bar ♯1. It is clear that this field is evolves cyclically with the same period as the one of the loads even in the case of shakedown as it is found analytically.

Finally, it is worth noting that all numerical results presented in this section are in an excellent agreement with the analytical ones.

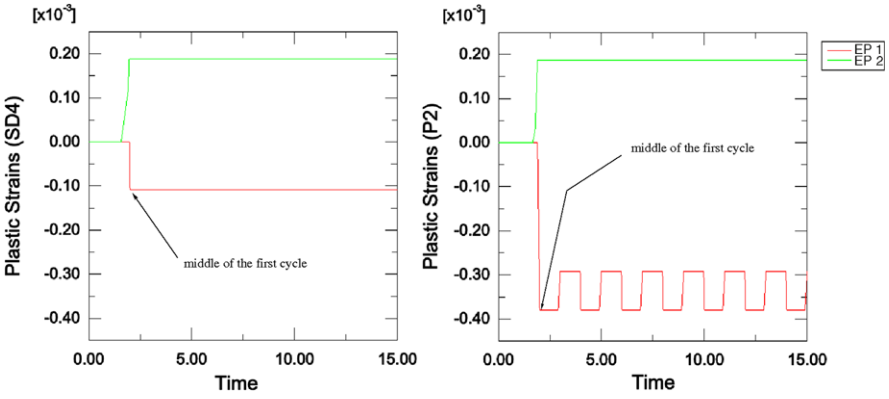

Fig. 5 Plastic strain evolution: shakedown $(SD4)$ (*left*) and alternating plasticity $(P2)$ (*right*)

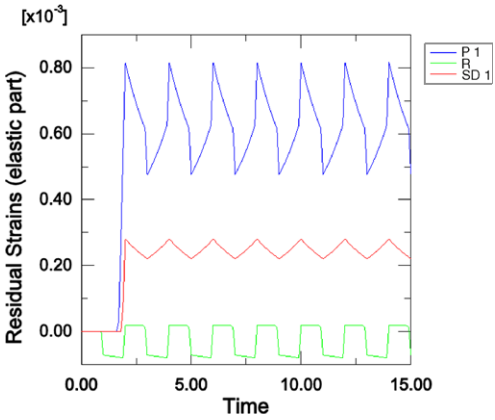

Fig. 6 Elastic residual strain evolution

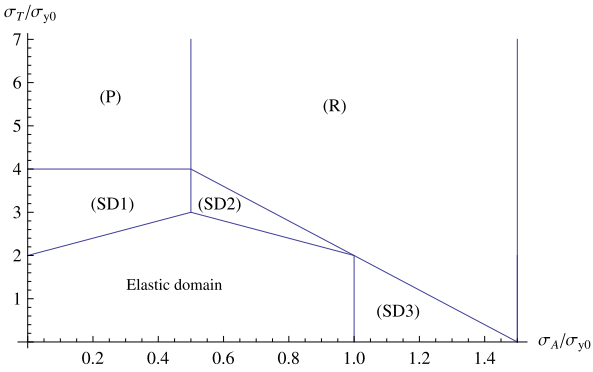

Fig. 7 Bree diagram of the two-bar system when the elastic modulus are constant

8 Discussion

Let us compare the Bree diagrams when the elastic properties are constant (Fig. 7) and when they are temperature-dependent (Fig. 3). For the last case, two new domains (SD2) and (P2) appear in the diagram. Further, the elastic and shakedown domains are bigger when the Young modulus and the yield stress change with temperature.

It is worth noting that depending on the coefficients A and B loss of the convexity of the elastic and shakedown domains may by pronounced as shown in Fig. 8. Recall that the convexity of yield function is the most important ingredient of the mathematical theory of elastoplasticity. It is our belief that it should be interesting to revisit the thermodynamic of continuum media with the assumption of temperature-dependence of elastic modulus and examine the convexity of the elastic domain.

Besides we found that the residual stresses are time-dependent when shakedown occurs. The explication of this fact is rather simple. In fact it is well known that the

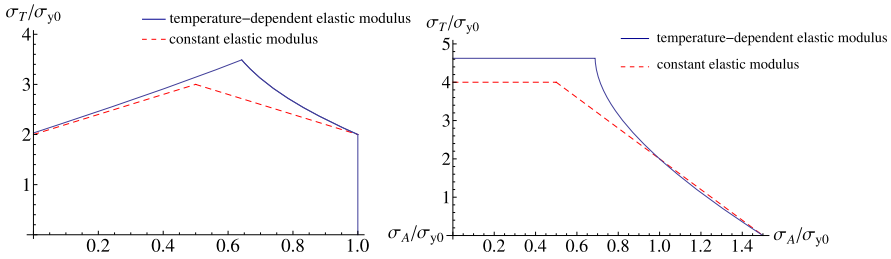

Fig. 8 Elastic domains (*left*) and shakedown zones (*right*) when the elastic modulus are constant and when they are temperature-dependent

residual stresses are solution of the following problem

$$\begin{cases} div\,\boldsymbol{\rho} = 0 \quad \text{in } \Omega \\ \boldsymbol{\varepsilon}^r = grad_S\,\mathbf{u}^r = \mathbf{S} : \boldsymbol{\rho} + \boldsymbol{\varepsilon}^p \quad \text{in } \Omega \\ \boldsymbol{\rho} \cdot n = 0 \quad \text{on } \Gamma_T \\ \mathbf{u}^r = 0 \quad \text{on } \Gamma_u \end{cases}$$

Thus, $\boldsymbol{\rho}$ is the solution of an elastic problem with initial strains equal to $\boldsymbol{\varepsilon}^p$. Therefore, $\boldsymbol{\rho}$ is linear with respect to $\boldsymbol{\varepsilon}^p$. Following Zarka et al. [16], one may write symbolically

$$\boldsymbol{\rho} = \mathbf{Z}_0 : \boldsymbol{\varepsilon}^p \tag{37}$$

where the linear operator $\mathbf{Z}_0$ introduced by Zarka et al., is symmetric, non-positive and generally singular. Furthermore, in our case, $\mathbf{Z}_0$ is temperature-dependent and thus time-dependent. Consequently $\boldsymbol{\rho}$ is time-dependent even if $\boldsymbol{\varepsilon}^p$ is constant (shakedown).

For the elastic residual strains, one does not dispose of theoretical arguments to confirm if $\boldsymbol{\eta}^e$ is constant or not when shakedown occurs. However, inspiring from the classical case and Eq. (9), Halphen has proposed a conjecture mentioned in Section 1 that says a sufficient condition for shakedown is that $\boldsymbol{\eta}^e$ is time-independent. Nevertheless, it is found analytically and numerically that this statement is not fulfilled and $\boldsymbol{\eta}^e$ is periodic.

9 Conclusion

This chapter attempts to give insight into the asymptotic response of solids subjected to cyclic thermomechanical loadings when the elastic properties vary with temperature. An academic but instructive example of a two-bar truss has been studied analytically and numerically. We have shown that the structure converges always to a periodic state (shakedown, alternating plasticity or ratcheting). Compared to the classical case, the Bree diagram is considerably modified: (i) the elastic and shakedown domains are bigger and (ii) new elastic and plastic shakedown appear (SD2

and P2) when elastic properties vary with the temperature. Further, loss of convexity of the elastic and shakedown domains may arise. The most important result is that the residual stress and strain field are time-dependent and are periodic with the same period as of the thermal load when shakedown occurs. It is also observed that for this simple structure, analytical and numerical results are in an excellent agreement.

References

1. Constantinescu, A., Van Dang, K., Maitournam, H.: A unified approach for high and low cycle fatigue based on shakedown concepts. Eng. Mater. Struct. **26**, 567–568 (2003)
2. Bleich, H.: Über die bemessung statisch unbestimmter stahltragwerke unter berüschsichtigung der elastisch-plastischen verhaltens des baustoffes. J. Bauingenieur **19**, 261–269 (1932)
3. Melan, E.: Theorie statisch unbestimmter Systeme aus ideal-plastischem Baustoff. Sitzber. Akad. Wiss. Wien, IIa **145**, 195–218 (1936)
4. Melan, E.: Zur plastizität des räumlichen Kontinuums. Ing.-Arch. **8**, 116–126 (1938)
5. Koiter, W.: General problems for elastic-plastic solids. In: Sneddon, Hill (ed.) Progress in Solid Mechanics, vol. 4, pp. 165–221. North-Holland, Amsterdam (1960)
6. Pham, D.C.: Shakedown static and kinematic theorems for elastic-plastic limited linear kinematic-hardening solids. Eur. J. Mech. A, Solids **56**, 1905–1915 (2008)
7. Pham, D.C.: On shakedown theory for elastic-plastic materials and extensions. J. Mech. Phys. Solids **56**, 1905–1915 (2008)
8. Bouby, C., de Saxcé, G., Tritsch, J.-B.: A comparison between analytical calculations of the shakedown load by the bipotential approach and step-by-step computations for elastoplastic materials with nonlinear kinematic hardening. Int. J. Solids Struct. **43**, 2670–2692 (2006)
9. Prager, W.: Shakedown in elastic plastic media subjected to cycles of load and temperature. In: La Plasticità nella Scienza delle Costruzioni. Proc. A. Dannuso Symp, Zanichelli, Bologna, pp. 239–244 (1956)
10. Borino, G.: Consistent shakedown theorems for materials with temperature dependent yield functions. Int. J. Solids Struct. **37**, 3121–3147 (2000)
11. Khôi Vu, D., Staat, M.: Shakedown analysis of structures made of materials with temperature-dependent yield stress. Int. J. Solids Struct. **44**, 4524–4540 (2007)
12. Halphen, B.: Elastic perfectly plastic structures with temperature dependent elastic coefficients. C. R., Méc. **33**, 617–621 (2005)
13. König, J.A.: A shakedown theorem for temperature dependent elastic moduli. Bull. Acad. Pol. Sci., Ser. Sci. Tech. **17**, 161 (1968)
14. Halphen, B., di Domizio, S.: Evolution des structures élastoplastiques dont les coefficients d'élasticité dépendent de la température. In: 17ème congrès français de mécanique, Troyes (2005)
15. di Domezio, S.: Structures élastoplastiques sous chargement cyclique: équation d'évolution de la contrainte résiduelle. Stage at Ecole Polytechnique (2005)
16. Zarka, J., Frelat, J., Inglebert, G., Kasmai-Navidi, P.: A New Approach in Inelastic Analysis of Structures. Ecole Polytechnique, Paris (1990)

A Multiphase Model for Assessing the Overall Yield Strength of Soils Reinforced by Linear Inclusions

Patrick de Buhan and Ghazi Hassen

Abstract Conceived as an extended homogenization procedure, a multiphase approach for ascertaining the macroscopic behavior of reinforced soil structures has been developed in the last years. This contribution is dedicated to the evaluation of the yield strength properties of soils reinforced by linear inclusions by making use of a homogenization procedure, in which the reinforced soil is regarded as a periodic composite, as a first calculation, and using the multiphase model. It appears from such a calculation that only the multiphase model is able to capture scale and boundary effects, which may play an important role in the yield design of reinforced structures. The decisive element is the introduction of a parameter characterizing the strength of the interaction between two continuous media ("phases") representing the soil and the reinforcing inclusions, respectively. A preliminary analysis suggests that such a parameter varies in direct proportion to the inverse of a scale factor.

1 Introduction

A large range of soil reinforcement techniques used to improve soil structures stiffness and strength consist in incorporating into the soil mass a distribution of unidirectional inclusions made of steel or concrete. Beyond the differences as regards the construction mode of such reinforced structures, they undeniably exhibit some common futures which can be summarized as follows:

- The reinforcing inclusions usually take the form of linear structural elements (metal or polymeric strips or bars, concrete piles, ...) incorporated into the soil mass following a regular (periodic) arrangement and one or several preferential orientations, in much the same way as for industrial fibre composite materials, although at a quite different scale.

P. de Buhan (✉) · G. Hassen
UR Navier, Ecole des Ponts ParisTech, Université Paris Est, 6 et 8 av. B. Pascal,
77455 Marne-la-Vallée, France
e-mail: patrick.debuhan@enpc.fr

G. Hassen
e-mail: ghazi.hassen@enpc.fr

G. Saxcé et al. (eds.), *Limit State of Materials and Structures*,
DOI 10.1007/978-94-007-5425-6_9,

- The mechanical properties of the reinforcing material are considerably higher than those of the native soil: concrete or steel yield strength is 1000–10000 times greater than that of a soft clay or a sand.
- The volume fraction of the reinforcing material is quite small, remaining in most cases lower than few percents.

The strong heterogeneity of the composite reinforced soil associated with the relatively high number of the reinforcing inclusions involved in such reinforcement techniques, makes it very difficult to set up appropriate design-oriented calculation methods in which the inclusions would be treated as individual elements embedded in the soil. Indeed, a fully three dimensional analysis to take into account the cylindrical shape of the reinforcements and a locally refined mesh to capture with sufficient accuracy the complex interaction between the soil and the inclusions would be required. This would lead to oversized numerical problems and thus a time consuming calculation methods incompatible with an engineering design approach.

As an alternative approach to direct numerical simulations, the periodic homogenization technique [1, 2] appears to be a good alternative since the heterogeneous composite material is replaced by a homogeneous anisotropic medium. Another way to set up design methods for soil structures reinforced with linear inclusions consists in the application of the multiphase model, which has been developed in the last decade.

The objective of this paper is to point out the shortcomings of such a homogenization procedure and to show how a multiphase approach, perceived as an extension of the homogenization concept, is able to capture "scale" as well as "boundary effects", which may have important consequences in the yield design of reinforced soils structures.

2 Macroscopic Strength Condition of a Unidirectionally Reinforced Soil

The determination of the macroscopic strength condition of a material reinforced by one single family of parallel cylindrical inclusions could be performed by making use of the homogenization theory for periodic media implemented in the context of yield design (limit analysis). It relies upon the solution to a yield design boundary value problem defined over the reinforced soil's representative unit cell sketched in Fig. 1 [1, 2].

Denoting by s the spacing between two neighboring inclusions, and by R and t the radius and the thickness of the reinforcing inclusions, respectively, the reinforcement volume fraction is equal to the ratio between the inclusion and the unit cell cross sectional areas:

$$\eta = \frac{2\pi Rt}{s^2} \tag{1}$$

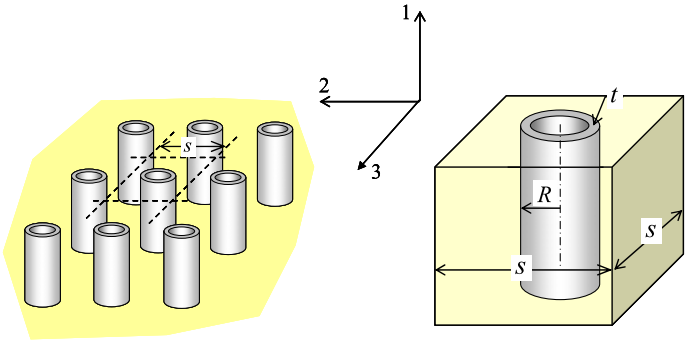

Fig. 1 Representative unit cell of a soil reinforced by tubular inclusions

As regards most types of reinforced soil structures, the volume fraction η is very small, rarely exceeding 5 %, whereas the strength of the reinforcing material is considerably higher than that of the soil. This situation can be mathematically obtained by making the volume fraction tend to zero while the product of this volume fraction by the reinforcing material's uniaxial yield strength σ_r^{Y} is kept constant:

$$\eta \to 0 \quad \text{as} \quad \eta\sigma_r^{\mathrm{Y}} = \sigma_0 = ct \tag{2}$$

where σ_0 may be interpreted as the tensile (compressive) resistance of the reinforcing inclusions per unit transverse area. Under such circumstances, it can be shown [3] that, assuming perfect bonding at the interface between the inclusion and the surrounding soil, the macroscopic strength condition of the reinforced soil simply reduces to:

$$F(\underline{\underline{\Sigma}}) \leq 0 \quad \Leftrightarrow \quad \begin{cases} \underline{\underline{\Sigma}} = \underline{\underline{\sigma}}^s + \sigma\, \underline{e}_1 \otimes \underline{e}_1 \\ f(\underline{\underline{\sigma}}^s) \leq 0, \quad |\sigma| \leq \sigma_0 \end{cases} \tag{3}$$

where $f(.)$ denotes the soil's strength condition. The above simplified criterion proves also valid for plane strain-loaded multilayered materials under the same condition as (2) [4, 5]. For a purely cohesive soil (soft clay) characterized by a cohesion or undrained shear strength equal to C, the macroscopic strength condition, expressed under plane strain conditions parallel to the reinforcement direction, writes [2]:

$$F(\underline{\underline{\Sigma}}) \leq 0 \quad \Leftrightarrow \quad \Sigma_{\mathrm{M}} - \Sigma_{\mathrm{m}} \leq 2C^{\mathrm{hom}}(\alpha) \tag{4}$$

where Σ_{M} (resp. Σ_{m}) is the major (resp. minor) principal stress and α its orientation with respect to the reinforcement direction. The reinforced soil thus appears to be a purely cohesive anisotropic medium, with its cohesion, represented in Fig. 2(b) in the form of a polar diagram, varying from that of the native soil (C) for $\alpha = \pm 45°$ to a maximum value equal to $C + \sigma_0/2$ for $\alpha = 0°, 90°$.

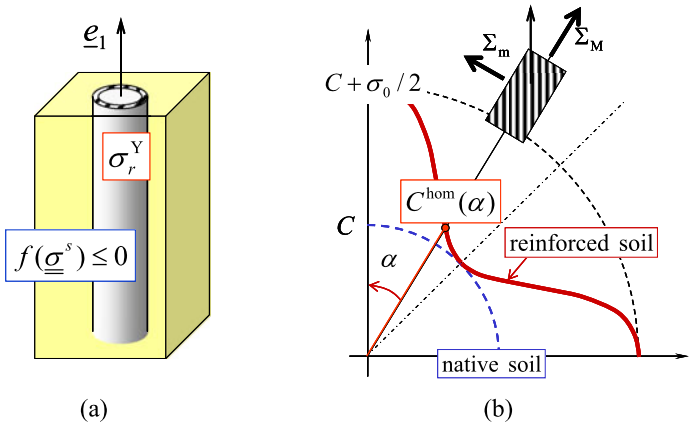

Fig. 2 (**a**) Representative unit cell of reinforced soil. (**b**) Polar diagram for a unidirectionally reinforced purely cohesive soil

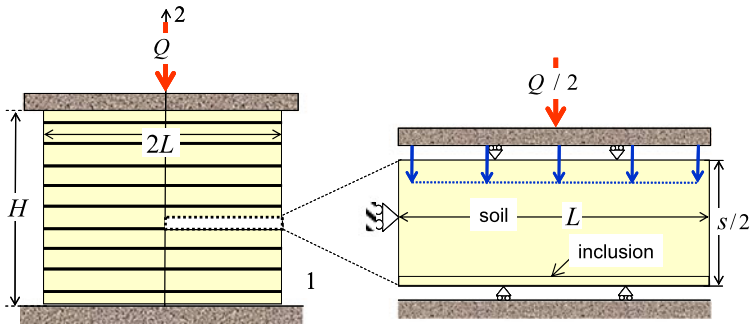

Fig. 3 Compressive strength of a purely cohesive reinforced block: initial and auxiliary problems

3 A Partial Validation of the Homogenization Approach

The problem under consideration is that of a block of height H and half-width L, subjected to a compression test in plane strain conditions in the Oxy-plane. This block has been reinforced with regularly placed horizontal inclusions (Fig. 3) and placed between two rigid planes in smooth contact with its upper and bottom sections. The upper plane is moving down and then applying a compressive loading Q to the block whereas the lower plane is fixed. The two lateral sides are stress free.

According to the homogenization procedure, the composite material is modeled as a homogeneous anisotropic purely cohesive medium for which the corresponding yield function is expressed by (4). Referring to the lower bound static approach of yield design for the above problem, a homogeneous stress field of the form:

$$\underline{\underline{\Sigma}} = \Sigma_{22} \underline{e}_2 \otimes \underline{e}_2 + \Sigma_{33} \underline{e}_3 \otimes \underline{e}_3, \quad \Sigma_{22} \le \Sigma_{33} \le 0 \tag{5}$$

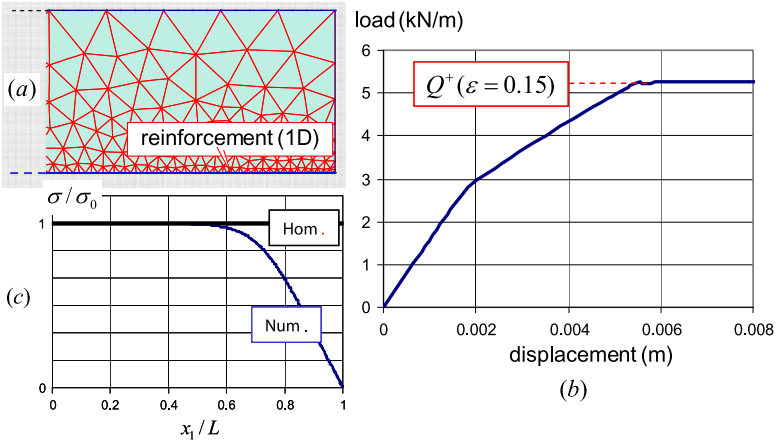

Fig. 4 Results of elastoplastic simulation for $\varepsilon = 0.15$: (**a**) finite element mesh; (**b**) computed load–displacement curve; (**c**) "at failure" stress distribution in the reinforcement

is considered, where the major principal stress is then equal to zero ($\Sigma_{11} = \Sigma_M = 0$) while the minimum (maximum compressive stress) is $\Sigma_m = \Sigma_{22}$, so that $\alpha = 0$. The strength condition (4) may thus be written:

$$\Sigma_M - \Sigma_m = 0 - \Sigma_{22} \leq 2C^{\text{hom}}(\alpha = 0^\circ) = \sigma_0 + 2C \tag{6}$$

It follows immediately that a lower bound value to the compressive strength of the reinforced block is:

$$Q^+_{\text{hom}} \geq 4CL[1 + \sigma_0/2C] \tag{7}$$

which turns out to be the exact value upon applying the upper bound kinematic approach.

The validity of such a procedure is now assessed by comparing the obtained compressive strength (7) with a direct numerical simulation of the same problem, where for the sake of simplicity, but without any loss of generality, the reinforced soil is modeled as a multilayered material in which the reinforcements are treated as 1D beam elements, equally spaced by a distance s throughout the block, so that a "scale factor" defined by the spacing to half-width ratio, may be introduced:

$$\varepsilon = s/L \tag{8}$$

Making use of the symmetry and the periodicity conditions, it could be easily proved that the numerical simulation of the plane strain compression test could be performed by solving the boundary value problem attached to a representative "slice" of the reinforced block (Fig. 2). The corresponding limit loads Q^+ have been evaluated numerically by means of the finite element computer code PLAXIS [6]. As sketched in Fig. 4, the soil mass is discretized into 6-noded triangular elements whereas the reinforcing inclusion is modeled as a beam. An elastoplastic calculation

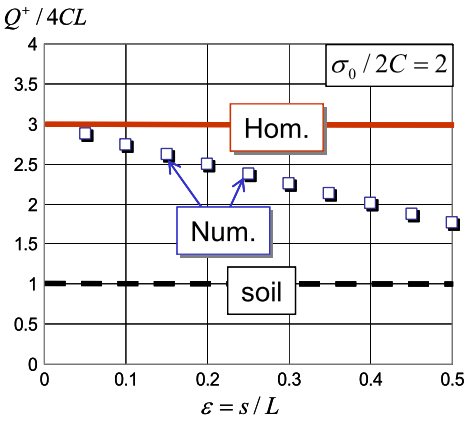

Fig. 5 Homogenization vs. f.e.m. numerical simulations

is performed, until failure, for several values of the scale factor ε ranging between 0.05 and 0.5. It is worth noting that the computational time for each elastoplastic calculation up to failure, represented by a load-displacement curve (Fig. 4(b)), does not exceed one minute on any standard PC.

Figure 4(c) displays the uniaxial stress distribution in the inclusion at failure and the corresponding distribution predicted by the homogenization theory. This comparison shows a perfect agreement of the results obtained by both methods in the central part of the reinforced structure. However, the f.e.m. and homogenization results strongly diverge when approaching the lateral sides of the block.

The variation of the non-dimensional parameter $Q^+/4CL$ as a function of the scale factor is represented in Fig. 5. The comparison between the numerical and homogenization method results clearly shows that the latter fails to capture the "scale effect" due to the variation of the scale factor. Indeed, the f.e.m numerical results converge to that predicted by the homogenization method as the scale factor tends to zero:

$$\lim_{\varepsilon \to 0} Q^+(\varepsilon) = Q^+_{\text{hom}} \tag{9}$$

thus confirming the well known convergence result of the homogenization approach, but the latter may significantly overestimate the actual value of the compressive resistance if the scale factor is not sufficiently small. Such a "scale effect" is obviously of no consequence as far as industrial composite materials are concerned (leaving aside purely local effects associated with brittle failure, such as delamination phenomena), but remains a relevant question for reinforced soils, since the scale factor is generally of the order of 0.1–0.3 for this kind of composite material.

4 Multiphase Model as an Extended Homogenization Method

An extension of the classical periodic homogenization method, namely the multiphase model, has been proposed in the last decade, allowing to assess the macro-

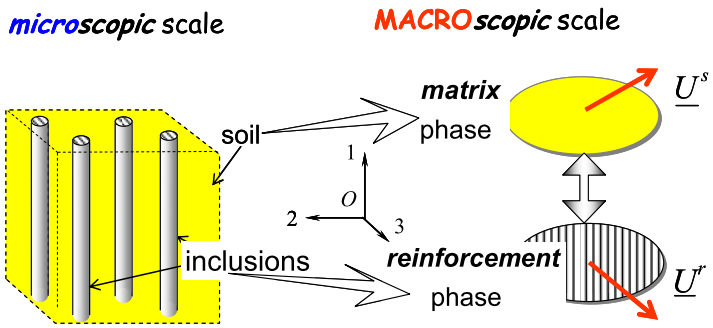

Fig. 6 Principle of the multiphase model for reinforced soils

scopic behavior of reinforced soil structures taking "scale" as well as "boundary" effects into account.

The intuitive idea of the multiphase model is to homogenize separately the soil on the one hand and the array of reinforcing inclusions, on the other hand. The thus obtained interacting continuous media, called the "matrix" and the "reinforcement" phases, are given two different kinematics, namely a velocity field $\underline{U}^s$ for the matrix, representing the soil mass, and $\underline{U}^r$ for the reinforcement phase (Fig. 6). The multiphase model could be derived from the virtual work method (see [7] for more details) and leads to the decomposition of the macroscopic total stress $\underline{\underline{\Sigma}}$ as a sum of the "partial" stresses relating to the soil and the reinforcement.

A more detailed presentation of the multiphase model may be found in [7] or [8], in the context of an elastic behavior of the different constituents. The general governing equations of the model, will now be presented in the context of the yield design theory.

The equilibrium equations are written for each phase separately, that is in the absence of any external body force, as:

$$\operatorname{div} \underline{\underline{\sigma}}^s + I \underline{e}_1 = 0 \tag{10}$$

for the matrix phase, representing the soil, and:

$$\operatorname{div}(\sigma \underline{e}_1 \otimes \underline{e}_1) - I \underline{e}_1 = 0 \tag{11}$$

for the reinforcement phase, where I denotes the interaction body force density. These equations are completed by stress conditions defined on the boundary surface of each phase independently. Referring to a yield design boundary problem for any such two-phase system, it is necessary to specify the strength condition at any point of each phase, namely:

$$f\left(\underline{\underline{\sigma}}^s\right) \leq 0 \quad \text{and} \quad |\sigma| \leq \sigma_0 \tag{12}$$

for the individual phases, along with an interaction strength condition of the form:

$$|I| \leq I_0 \tag{13}$$

In the situation of "perfect bonding", characterized by the fact that the interaction strength parameter I_0 takes an infinite value, it is quite apparent from summing up Eqs. (10) and (11), and thus eliminating the interaction force density, that the yield design homogenization method is recovered.

The stability analysis of a block of reinforced soil, previously considered in the light of the homogenization method, is now revisited within the context of the multiphase model. The compressive strength of the reinforced block is thus defined as the maximum value of Q for which it is possible to exhibit a couple of stress fields, $\underline{\underline{\sigma}}^s$ in the matrix phase and σ in the reinforcement phase, along with an interaction force density I, satisfying both the equilibrium equations (10) and (11) along with the boundary conditions specified for each phase independently, and the respective strength conditions (12) and (13).

It is to be noted that the strength properties of the multiphase system depend on the strength properties of the different constituents: the soil's cohesion C for the matrix and the reinforcement uniaxial strength density σ_0 for the reinforcement phase, whereas the interaction strength parameter I_0 depends on several parameters and could be determined through a numerical procedure which is presented in Sect. 5.

The kinematic approach of yield design is based on the "dualization" of the equilibrium equations of the multiphase system by making use of the virtual work principle. Denoting by $\{\hat{\underline{U}}^s, \hat{\underline{U}}^r\}$ any virtual velocity field, kinematically admissible for the boundary value problem, this principle writes:

$$W_e\left(\underline{U}^s, \underline{U}^r\right) = W_i\left(\underline{U}^s, \underline{U}^r\right) \tag{14}$$

where W_e (resp. W_i) represents the virtual work of external (resp. internal) efforts for the two-phase system. It is worth noting that the interaction body force density I exerted on the matrix phase must be considered as an external effort for the latter but, as regards the multiphase system as a whole, this volume density is an internal effort since it corresponds to an interaction between two subsystems (matrix and reinforcement phases) of the reinforced volume Ω.

In the case of a loading depending on n parameters, the virtual work of external forces writes:

$$W_e\left(\underline{U}^s, \underline{U}^r\right) = \int_{\partial\Omega} \left(\underline{T}^s.\underline{U}^s + \underline{T}^r.\underline{U}^r\right) \mathrm{d}S = \underline{Q}.\underline{\dot{q}} \tag{15}$$

where $\underline{Q}$ is the vector of the loading parameters (compressive resultant force in the above problem) and $\underline{\dot{q}}$ the associated kinematic parameters (vertical velocity of the reinforced block upper section).

On the other hand, the virtual work of internal forces is equal to the sum of the contribution of each phase and the interaction prevailing between them:

$$W_i\left(\underline{U}^s, \underline{U}^r\right) = \int_{\Omega} \left(\underline{\underline{\sigma}}^s : \underline{\underline{d}}^s + \sigma\, d + I\,\dot{\Delta}\right) \mathrm{d}\Omega \tag{16}$$

where $\underline{\underline{d}}^s$, d and $\dot{\Delta}$ are the strain rate variables, defined as:

$$\underline{\underline{d}}^s = \frac{1}{2}\left(\underline{\underline{\text{grad}}}\,\underline{U}^s + {}^T\underline{\underline{\text{grad}}}\,\underline{U}^s\right), \quad d = \frac{\partial \hat{U}_1^r}{\partial x_1}, \quad \dot{\Delta} = \hat{U}_1^r - \hat{U}_1^s \tag{17}$$

The *maximum resisting work* defined as the maximum of the work of internal efforts, satisfying the strength conditions (12) and (13), in the virtual velocity field $\{\underline{\hat{U}}^s, \underline{\hat{U}}^r\}$:

$$W_{mr}\left(\underline{U}^s, \underline{U}^r\right) = \int_\Omega \left(\pi^s\left(\underline{\underline{d}}^s\right) + \pi^r(d) + \pi^I(\dot{\Delta})\right) \mathrm{d}\Omega \tag{18}$$

where π^m, π^r and π^I denote the support functions of the matrix, the reinforcement phase and the interaction, respectively:

$$\begin{aligned} \pi^s(\underline{\underline{d}}^s) &= \sup\left\{\underline{\underline{\sigma}}^s : \underline{\underline{d}}^s;\ f\left(\underline{\underline{\sigma}}^s\right) \le 0\right\} \\ \pi^r(d) &= \sup\left\{\sigma d;\ |\sigma| \le \sigma_0\right\} \\ \pi^I(\dot{\Delta}) &= \sup\left\{I\dot{\Delta};\ |I| \le I_0\right\} \end{aligned} \tag{19}$$

Combining the virtual work principle (14) and (15) with the definition of the maximum resisting work given by Eqs. (18) and (19), the necessary condition of stability may be written:

$$\forall\left\{\underline{U}^s, \underline{U}^r\right\}\text{K.A.}, \qquad \underline{Q}.\underline{\dot{q}} \le W_{mr}\left(\underline{U}^s, \underline{U}^r\right) \tag{20}$$

4.1 Lower Bound Static Approach

The lower bound static approach is implemented by making use of the following stress field in the reinforced block modeled as a two-phase system:

$$\sigma = \sigma(x_1) \quad \text{with} \quad \sigma(x_1 = \pm L) = 0 \tag{21}$$

for the reinforcement phase,

$$\begin{cases} \sigma_{11}^s(x_1) = -\sigma(x_1) \\ \sigma_{22}^s(x_1) = \sigma_{33}^s(x_1) = -2C - \sigma(x_1) \\ \sigma_{ij}^s = 0 \quad \text{if } i \ne j \end{cases} \tag{22}$$

for the matrix phase, and

$$I = \frac{\mathrm{d}\sigma}{\mathrm{d}x_1} = \sigma'(x_1) \tag{23}$$

for the interaction.

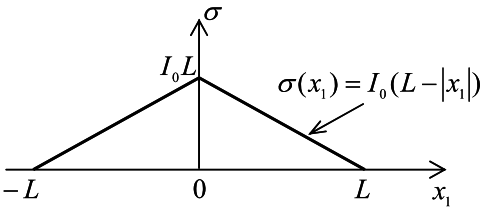

Fig. 7 Stress distribution in the reinforcement phase ($\chi \leq 1$)

It can be easily shown that this stress field complies with the equilibrium equations (10) and (11), along with the strength conditions (12) and (13). The corresponding compressive force in equilibrium with such a stress field is given by:

$$Q = -\int_{-L}^{L} \sigma_{22}^{s}(x_1)\,\mathrm{d}x_1 = 4CL + \int_{-L}^{L} \sigma(x_1)\,dx_1 \tag{24}$$

The optimal (i.e. maximum) value of this compressive force depends on the relative importance of the reinforcement phase uniaxial strength density with respect to the interaction strength parameter. Introducing the non dimensional parameter:

$$\chi = \frac{I_0 L}{\sigma_0} \tag{25}$$

the following two different cases, depending on the value of χ, are considered:

- $\chi \leq 1$ ($I_0 L \leq \sigma_0$). The interaction force density I is chosen so as to be equal to the corresponding strength I_0. Combining Eqs. (21), (22) and (23), it comes out that the internal efforts in the multiphase system are of the following form (Fig. 7):

$$\begin{cases} \sigma(x_1) = -\sigma_{11}^{s}(x_1) = 2C - \sigma_{22}^{s}(x_1) = I_0(L - |x_1|) \\ |I| = I_0 \end{cases} \tag{26}$$

  which comply with the equilibrium and the strength conditions. It follows that:

$$Q^{+}_{\text{mult.}} \geq 4CL + I_0 L^2 \tag{27}$$

- $\chi \geq 1$ ($I_0 L \geq \sigma_0$). The generalized stress field defined on the reinforced block given by (Fig. 8):

$$\sigma(x_1) = -\sigma_{11}^{s}(x_1) = 2C - \sigma_{22}^{s}(x_1) = \text{Min}\left\{I_0(L - x_1); \sigma_0\right\} \tag{28}$$

  which complies with the above equilibrium and strength requirements, leading to the following lower bound for the reinforced block compressive resistance:

$$Q^{+}_{\text{mult.}} \geq 4CL + 2\sigma_0 L\left[1 - \frac{\sigma_0}{2I_0 L}\right] \tag{29}$$

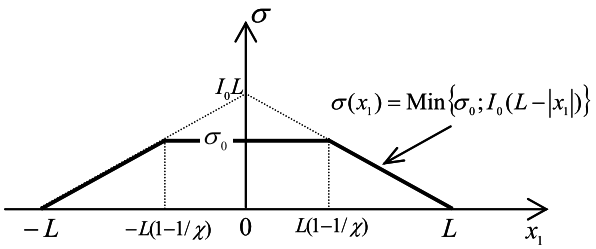

Fig. 8 Stress distribution in the reinforcement phase ($\chi \geq 1$)

4.2 Upper Bound Kinematic Approach

The upper bound kinematic approach is implemented by considering the following virtual velocity field defined for each phase separately:

$$\underline{\hat{U}}^s = \frac{U}{H}(x_1\underline{e}_1 - x_2\underline{e}_2) \tag{30}$$

for the matrix phase, and

$$\underline{\hat{U}}^r = \begin{cases} -\frac{U}{H}x_2\underline{e}_2 & \text{if } \chi \leq 1 \\ \begin{cases} \frac{U}{H}(x_1\underline{e}_1 - x_2\underline{e}_2) & |x_1| \leq L(1-\chi^{-1}) \\ \frac{U}{H}(L(1-\chi^{-1})\underline{e}_1 - x_2\underline{e}_2) & |x_1| \geq L(1-\chi^{-1}) \end{cases} & \text{if } \chi \geq 1 \end{cases} \tag{31}$$

for the reinforcement phase.

The calculation of the maximum resisting work leads to the following expression:

$$W_{mr}\left(\underline{\hat{U}}^s, \underline{\hat{U}}^r\right) = 4CLU + \begin{cases} I_0L^2U & \text{if } \sigma_0 \geq I_0L \\ 2\sigma_0LU[1 - \frac{\sigma_0}{2I_0L}] & \text{if } \sigma_0 \leq I_0L \end{cases} \tag{32}$$

On the other hand, the work of the external forces in the considered mechanism is equal to the product of the applied effort Q by the corresponding velocity U of the upper section of the block. The upper bound kinematic approach of yield design finally leads to the following upper bound value for

$$Q^+_{\text{mult.}} \leq 4CL + \begin{cases} I_0L^2 & \text{if } \sigma_0 \geq I_0L \\ 2\sigma_0L[1 - \frac{\sigma_0}{2I_0L}] & \text{if } \sigma_0 \leq I_0L \end{cases} \tag{33}$$

hence the exact value of the compressive resistance predicted by the multiphase model.

It can be observed that in the situation of perfect bonding the above expressions reduce to that derived from the homogenization approach:

$$Q^+_{\text{mult.}}(\chi \to \infty) = Q^+_{\text{hom}} = 4CL[1 + \sigma_0/2C] \tag{34}$$

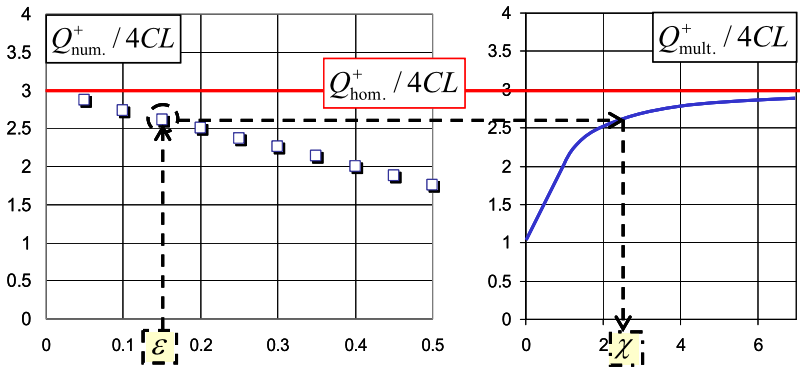

Fig. 9 Identification procedure for the interaction strength parameters ($\sigma_0 = 4C$)

5 Identification of the Interaction Strength Parameter

The curve sketched on the right-hand side of Fig. 9 represents the results of the multiphase approach expressed in terms of variation of the non dimensional compressive resistance $Q^+/4CL$ as a function of the parameter χ, for $\sigma_0 = 4C$. On the left-hand side of the same figure, are reported the results of the f.e.m.-based numerical simulations performed by using Plaxis, expressed in terms of the variation of $Q^+/4CL$ as a function of the scale factor ε.

Starting from these representations, the relationship between the scale factor ε and the parameter χ can be established. The first step of this procedure consists in representing the evolution of $\chi(\varepsilon)$ which could be then approximated by an analytical expression (Fig. 10). It appears that the obtained series of points is best fitted by an analytical curve which obeys the following approximate equation:

$$\chi \cong 0.4\varepsilon^{-1} \tag{35}$$

which means that χ, and hence the interaction strength parameter I_0, is inversely proportional to the scale factor. It is important to notice that the coefficient of proportionality (equal to 0.4 in the present case), and then the interaction strength parameter I_0, can therefore be determined from one single numerical simulation. A more thorough and detailed analysis (which is beyond the scope of the present paper) would certainly show that this coefficient of proportionality depends on the soil's cohesion, since no failure is considered at the soil-inclusion interface at the microscopic scale.

The combination of the relationships (33) and (35) finally leads to the following expression of the compressive strength as a function of the scale factor:

$$\frac{Q^+_{mult.}}{4CL} = \frac{Q^+_{num.}}{4CL} = \begin{cases} 3 - 2.5\varepsilon & \text{if } \varepsilon \leq 0.4 \\ 1 + 0.4/\varepsilon & \text{if } \varepsilon \geq 0.4 \end{cases} \tag{36}$$

This prediction, obtained from the application of the multiphase approach in the field of yield design, tends to the results of the homogenization approach for very

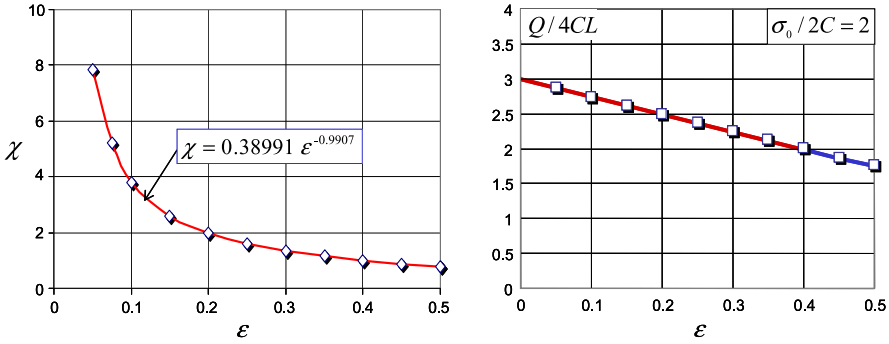

Fig. 10 Identification of the interaction strength parameter and comparison between the numerical results and the multiphase model-based predictions

small values of ε and appears to linearly decrease down to a value of the scale factor equal to 0.4 (Fig. 10).

6 Concluding Remarks

It has been shown in this contribution that the multiphase model, developed in the context of yield design, is not subject to the limitations of the classical periodic homogenization method, since it allows to capture scale and boundary effects, which may play a decisive role in the reinforced-soil structures design. This is achieved through the introduction of a matrix-reinforcement interaction strength parameter, accounting, at the macroscopic scale, for a possible slippage between the reinforcing inclusion and the surrounding ground. Such a parameter could be identified, as shown in Sect. 5, through one f.e.m.-based elastoplastic calculation performed on a unit cell. The homogenization results could be recovered as a particular case of the multiphase approach, when the interaction strength parameter I_0 tends to infinity (perfect bonding assumption), which corresponds to a vanishing scale factor ε.

It is worth noting that a limited interaction strength between phases, at the *macroscopic* scale, should be taken into account even in the case of *perfect bonding at the microscopic scale*, that is unlimited strength, at the soil-inclusion interface, thus assuming that the soil is perfectly adherent to the reinforcement.

From an engineering design and optimization viewpoint, the multiphase model is a robust tool, combining the decisive advantages of the classical homogenization method with its ability to capture scale and boundary effects, in order to analyse the stability of reinforced soil structures, as illustrated in [9] for reinforced earth retaining walls.

References

1. Suquet, P.: Elements of homogenization for inelastic solid mechanics. In: Homogenization for Composite Media. CISM Lecture Notes, vol. 272, pp. 155–182. Springer, Berlin (1985)
2. de Buhan, P.: A fundamental approach to the yield design of reinforced soil structures. Dr. Sc. Thesis, UMPC, Paris (1986) (in French)
3. de Buhan, P., Taliercio, A.: A homogenization approach to the yield strength of composite materials. Eur. J. Mech. A, Solids **10**(2), 129–154 (1991)
4. Sawicki, A.: Yield conditions for layered composites. Int. J. Solids Struct. **17**(10), 969–979 (1981)
5. de Buhan, P.: Macroscopic yield strength of a strip reinforced material. C. R. Acad. Sci., Ser. II **301**, 557–560 (1985)
6. Vermeer, P.A., Brinkgreve, R.BJ.: Finite Element Code for Soil and Rock Analysis. Rotterdam, Balkema (1995)
7. Sudret, B., de Buhan, P.: A multiphase model for materials reinforced by linear inclusions. C. R. Acad. Sci., Série IIb **327**, 7–12 (1999)
8. de Buhan, P., Sudret, P.: Micropolar multiphase model for materials reinforced by linear inclusions. Eur. J. Mech. A, Solids **19**, 669–687 (2000)
9. Thai Son, Q., Hassen, G., de Buhan, P.: A multiphase approach to the stability analysis of reinforced earth structures accounting for soil-strip failure condition. Comput. Geotech. **36**, 454–462 (2009)

Limit Analysis of a Soil Reinforced by Micropile Group: A Decomposition Approach

Z. Kammoun, J. Pastor, and H. Smaoui

Abstract The behavior of soils reinforced by micropile networks is still not fully understood due to the lack of accurate modelling capabilities. Particularly, the complex geometry of large soil-micropile systems makes accurate calculation of the bearing capacity of the reinforced soil a computational challenge. This complexity requires highly detailed and finely discretized models to achieve reasonable accuracy using direct numerical methods. Such models lead to large scale numerical optimization problems that are hardly tractable using a personal computer.

Recently a decomposition strategy with domain overlap has proved successful in solving very large kinematic and static limit analysis problems with limited computing resources. It consists of splitting the original problem into limit analysis subproblems that are smaller in size.

The present paper reports enhancements made to the original decomposition method. In particular, the method is made capable of solving the classical punch problem with Tresca or Coulomb soils. This benchmark problem is considered as a limit case of a soil reinforced by micropiles.

The paper then describes the application of the decomposition method to determine rigorous kinematic and static bounds to the bearing capacity of a soil reinforced by a micropile group according to a 2D plane strain model.

1 Introduction

A micropile is a pile with a diameter no greater than 250 mm, generally in the range 75 to 200 mm, usually with an aspect ratio of 200. Micropile technique was initially

Z. Kammoun (✉) · H. Smaoui
Ecole Nationale d'Ingénieurs de Tunis, LR11ES16 Laboratoire de Matériaux, Optimisation et Energie pour la Durabilité, Université de Tunis El Manar, 1002, Tunis, Tunisie
e-mail: kammounzied@yahoo.fr

H. Smaoui
e-mail: hichem.smaoui@enit.rnu.tn

J. Pastor
Laboratoire LOCIE, Polytech'Savoie, Université de Savoie, 73376 Le Bourget du Lac, France
e-mail: joseph.pastor@univ-savoie.fr

G. Saxcé et al. (eds.), *Limit State of Materials and Structures*,
DOI 10.1007/978-94-007-5425-6_10,

developed by the Fondedile company under the authority of F. Lizzi [5] as early as 1952. Micropiles were used for the first time in Italy in soil reinforcement of existing buildings and were then named root piles (*pali radice*). Within the timeframe of half a century, the technique has been applied all over the world [2].

The ease of their execution makes micropiles suitable for foundation works beneath existing buildings. Landmark examples are the Orsay railway station works for the development of a museum, "la Maladière" stadium in Neuchâtel in Switzerland (1100 micropiles) and the international airport of Boston (800 micropiles).

The complex geometry of large soil-micropile systems makes accurate calculation of the bearing capacity of the reinforced soil difficult because of the large size of the associated finite element model. As a strategy to handle problem sizes beyond available machine capacities, it is common to split the original problem into limit analysis (LA) subproblems that are smaller in size or simpler to solve.

In the present paper, the decomposition method, proposed in [7] and [8] in the framework of mixed kinematic limit analysis and extended in [3] and [4] to the static limit analysis problem, is adapted and applied to determine upper and lower bounds for the bearing capacity of micropile groups. The paper begins with a brief presentation of limit analysis followed by a description of the decomposition method. Next, the decomposition is applied to the punch problem (with Tresca or Coulomb soil), a representation of Prandtl's classical problem with finite domain. This benchmark example is considered here for (i) being a simple problem for which the solution is known a priori, (ii) being interpretable as a limit case of a soil reinforced by micropiles, that is the case with no reinforcement, (iii) exhibiting a feature that has not been tested so far in decomposition, that is the absence of a loaded zone in some subproblems.

Finally, the decomposition is exploited in the calculation of lower and upper bounds for the bearing capacity of examples of micropile groups.

2 Succinct Presentation of Limit Analysis

For the sake of clarity, without any loss in generality, we consider here that the velocity fields are continuous.

According to Salençon [9], a stress tensor field σ is said to be admissible if it is both statically admissible (SA, i.e., equilibrium equations, stress vector continuity, and stress boundary conditions are verified) and plastically admissible (PA, i.e., $f(\sigma) \leq 0$, where $f(\sigma)$ is the (convex) plasticity criterion of the material). Similarly, a strain rate tensor field v is admissible if it is kinematically admissible (KA, i.e., derived from a piecewise continuous velocity vector field u, with bounded discontinuities $[u]$, such that the velocity boundary conditions are verified) and plastically admissible (PA, i.e., the associated flow rules (2a), (2b) are verified).

A solution to the LA problem is a pair of fields (σ, v) where σ and v are both admissible and associated by the normality law. Classically, these solutions can be

found or approached using two methods. The first one, involving only the stresses as variables, is the statical (or lower bound) method. The second one, involving only the displacement velocities as variables, is the classical kinematic (or upper bound) method.

2.1 The Kinematic Method

Let us assume, as in [9], that the virtual power rate of the external loads P_{ext} can be written as the scalar product of a loading vector Q, whose components are called here loading parameters; and a generalized velocity vector $q = q(u)$, the components of which are called kinematic parameters. Following [1], let us consider a KA virtual velocity field u; the virtual power principle (VPP) states that the stress tensor fields σ, the stress vector field T (on the velocity discontinuity surfaces), and the vector Q are in equilibrium if, for any KA u, the following variational equation holds:

$$P_{\text{ext}} = Q \cdot q(u) = \int_V \sigma : v \, dV + \int_{S_d} T \cdot [u] \, dS. \tag{1}$$

In (1), V is the volume of the mechanical system, and S_d is the union of the velocity discontinuity surfaces. The results in terms of Q will be interpreted as a kinematic bound if, at the appropriate points of V, the variables verify the following conditions, where u is KA and q^d is a fixed value of $q(u)$:

$$v = \lambda \frac{\partial f}{\partial \sigma}, \quad \lambda f(\sigma) = 0, \ \lambda \geq 0, \ f(\sigma) \leq 0; \tag{2a}$$

$$[u] = \xi \frac{\partial f_{nt}}{\partial T}, \quad \xi f_{nt}(T) = 0, \ \xi \geq 0, \ f_{nt}(T) \leq 0; \tag{2b}$$

$$q(u) = q^d. \tag{2c}$$

The criterion $f_{nt}(T)$ results from the projection of the plasticity criterion $f(\sigma)$ on the Mohr plane, where n is the normal to the element of the velocity discontinuity surface and $T = (\sigma_{nn}, \sigma_{nt})$ is the stress vector on this element. More precisely, $f_{nt}(T)$ is the solution of the following system:

$$f(\sigma_{nn}, \sigma_{tt}, \sigma_{nt}) = 0; \qquad \frac{\partial f}{\partial \sigma_{tt}} = 0. \tag{3}$$

It is worth noting that, if (2a) and (2b) are verified, the quantities $\sigma : v$ and $T \cdot [u]$ become the *convex* unit dissipated powers $\pi_V(v)$ and $\pi_d([u])$ of LA, respectively, i.e.:

$$\pi_V(v) = \sigma : v; \qquad \pi_d\big([u]\big) = T \cdot [u]. \tag{4}$$

Fig. 1 The punch problem

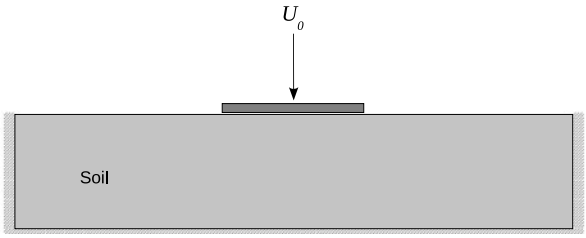

2.2 The Statical Method

The set of admissible loadings $Q = Q(\sigma)$, i.e. which are linearly associated with SA stress fields σ, forms a convex K in $\mathbb{R}^n$ and the n components of Q are called loading parameters.

Finding the solution of the static LA problem consists in finding an admissible field σ at the boundary ∂K of K by solving the following optimization problem

$$Q_{lim} = \left(Q_1^d, \ldots, \lambda_0 Q_i^d, \ldots, Q_n^d\right) \tag{5a}$$

$$\lambda_0 = \max\left\{\lambda,\, Q(\sigma) = \left(Q_1^d, \ldots, \lambda Q_i^d, \ldots, Q_n^d\right)\right\} \tag{5b}$$

where σ is an admissible stress field and Q^d a given admissible loading. This is the static, or lower bound method of LA that will be used here.

3 Decomposition of the LA Problem

3.1 The Kinematic Problem

For ease of presentation the decomposition of the kinematic problem is illustrated by applying it to the punch problem (Fig. 1).

A rigid plate, of width b supported by a soil, undergoes a downward motion with a uniform vertical velocity U_0 caused by a vertical force F applied at its center. Taking symmetry into account, only the left half of the plate, denoted V, is modeled. The domain V is meshed into 8×2 rectangles divided each into four triangles (Fig. 2). In the sequel, this mesh will be referred to as the target mesh (the mesh size will be defined by the number of its rectangular cells). The material of the soil is homogeneous, isotropic and is governed by the von Mises (or Tresca) criterion with cohesion c or by Coulomb's law with cohesion c and a friction angle φ. At the soil-plate interface, perfect bonding is assumed. This translates into kinematic boundary conditions in the soil given by prescribed vertical velocities equal to U_0 and zero tangential velocities. The static boundary conditions in the soil in contact with the plate are defined by unrestricted tangential stresses and by a normal stress resultant equal to the applied load F.

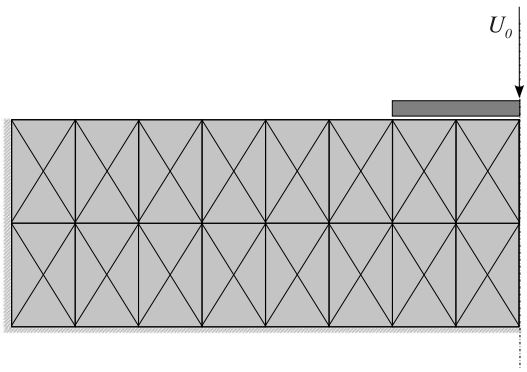

Fig. 2 Target mesh for domain V

The limit analysis problem associated with the load F applied to the soil domain V, discretized according to the target mesh, will be called the target problem and denoted P. It is defined by a unique loading parameter $Q = \frac{F}{bc}$ associated with the kinematic parameter $q^d = U_0$.

3.1.1 The Starting Problem

The decomposition procedure is initiated by solving a preliminary problem P_0, called the starting problem, which is small enough in size to be solvable using the available solution means. This problem is considered exclusively in the first iteration to provide an initial admissible velocity field for problem P.

A convenient choice for problem P_0 consists in replacing the target mesh by a coarser mesh made of a quarter (4×1) of the target number of rectangular cells, as shown in Fig. 3.

The solution of the starting problem provides an estimate of the velocities u^A and u^C at nodes A and C, respectively. The velocity u^B at B is deduced by linear interpolation. These three velocities are collected to form a vector U^{11} to be used in writing the boundary conditions for the subproblems in Step 2.

3.1.2 The Second Step

In Step 2 of the first iteration, the domain V is partitioned into 2 sub-domains, denoted V_{2i} $(i = 1, 2)$, bounded by the interface ABC (Fig. 3). To each subdomain V_{2i}, meshed into 4 cells, is associated an independent limit analysis subproblem denoted P_{2i}. The functional to be minimized in each of these subproblems is the power dissipated within the corresponding subdomain. The assembly of the optimal subproblem solutions gives an admissible solution for the target problem P over the complete domain V. Therefore, the sum of the subproblem powers can be set equal to FU_0. At this Step, the dissipated power is less than or equal to that of the starting problem. For the solution process to proceed from one iteration to another, the velocities (U^{11}) at the interface need to be updated. It should be noted that, in subsequent iterations, Step 2 will be repeated in the same way as presented above.

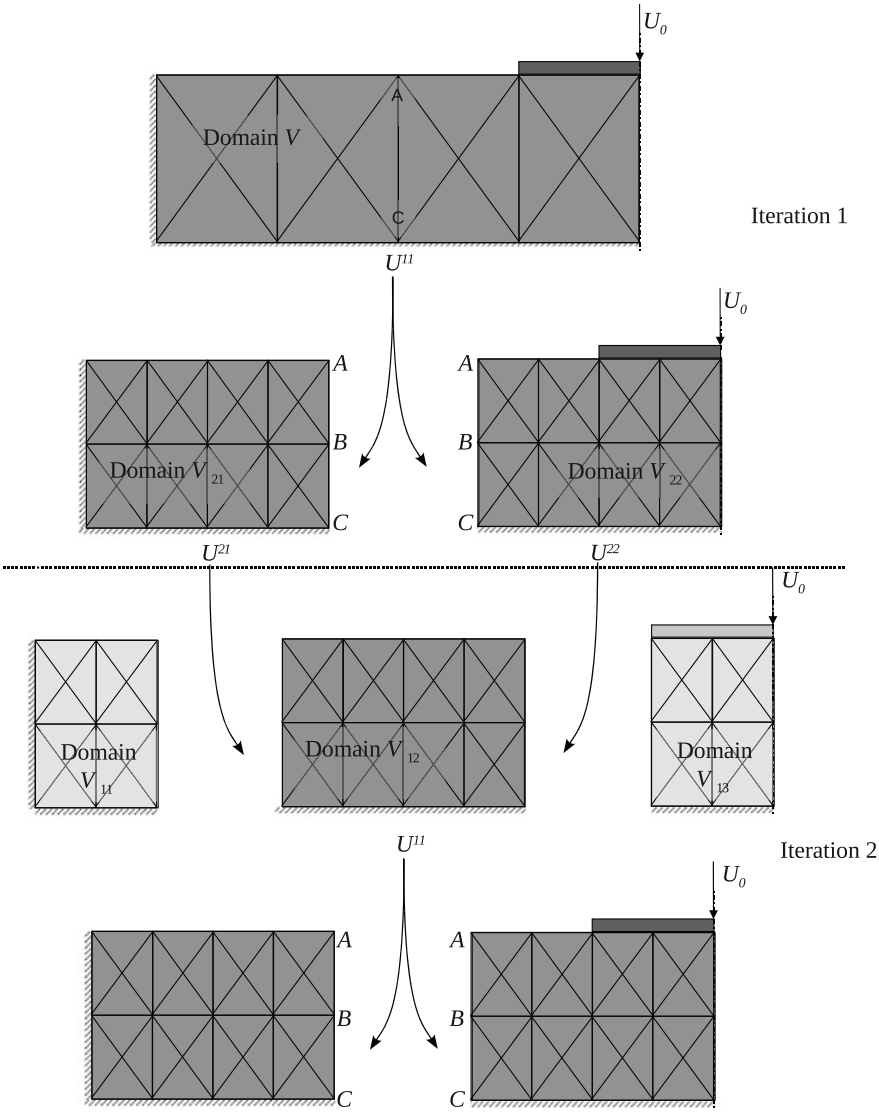

Fig. 3 Decomposition flow diagram

3.1.3 The Iterative Process

In subsequent iterations, the aim of the first step, labeled Step 1, is to improve the values of the velocities at the interface. For this purpose, the domain V is partitioned, without change in the discretization, into different sets of subdomains, denoted V_{1i} (Fig. 3), such that the interfaces between subdomains V_{2i} lie in the interior of subdomains V_{1i}. In an analogous way to Step 2, to each set V_{1i} is associated a LA

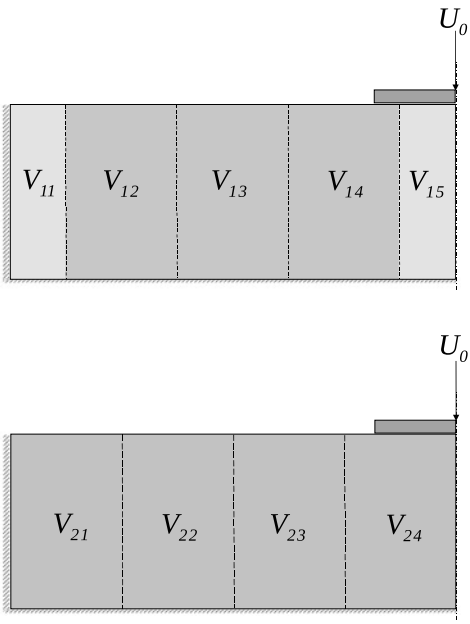

Fig. 4 The two partitions of the punch problem

subproblem P_{1i}. The velocities U^{2i} $(i = 1, 2)$ imposed at the interfaces are provided from the preceding step. The interface in Step 2 being in the interior of subdomain V_{12}, solving subproblem P_{12} allows the interface velocities to evolve. From the second iteration onward, all iterations are similar. The iterative process terminates when the progress in the solution from one iteration to another becomes small.

3.1.4 Partition into Many Subdomains

In general, the domain is partitioned into as many sub-domains as needed to bring the sub-problem down to a desired size. For instance, in the next section the decomposition is applied to the punch problem using a five sub-domain partition in Step 1 (Fig. 4).

For the first Step of the second and following iterations, solving only the three subproblems P_{12}, P_{13} and P_{14} is sufficient for updating the interface velocities previously blocked during Step 2.

3.2 Decomposition of the Static Problem

Using the punch problem again as an example, with a single loading parameter $Q = \frac{F}{bc}$ associated with the kinematic parameter $q^d = U_0$, the decomposition of the static problem proceeds in a manner basically similar to the decomposition of

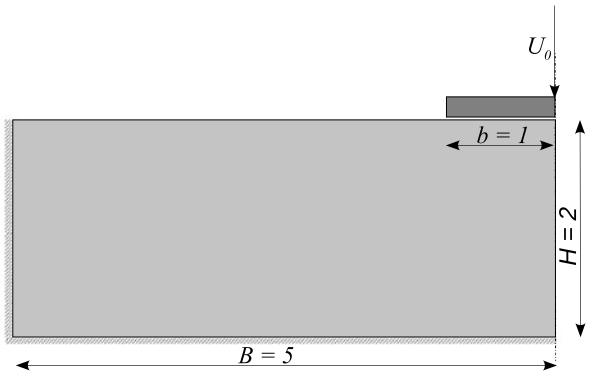

Fig. 5 Geometric data for the punch problem

the kinematic problem. In the first iteration, a starting problem P_0 is constructed. The domain V_0 associated to problem P_0 is discretized into four times fewer finite elements than the target problem domain V. As shown in Fig. 4, the domain V is partitioned alternatively into four sub-domains denoted V_{2i} or five sub-domains denoted V_{1i}. Solving problem P_0 constitutes the first step in this first iteration. The solution of problem P_0 provides a statically admissible first approximation of the stress field, including at the interfaces between sub-domains V_{2i}, as well as a lower bound for the limit load.

In the second step of the present iteration, stress components at the interfaces, obtained from the solution of problem P_0, are collected into so called interface stress vectors T_{1j}. The latter will serve in defining the boundary conditions for sub-problems (P_{2i}).

To cause changes in the stress field when solving these sub-problems, an alternative sub-problem formulation definition is proposed as follows. For each of sub-problems (P_{21}) to (P_{23}), the cohesion is treated as a variable parameter and solving problem P_{2i} consists in minimizing the corresponding cohesion subject to static admissibility constraints. This leads to solutions that are plastically admissible with maximal strength reserve. The solution of problem (P_{24}) provides the load resulting from the sub-problems of Step 1. The above process is repeated in the subsequent steps while alternating the domain partitions V_{1i} and V_{2i}.

4 Numerical Results for the Punch Problem

To assess the performance of the decomposition approach in solving the kinematic problem, the punch problem is solved using the data given in Fig. 5. For a Tresca soil with cohesion c the exact solution should be identical to that of a punch over a semi-infinite medium, known to be $F/(bc) = \pi + 2$. This is because Prandtl's mechanism, which corresponds to the exact solution of the semi-infinite soil, can be fitted in the selected volume. This allows comparison of results to a known exact solution.

Table 1 Kinematic bound $\frac{F}{bc}$ for the punch problem with a Tresca soil

Mesh	Number of elements	Direct			Decomp. (1 iter.)		
		$F/(bc)$	Accuracy	CPU(s)	$F/(bc)$	Accuracy	CPU(s)
40×18	2880	5.1787	3.5×10^{-7}	578	5.2681	3.6×10^{-7}	15
80×36	11520	5.1607	4.4×10^{-7}	3595	5.1629	4.6×10^{-7}	1985
160×72	46080	5.1519	7.1×10^{-7}	38211	5.1526	5.5×10^{-7}	21912
320×144	184320	—	—	—	5.1476	3.8×10^{-7}	184550

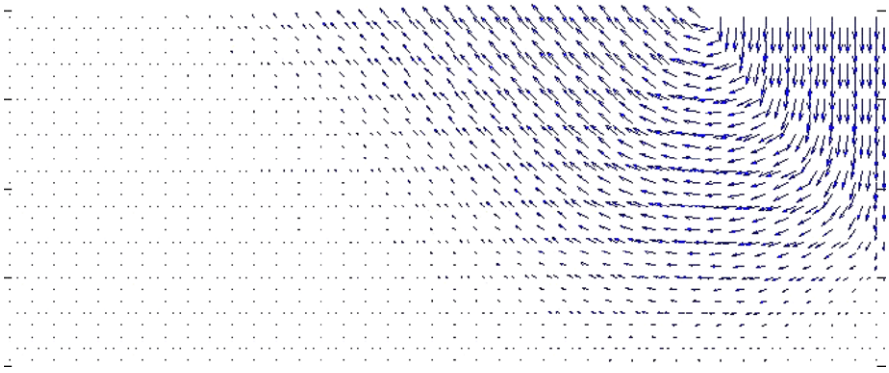

Fig. 6 Velocity field in the punched soil. First iteration of the decomposition

4.1 Kinematic Solution

Upper bounds for the punch problem are determined based on different levels of discretization and using both the direct approach and a single iteration of the decomposition method for solving the kinematic problem. The decomposition is applied based on the domain partitions shown in Fig. 4.

The numerical optimization problems arising from the limit analysis (sub)problems involved in the present example, as well as all subsequent examples treated in this paper, are all solved using the conic programming code MOSEK [6] and run on a Mac Pro 3 GHz machine with 12 Gb of RAM.

Table 1 shows the upper bounds obtained for the punch problem based on various discretizations. In a first series of runs the soil is characterized by a Tresca criterion with cohesion $c = 1$. For large mesh size (184 320 elements), the problem can only be solved using decomposition, giving the upper bound 5.1476 and a relative error of 0.12 % with respect to the exact solution.

The velocity field resulting from the first iteration is visualized in Fig. 6 for an 80×36 mesh (Tresca, $c = 1$). The failure mechanism can be clearly seen, with the velocities gradually decreasing downward until they vanish at the substrate. Considering a soil governed by a Coulomb criterion with the same cohesion $c = 1$ and a friction angle φ, the upper bound is determined for various friction angles, based on

Table 2 Kinematic bound $\frac{F}{bc}$ for the punch problem (Coulomb soil, 11520 elements)

φ (°)	Decomp. it1	Direct	Relative err.
0	5.1628	5.1607	0.04 %
5	6.5075	6.5062	0.02 %
10	8.3773	8.3752	0.03 %
15	11.0497	11.043	0.06 %
20	15.1819	15.1621	0.13 %
25	22.3637	22.3236	0.18 %
30	36.6335	36.5231	0.30 %

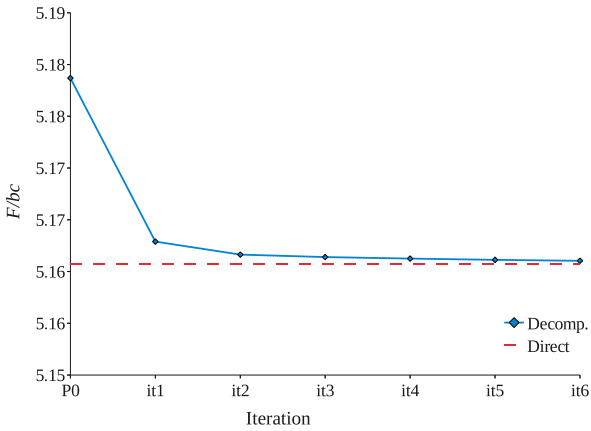

Fig. 7 Decomposition iteration history

an 80 × 36 mesh (11 520 finite elements). Table 2 shows the upper bounds obtained using direct problem solution and using a single iteration of the decomposition for different values of the friction angle. The relative error of the decomposition result with respect to the direct solution is less than 0.3 %.

The iteration history displayed in Fig. 7 for the Tresca soil shows that a few iterations are needed to converge to the target value known from the direct solution.

4.2 Static Solution

The static problem is solved to determine lower bounds for the punch problem with a Tresca soil. Different mesh sizes are considered. Calculations are carried out by solving the problem both directly and using one iteration of the decomposition method based on the same domain partitions as in the kinematic case (Fig. 4). All (sub)problems are solved using the MOSEK code run on the Mac Pro 3 GHz machine.

Post analysis verification of constraint violation shows that accuracy of the solution varies from 10^{-9} for a 1600 element to 10^{-5} for a 102400 element mesh. With

Table 3 Static bound F/bc for punch problem (Tresca soil)

Mesh	Number of elem.	Decomp. it1	Direct	Error/direct	Error/theoretical
40×10	1600	5.0989	5.1094	0.21 %	0.83 %
80×20	6400	5.1185	5.1236	0.1 %	0.45 %
160×40	25600	5.1277	5.1329	0.1 %	0.27 %
360×80	102400	5.1358	5.1372	0.03 %	0.11 %
720×160	409600	5.1387	—	—	0.06 %

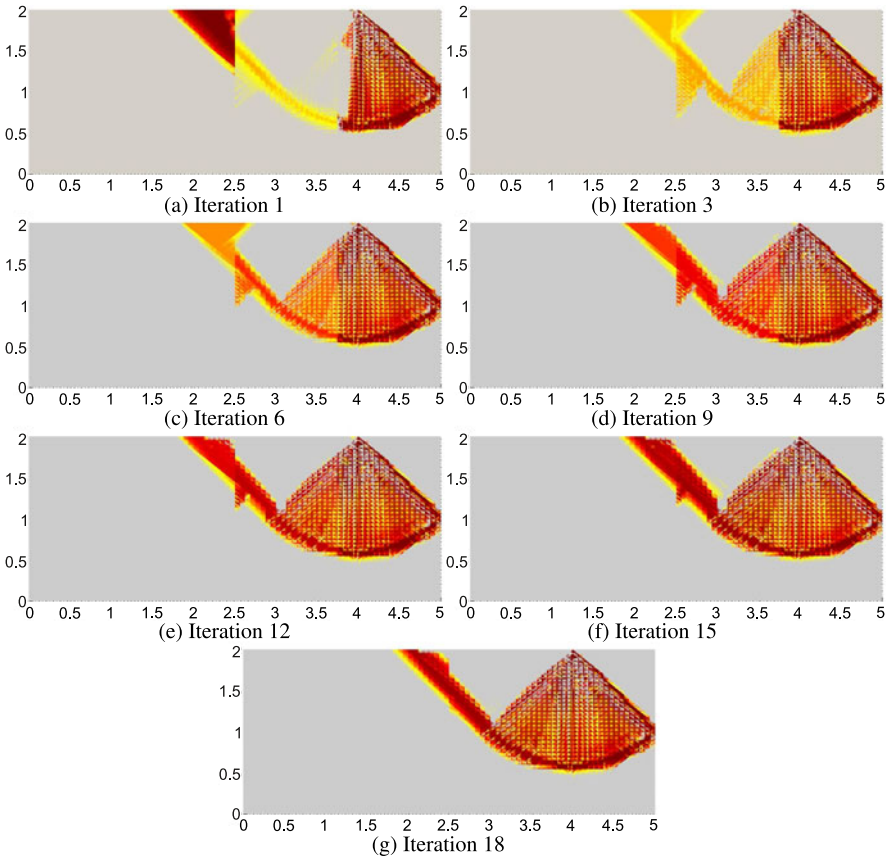

Fig. 8 Visualization of failure zones in the soil

a 409600 element discretization, the direct solution appears to be impossible using the same machine with 12 Gb of RAM.

For this run, the decomposition result is within 0.06 % of the theoretical solution (Table 3). For the 80×40 mesh, the decomposition is exceptionally carried out up to the 18th iteration and the evolution of the failure zone throughout the iterations

Table 4 Static bounds ($F/(b\,c)$) for the punch problem (Tresca and Coulomb)

φ (°)	Initial	Decomp. it1	Direct
0	5.125	5.128	5.133
5	6.462	6.467	6.468
10	8.304	8.308	8.316
15	10.910	10.920	10.928
20	14.884	14.903	14.934
25	21.710	21.759	21.867
30	34.920	35.094	35.402

is visualized in Figs. 8 ((a)–(g)). These figures show the zones where the failure criterion lies in the narrow range -0.005 to 0. A Prandtl like mechanism is clearly exhibited as early as the first iteration except in the neighborhood of the interface. The disturbance in the stress field near the interface is seen to gradually diminish and eventually vanish. Next, a Coulomb soil is considered and a series of problems are solved with the same 80×40 mesh and different values of friction angle. Table 4 displays the static bounds for the Tresca and Coulomb criteria with cohesion $c = 1$ and friction angle φ varying from 5 to 30.

It is noted that, as observed with the Tresca criterion, a large improvement in the bound is achieved at the first iteration for all the tested friction angles.

The iteration history of the lower bound is plotted in Fig. 9 for the Tresca soil based on an 80×40 mesh. It shows that a few iterations only are needed to closely approach the target solution.

5 Bearing Capacity of Micropile Groups

5.1 Problem Description

The problem addressed in this work is that of a soil, bounded below by a substrate at depth H, to be reinforced by a group of micropiles, as shown in Fig. 10, with the purpose of supporting a load F. In the two dimensional representation adopted here the problem is interpreted as a plane strain one.

The numerical limit analysis (sub)problems are all solved using the same MOSEK code and Mac Pro machine as in the punch problem example.

5.2 Soil Reinforced with 9 Micropiles

Let us consider the following example of a soil reinforced with 9 micropiles. The soil is characterized by a Coulomb criterion with a cohesion of 10 kPa and friction

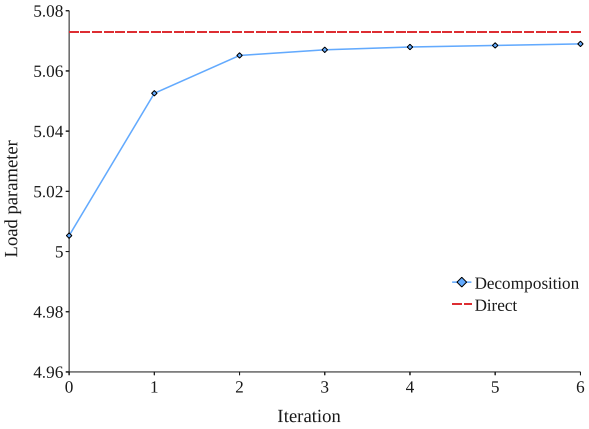

Fig. 9 Iteration history for the Tresca criterion

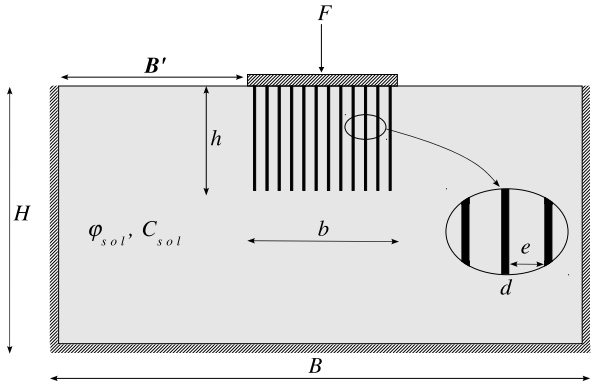

Fig. 10 Soil reinforced by a micropile group

Table 5 Geometric data of the reinforced soil (in meters)

H	h	B	d	Number of micropiles
10	5	24	0.1	9

angle $\varphi = 10°$. It is reinforced with micropiles characterized by a Tresca material with a cohesion of 10 MPa.

The geometry of the problem is summarized in Table 5.

It should be noted that the total load applied to the base is equal to F. Since the problem is symmetric, only half of the domain is modeled and the load to be maximized is reduced to $\frac{F}{2}$.

Table 6 shows the solutions obtained for different spacings between micropiles (e in Fig. 10) using the direct approach and the decomposition limited to the first iteration.

For meshes composed of more than 80.000 triangles for the static approach and 20.000 triangles for the kinematic approach, the MOSEK code fails to give fully optimal and admissible post-analyzed solutions. Beyond this limit, decomposition

Table 6 Soil reinforced with 9 micropiles

Spacing (m)			Mesh	$\frac{F}{2}$ (kN)	Accuracy	CPU (s)	Relative gap (%)
0.9	direct	static	480×30	482.21	1.6×10^{-7}	106	39.69
		kinem.	480×10	673.58	0.004	188	
	decomp.	static	960×60	486.23	3.4×10^{-5}	780	16.33
		kinem.	480×40	565.64	7.2×10^{-5}	2227	
0.7	direct	static	480×30	398.75	8.8×10^{-8}	119	49.02
		kinem.	480×10	594.20	7.9×10^{-5}	203	
	decomp.	static	960×60	403.27	1.6×10^{-4}	1043	20.46
		kinem.	480×40	485.79	9.3×10^{-4}	2637	
0.5	direct	static	480×30	322.39	5.4×10^{-8}	131	41.34
		kinem.	480×10	455.68	9.2×10^{-4}	207	
	decomp.	static	960×60	325.56	4.5×10^{-5}	980	16.98
		kinem.	480×40	380.84	5.2×10^{-5}	1672	
0.3	direct	static	480×30	247.13	1.8×10^{-8}	99	31.17
		kinem.	480×10	324.15	7.1×10^{-6}	99	
	decomp.	static	960×60	249.32	3.4×10^{-5}	757	11.51
		kinem.	480×40	278.01	2.7×10^{-5}	1474	

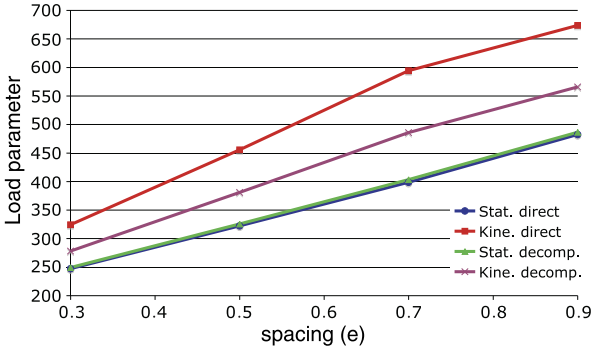

Fig. 11 Bounds for direct approach and decomposition

using 4-sub-domain partitions still converges using up to 300.000 triangles for the static approach and 80.000 triangles for the kinematic approach.

Decomposition has made possible a reduction by half of the gap between the upper and the lower bounds relative to the static bound with some improvement in the quality of the kinematic solution.

Figure 11 shows that the gap between static and kinematic bounds increases with spacing between micropiles.

Visualization of the failure zone (failure criterion) shows that the failure mechanism varies with spacing. For small spacing (Fig. 13), the failure zone in the soil

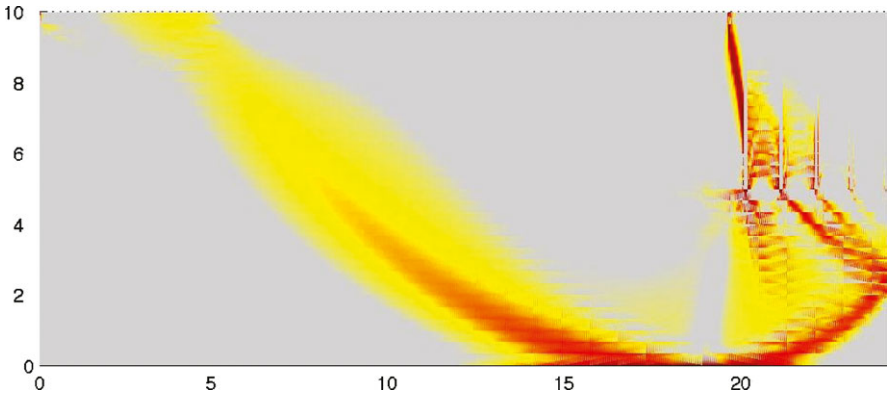

Fig. 12 Failure zone for 0.9 m spacing

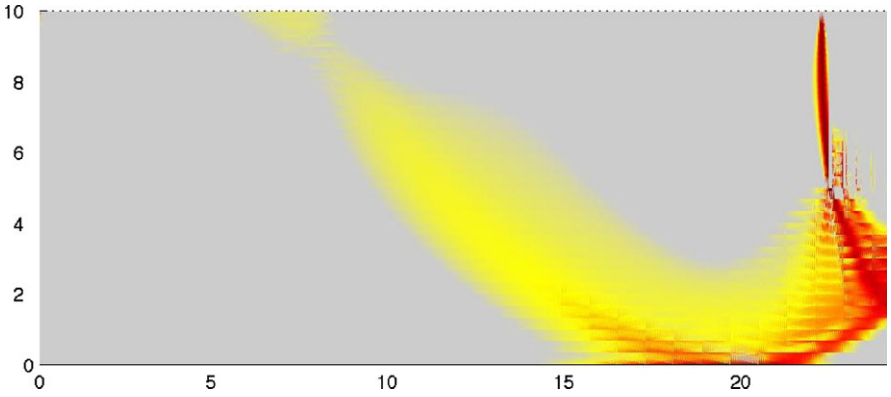

Fig. 13 Failure zone for 0.3 m spacing

is limited to the lower third of the reinforced zone, whereas for a 0.9 m spacing (Fig. 12), the failure zone covers two thirds of the depth of the reinforced zone.

5.3 Soil Reinforced by 17 Micropiles

In this example a Tresca soil with cohesion $c = 10$ kPa is reinforced with 17 micropiles made out of a Tresca material with cohesion $c = 5000$ kPa. The geometric data of the problem are given in Table 7.

Consider target problems modeled with an 800×16 mesh for the static approach and an 800×24 mesh for the kinematic approach. The solutions of all subproblems of the first iteration of the decomposition algorithm are reported in Table 8. In the static problem, the sub-problems (P_{21}), (P_{22}) and (P_{23}) need not be treated if the process is to be terminated at the first iteration. Their actual involvement in the

Table 7 Geometric data for a soil reinforced with 17 micropiles

H	h	B	d	e
20	15	80	0.2	0.8

Table 8 Bounds for bearing capacity of soil reinforced with 17 micropiles (Coarse discretization)

Sub-probl.	$Q = \frac{F}{2}$ (kN)		Accuracy		CPU (s)	
	Stat.	kinem.	Stat.	kinem.	Stat.	kinem.
0	736.2	1142.8	1.0×10^{-6}	2.3×10^{-5}	23	1169
11	–	1.6	4.7×10^{-7}	2.2×10^{-6}	49	1533
12	–	82.2	4.3×10^{-7}	5.7×10^{-6}	48	148
13	–	290.3	9.1×10^{-6}	6.7×10^{-6}	33	1878
14	781.7	709.6	6.1×10^{-5}	6.1×10^{-5}	32	1909
1^{st} it.	781.7	1083.8	6.1×10^{-5}	6.1×10^{-5}	183	6636

process begins at the second iteration because the associated sub-domains are not directly subjected to the applied load.

Conducting a single iteration of the decomposition algorithm, the relative difference between upper and lower bounds decreases from 55.23 % to 38.64 %.

Further improvement in the upper and lower bounds requires finer discretization, which leads to problem size that cannot be handled using the same domain partitions. A decomposition into smaller sub-domains would be needed to solve such a large problem. Using a finer partition, say with 9 (resp. 8) subdomains in Step 1 (resp. Step 2), the decomposition can be carried out at a single level, similarly to the example with 5 (resp. 4) subdomains. An alternative strategy is a multilevel scheme where each subproblem at one level of the decomposition is solved recursively by another level decomposition.

6 Conclusion

Rational sizing of soil reinforcement by micropile groups requires proper modeling of the soil-micropile system. Numerical methods for limit analysis are suitable for handling the geometric and behavioral complexities of the soil-micropiles system, however, they give rise to large size numerical nonlinear optimization problems. In the presented work, the decomposition approach has been adapted to the case of a Coulomb soil. Furthermore, for a Tresca as well as a Coulomb soil, the decomposition made it possible to solve larger problems than the direct method would allow, using the same machine. This led to an improvement of the lower and upper bounds for the bearing capacity of a soil reinforced by micropile groups. The gap between upper and lower bounds has been reduced by half compared to the best possible direct solution. The success of the decomposition method paves the way

to the treatment of the three dimensional problem which allows a far more realistic representation of the real soil-micropile system.

References

1. Anderheggen, E., Knopfel, H.: Finite element limit analysis using linear programming. Int. J. Solids Struct. **8**, 1413–1431 (1972)
2. Estephan, R.: Contribution aux méthodes de calcul des groupes et des réseaux de micropieux. Thèse de doctorat, ENPC, CERMES, Marne la Vallée (2003)
3. Kammoun, Z.: Prévision de la charge limite des sols renforcés par réseaux de micropieux. Thèse de doctorat, Université de Savoie et Ecole Nationale d'Ingénieurs de Tunis (2010)
4. Kammoun, Z., Pastor, F., Smaoui, H., Pastor, J.: Large static problem in numerical limit analysis: A decomposition approach. Int. J. Numer. Anal. Methods Geomech. (2010). doi:10.1002/nag.887
5. Lizzi, F.: The 'pali radice' (root piles)—a state of the art report. In: Symposium on Recent Developments in Ground Improvement Techniques, Bangkok, Thailand (1982)
6. MOSEK ApS: C/O Symbion Science Park, Fruebjergvej 3. Box 16, 2100 Copenhagen ϕ, Denmark (2002)
7. Pastor, F.: Résolution par des méthodes de point intérieur de problèmes de programmation convexe posés par l'analyse limite. Thèse de Doctorat, Facultés Universitaires Notre-Dame de la Paix Namur (2007)
8. Pastor, F., Loute, E., Pastor, J.: Limit analysis and convex programming: A decomposition approach of the kinematic mixed method. Int. J. Numer. Methods Eng. **78**, 254–274 (2009)
9. Salençon, J.: Théorie de la Plasticité Pour les Applications à la Mécanique des Sols. Eyrolles, Paris (1974)

An Extension of Gurson Model to Ductile Nanoporous Media

L. Dormieux and D. Kondo

Abstract We extend the classical Gurson model for ductile porous media by incorporating the surface/interface stresses effect which characterizes pores at nanoscale. For interface stresses obeying a von Mises criterion, we derive closed-form expressions of the parametric equations defining the yield surface. The magnitude of the interface effect is proved to be controlled by a non dimensional parameter depending on the voids characteristic size. It is observed that nanoporous materials can be made more strengthened than non-porous counterparts.

Keywords Ductile nanoporous materials · Micromechanics · Surface stress · Interfaces · Nanovoids · Yield function · Gurson model

1 Introduction

Investigation of size-dependent effects in nanomaterials including materials containing nano-voids has focused the attention of many researchers during the last decade. Early works have tried to model the transition zone between the nano-inclusion and the surrounding matrix as a thin but still three-dimensional layer [1, 2]. An alternative approach consists in adopting an interface description which is two-dimensional in nature. Concerning inclusion size effects on the effective elastic properties, some progresses have been gained in their understanding. Classical homogenization schemes as well as first order bounds in the theory of elastic heterogeneous media have been extended in order to incorporate interface and interface stresses (see e.g. [3–5]). Recent studies by [6] and [7] extended Hashin-Shtrikman bound to the above class of materials.

In contrast, it seems that few attention has been paid so far to the question of the effective strength of nanomaterials with account for interface effects. Mention can

L. Dormieux (✉)
Laboratoire Navier, UMR 8205 CNRS, ENPC, Champs-sur-Marne, France
e-mail: dormieux@enpc.fr

D. Kondo
Institut D'Alembert, UMR 7190 CNRS, UPMC, Paris, France
e-mail: djimedo.kondo@upmc.fr

G. Saxcé et al. (eds.), *Limit State of Materials and Structures*,
DOI 10.1007/978-94-007-5425-6_11,

be made of recent works by [8] who used the modified secant moduli approach. In the context of the ductile failure of porous materials, the Gurson model [9] is well known to provide an efficient approach of the strength reduction due to the porosity. The purpose of the present paper is to extend this model in order to capture the influence of interface stresses.

To begin with, in view of subsequent extensions, the basic features of the classical Gurson approach are recalled. Then, the mechanical model of interface stress is introduced. Finally, the case of interface stresses obeying a von Mises failure criterion is considered.

2 Ductile Failure of Porous Media and Gurson Model

Let us consider a *r.e.v.* Ω of a porous material with porosity f. The solid domain is $\Omega^s \subset \Omega$. The average on Ω (resp. Ω^s) of a field $a(\underline{z})$ is denoted by $\overline{a}$ (resp. $\overline{a}^s$):

$$\overline{a} = \frac{1}{|\Omega|}\int_{\Omega} a(\underline{z})\, dV; \qquad \overline{a}^s = \frac{1}{|\Omega^s|}\int_{\Omega^s} a(\underline{z})\, dV \tag{1}$$

Let $\boldsymbol{\Sigma}$ and $\mathbf{D}$ respectively denote the macroscopic stress and strain rate tensors. $\mathscr{V}(\mathbf{D})$ is the set of microscopic velocity fields, $\underline{v}(\underline{z})$ being kinematically admissible with $\mathbf{D}$. The latter are defined by uniform strain boundary conditions:

$$\mathscr{V}(\mathbf{D}) = \left\{\underline{v},\ (\forall \underline{z} \in \partial\Omega)\ \underline{v}(\underline{z}) = \mathbf{D}\cdot\underline{z}\right\} \tag{2}$$

Let us consider a microscopic stress field $\boldsymbol{\sigma}(\underline{z})$ in equilibrium with $\boldsymbol{\Sigma}$ in the sense of the average rule $\boldsymbol{\Sigma} = \overline{\boldsymbol{\sigma}}$. Hill's lemma states that:

$$\boldsymbol{\Sigma} : \mathbf{D} = \frac{1}{|\Omega|}\int_{\Omega} \boldsymbol{\sigma} : \mathbf{d}\, dV \tag{3}$$

The strength of the solid phase is characterized by the convex set G^s of admissible stress states, which in turn is defined by a convex strength criterion $f^s(\sigma)$:

$$G^s = \left\{\sigma,\ f^s(\sigma) \leq 0\right\} \tag{4}$$

The dual definition of the strength criterion consists in introducing the support function $\pi^s(\mathbf{d})$ of G^s, which is defined on the set of symmetric second order tensors $\mathbf{d}$ and is convex w.r.t. $\mathbf{d}$:

$$\pi^s(\mathbf{d}) = \sup\left(\boldsymbol{\sigma} : \mathbf{d}, \boldsymbol{\sigma} \in G^s\right) \tag{5}$$

$\pi^s(\mathbf{d})$ represents the maximum "plastic" dissipation capacity the material can afford. In the absence of interface effect, the macroscopic counterpart of $\pi^s(\mathbf{d})$ is defined as:

$$\Pi^{hom}(\mathbf{D}) = (1-f) \inf_{\underline{v}\in\mathscr{V}(\mathbf{D})} \overline{\pi^s(\mathbf{d})}^s \quad \text{with} \quad \mathbf{d} = \frac{1}{2}\left(\operatorname{grad}\underline{v} + {}^t\operatorname{grad}\underline{v}\right) \tag{6}$$

Using Eq. (3) together with the definition equation (6), it can be shown that Π^{hom} is the support function of the domain G^{hom} of macroscopic admissible stresses:

$$\Pi^{hom}(\mathbf{D}) = \sup\left(\boldsymbol{\Sigma} : \mathbf{D},\ \boldsymbol{\Sigma} \in G^{hom}\right) \tag{7}$$

The limit stress states at the macroscopic scale are shown to be of the form $\boldsymbol{\Sigma} = \partial \Pi^{hom} / \partial \mathbf{D}$.

Starting from this general framework, the classical Gurson approach devoted to porous media deals with the case of a von Mises solid phase:

$$f^s(\boldsymbol{\sigma}) = \frac{3}{2}\boldsymbol{\sigma}_d : \boldsymbol{\sigma}_d - \sigma_o^2 \tag{8}$$

where $\boldsymbol{\sigma}_d$ is the deviatoric part of $\boldsymbol{\sigma}$. The support function $\pi^s(\mathbf{d})$ accordingly reads:

$$\begin{aligned} &\operatorname{tr}\mathbf{d} = 0 : \pi^s(\mathbf{d}) = \sigma_o d_{eq} \quad \text{with } d_{eq} = \sqrt{\frac{2}{3}\mathbf{d} : \mathbf{d}} \\ &\operatorname{tr}\mathbf{d} \neq 0 : \pi^s(\mathbf{d}) = +\infty \end{aligned} \tag{9}$$

The Gurson model introduces two simplifications. It first consists in representing the morphology of the porous material by a hollow sphere instead of the *r.e.v.* Let R_e (resp. R_i) denote the external (resp. cavity) radius. The volume fraction of the cavity in the sphere is equal to the porosity $f = (R_i/R_e)^3$. Then, instead of seeking the infimum in Eq. (6), $\Pi^{hom}(\mathbf{D})$ is estimated by a particular microscopic velocity field $\underline{v}(\underline{z})$. In the solid, the latter is defined as the sum of a linear part involving a second order tensor $\mathbf{A}$ and of the solution to an isotropic expansion in an incompressible medium. In spherical coordinates, it thus reads:

$$\underline{v}^G(\underline{z}) = \mathbf{A} \cdot \underline{z} + \alpha \frac{R_i^3}{r^2}\underline{e}_r \tag{10}$$

In the pore, the strain rate is defined from the velocity at the cavity wall:

$$\mathbf{d}^I = \mathbf{A} + \alpha \mathbf{1} \tag{11}$$

The local condition $\operatorname{tr}\mathbf{d} = 0$ has to be satisfied in the case of a von Mises material (see Eq. (9)). It follows then that $\mathbf{A}$ is a deviatoric tensor: $\operatorname{tr}\mathbf{A} = 0$. Furthermore, the boundary condition equation (2) at $r = R_e$ yields:

$$\mathbf{D} = \mathbf{A} + \alpha f \mathbf{1} \tag{12}$$

which reveals that $\mathbf{A}$ is the deviatoric part $\mathbf{D}_d$ of $\mathbf{D}$, while α is related to its spherical part:

$$\mathbf{A} = \mathbf{D}_d; \quad \alpha = \frac{1}{3f}\operatorname{tr}\mathbf{D} \tag{13}$$

The combination of Eq. (11) and Eq. (13) also yields:

$$\mathbf{d}^I = \mathbf{D}_d + \frac{\mathrm{tr}\,\mathbf{D}}{3f}\mathbf{1} \tag{14}$$

Recalling Eq. (6), the use of $\underline{v}^G$ (giving strain rate $\mathbf{d}^G$) provides an upper bound of Π^{hom}:

$$\Pi^{hom}(\mathbf{D}) \leq (1-f)\overline{\pi^s\left(\mathbf{d}^G\right)}^s \tag{15}$$

Using Eq. (9), the derivation of the right hand side in Eq. (15) requires to determine the average of d_{eq} over Ω^s. In order to obtain an analytical expression, it is convenient to apply the following inequality to $\mathscr{G} = \mathbf{d} : \mathbf{d} = 3d_{eq}^2/2$ [9]:

$$\int_{\Omega^s} \sqrt{\mathscr{G}(r,\theta,\varphi)}dV \leq 4\pi \int_{R_i}^{R_e} r^2 \left(\langle \mathscr{G} \rangle_{\mathscr{S}(r)}\right)^{1/2} dr \tag{16}$$

where $\mathscr{S}(r)$ is the sphere of radius r and $\langle \mathscr{G} \rangle_{\mathscr{S}(r)}$ is the average of $\mathscr{G}(r,\theta,\varphi)$ over all the orientations:

$$\langle \mathscr{G} \rangle_{\mathscr{S}(r)} = \frac{1}{4\pi r^2} \int_{\mathscr{S}(r)} \mathscr{G}(r,\theta,\varphi)\, dS \tag{17}$$

This eventually yields the following upper bound of $\Pi^{hom}(\mathbf{D})$:

$$\Pi_G^{hom}(\mathbf{D}) = \sigma_o f D_{eq} \left(\xi\left(\mathrm{arcsinh}(\xi) - \mathrm{arcsinh}(f\xi)\right) + \frac{\sqrt{1+f^2\xi^2}}{f} - \sqrt{1+\xi^2} \right) \tag{18}$$

with $D_{eq} = \sqrt{2\mathbf{D}_d : \mathbf{D}_d/3}$ and $\xi = 2\alpha/D_{eq}$. In the standard case (no interface effect), it is emphasized that the pore size R_i does not matter by itself since only the ratio $R_i/R_e = f^{1/3}$ intervenes in the expression Eq. (18).

The last step is the derivation of the limit states $\boldsymbol{\Sigma} = \partial \Pi_G^{hom}/\partial \mathbf{D}$. It is first observed that $\Pi_G^{hom}(\mathbf{D})$ is in fact a function of $\mathbf{D}$ through α and D_{eq}:

$$\boldsymbol{\Sigma} = \frac{\partial \Pi_G^{hom}}{\partial \alpha}\frac{\partial \alpha}{\partial \mathbf{D}} + \frac{\partial \Pi_G^{hom}}{\partial D_{eq}}\frac{\partial D_{eq}}{\partial \mathbf{D}} \tag{19}$$

where

$$\frac{\partial \alpha}{\partial \mathbf{D}} = \frac{1}{3f}\mathbf{1}; \qquad \frac{\partial D_{eq}}{\partial \mathbf{D}} = \frac{2}{3D_{eq}}\mathbf{D}_d \tag{20}$$

The combination of Eq. (19) and Eq. (20) also yields:

$$\mathrm{tr}\,\boldsymbol{\Sigma} = \frac{1}{f}\frac{\partial \Pi_G^{hom}}{\partial \alpha}; \qquad \Sigma_{eq} = \sqrt{3\boldsymbol{\Sigma}_d : \boldsymbol{\Sigma}_d/2} = \frac{\partial \Pi_G^{hom}}{\partial D_{eq}} \tag{21}$$

In turn, Eq. (18) leads to:

$$\begin{aligned} \operatorname{tr} \boldsymbol{\Sigma} &= 2\sigma_o\big(\operatorname{arcsinh}(\xi) - \operatorname{arcsinh}(f\xi)\big) \\ \Sigma_{eq} &= \sigma_o\left(\sqrt{1+f^2\xi^2} - f\sqrt{1+\xi^2}\right) \end{aligned} \tag{22}$$

Eliminating ξ between the spherical and deviatoric parts of $\boldsymbol{\Sigma}$ eventually leads to the well known Gurson strength criterion:

$$\frac{\Sigma_{eq}^2}{\sigma_o^2} + 2f\cosh\left(\frac{\operatorname{tr}\boldsymbol{\Sigma}}{2\sigma_o}\right) - 1 - f^2 = 0 \tag{23}$$

This equation characterizes the boundary of the domain G_G^{hom} which support function is Π_G^{hom}. This domain is in fact an upper bound of the exact domain G^{hom} of macroscopic admissible stresses, that is, $G^{hom} \subset G_G^{hom}$.

3 Interfaces and Interface Stresses

The recent literature devoted to nanocomposites has extensively presented the concepts of interface and interface stresses [4, 10–13]. In fact, these concepts are already present in the modeling of capillary forces [14]. The interface itself is a mathematical model for a thin layer between two phases across which the traction vector undergoes a discontinuity. In contrast, the displacement and the tangential strain components are continuous (see [3]). Introducing the local unit normal vector $\mathbf{n}$ to the interface S, the stress discontinuity $[\boldsymbol{\sigma}]\cdot\mathbf{n}$ is related to the interface stresses $\boldsymbol{\tau}$ by the generalized Laplace equations which physically represent the condition for the mechanical equilibrium of the interface [15]:

$$\begin{aligned} \mathbf{n}\cdot[\boldsymbol{\sigma}]\cdot\mathbf{n} &= -\boldsymbol{\tau} : \boldsymbol{\kappa} \\ \mathbf{P}\cdot\mathbf{n} &= -\nabla_S\cdot\boldsymbol{\tau} \end{aligned} \tag{24}$$

where $\nabla_S\cdot$ denotes the divergence operator defined on the interface S; tensor $\mathbf{P} = \mathbf{1} - \mathbf{n}\otimes\mathbf{n}$ and $\boldsymbol{\kappa}$ is the curvature tensor. The stress state $\boldsymbol{\tau}$ locally meets the plane stress conditions w.r.t. the tangent plane to the interface. We herein consider that the pore/solid boundary is such an interface.

The interface stresses also manifest themselves by a specific contribution to the energy $\mathscr{W}$ developed by the internal forces in the strain rate field $\mathbf{d}$:

$$\mathscr{W} = \int_\Omega \boldsymbol{\sigma} : \mathbf{d}\, dV = \int_{\Omega^s} \boldsymbol{\sigma} : \mathbf{d}\, dV + \int_S \boldsymbol{\tau} : \mathbf{d}\, dS \tag{25}$$

From a mathematical point of view, Eq. (25) amounts to saying that the internal forces can be represented by the sum of a standard Cauchy stress field $\boldsymbol{\sigma}$ in the solid

and by a Dirac distribution $\boldsymbol{\tau}$ of stresses of support S. Hence, the integral in the left-hand side of Eq. (25) must be understood in the sense of the distribution theory.

Since the interface stress state is a plane stress one, the work it develops in the strain rate $\mathbf{d}$ only depends on the projection $\mathbf{d}^{int}$ of $\mathbf{d}$ on the local tangent plane, which is defined as [5]:

$$\mathbf{d}^{int} = \mathbb{T} : \mathbf{d} \quad \text{with } \mathbb{T} = \mathbf{P}\underline{\otimes}\mathbf{P} \tag{26}$$

with $\mathbf{A}\underline{\otimes}\mathbf{B}_{ijkl} = (A_{ik}B_{jl} + A_{il}B_{jk})/2$.

The surface integral in the expression of $\mathscr{W}$ has a counterpart in the homogenized support function $\Pi^{hom}(\mathbf{D})$ which now reads:

$$\Pi^{hom}_{int}(\mathbf{D}) = \inf_{\underline{v}\in\mathscr{V}(\mathbf{D})}\left((1-f)\overline{\pi^s(\mathbf{d})}^s + \frac{1}{|\Omega|}\int_S \pi^{int}(\mathbb{T}:\mathbf{d})\,dS\right) \tag{27}$$

π^{int} denotes the support function of the domain G^{int} of admissible surface stresses (see also Eq. (5)):

$$\pi^{int}(\mathbb{T}:\mathbf{d}) = \sup\left(\boldsymbol{\tau} : \mathbb{T} : \mathbf{d}, \boldsymbol{\tau} \in G^{int}\right) \tag{28}$$

It is emphasized that the latter meet the local plane stress conditions.

The extension of the Gurson model to interface effects simply consists in estimating the support function $\Pi^{hom}(\mathbf{D})$ by the upper bound obtained for the velocity field $\underline{v}^G$ introduced in Eq. (10):

$$\Pi^{hom}_{G,int}(\mathbf{D}) = \Pi^{hom}_{G}(\mathbf{D}) + \frac{1}{|\Omega|}\int_S \pi^{int}\left(\mathbb{T}:\mathbf{d}^G\right)dS \tag{29}$$

Clearly, we are left with the determination of the interface correcting term, which has to be added to the standard expression (18).

4 Extension of the Gurson Model: The von Mises Interface

We now assume that the strength of the interface can be described by a von Mises criterion

$$\frac{3}{2}\boldsymbol{\tau}_d : \boldsymbol{\tau}_d - k^2_{int} \leq 0 \tag{30}$$

in *plane stress* condition, where $\boldsymbol{\tau}_d$ denotes the deviatoric part of the interface stress $\boldsymbol{\tau}$. The strength of the interface is then similar in nature to that of the matrix, up to the fact that it has a bidimensional character. In the local tangent plane which unit normal vector is $\underline{n} = \underline{e}_r$, the support function of the domain G^{int} then reads (see [16]):

$$\pi(\mathbb{T}:\mathbf{d}) = 2k^{int}\sqrt{\frac{1}{3}\left(d^2_{\theta\theta} + d^2_{\varphi\varphi} + d^2_{\varphi\theta} + d_{\theta\theta}d_{\varphi\varphi}\right)} \tag{31}$$

where k^{int} has the physical dimension of a membrane stress, that is, a force per unit length. The tensor $\mathbf{d}$ whose components appear in Eq. (31) is the pore strain rate $\mathbf{d}^I$ given in Eq. (14), which is then projected on the tangent plane by the operator $\mathbb{T}$. The projection operator $\mathbb{T}(\theta, \varphi)$ depends on the location on the spherical cavity wall (see Eq. (26)):

$$\mathbb{T} = \mathbf{P} \underline{\otimes} \mathbf{P} \quad \text{with } \mathbf{P} = \mathbf{1} - \underline{e}_r \otimes \underline{e}_r \tag{32}$$

The components of the strain rate tensor appearing in Eq. (31) are then given by

$$d_{\alpha\beta} = \underline{e}_\alpha \overset{s}{\otimes} \underline{e}_\beta : \mathbb{T} : \mathbf{d}^I \tag{33}$$

with $\alpha,\ \beta = \theta$ or φ, that is:

$$d_{\alpha\beta} = \mathbf{T}^{\alpha\beta} : \mathbf{d}^I \tag{34}$$

with $\mathbf{T}^{\alpha\beta} = \underline{e}_\alpha \overset{s}{\otimes} \underline{e}_\beta : \mathbb{T}$. It is therefore convenient to introduce the fourth-order tensor $\mathbb{M}$:

$$\mathbb{M} = \mathbf{T}^{\varphi\varphi} \otimes \mathbf{T}^{\varphi\varphi} + \mathbf{T}^{\theta\theta} \otimes \mathbf{T}^{\theta\theta} + \mathbf{T}^{\varphi\theta} \otimes \mathbf{T}^{\varphi\theta} + \mathbf{T}^{\varphi\varphi} \otimes \mathbf{T}^{\theta\theta} \tag{35}$$

such that

$$\pi^{int}(\mathbb{T} : \mathbf{d}) = 2k_{int}\sqrt{\frac{1}{3}\mathbf{d}^I : \mathbb{M} : \mathbf{d}^I} \tag{36}$$

In order to determine the contribution Π^{int} of the interface to $\Pi^{hom}(\mathbf{D})$ (see Eq. (27)), we are left with the integration over the spherical interface:

$$\Pi^{int} = \frac{2k_{int}}{|\Omega|}\int_S \sqrt{\frac{1}{3}\mathbf{d}^I : \mathbb{M} : \mathbf{d}^I}\, dS \tag{37}$$

As in the classical derivation of the Gurson criterion, we have to replace Π^{int} by an upper bound in order to obtain an analytical expression:

$$\Pi^{int} \leq \frac{2k_{int}R_i^2}{|\Omega|}\sqrt{\frac{4\pi}{3}\int_{S_o} \mathbf{d}^I : \mathbb{M} : \mathbf{d}^I\, dS} \tag{38}$$

where S_o is the (boundary of the) unit sphere. Since $\mathbf{d}^I$ is a constant, the right hand side in Eq. (38) can be put in the form:

$$\Pi^{int} \leq \frac{2k_{int}R_i^2}{|\Omega|}\sqrt{\frac{4\pi}{3}\,\mathbf{d}^I : \left(\int_{S_o} \mathbb{M}(\theta, \phi)\, dS\right) : \mathbf{d}^I} \tag{39}$$

Noting from Eq. (35) that:

$$\int_{S_o} \mathbb{M}\, d\sigma = \pi\left(\frac{6}{5}\mathbb{K} + 4\mathbb{J}\right) \tag{40}$$

the contribution of the interface to $\Pi^{hom}(\mathbf{D})$ can be estimated by the following upper bound:

$$\begin{aligned}\Pi^{int} &\leq 6f\frac{k_{int}}{R_i}\sqrt{\mathbf{d}^I : \left(\frac{1}{10}\mathbb{K}+\frac{1}{3}\mathbb{J}\right) : \mathbf{d}^I} \\ &= 3f\frac{k_{int}}{R_i}D_{eq}\sqrt{\xi^2+\frac{3}{5}} \quad \text{with } \xi = 2\alpha/D_{eq}\end{aligned} \tag{41}$$

in which it is recalled that R_i represents the radius of the pores. The term provided by (41) is to be added to Eq. (18) in view of the derivation of the strength criterion. The comparison of the respective contributions of the solid equation (18) and of the interface equation (41) is controlled by the nondimensional parameter

$$\Gamma = k_{int}/(R_i\sigma_o) \tag{42}$$

which is pore size-dependent. The smaller the pores the greater the influence of the interface effects on the strength.

We note that Eq. (19) and Eq. (21) are still valid provided that Π_G^{hom} is replaced by $\Pi_{G,int}^{hom} = \Pi_G^{hom} + \Pi^{int}$. This leads to the parametric equations

$$\begin{aligned}\text{tr}\,\boldsymbol{\Sigma} &= \sigma_o\left(2\big(\text{arcsinh}(\xi) - \text{arcsinh}(f\xi)\big) + \Gamma\frac{6\xi}{\sqrt{\xi^2+3/5}}\right) \\ \Sigma_{eq} &= \sigma_o\left(\sqrt{1+f^2\xi^2} - f\sqrt{1+\xi^2} + \Gamma\frac{9f}{5\sqrt{\xi^2+3/5}}\right)\end{aligned} \tag{43}$$

Note that this boundary is symmetric w.r.t. the $\text{tr}\,\boldsymbol{\Sigma} = 0$ axis. Let us emphasize that, by the presence of term $\Gamma = k_{int}/(R_i\sigma_o)$, (43) explicitly shows that the yield strength depends on the voids size. In order to get a closer insight into the influence of the interface on the effective strength, it is useful to provide an analytical approximation of the boundary of the domain defined by Eq. (43) in the form $\mathscr{F}(\Sigma_{eq}, \text{tr}\,\boldsymbol{\Sigma}) = 0$. This can be done by means of expansions of Eq. (43) in the vicinity of $\xi = 0$ and $\xi = \infty$. First, in the vicinity of the maximum deviatoric strength ($\xi = 0$, low stress triaxiality), the boundary can be approximated by a parabola in the $(\text{tr}\,\boldsymbol{\Sigma}, \Sigma_{eq})$ plane:

$$\frac{\Sigma_{eq}}{\sigma_o} = 1 - f + \Gamma\frac{9f}{\sqrt{15}} - \frac{f}{8(1-f+\Gamma\sqrt{15})}\left(\frac{\text{tr}\,\boldsymbol{\Sigma}}{\sigma_o^2}\right)^2 \tag{44}$$

In turn, in the vicinity of the pure isotropic tensile/compression loading ($\xi = \pm\infty$), the boundary can be approximated by another parabola:

$$\frac{\Sigma_{eq}^2}{\sigma_o^2} = \frac{3}{2}\left(1 - f^2 + \frac{18}{5}\Gamma f^2\right)\left(-\frac{2}{3}\log f + 2\Gamma \pm \frac{\text{tr}\,\boldsymbol{\Sigma}}{3\sigma_o}\right) \tag{45}$$

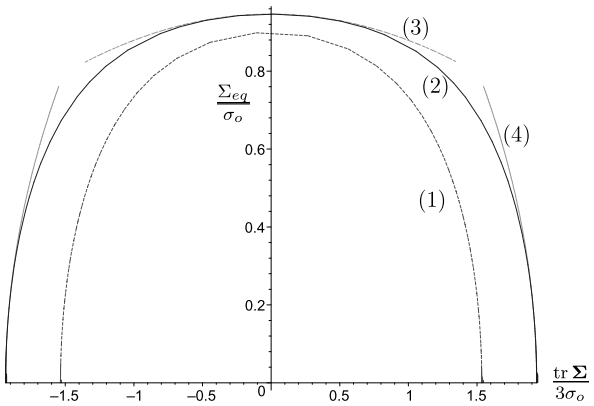

Fig. 1 (*1*): classical Gurson model; (*2*): extended Gurson model with $f = 0.1$ and $\Gamma = 0.2$; (*3*): parabola of (44); (*4*): parabola of (45)

Illustrations of the results are provided on Fig. 1. Continuous lines correspond to the parametric formulation of the macroscopic yield function (see (43)) while discontinuous lines are associated to the two above expansions derived in the form of parabola. First, the results clearly show a significant effect of the void size. Note that k_{int} being fixed, a decrease of R_i is represented by an increase of Γ. Moreover, the two proposed expansions appear accurate for a large range of triaxiality.

5 Isotropic Tensile/Compressive Strength

In the framework of the geometrical model of hollow sphere, the classical Gurson model (no interface stress) is known to provide an exact result as regards the isotropic tensile/compressive strength.

With $\Sigma_{eq} = 0$, the solutions to Eq. (23) are the isotropic stress tensors $\pm\Sigma^+\mathbf{1}$ with $\Sigma^+ = -2\sigma_o \log f/3$. As a matter of fact, the Gurson approach shows that an admissible isotropic macroscopic stress state $\boldsymbol{\Sigma} = \Sigma\mathbf{1}$ is subjected to the condition $|\Sigma| \leq \Sigma^+$. Conversely, let us consider the microscopic stress state defined in the solid in spherical coordinates by:

$$\boldsymbol{\sigma} = \varepsilon \frac{3\Sigma^+}{2\log f}\left(2\log\frac{R_i}{r}\,\mathbf{1} - \mathbf{P}\right) \quad \text{with } \varepsilon = \pm 1 \tag{46}$$

It is readily seen that the latter is in equilibrium with the macroscopic stress state $\varepsilon\Sigma^+\mathbf{1}$ since it satisfies the momentum balance condition $\mathrm{div}\,\boldsymbol{\sigma} = 0$ and the boundary conditions $\boldsymbol{\sigma}\cdot\underline{e}_r = 0$ at $r = R_i$ and $\boldsymbol{\sigma}\cdot\underline{e}_r = \varepsilon\Sigma^+\underline{e}_r$ at $r = R_e$. Furthermore, it meets the von Mises criterion equation (8). This proves that such a macroscopic stress state is admissible and furthermore, that Σ^+ is indeed the isotropic tensile/compressive strength.

Let us now examine the effect of interface stresses on the isotropic tensile/compressive strength. Consider the case of the von Mises interface. According to the extended Gurson model equation (45), the necessary condition for an isotropic

macroscopic stress state $\boldsymbol{\Sigma} = \Sigma \mathbf{1}$ to be admissible reads $|\Sigma| \leq \Sigma^+ + 2\Gamma\sigma_o$. Conversely, let us consider the microscopic stress state defined in the solid in spherical coordinates by:

$$\boldsymbol{\sigma} = \varepsilon\left(\frac{3\Sigma^+}{2\log f}\left(2\log\frac{R_i}{r}\,\mathbf{1} - \mathbf{P}\right) + 2\Gamma\sigma_o\mathbf{1}\right) \quad \text{with } \varepsilon = \pm 1 \tag{47}$$

and on the interface S by $\boldsymbol{\tau} = \varepsilon k_{int}\mathbf{P}$ (recall that $k_{int} = \Gamma\sigma_o R_i$). It satisfies the momentum balance equation $\operatorname{div}\boldsymbol{\sigma} = 0$ and the boundary condition $\boldsymbol{\sigma}\cdot\underline{e}_r = \varepsilon(\Sigma^+ + 2\Gamma\sigma_o)\underline{e}_r$ at $r = R_e$. It also satisfies the generalized Laplace equations (24). Furthermore, it meets the von Mises interface criterion equation (30). This establishes that $\Sigma^+ + 2\Gamma\sigma_o$ is the isotropic tensile/compressive strength.

References

1. Walpole, L.J.: Coated inclusions in an elastic medium. Math. Proc. Camb. Philos. Soc. **83**, 495–506 (2000)
2. Marcadon, V., Hervé, E., Zaoui, A.: Micromechanical modelling of packing and size effects in particulate composites. Int. J. Solids Struct. **44**, 8213–8228 (2007)
3. Duan, H.L., Wang, J., Huang, Z.P., Karihaloo, B.L.: Size-dependent effective elastic constants of solids containing nano-inhomogeneities with interface stress. J. Mech. Phys. Solids **53**, 1574–1596 (2005)
4. Sharma, P., Ganti, S.: Size-dependent Eshelby's tensor for embedded nano-inclusions incorparating surface/interface. J. Appl. Mech. **71**, 663–671 (2004)
5. Quang, H.L., He, K.C.: Variational principles and bounds for elastic inhomogeneous materials with coherent imperfect interfaces. Mech. Mater. **40**, 865–884 (2008)
6. Brisard, S., Dormieux, L., Kondo, D.: Hashin.shtrikman bounds on the bulk modulus of a nanocomposite with spherical inclusions and interface effects. Comput. Mater. Sci. **48**, 589–596 (2010)
7. Brisard, S., Dormieux, L., Kondo, D.: Hashin.shtrikman bounds on the shear modulus of a nanocomposite with spherical inclusions and interface effects. Comput. Mater. Sci. **50**, 403–410 (2010)
8. Zhang, W.X., Wanga, T.J., Chen, X.: Effect of surface/interface stress on the plastic deformation of nanoporous materials and nanocomposites. Int. J. Plast., pp. 957–975 (2010)
9. Gurson, A.L.: Continuum theory of ductile rupture by void nucleation and growth: part i, yield criteria and flow rules for porous ductile media. J. Eng. Mater. Technol. **99**, 2–15 (1977)
10. Orowan, E.: Surface energy and surface tension in solids and liquids. Proc. R. Soc. A **316**, 473–491 (1970)
11. Gurtin, M.E., Murdoch, A.I.: Continuum theory of elastic material surfaces. Arch. Ration. Mech. Anal. **57**, 291–323 (1975)
12. Spaepen, F.: Interfaces and stresses in thin films. Acta Mater. **48**, 31–42 (2000)
13. Duan, H.L., Wang, J., Huang, Z.P., Luo, Z.Y.: Stress-concentration tensors of inhomogeneities with interface effects. Mech. Mater. **37**, 723–736 (2005)
14. Israelachvili, J.: Intermolecular and Surface Forces. Academic Press, San Diego (1992)
15. Povstenko, Y.Z.: Theoretical investigation of phenomena caused by heterogeneous surface tension in solids. J. Mech. Phys. Solids **41**, 1499–1514 (1993)
16. Salençon, J.: Calcul à la rupture et analyse limite. Presses de l'ENPC (1983)

Limit Analysis and Conic Programming for Gurson-Type Spheroid Problems

F. Pastor, P. Thoré, D. Kondo, and J. Pastor

Abstract In his famous 1977-paper, Gurson used the kinematic approach of Limit Analysis (LA) about the hollow sphere model with a von Mises solid matrix. The computation led to a macroscopic yield function of the "Porous von Mises"-type materials. Several extensions have been further proposed in the literature, such as those accounting for void shape effects by Gologanu et al. (J. Eng. Mater. Technol. 116:290–297, 1994; Continuum Micromechanics, Springer, Berlin, 1997), among others. To obtain pertinent lower and upper bounds to the exact solutions in terms of LA, we have revisited our existing kinematic and static 3D-FEM codes for spherical cavities to take into account the model with confocal spheroid cavity and boundary. In both cases, the optimized formulations have allowed to obtain an excellent efficiency of the resulting codes. A first comparison with the Gurson criterion does not only show an improvement of the previous results but points out that the real solution to the hollow sphere model problem depends on the third invariant of the stress tensor. A second series of tests is presented for oblate cavities, in order to analyze the above-mentioned works in terms of bound and efficiency.

F. Pastor
Laboratoire de mécanique de Lille (LML), UMR 8107 CNRS, Villeneuve d'Ascq, France
e-mail: franck.pastor@skynet.be

P. Thoré · J. Pastor (✉)
Laboratoire LOCIE, Polytech' Annecy-Chambéry, Université de Savoie, 73376 Le Bourget du Lac, France
e-mail: joseph.pastor@univ-savoie.fr

P. Thoré
e-mail: philippe.thore@orange.fr

D. Kondo
Institut D'Alembert, Université Pierre et Marie Curie, UMR 7190 CNRS, 75252 Paris Cedex 05, France
e-mail: djimedo.kondo@upmc.fr

G. Saxcé et al. (eds.), *Limit State of Materials and Structures*,
DOI 10.1007/978-94-007-5425-6_12,

1 Introduction

As regards the ductile failure of porous materials, the celebrated plasticity criterion of Gurson [8] is based on a micro-macro approach and on limit analysis (LA). Gurson's model treats a hollow von Mises sphere or cylinder with macroscopic strain imposed on its boundary. The computation, performed under uniform strain rate boundary conditions, leads to a macroscopic yield function for the "Porous von Mises"-type materials.

Gurson's analysis consists in the use of the LA kinematic approach in order to obtain an upper bound to the macroscopic criterion of the spherically porous material, at least in the sense of the Composite Sphere Assemblage of Hashin. An efficient parametric refinement of Gurson's model has been proposed in [24] and [25] to define the widely used Gurson-Tvergaard-Needleman (GTN) model. More recently, several extensions of the Gurson model have been proposed, the probably most important developments being those accounting for void-shape effects [4, 7, 14]. Mention can also be made of models taking into account plastic anisotropy [1, 13].

On the other hand, using a finite element discretization of the mechanical systems, both static and kinematic methods of LA have been elaborated to obtain rigorous lower and upper bounds in order to control Gurson's kinematic approaches for cylindrical as well as spherical cavities, first reported in [20]. In [3] and [19], these two LA approaches made it possible to numerically determine the yield criteria of a cylindrically porous material, also proving that the Gurson criterion is approximate, and does not exhibit the corner of the exact criterion on the mean stress axis in plane strain. On the contrary, in the subsequent work [23] the Gurson criterion appears to be satisfactory for materials with spherical cavities, unfortunately without considering the dissymmetry as in the present work.

The main advantage of these LA numerical approaches is that they give rigorous lower and upper bounds to the macroscopic criterion together with their controllability *a posteriori* from the final optimal solution. This capability to control numerical or analytical results is central and was used in [18], and in [22] for example.

In the present paper, we briefly present the extension in [15] of the 3D static and kinematic codes of [23] for von Mises matrices to the spheroid (confocal) cavity case. Then, comparisons with previously mentioned works for spherical and oblate cavites conditions are presented and discussed.

2 The Hollow Spheroid Model

The considered hollow spheroid model is made up of a single spheroidal cavity embedded in a confocal spheroidal cell. The solid matrix is an isotropic, homogeneous, and rigid-plastic von Mises material. Figure 1 presents the geometrical model, where the given aspect ratio a_1/b_1 and porosity f allow to determine the characteristics a_2 and b_2 of the confocal spheroidal boundary. Let us consider the three-dimensional point of view, and denote Σ and E the macroscopic stress and

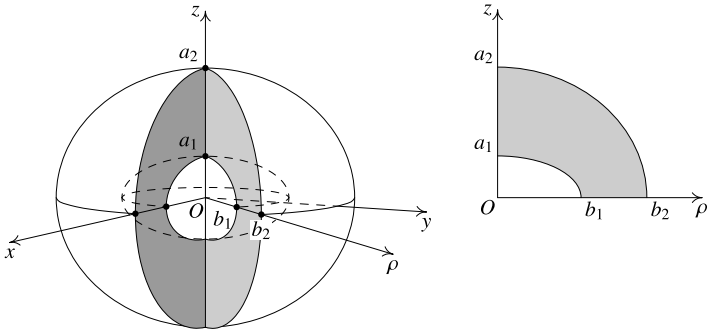

Fig. 1 The hollow spheroid model ($a_1/b_1 = 0.5,\ f = 0.1$)

strain rate tensors. These quantities are classically related to the microscopic fields by their average over the model of volume V:

$$\Sigma_{ij} = \frac{1}{V}\int_V \sigma_{ij}\, dV; \qquad E_{ij} = \frac{1}{2V}\int_{\partial V} (u_i n_j + u_j n_i)\, dS, \tag{1}$$

where ∂V denotes the external boundary of the model, and u the velocity vector.

Under the Hill-Mandel boundary conditions, here $u_i = E_{ij}x_j$ on the external boundary, the overall virtual dissipated power $P_{\text{tot}} = \Sigma_{ij}E_{ij}$ can be written as follows:

$$P_{\text{tot}} = V(\Sigma_{\text{m}}E_{\text{m}} + \Sigma_{\text{ps}}E_{\text{ps}} + \Sigma_{\text{gps}}E_{\text{gps}} + \Sigma_{yz}2E_{yz} + \Sigma_{zx}2E_{zx} + \Sigma_{xy}2E_{xy}), \tag{2}$$

where the macroscopic stresses (the loading parameters in terms of limit analysis) and the associated strain rates are here defined as:

$$\Sigma_{\text{m}} = \frac{1}{3}(\Sigma_x + \Sigma_y + \Sigma_z); \qquad \Sigma_{\text{gps}} = \frac{(\Sigma_x + \Sigma_y)}{2} - \Sigma_z; \tag{3}$$

$$\Sigma_{\text{ps}} = \frac{\sqrt{3}}{2}(\Sigma_x - \Sigma_y);$$

$$\Sigma_{yz}; \quad \Sigma_{zx}; \quad \Sigma_{xy}; \tag{4}$$

$$E_{\text{m}} = (E_x + E_y + E_z); \qquad E_{\text{gps}} = \frac{2}{3}\left(\frac{(E_x + E_y)}{2} - E_z\right); \tag{5}$$

$$E_{\text{ps}} = \frac{1}{\sqrt{3}}(E_x - E_y);$$

$$2E_{yz}; \quad 2E_{zx}; \quad 2E_{xy}. \tag{6}$$

In these definitions the subscripts (*gps* for generalized plane strain, and *ps* for plane strain) were defined in [19], as $\Sigma_{\text{gps}} = 0$ is the usual relation in plane strain for the von Mises material. From the matrix isotropy and the spheroidal geometry

of the model, the resulting material is transversally isotropic around the axis z. Here is investigated the macroscopic criterion $g(\Sigma)$ in the $(Oxyz)$ anisotropy frame.

To compare with Gologanu's axisymmetric results, we search for the projection of $g(\Sigma)$ on the $(\Sigma_{\text{gps}}, \Sigma_{\text{m}})$ plane by optimizing Σ_{gps} for fixed uniform stresses Σ_{m}, the other stress components defined in (4) being free. Then $\frac{\partial g}{\partial \Sigma_{ij}} = 0 = 2E_{ij}$ for $i \neq j$, and $\frac{\partial g}{\partial \Sigma_{\text{ps}}} = 0 = E_{ps}$ since the macroscopic material verifies the normality law. As a final result, loadings can be restricted to the principal macroscopic strain rates E (as well as Σ since $(Oxyz)$ is a transverse-isotropy frame) with $E_{\text{ps}} = 0$.

Moreover, all the axes in the horizontal plane of Fig. 1 are equivalent; therefore, in the above-mentioned projection problem we also impose, although this is not mandatory, $\Sigma_x = \Sigma_y$ as well as $E_x = E_y$ in fact. Indeed, when non imposed *a priori*, these equalities are always verified in the optimal solutions, giving by the way a good control of the mesh quality.

Finally, the overall external power P_{tot} here reduces to:

$$P_{\text{tot}} = V(\Sigma_{\text{m}} E_{\text{m}} + \Sigma_{\text{gps}} E_{\text{gps}}). \tag{7}$$

Therefore, the one-eighth of the hollow spheroid is meshed into tetrahedral elements as shown in Fig. 2. This mesh respects the symmetries of the problem since the vertical coordinate planes are equivalent regarding the distribution of elements, giving rise to a well-conditioned numerical problem. Note that the macroscopic equivalent stress Σ_{eqv} is, in the present case, linked to Σ_{gps} by:

$$\Sigma_{\text{eqv}}^2 = \frac{3}{2}\,\text{dev}(\Sigma) : \text{dev}(\Sigma) = \Sigma_{\text{gps}}^2 = (\Sigma_x - \Sigma_z)^2, \tag{8}$$

where $\text{dev}(\Sigma)$ is the deviatoric part of Σ.

Hereafter, we first briefly present both lower/upper limit analysis approaches which have recently been detailed in [15]. The basis of the development of these numerical tools are their versions presented in [23] for spherical cavities; therefore we only detail here the modifications and improvements implemented for the present case. In a second step, results are analyzed and compared to those provided in [6] and [7] for oblate models under uniform strain rate boundary conditions.

3 Limit Analysis: The Static Method

3.1 The von Mises Criterion

As classically, the criterion is written as:

$$f(\sigma) = \sqrt{J_2} \quad \text{with } J_2 = \frac{1}{2}\text{tr}\left(s^2\right) \quad \text{and} \quad s = \sigma - \frac{1}{3}\text{tr}(\sigma)\delta, \tag{9}$$

where δ is the second order unit tensor.

Then in an (x, y, z) reference frame, the full 3D criterion reads:

$$\sqrt{\left[\frac{2}{\sqrt{3}}\left(\frac{\sigma_x+\sigma_y}{2}-\sigma_z\right)\right]^2+(\sigma_x-\sigma_y)^2+(2\tau_{yz})^2+(2\tau_{zx})^2+(2\tau_{xy})^2}\leq 2k. \tag{10}$$

The constant k is the limit in pure shear, also given by $\sigma_0/\sqrt{3}$ where σ_0 is the tensile strength of the von Mises material. It should be noted that (10) can be written, after obvious changes of variables, as a conic constraint for the conic optimizer MOSEK [12]:

$$\sqrt{\sum_{j=1}^{5} x_j^2}\leq x_6=2k. \tag{11}$$

3.2 Numerical Implementation

For each aspect ratio a_1/b_1, the inner and outer matrix boundaries of the spheroid mesh are adapted from the spherical case to obtain their confocal forms in the final mesh. Each triangle of a polyhedral surface n is the top basis of a prism whose the bottom basis is the corresponding triangle of the surface $n-1$, and so on going to the cavity. Each prism is divided into two tetrahedrons and three pyramids. Each pyramid is also divided into four tetrahedrons. Hence, each prism is meshed using 14 tetrahedral elements. For example the mesh of Fig. 2 involves 4 concentric layers ($nlay = 4$) of 4×4 prisms ($ndiv \times ndiv$, $ndiv = 4$) each, resulting finally in $nlay \times ndiv^2 \times 14 = 896$ tetrahedrons As the model boundaries are not homothetic and the practical number of triangles forming the resulting polyhedral mesh boundaries is not infinite, the resulting mesh porosity does not exactly equal the input porosity. Then, in a first step for each case of porosity and aspect ratio, the distribution of the angle α (see Fig. 2 right) is optimized to precisely retrieve the desired porosity by progressively concentrating this distribution towards the most curved zone. In a final step the radial distribution of the spheroid layers is also optimized to obtain the best value for the isotropic loading ($\Sigma_{\text{gps}} = 0$) with the static code.

The local stress field is chosen as linearly varying in x, y, z in each tetrahedral element, and represented by a 6-component tensor σ for each vertex of this tetrahedral element. Consequently this stress field can be discontinuous across any element boundary, which has been proven to be indispensable in the finite element static approach [17]. Finally, to reduce the size of the constraint matrix of the numerical problem, a change of variables $\sigma \rightarrow (x_0, \ldots, x_5)$ is performed, where $x_0 = \operatorname{tr}\sigma$ and x_1 to x_5 defined in (11), so that only the definition of x_6 is needed as a new constraint (and a new auxiliary variable) for each tetrahedron vertex.

To get a statically admissible microscopic stress field, the definition of the macroscopic stresses and of the selected loading parameters, the equilibrium equations

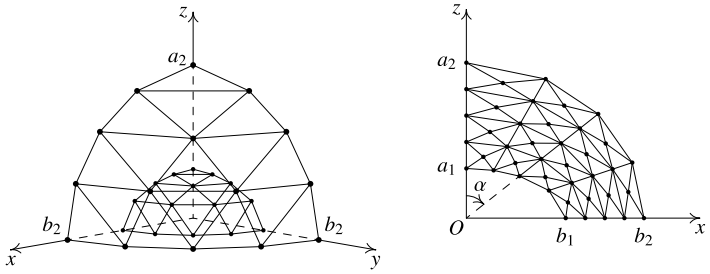

Fig. 2 General view and Oxz plane of a 896-tetrahedron mesh ($a_1/b_1 = 0.5$, $f = 0.1$)

and the stress vector continuity across the inter element triangles, the boundary and symmetry conditions give rise to a final matrix of equality constraints.

To enforce the stress field to be plastically admissible, the criterion (10) is imposed at each apex of the tetrahedron; hence, due to its convexity, the criterion is fulfilled anywhere in the element. For each tetrahedron the four conic inequalities are directly handled by MOSEK by simply indicating the names of the variables x_i involved in the criteria (11). The final numerical problem is a constrained conic programming one, which is a specificity of MOSEK.

Finally, concerning the objective functional to be optimized, Σ_{m} is given successive desired values and Σ_{gps} is minimized; when Σ_{m} is close to its maximum value, then Σ_{gps} is fixed and Σ_{m} is maximized for better convergence of the optimization process.

4 Limit Analysis: The Kinematic Method

4.1 Dissipated powers

Let us recall that, from the virtual power principle, the total dissipated power P_{tot} here reads:

$$\Sigma_{\mathrm{m}} E_{\mathrm{m}} + \Sigma_{\mathrm{gps}} E_{\mathrm{gps}} = (P_{\mathrm{vol}} + P_{\mathrm{disc}})/V = P_{\mathrm{tot}}/V, \tag{12}$$

where the volumic dissipated power $P_{\mathrm{vol}} = \int_{V_{\mathrm{m}}} \pi(d)\, dV$ and $\pi(d)$ is now defined as:

$$\pi(d) = 2k\sqrt{\left(\frac{\sqrt{3}}{2}(d_{xx} + d_{yy})\right)^2 + \left(\frac{1}{2}(d_{xx} - d_{yy})\right)^2 + d_{yz}^2 + d_{zx}^2 + d_{xy}^2}. \tag{13}$$

The power dissipated by the velocity jump $[u]$ on the discontinuities is given by:

$$P_{\mathrm{disc}} = \int_{S_{\mathrm{d}}} \pi\big([u]\big)\, dS = \int_{S_{\mathrm{d}}} k\big|[u_t]\big|\, dS = \int_{S_{\mathrm{d}}} k\sqrt{[u_{t_1}]^2 + [u_{t_2}]^2}\, dS, \tag{14}$$

where S_{d} is the set of discontinuity surfaces; for each discontinuity surface, $[u_{t_1}]$ and $[u_{t_2}]$ are the tangential displacement velocity jumps in an orthonormal frame (n, t_1, t_2) whose n is normal to this discontinuity surface.

4.2 Numerical Implementation

The above-mentioned mesh type is also used for the kinematic approach. The displacement velocity field is chosen as linearly varying in x, y, z in each tetrahedral element, and any triangular surface common to two contiguous tetrahedrons is a potential surface of velocity discontinuity. Then the variables are (u_x, u_y, u_z) velocity vectors located at the apices of each tetrahedron.

To get a kinematically admissible velocity field, the definition of the selected macroscopic variables E_{m}, E_{gps}, E_{ps} from E_{xx}, E_{yy}, E_{zz}, the incompressibility and symmetry conditions, and the strain rate loading ones (i.e. $u_i = E_{ij} x_j$ on each apex on the boundary triangles) form a final constraint matrix.

Concerning the definition of the functional to be optimized, by taking into account (13), we can upper bound the volumetric dissipated power in the tetrahedron by writing:

$$\pi(d) \leq Y; \qquad P_{\mathrm{vol}}^{\mathrm{el}} \leq V^{\mathrm{el}}\, Y \tag{15}$$

for each tetrahedron whose volume is denoted V^{el}. The first inequality in (15) gives one conic constraint and one non-negative auxiliary variable Y for each element.

As the velocity jump $[u]$ is linear on each triangular discontinuity side, whose surface is denoted S^{side}, we use the convexity of $\pi([u])$ to upper bound P_{disc} by writing at each apex i of the side ($i = 1$ to 3):

$$\pi\big([u]_i\big) \leq Z_i, \tag{16}$$

where the Z_i are new non-negative auxiliary variables, and $P_{\mathrm{disc}}^{\mathrm{side}} \leq S^{\mathrm{side}}\,(Z_1 + Z_2 + Z_3)/3$, resulting in three conic constraints for each discontinuity side. Then, using these definitions and after integrations over the mesh, we substitute the final upper bound $P_{\mathrm{tot}}^{\mathrm{ub}}$ for P_{tot} in the following.

In the present case of two loading parameters, Σ_{m} and Σ_{gps}, the following functional is used to define the points of the macroscopic criterion for zero or small absolute values of Σ_{gps}:

$$\Sigma_{\mathrm{m}} = \min\big(P_{\mathrm{tot}}^{\mathrm{ub}}/V - \Sigma_{\mathrm{gps}}^0\, E_{\mathrm{gps}}\big)/E_{\mathrm{m}}^0, \quad \text{with } E_{\mathrm{m}}^0 = 1. \tag{17}$$

To obtain other non-zero $(\Sigma_{\mathrm{m}}^0, \Sigma_{\mathrm{gps}})$ points, we chose the following functional, for better convergence, as in the static case:

$$\Sigma_{\mathrm{gps}} = \min\big(P_{\mathrm{tot}}^{\mathrm{ub}}/V - \Sigma_{\mathrm{m}}^0\, E_{\mathrm{m}}\big)/E_{\mathrm{gps}}^0, \quad \text{with } E_{\mathrm{gps}}^0 = \pm 1. \tag{18}$$

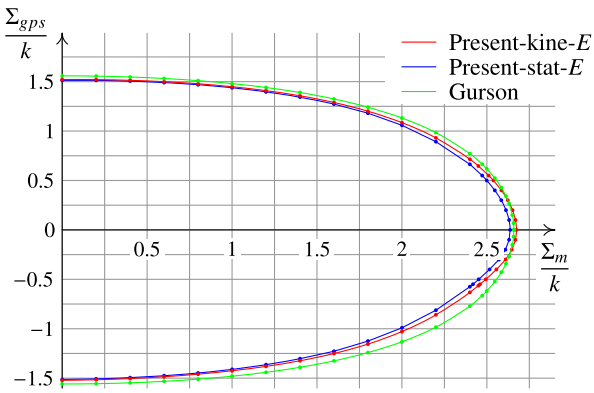

Fig. 3 Comparison with the Gurson criterion ($a_1/b_1 = 1$, $f = 0.1$)

Remark For both static and kinematic methods the final conic problem is solved using MOSEK, and the admissible character of the optimal solution field is checked *a posteriori*.

5 The Tests

Under uniform strain rate on the boundary, in the static case the mesh involves 13 layers of 12×12 prisms (with triangular basis) composed of 14 tetrahedrons, resulting in a conic programming problem handling about 730,000 variables and 658,000 constraints. In the kinematic case the mesh is the same, but with $11 \times 11 \times 11$ prisms resulting in 663,000 variables and 445,000 constraints. CPU times are about 3,000 seconds in the static case and 5,000 seconds in the kinematic one, with the release 5 of MOSEK on a recent Apple Mac Pro (using one core). For uniform stress loading, the figures are similar. In both cases the memory limitation of this release does not allow to consider more refined meshes. These CPU times also explain that obtaining the full numerical yield criterion, (then with meshes not limited to the one-eighth of the spheroid) and for various other geometries, does not seem realistic without defining a specific decomposition of the problem as in [16] and [9], at least for the moment.

Since the von Mises criterion is an even function in terms of stress, we limit the study to nonnegative values of Σ_m. In this section, the loading is axisymmetric for all tests and $\Sigma_{\text{eqv}} = |\Sigma_{\text{gps}}|$. We begin by testing the codes in the spherical cavity case to compare with the Gurson criterion in the whole $\Sigma_m \geq 0$ half plane. Then we analyze the oblate case with a ratio $a_1/b_1 = 0.2$ (see Fig. 1) for the case of uniform strain rate (E) on the boundary to compare the solutions with the analytical results of [6, 7] where the results are given in terms of $\Sigma_z - \Sigma_\rho = -\Sigma_{\text{gps}}$.

Table 1 Comparison of Gurson criterion and present kinematic results for negative Σ_{gps} and $f = 0.3$

Σ_m	-(Gurson Σ_{eqv})	-(3D-kine Σ_{gps})
0.0	1.21244	1.17101
0.2	1.20122	1.15328
0.4	1.16658	1.10820
0.6	1.10521	1.03030
0.8	1.01017	0.91075
1.0	0.86703	0.73865
1.2	0.63821	0.49854
1.26587	0.52497	0.4
1.32245	0.39332	0.3
1.36344	0.24993	0.2
1.38674	0.09075	0.1
1.39023	0.0	0.07634
1.39432	–	0.0

5.1 Spherical Cavity, Uniform Strain Rate Loading

The celebrated Gurson criterion reads:

$$\frac{\Sigma_{\text{eqv}}^2}{3k^2} + 2f\cosh\left(\frac{\sqrt{3}\Sigma_m}{2k}\right) = 1 + f^2. \tag{19}$$

Figure 3 gives the lower bounds (green color) and upper bounds (red color) together with the graph of Gurson's criterion. The numerical bounds are very close to each other and the Gurson graph is always beyond the kinematical approach, except at the vicinity of the Σ_{m} axis, as expected from the exact nature of the solution of Gurson on this axis.

More surprisingly, it can be seen that the real criterion is not really symmetric with respect to the horizontal axis; this means (from (8)) that, even for spherical cavities, the criterion depends on the third invariant of the macroscopic stress; this feature has been observed by Danas et al. [2] using a non linear homogenization method and recently confirmed in [21]. Up to our knowledge a possible small influence of the third stress invariant for "porous von Mises" materials was first noted in [5], through an only kinematic numerical approach based on some of the *continuous* velocity fields of Lee and Mear [11].

It can also be concluded that using the Gurson criterion in the usual ($\Sigma_{\text{eqv}} = |\Sigma_{\text{gps}}|, \Sigma_{\text{m}}$) frame is not pertinent; indeed, for a porosity of 0.3 (usual value in geotechnics and polymers) the results of Table 1 show that the difference between Gurson's values and our present 3D-kinematic results for negative Σ_{gps} becomes really significant.

Remark For $\Sigma_m = 0$ and $f = 0.1$, the Hashin-Strikmann (H-S) upper bound given by Willis and others (see [10]) (here $1.5093 = \sqrt{3}(1-f)/\sqrt{1+2f/3}$), is lower

Table 2 Comparison of Gurson and 3D-FEM results to Hashin-Strikman bounds ($\Sigma_m = 0$)

f	Σ_{eqv}^{Gurson}	Σ_{gps}^{stat}	Σ_{gps}^{kine}	H-S bound
0.01	1.71473	1.70501	1.70832	1.70904
0.1	1.55885	1.51393	1.52016	1.50935
0.2	1.38564	1.33165	1.34035	1.30158
0.3	1.21244	1.16114	1.17101	1.10680
0.4	1.03923	0.98765	1.00029	0.92338
0.5	0.86602	0.80637	0.82311	0.75

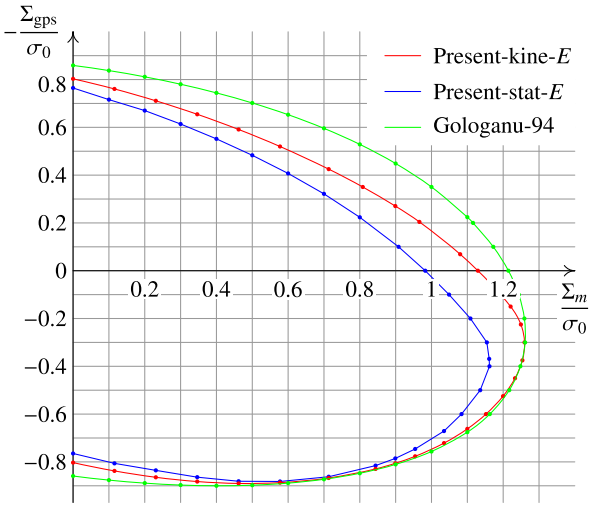

Fig. 4 Comparison of the 1994-Gologanu criterion with numerical bounds. The aspect ratio is taken as $a_1/b_1 = 0.2$ and the porosity f equal to 0.1

than the present static value, 1.5139. This static bound is obtained by using a mesh of 13 layers of 12×12 triangles generating 26,208 discontinuous linear tetrahedrons, i.e., a very refined 3D-mesh for the discretized one-eighth of sphere. Taking into account the fact that the exact value on the horizontal axis is just situated between the very close static and kinematic values, this should indicate that the hollow sphere model does not strictly account for the randomly porous hypothesis of the H-S bounds. Finally the results of Table 2 confirm this conclusion, since the static results are no longer close to the H-S bounds for greater porosity values.

5.2 Confocal Oblate Cavity, Uniform Strain Rate Loading

In this section we compare our results with the analytic criterion of Gologanu [6] and its improved version in [7], under uniform strain rate at the boundary. Figures 4 and 5 give the present results together with those of Gologanu et al. for $f = 0.1$.

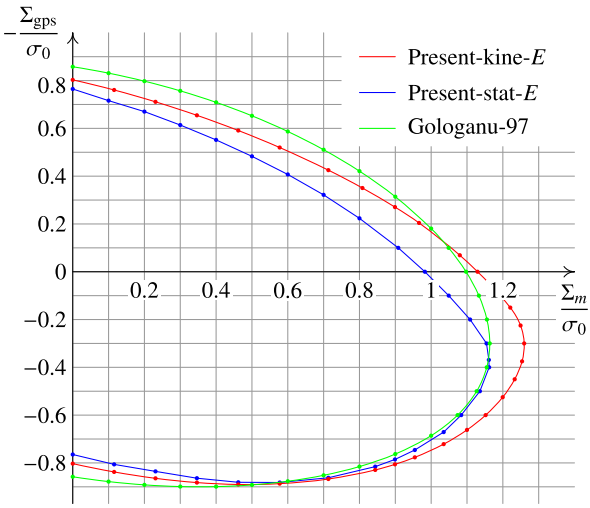

Fig. 5 Comparison of the 1997-Gologanu criterion with numerical bounds. $a_1/b_1 = 0.2$, $f = 0.1$

It first appears that the numerical bounds provide yield surfaces satisfactorily close to each other, in particular for the lowest porosity. Moreover, for this low porosity, the first approximate yield surface given by Gologanu et al. in 1994, based on axisymmetric fields proposed by Lee and Mear [11], is largely beyond our upper bound and overestimates the exact criterion in a large part of the stress domain. *A contrario* the second criterion of Gologanu et al. denotes a significant improvement of the previous Gologanu approach, with a slight localized violation of the numerical static approach possibly due to the loss of the upper bound character, resulting from the approximations done by these authors.

6 Conclusion

In the present paper, we have presented the extension of our previous 3D static and kinematic FEM codes for von Mises matrices to the spheroid (confocal) cavity case. On purpose of validation the first applications concern the Gurson model, and reveal that this criterion is not so near to the real solution, which depends on the third stress invariant in a non-negligible manner. The following tests concern the spheroid confocal cavity case and the last Gologanu criterion should be preferred in the case of uniform strain rate on the boundary.

References

1. Benzerga, A.A., Besson, J.: Plastic potentials for anisotropic porous solids. Eur. J. Mech. A, Solids **20**, 397–434 (2001)
2. Danas, K., Idiart, M.I., Castañeda, P.P.: A homogenization-based constitutive model for isotropic viscoplastic porous media. Int. J. Solids Struct. **45**, 3392–3409 (2008)

3. Francescato, P., Pastor, J., Riveill-Reydet, B.: Ductile failure of cylindrically porous materials. Part i: plane stress problem and experimental results. Eur. J. Mech. A, Solids **23**, 181–190 (2004)
4. Garajeu, M., Suquet, P.: Effective properties of porous ideally plastic or viscoplastic materials containing rigid particles. J. Mech. Phys. Solids **45**, 873–902 (1997)
5. Gologanu, M.: Etude quelques problèmes de rupture ductile des métaux. Thèse de doctorat, Université Paris-6 (1997)
6. Gologanu, M., Leblond, J., Perrin, G., Devaux, J.: Approximate models for ductile metals containing non-spherical voids—case of axisymmetric oblate ellipsoidal cavities. J. Eng. Mater. Technol. **116**, 290–297 (1994)
7. Gologanu, M., Leblond, J., Perrin, G., Devaux, J.: Recent extensions of gurson's model for porous ductile metals. In: Suquet, P. (ed.) Continuum Micromechanics. Springer, Berlin (1997)
8. Gurson, A.L.: Continuum theory of ductile rupture by void nucleation and growth—part I: yield criteria and flow rules for porous ductile media. J. Eng. Mater. Technol. **99**, 2–15 (1977)
9. Kammoun, Z., Pastor, F., Smaoui, H., Pastor, J.: Large static problem in numerical limit analysis: a decomposition approach. Int. J. Numer. Anal. Methods Geomech. **34**, 1960–1980 (2010)
10. Leblond, J.B., Perrin, G., Suquet, P.: Exact results and approximate models for porous viscoplastic solids. Int. J. Plast. **10**, 213–235 (1994)
11. Lee, B., Mear, M.: Axisymmetric deformation of power-law solids containing a dilute concentration of aligned spheroidal voids. J. Mech. Phys. Solids **40**, 1805–1836 (1992)
12. MOSEK ApS: C/O Symbion Science Park, Fruebjergvej 3, Box 16, 2100 Copenhagen ϕ, Denmark (2002)
13. Monchiet, V., Cazacu, O., Charkaluk, E., Kondo, D.: Macroscopic yield criteria for plastic anisotropic materials containing spheroidal voids. Int. J. Plast. **24**, 1158–1189 (2008)
14. Monchiet, V., Charkaluk, E., Kondo, D.: An improvement of Gurson-type models of porous materials by using Eshelby-like trial velocity fields. C. R., Méc. **335**, 32–41 (2007)
15. Pastor, F., Kondo, D., Pastor, J.: Numerical limit analysis bounds for ductile porous media with oblate voids. Mech. Res. Commun. **38**, 250–254 (2011)
16. Pastor, F., Loute, E., Pastor, J.: Limit analysis and convex programming: a decomposition approach of the kinematical mixed method. Int. J. Numer. Methods Eng. **78**, 254–274 (2009)
17. Pastor, J.: Analyse limite: détermination numérique de solutions statiques complètes. Application au talus vertical. J. Méc. Appl. **2**, 167–196 (1978)
18. Pastor, J., Castaneda, P.P.: Yield criteria for porous media in plane strain: second-order estimates versus numerical results. C. R., Méc. **330**, 741–747 (2002)
19. Pastor, J., Francescato, P., Trillat, M., Loute, E., Rousselier, G.: Ductile failure of cylindrically porous materials. part II: other cases of symmetry. Eur. J. Mech. A, Solids **23**, 191–201 (2004)
20. Thai-The, H., Francescato, P., Pastor, J.: Limit analysis of unidirectional porous media. Mech. Res. Commun. **25**, 535–542 (1998)
21. Thoré, P., Pastor, F., Kondo, D., Pastor, J.: Hollow sphere models, conic programming and third stress invariant. Eur. J. Mech., A Solids (2010, in press)
22. Thoré, P., Pastor, F., Pastor, J., Kondo, D.: Closed form solutions for the hollow sphere model with Coulomb and Drucker-Prager materials under isotropic loadings. C. R. Méc., Acad. Sc. Paris **337**, 260–267 (2009)
23. Trillat, M., Pastor, J.: Limit analysis and Gurson's model. Eur. J. Mech. A, Solids **24**, 800–819 (2005)
24. Tvergaard, V.: Influence of voids on shear band instabilities under plane strain conditions. Int. J. Fract. Mech. **17**, 389–407 (1981)
25. Tvergaard, V., Needleman, A.: Analysis of the cup-cone fracture in a round tensile bar. Acta Metall. **32**, 157–169 (1984)